UNIVERSITY OF SOUTHAMPTON

FACULTY OF ENGINEERING AND THE ENVIRONMENT

Institute of Sound and Vibration Research

Tracking Sperm Whales Using Passive Acoustics And Particle Filters

by

Mark Lyndon Hadley

Thesis for the degree of Doctor of Philosophy

February 2011

UNIVERSITY OF SOUTHAMPTON

ABSTRACT

FACULTY OF ENGINEERING AND THE ENVIRONMENT

INSTITUTE OF SOUND AND VIBRATION RESEARCH

Doctor of Philosophy

TRACKING SPERM WHALES USING PASSIVE ACOUSTICS AND PARTICLE FILTERS

by Mark Lyndon Hadley

Passive acoustics provides a powerful tool for marine mammal research and mitigation of the risk posed by high energy anthropogenic acoustic activities through monitoring animal positions. Animal vocalisations can be detected and utilised in poor visibility conditions and while animals are dived. Marine mammal research is often conducted on restricted financial budgets by non-government organisations and academic institutions from boats or ships towing hydrophone arrays often comprising only two elements. The arrival time-delay of the acoustic wavefront from the vocalising animals across the array aperture is computed, often using freely available software, and typically regarded as the bearing of the animal to the array. This methodology is limited as it provides no ranging information and, until a boat manoeuvre is performed, whether the animal is to the left or right of the array remains ambiguous. Methods of determining range that have been suggested either negate the fact the animal is moving, rely on robust detection of acoustic reflections, rely on accurate equipment calibration and knowledge of the animal's orientation or require modification of hydrophone equipment.

There is a clear need to develop an improved method of estimating animal position as relative bearing, range and elevation to a hydrophone array or boat based on time-delay measurements. To avoid the costs of upgrading hydrophone arrays, and potentially the size of the vessels required to tow them, a software solution is desirable. This thesis proposes that the source location be modelled as a probability density function and that the source location is estimated as the mean. This is developed into a practical method using particle filters to track sperm whales. Sperm whales are the ideal subject species for this kind of development because the high sound pressure levels of their impulsive vocalisations (up to 236 dB re 1 μPa) makes them relatively simple to detect. Simulation tracking results demonstrate particle filters are capable of tracking a manoeuvring target using time-delay measurements. Tracking results for real data are presented and compared to the pseudotrack reconstructed from a tag equipped with accelerometers, magnetometers, a depth sensor and an acousitc recorder placed on the subject animal. For the majority of datasets the animal is tracked to a position relatively close to the surface sighting position. Sperm whales are typically encountered in groups, therefore a viable tracking solution needs to be capable of tracking multiple animals. A multiple hypothesis tracking method is proposed and tested for associating received vocalisations with animals, whereby vocalisations are correctly associated for periods exceeding 15 minutes.

Contents

List of Figures

List of Algorithms

List of Tables

List of Symbols

$\mathcal{A}$	State parameter sigma point vector
$\{\mathcal{A}\}_n$	State parameter sigma point vector set
A	System noise rejection function maximum gradient
A_1 to A_5	Defined in section 2.7.1
A^{amp}	Amplitude
$\mathbf{a}_k$	System state parameter vector at time k
$\mathbf{a}_k^{\text{car}}$	System state parameter vector at time k in Cartesian coordinates
$\mathbf{a}_k^{\text{MPC}}$	System state parameter vector at time k in modified polar coordinates
$\mathbf{a}_k^{\text{MSC}}$	System state parameter vector at time k in modified spherical coordinates
$\mathbf{a}\left(t_k\right)$	System state parameter vector at continuous time t_k
$\hat{\mathbf{a}}_k$	System state parameter vector estimate at time k
$\hat{\mathbf{a}}_{k\|k-1}$	System state parameter vector prediction at time k
$\hat{\mathbf{a}}_{k\|k}^{\text{MMSE}}$	Minimum mean squared error system state parameter vector estimate at time k
$\hat{\mathbf{a}}_{k\|k}^{\text{MAP}}$	Maximum a-priori system state parameter vector estimate at time k
$\bar{\mathbf{a}}_k$	Mean of a set of system state parameter vectors
$\check{\mathbf{a}}_k$	A term in someway related to $\mathbf{a}_k$
$\dot{\mathbf{a}}_k$	Velocity components of the system state parameter vector
$\ddot{\mathbf{a}}_k$	Maximum acceleration components of the system state parameter vector
$\ddot{\mathbf{a}}^{\max}$	Acceleration components of the system state parameter vector
$\{\mathbf{a}\}_n$	nth system state parameter vector of a set
$\mathcal{B}$	Measurement sigma point
$\{\mathcal{B}\}_n$	Set of measurement sigma points
B	The system parameter value at which point the maximum gradient of the system noise sample rejection function occurs
$\mathbf{b}_k$	Measurement vector at time k
$\hat{\mathbf{b}}_{k\|k-1}$	Measurement vector prediction at time k

$\tilde{\mathbf{b}}_k$	Measurement innovation vector at time k
$\mathbf{C}$	MHT hypothesis matrix
C	The offset of the system noise sample rejection function
c	Effective sound propagation speed
d	Separation between acoustic receivers
$d^{\text{front,rear}}$	Separation between the front and rear hydrophone element pairs
d_k^{tow}	The length of the hydrophone array tow cable
$\mathbb{E}\{\ \}$	Expectation operator
$\mathbf{e}_k$	System noise vector at time k
$\mathbf{e}(t_k)$	System noise vector at continuous time t_k
e_x	System noise x-dimension position sample
$e_{\dot{x}}$	System noise x-dimension velocity sample
$e_{\ddot{x}}$	System noise x-dimension acceleration sample
e_y	System noise y-dimension position sample
$e_{\dot{y}}$	System noise y-dimension velocity sample
$e_{\ddot{y}}$	System noise y-dimension acceleration sample
e_z	System noise z-dimension position sample
$e_{\dot{z}}$	System noise z-dimension velocity sample
$e_{\ddot{z}}$	System noise z-dimension acceleration sample
$\mathbf{F}$	Time invariant system matrix
$\mathbf{F}_k$	Time variant system matrix
$\boldsymbol{f}_k(\ )$	Time variant measurement function
$\boldsymbol{f}(\ )$	Time invariant measurement function
$\mathbf{G}_{k-1}$	Time variant system noise scaling matrix
$\boldsymbol{g}(\ )$	Abstract function
$\mathbf{H}$	Time invariant measurement matrix
$\mathbf{H}_k$	Time variant measurement matrix
$\boldsymbol{h}_k(\ )$	Time variant measurement function
$\boldsymbol{h}(\ )$	Time invariant measurement function
$\boldsymbol{h}^{\text{signal}}(\ ,\{\boldsymbol{\Theta}_k\}_n)$	Transfer function determined by the propagation channel parameters $\{\boldsymbol{\Theta}_k\}_n$
$\mathbf{I}$	Identity matrix
I	Abstract integral
$\hat{I}$	Abstract integral approximation
$\tilde{I}$	Abstract integral approximation error
$\mathbf{i}$	MHT constraint uniform vector, $[1, 1, \ldots, 1]'$
$\mathbf{J}$	Meant adaptive motion model adaptation matrix
j	Imaginary number, $\sqrt{-1}$
$\mathbf{K}_k$	Kalman gain matrix
k	Time index
$\mathbf{L}$	Control vector scaling matrix

$\mathbf{l}$	MHT track scores vector
$\mathbf{l}^{\text{2nd}}$	MHT secondary track scores vector
l_k	MHT track score
l_k^{2nd}	MHT secondary track score
$l_{\text{threshold}}^{\text{2nd}}$	MHT secondary track score inactive track threshold
M	Secondary end index
m	Secondary indexing
$\mathcal{O}(\,)$	order of
$\mathcal{N}(\,)$	Normal distribution function
N	Primary end index
$N_{\mathcal{A}}$	Number of state parameter sigma points
$N_{\mathbf{a}}$	State parameter vector dimensionality $\mathbf{a}$
N_a	Number of state parameter vector in a set
$N_{\mathbf{b}}$	State parameter vector dimensionality $\mathbf{b}$
$N_{\mathbf{r}}$	Number of receivers in a set
$N_{\mathbf{w}}$	Number of particle weights in a set
N_{eff}	Number of effective particles
$\hat{N}_{\text{eff}}$	Approximate number of effective particles
N_{meas}	Number of measurements utilised in MHT tracker
N_{thresh}	Threshold for number of effective particles
n	Primary indexing
$\{n\}_m$	mth index in a set of indices
$\mathbf{P}_{k\|k-1}$	Mean square error matrix prediction at time k
$\mathbf{P}_{k\|k}$	Mean square error matrix at time k
$p(\,)$	Probability density function
$\mathbf{Q}$	System noise variance scaling matrix for position and velocity
$\mathbf{Q}_3$	System noise variance scaling matrix for position, velocity and acceleration
$q(\,)$	Importance density function
$q(\,)_{\text{opt}}$	Optimal importance density function
$q(\,)_{\text{prior}}$	Importance density function derived from transitional prior density
$q(\,)_{\text{LLPF}}$	Locally linearised particle filter importance density function
$\mathbb{R}$	Set of real numbers
$\mathbf{R}$	Matrix of sensor positions
$\mathbf{R}_{\mathbf{aa}}$	Auto-covariance matrix of vector $\mathbf{a}$
$\mathbf{R}_{\mathbf{ab}}$	Cross-covariance matrix of vectors $\mathbf{a}$ and $\mathbf{b}$
$\mathbf{r}_k$	Receiver position at time k
$\{\mathbf{r}_k\}_n$	The nth receiver at time k
r_k	Target slant range from receiver/receiver array
$\dot{r}_k$	Rate of change of target range from receiver/receiver array

r^{horiz}	Horizontal range between target and receiver/receiver array
$r^{\text{horiz,rear}}$	Horizontal range between target and rear hydrophone pair in section 2.7.1
$r^{\text{direct,front}}$	Slant range of an acoustic source to the front hydrophone pair, section 2.7.1
$r^{\text{direct,rear}}$	Slant range of an acoustic source to the rear hydrophone pair, section 2.7.1
$r^{\text{front,rear}}$	The difference in direct acoustic propagation slant ranges between the front and rear hydrophone element pairs 2.7.1
$r^{\text{direct-rear,reflec-rear}}$	The difference in direct and reflected slant ranges of an acoustic source to the rear hydrophone pair, section 2.7.1
$\mathbf{s}_k$	Time series signal vector at k
$\mathbf{s}_k(n)$	Time series vector for signal on channel n at time k
$\mathbf{s}_k^{\text{source}}$	Time series vector for signal at source at time k
$\mathbf{s}_k^{\text{beam}}$	Time series vector for signal output by a beam-former
$\mathcal{T}$	Manoeuvre time constant
T	Time invariant sampling period
T_k	Time variant sampling period
$t(n)$	Acoustic propagation time to receiver n
t_k	Continuous time t at discrete time index k
$\mathcal{U}[\,]$	Uniform distribution function
$\mathbf{u}_k$	Deterministic system control vector at time k
$\mathbf{u}(t_k)$	Deterministic system control vector at continuous time t_k
$\mathbf{v}_k$	Measurement noise vector at time k
$\mathbf{v}_k(n)$	Measurement noise time series vector on channel n
$\mathcal{W}$	Sigma point weight
$\{\mathcal{W}\}_n$	nth sigma point weight in a set
$w^*_{m,n}$	mth FIR filter nth coefficient
$\tilde{w}(\,)$	Un-normalised weighting function
$\tilde{w}$	Un-normalised particle weight
$w(\,)$	normalised weighting function
w	particle weight
w_k	particle weight at time k
$\{w\}_n$	nth particle weight of a set
x	Cartesian coordinate system x-dimension position
$\dot{x}$	Cartesian coordinate system x-dimension velocity
$\ddot{x}$	Cartesian coordinate system x-dimension acceleration
y	Cartesian coordinate system y-dimension position
$\dot{y}$	Cartesian coordinate system y-dimension velocity
$\ddot{y}$	Cartesian coordinate system y-dimension acceleration
z	Cartesian coordinate system z-dimension position
$\dot{z}$	Cartesian coordinate system z-dimension velocity

$\ddot{z}$	Cartesian coordinate system z-dimension acceleration
z^{whale}	Whale depth in section 2.7.1
z^{rear}	Rear hydrophone pair depth in section 2.7.1
z^{-1}	Filter delay one sample in figure 2.5
α	Received angle of an acoustic wavefront
$\alpha^{\text{direct,rear}}$	Received angle of an acoustic wavefront via the direct propagation path to the front element pair in section 2.7.1
α^{global}	Received angle of an acoustic wavefront between the front and rear hydrophone pairs propagating via direct propagation paths in section 2.7.1
β_k	Target heading relative to observer heading at time k
$\dot{\beta}_k$	Target heading angular velocity at time k
γ_k	Target pitch angle relative to horizontal at time k
$\dot{\gamma}_k$	Target pitch angular velocity at time k
$\mathbf{\Gamma}_{\mathbf{s}(n)\mathbf{s}(m)}(\omega)$	Coherence function of signals on channels n and m
$\mathbf{\Delta}$	Difference in parameter affecting a vector or matrix
δ	Difference in parameter affecting a value
$\delta\,()$	Delta function
$\{\epsilon\}_n$	nth sample in a discrete approximation of a cumulative density function
ζ	Singer motion model parameter
η	Singer motion model parameter
$\mathbf{\Theta}_k$	Propagation channel parameter vector at time k
$\hat{\mathbf{\Theta}}_k$	Propagation channel parameter vector estimate at time k
$\Theta_k(n)$	nth propagation channel parameter at time k in chapter 2 and control vector rotation matrix in chapter 4
$\{\mathbf{\Theta}_k\}_n$	Propagation channel n parameter vector at time k
$\dot{\theta}_k^{\text{boat}}$	Boat heading angular velocity at time k
$\boldsymbol{\iota}$	Defined in (2.28)
$\{\mu\}_m$	mth sample drawn from a uniform distribution
$\nu^{\text{local,rear}}$	The inclination angle of the front hydrophone element pair in section 2.7.1
ν^{global}	The inclination angle from the rear to the front hydrophone element pair in section 2.7.1
ξ	Hypothesis which is most likely associated with the measurement $\mathbf{b}_{k-N_{\text{meas}}}$
$\boldsymbol{\rho}$	Beam-forming steering vector
ρ_1, ρ_2, ρ_3	Defined in (2.30), (2.30), (2.30)
σ	MHT design parameter
$\boldsymbol{\tau}$	Vector of arrival time-delays of an acoustic wavefront between one receiver and multiple others

τ	Arrival time-delay of an acoustic wavefront across two receivers
$\dot{\tau}$	Rate of change in time-delay
$\tau(1,n)$	Arrival time-delay of an acoustic wavefront across receivers 1 and n
υ	Target speed
υ_k	Target speed at time k
υ_k^{boat}	Boat speed at time k
Φ_k	Vector describing MHT hypothesis trees
ϕ	Bearing of an acoustic of target to receiver/receiver array
$\dot{\phi}$	Bearing angular velocity of target to receiver/receiver array
$\boldsymbol{\chi}(\,)$	Target speed sample rejection function
$\Psi(\,)$	Least squares error function
ψ	Elevation angle of target to receiver/receiver array
$\dot{\psi}$	Elevation angular velocity of target to receiver/receiver array
$\boldsymbol{\Omega}_{\mathbf{s}(n)\mathbf{s}(m)}(\omega)$	Cross-power spectra of signals on channels n and m
$\boldsymbol{\Omega}_{\mathbf{s}(n)\mathbf{s}(n)}(\omega)$	Auto-power spectra of signal on channel n
ω	Angular velocity
$F(\,)$	Abstract function
$\exp\{\,\}$	Exponent
$\text{var}\{\,\}$	Variance

Academic Thesis: Declaration Of Authorship

I, Mark Hadley

declare that this thesis and the work presented in it are my own and has been generated by me as the result of my own original research.

Tracking Sperm Whales Using Passive Acoustics and Particle Filters

I confirm that:

1. This work was done wholly or mainly while in candidature for a research degree at this University;

2. Where any part of this thesis has previously been submitted for a degree or any other qualification at this University or any other institution, this has been clearly stated;

3. Where I have consulted the published work of others, this is always clearly attributed;

4. Where I have quoted from the work of others, the source is always given. With the exception of such quotations, this thesis is entirely my own work;

5. I have acknowledged all main sources of help;

6. Where the thesis is based on work done by myself jointly with others, I have made clear exactly what was done by others and what I have contributed myself;

7. Either none of this work has been published before submission, or parts of this work have been published as: [please list references below]:

Signed: Mark Hadley

Date: 13th June 2011

Acknowledgements

Firstly the biggest thank you goes to Professor Paul White for his supervision, help and advice over the last few years and especially his willingness to put down whatever he was doing when I wondered into his office, took a seat and started asking questions and for advice on whatever I happened to be having problems with. I couldn't have done it without you Paul! I also need to thank Professor Tim Leighton, my co-supervisor.

A big thank you goes to Dr. Patrick Miller at the Sea Mammal Research Unit at the University of St. Andrews and his team, Ana Catarina Alves, Riccardo Antunes, Eva Hartvig and Filipa Samarra. It was through Patrick that we were able to take part in the 3S project field work which provided the data used in the results chapters of this thesis, without which I would have had great difficulty finding a dataset with towed array recordings and DTAG data. Ana, Riccardo, Eva and Filipa put up with my endless questions and bugging!

Another huge thank you goes to the Song of the Whale team, both the former IFAW members and the current MCR members, Richard McLanaghan, Anna Moscrop, Oliver Boisseau, Tim Lewis, Claire Lacey, Magnus Danbolt, Bridget Jones and Mat Jerram. Song of the Whale was the first boat I went to sea on and over the last few years was my home for several months. Thanks to Richard and Anna for taking me on as a field assistant for the 2007 field season, Tim and Olly for providing me with data for the work in earlier stages of this project, Claire for teaching me there is more than one type of dolphin and Mat for the sophistcated conversation and cups of tea on night watches!

It was the time I spent on Song of the Whale that inspired the towed hydrophone array direction this work took and set the precedent that everything I developed should be practical and useable with the equipment carried by SOTW and the many similar style of marine mammal research vessels in operation.

And finally thanks to my Mum and Dad.

Chapter 1

Introduction

Acoustics play a key role in marine mammal research, specifically on cetaceans. As anthropogenic ocean activity, and therefore oceanic noise, increases so too do the needs for research on marine mammals and methods for the mitigation of the potential harm they may be subject too. This thesis presents a novel method for tracking dived and vocalising marine mammals using two element towed hydrophone arrays.

1.1 Acoustics in Marine Mammal Research

Passive acoustics provides a powerful tool in the study of marine mammals. Acoustics can be utilised to detect vocalising animals that are dived and when visibility conditions are poor such as during bad weather and at night. How powerful a tool passive acoustics provides depends on the subject species, sperm whales are particularly vocal and produce clicks at high sound pressure levels so can be detected relatively easily and from greater ranges than species that are less vocal and vocalise at lower sound pressure levels. Establishing range estimates from acoustics is also often a non-trivial task. A wide variety of acoustics themed literature covering research utilising acoustics and developing acoustic based research methodologies exists. Research where acoustics have been utilised include regional population studies [1–6], local population density estimates [7], behavioural studies [8–13] and physical vocalising structures and vocalisation waveforms [14–19]. The literature developing acoustics based methodologies covers localisation from fixed hydrophone arrays [20–27], localisation from towed hydrophone arrays [28–30], detection and classification [31–34] and investigations into detection rates and array configurations [35–37]. These methods have been developed for a variety of subject species including sperm whales (*Physeter macrocephalus*) [3], Cuvier's beaked whales (*Ziphius cavirostris*) [11], Blainville's beaked whales (*Mesoplodon densirostris*) [6], harbour porpoises (*Phocoena phocoena*) [4], blue whales (*Balaenoptera musculus*) [12], fin whales (*Balaenoptera physalus*) [2], north Atlantic right whales (*Eubalaena glacialis*) [8] and bowhead whales (*Balaena mysticetus*) [1].

1.2 Anthropogenic Acoustic Threats to Marine Mammals

Recently there has been growing concern regarding the impact of anthropogenic noise on marine mammals, particularly from military active sonar exercises and seismic surveying for oil and gas [38–41]. Military active sonar exercises are regarded as responsible for several mass cetacean stranding events [42], particularly of beaked whales, notably May 1996 in Greece [43], March 2000 in the Bahamas [44] and September 2002 in the Canary Islands [45–47]. To mitigate the risk posed by these kinds of activities it is necessary to monitor for the presence of marine mammals, for which acoustics provides a useful tool.

1.3 Towed Hydrophone Arrays

The most common hydrophone array configuration utilised in many marine mammal acoustic based research projects is a towed hydrophone array consisting of two hydrophone elements spaced between 25 cm and 300 cm [3–5, 12]. These hydrophone array configurations provide a single time-delay measurement representing the difference in arrival time of an acoustic wavefront between the receivers. This time-delay is commonly assumed to be a measure of bearing of the animal from the axis between the two receiving sensors where it remains ambiguous as to whether the source animal is to the left or right of the array and how far the animal is. Resolving the left-right ambiguity is possible by manoeuvring the array and observing the change in measured time-delay [3]. The time-delay measurement is, in fact, a function of both the animal horizontal bearing and vertical elevation angles, therefore the ambiguity of the animal's position is characterised as a hyperboloid centred on the array axis. It has been proposed that range can be resolved using acoustic reflections [28, 29, 48], triangulation [3] or received sound pressure levels [20]. All three of these methods suffer from major drawbacks, surface reflections often can not be robustly detected, triangulation methods fail to account for the motion of the animal and the use of sound pressure levels requires knowledge of environmental parameters, vocalisation directionality properties that are unlikely to be available and accurate equipment calibration.

Appropriate computer software, such as PAMGUARD [49], can compute an assumed horizontal angle from which vocalisations are received given the measured time-delay. When operated by a suitably skilled individual such a tracking system can be effective, however, reliability is dependent on the operator's tracking skills. As the number of vocalising animals increases so too does the workload placed on the operator and the effectiveness of the tracking system is likely to decrease. Range information can be acquired through triangulation by using two pairs of hydrophone elements in the array so that two time-delay measurements are computed for each received click. However, even if utilising arrays comprising of two hydrophone element pairs, a left-right ambiguity remains and depth information can not be established without robust detection of acoustic reflections. Many marine mammal research projects operate with limited financial resources so acquisition of new hydrophones arrays or larger towing vessels, required for towing larger hydrophone arrays, may not be possible.

A clear need exists for a robust automated software based tracking method capable of estimating bearing, range and elevation of an animal from time-delay measurements from any configuration of towed hydrophone array, particularly two element arrays. Developments for two element hydrophone arrays could later be expanded to include the additional information provided by additional elements as future work. It is proposed that estimating these parameters from successive time-delay measurements can be achieved by modelling the source location ambiguity as a probability density function (PDF) so that all possible locations can be modelled and maintained between estimate updates. A point representing the source location can then be estimated as the mean of the PDF.

1.4 Particle Filters and the Proposed Tracking Solution

Tracking filters are recursive Bayesian estimators that have been utilised in various forms in tracking applications since the 1960s when Kalman first reported development of the Kalman filter [50]. Target states are estimated from a prior distribution that models how the system evolves over time and the measurement PDF defined by the measurement and statistical parameters of the measurement noise process. Particle filters are a category of tracking filter based on sequential Monte-Carlo simulations that became a practical solution to tracking problems in 1993 when the necessary computing power became readily available [51–54].

Particle filters have been utilised in a variety of applications including maritime and aviation angle-only measurement tracking [55], navigation [56] and computer vision [57]. Particle filters have been widely reported to provide effective tracking solutions where the measurements are angle-only measurements and the problem is to estimate target range [55,58–61]. It is proposed that by applying similar methods the bearing, range and elevation angle of a whale can be passively tracked from the time-delay measurements measured across the array aperture.

Sperm whales are the ideal candidate species for developing tracking methods because the impulsive characteristics, source sound pressure levels (up to 236 dB re 1 μPa peak-to-peak) and central frequency (15 kHz) of their vocalisations allows for propagation over significant ranges rendering them relatively easy to detect [13–16].

1.5 Thesis Structure

Chapter 2 discusses acoustic localisation methods generally and those developed specifically for tracking sperm whales. Chapter 2 then proceeds to develop and describe in more detail the proposed tracking method. The conceptual tracking problem and its solution are presented in chapter 3; followed by derivation of the Kalman filter, discussions of the extended and unscented Kalman filters, a conceptual derivation of the particle filter and discussion of the sampling importance re-sampling (SIR), auxiliary SIR and locally linearised particle filters. Application of tracking filters, namely the SIR particle filter, to sperm whale tracking

is discussed. Chapter 4 discusses motion modelling, tracking coordinate systems and sperm whale motion. Following these sections an appropriate sperm whale tracking motion model is developed and coordinate system presented. Chapter 5 tests the proposed tracking system on simulated data. The complexity of the problem is increased over the course of the chapter to test the algorithm's performance and consistency. Sperm whales are often encountered in groups, therefore a viable tracking solution needs to be capable of correctly associating each received vocalisation with the individual animal that produced it. Chapter 6 addresses this issue using a multiple hypothesis tracker. Tracking of real sperm whales with the developed algorithms is presented in chapter 7. Conclusions and suggestions for further work are discussed in chapter 8.

This thesis makes the following contributions to tracking and marine mammal research:

1. Proposition that acoustic localisation of a sperm whale using a two element towed array should model the ambiguity of the animal's position as a PDF where the mean of the PDF is regarded as the animal location.

2. Modelling sperm whale motion so that changes in heading, pitch and speed are normally distributed but speed samples are subject to a rejection function that prevents the model achieving unrealistically high speeds due to a lack of range information in the measurements.

3. An MHT based algorithm to associate received vocalisations with click trains from individual animals and discriminate against clutter using the time-delay measurement for each received click.

4. Implementation of spatial tracking using particle filtering to localise the animal using time-delay measurements from a two element towed hydrophone array.

Chapter 2

Acoustic Localisation

Acoustic localisation is the computation of the position of an acoustic source via an array of acoustic sensors in known positions. Source location is computed based on differences in propagation time of the sound from source to each receiver. The configuration of the array depends on the application and the environment. For acoustic sperm whale tracking the hydrophone array is most commonly of a linear configuration so that it can easily be towed behind a boat, however fixed wide or small aperture arrays may also be used.

This chapter reviews current methods of localising an acoustic source, in particular sperm whales and other marine mammals using either a fixed hydrophone array or a towed array. Section 2.1 conceptualises the localisation problem as the inverse of the forward propagation model. Computation of arrival time differences are discussed in section 2.2 and beamforming as a method of determining the direction of an acoustic source is described in section 2.3. A discussion on hydrophone array configurations is presented in section 2.4 and using surface reflection detections to create virtual sensors is described in section 2.5. Localisation methods for both fixed and towed hydrophone arrays are presented in sections 2.6 and 2.7. Finally the proposed novel method of localising using tracking filters in conjunction with towed linear arrays is presented in section 2.8.

2.1 Localisation Problem

Propagation of an acoustic wavefront from an acoustic source at position $\mathbf{a}_k$ to a set of $N_{\mathbf{r}}$ receivers at positions $\{\mathbf{r}_k\}_{1:N_{\mathbf{r}}}$ to give a set of measured delays $\mathbf{b}_k$ can be modelled as [22]:

$$\mathbf{b}_k = \boldsymbol{h}\left(\mathbf{a}_k; \boldsymbol{\Theta}_k\right) + \mathbf{v}_k \tag{2.1}$$

where $\boldsymbol{h}$ models the function transforming the position of the acoustic source to the measured time-delays, $\boldsymbol{\Theta}_k$ are the parameters affecting the propagation channels at time k such as water temperature and salinity [62] and $\mathbf{v}_k$ is a noise process that characterises the errors in the time-delay measurement process.

The model (2.1) can be inverted to provide a conceptual solution to the localisation problem whereby the acoustic source location is:

$$\mathbf{a}_k = \boldsymbol{h}^{-1}\left(\mathbf{b}_k; \boldsymbol{\Theta}_k\right) \tag{2.2}$$

The noise term $\mathbf{v}_k$ has been omitted because it is unknown. Omission can be justified if $\mathbf{v}_k$ is assumed to be a normally distributed zero-mean random process so that $\mathbb{E}\{\mathbf{v}_k\} = 0$. It is unlikely that the exact channel parameters $\boldsymbol{\Theta}_k$ will be available, especially when the propagation medium is sea water, in this case an assumed or estimated parameter set $\hat{\boldsymbol{\Theta}}_k$ may be used instead so that the approximated inverse of (2.1) is [22]:

$$\hat{\mathbf{a}}_k = \boldsymbol{h}^{-1}\left(\mathbf{b}_k; \hat{\boldsymbol{\Theta}}_k\right) \tag{2.3}$$

Two sources of error exist, if $\hat{\boldsymbol{\Theta}}_k \neq \boldsymbol{\Theta}_k$ then $\hat{\mathbf{a}}_k \neq \mathbf{a}_k$ and the effects of $\mathbf{v}_k$ have been ignored.

If statistical parameters of $\mathbf{v}_k$ are known then localised linear approximations of the model can be made to evaluate the effects of $\mathbf{v}_k$ on $\hat{\mathbf{a}}_k$ [22]. The effects of errors in a single model parameter $\hat{\Theta}_k(n)$ can also be quantified as a change in source location $\delta\hat{\mathbf{a}}_k$ given the change in that parameter:

$$\delta\hat{\mathbf{a}}_k = \frac{\Delta\boldsymbol{h}^{-1}\left(\mathbf{b}_k; \hat{\boldsymbol{\Theta}}_k\right)}{\delta\Theta_k(n)}\delta\Theta_k(n) \tag{2.4}$$

where $\Theta_k(n)$ is the nth component of the propagation parameter vector $\boldsymbol{\Theta}_k$ and $\Delta\boldsymbol{h}^{-1}\left(\mathbf{b}_k; \hat{\boldsymbol{\Theta}}_k\right)/\delta\Theta_k(n)$ is the model sensitivity. Generally sources closer to the geometric centre of the array are less sensitive to errors in model parameters [22].

2.2 Time-Delay Estimation

A sound wavefront propagating from source position $\mathbf{a}_k$ to sensors at positions $\{\mathbf{r}_k\}_1$ and $\{\mathbf{r}_k\}_2$ will arrive at each sensor with a time difference τ, so that the received signals can be modelled as [63, 64]:

$$\mathbf{s}_k(1) = \boldsymbol{h}_k^{\text{signal}}\left(\mathbf{s}_k^{\text{source}}, \{\boldsymbol{\Theta}_k\}_1\right) + \mathbf{v}_k(1) \tag{2.5}$$

$$\mathbf{s}_k(2) = \boldsymbol{h}_{k+\tau}^{\text{signal}}\left(\mathbf{s}_k^{\text{source}}, \{\boldsymbol{\Theta}_k\}_2\right) + \mathbf{v}_k(2) \tag{2.6}$$

where $\boldsymbol{h}_k^{\text{signal}}(\ )$ represents the combined transfer function of the acoustic propagation channel from source to receiver and the transfer function of receiving equipment, $\mathbf{s}_k^{\text{source}}$ is the acoustic signal at the source, $\mathbf{s}_k(1)$ is the signal received on channel 1 and $\mathbf{v}_k(1)$ is a noise process affecting the signal received on channel 1. The arrival time-delay τ can be found by cross-correlating the two signals:

$$\mathbf{s}_k(1) \bigstar \mathbf{s}_k(2) = \sum_{k=-\infty}^{\infty} \mathbf{s}_\tau(1)\mathbf{s}_{k+\tau}(2) \tag{2.7}$$

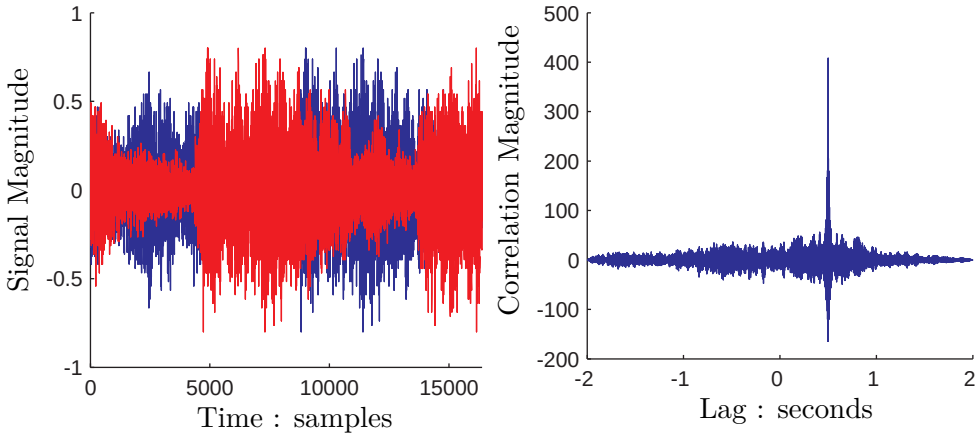

(a) A sperm whale click received by two acoustic sensors at different positions

(b) The cross-correlation function of the two signals in (a)

Figure 2.1: The signals received from the same acoustic wavefront arriving at two spatially separated sensors are shown in (a). The cross-correlation function of the two signals is shown in (b). The peak in the cross-correlation function indicates the arrival time-delay between the two sensors.

where ★ denotes cross-correlation function the maximum of which is at lag τ which corresponds to the arrival time-delay. An example of the cross-correlation process for measuring time-delay is shown in figure 2.1. Figure 2.1(a) shows the signals of a sperm whale click received by two acoustic sensors, one in red and one in blue. The cross-correlation function of the two signals is shown in figure 2.1(b), where the peak in the function represents the point of maximum correlation and therefore the delay in arrival.

If the source is at long range it can be assumed that the source is in the array's far-field and that the wavefront is planar. Given the distance between the sensors and the effective propagation speed of the wavefront then the time-delay τ can be transformed to a received angle α. This angle is the direction of the source from the axis of the sensor pair, so that a forward end-fire arrival is 0 rads and rearward end-fire arrival is π rads:

$$\alpha = \cos^{-1} \frac{c}{d}\tau \tag{2.8}$$

where d is the distance between the sensors and c is the effective sound propagation speed. The angle α is a function of bearing, ϕ,and elevation, ψ, of the source from the sensor pair:

$$\alpha = \cos^{-1} (\cos\psi \cos\phi) \tag{2.9}$$

Multiple solutions satisfy this function for any given α. The time-delay (and hence α) is independent of source range, therefore if ϕ and ψ are unchanged but the source range is decreased or increased the time-delay will remain the same. In practice this causes a source location ambiguity whereby the source can lie anywhere on the surface of a hyperboloid centred on the axis between the sensors. In 2D (no elevation parameter) ϕ and α are equal and the ambiguity is a hyperbola [65], as illustrated in figure 2.2.

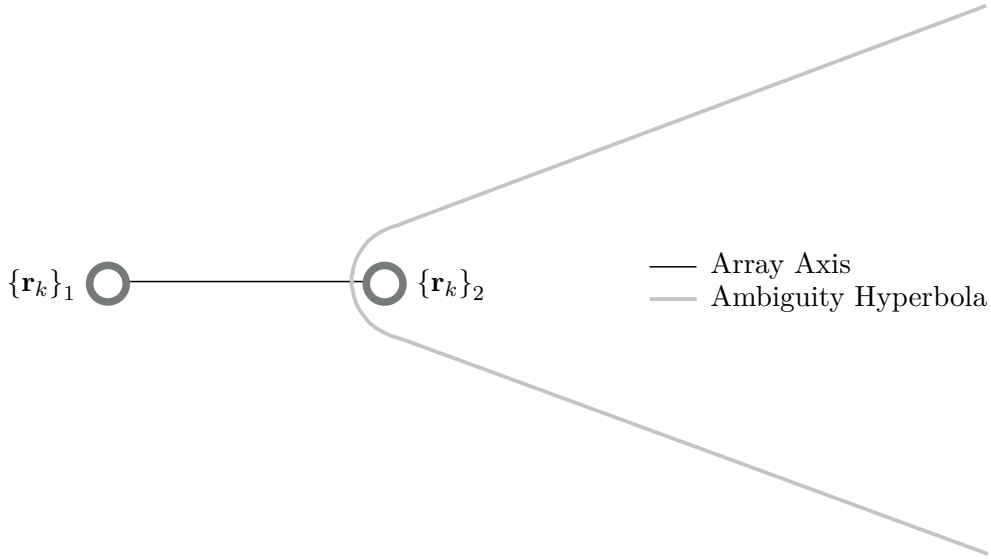

Figure 2.2: The hyperbola shaped source location ambiguity curve obtained from time-delay τ

2.2.1 Measurement Error

Typically the signals will be processed digitally so τ will be measured in samples which results in a quantisation error in the computation of α. This error can be quantified using a first-order Taylor series expansion. The received angle can be described as the cosine function of an arrival $\pm$ some variation (or error) $\delta\tau$:

$$\alpha = \cos^{-1}\left(\frac{c}{d}\tau + \frac{c}{d}\delta\tau\right) \tag{2.10}$$

The first-order Taylor series approximation is:

$$\boldsymbol{g}\left(x + \delta x\right) \simeq \boldsymbol{g}\left(x\right) + \delta x \boldsymbol{g}'\left(x\right) \tag{2.11}$$

In the case of the inverse cosine function the first order Taylor series terms are:

$$\boldsymbol{g}\left(x\right) = \cos^{-1} x \quad \boldsymbol{g}'\left(x\right) = -\frac{1}{\sqrt{1-x^2}} \tag{2.12}$$

Applying the terms of (2.12) to (2.10) and substituting into (2.11) yields:

$$\alpha \simeq \cos^{-1}\frac{c}{d}\tau - \frac{c}{d}\frac{\delta\tau}{\sqrt{1-\tau^2}} \tag{2.13}$$

If the first term of (2.13) is the clean reception angle given τ then the variance of the distribution is given by the square of the second term:

$$\mathrm{var}\left\{\alpha\right\} = \frac{c^2 \mathrm{var}\left\{\delta\tau\right\}}{d^2\left(1-\tau^2\right)} \tag{2.14}$$

This shows that if $\mathrm{var}\left\{\tau^c/_d\right\}$ is fixed, then as $|\tau^c/_d|$ increases so too does $\mathrm{var}\left\{\alpha\right\}$. In practice this means there is a measurement error due to quantisation that increases as the target angle

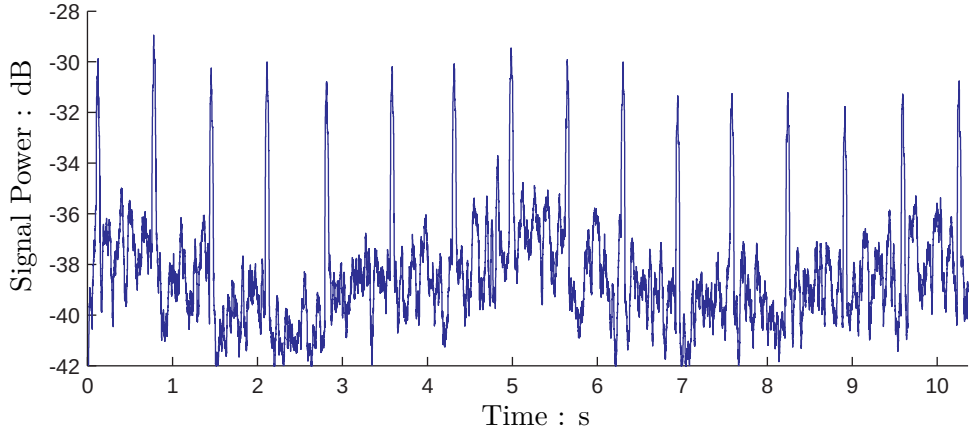

Figure 2.3: The signal envelope of a sperm whale click train

nears end-fire.

2.2.2 Time-Delay Coherence

The robustness of cross-correlation for time-delay estimation is largely dependent on the coherence of the signals received on the two sensors. The coherence function $\mathbf{\Gamma}_{\mathbf{s}(1)\mathbf{s}(2)}(\omega)$ is defined as the cross-power spectrum of signals received by the two sensors, $\mathbf{\Omega}_{\mathbf{s}(1)\mathbf{s}(2)}(\omega)$, over the square root of the product of the two auto-power spectra, $\mathbf{\Omega}_{\mathbf{s}(1)\mathbf{s}(1)}(\omega)$ and $\mathbf{\Omega}_{\mathbf{s}(2)\mathbf{s}(2)}(\omega)$ of the two signals, [64]:

$$\mathbf{\Gamma}_{\mathbf{s}(1)\mathbf{s}(2)}(\omega) = \frac{\mathbf{\Omega}_{\mathbf{s}(1)\mathbf{s}(2)}(\omega)}{\sqrt{\mathbf{\Omega}_{\mathbf{s}(1)\mathbf{s}(1)}(\omega)\,\mathbf{\Omega}_{\mathbf{s}(2)\mathbf{s}(2)}(\omega)}} \tag{2.15}$$

If coherence is low, $\mathbf{\Gamma}_{\mathbf{s}(1)\mathbf{s}(2)}(\omega) \ll 1$, then there is more likely to be error in the time-delay estimation and therefore error in the respective received angle as described in section 2.2.1. Coherence is largely dependent on the signal-to-noise ratio (SNR) which decreases as the distance between the two sensors increases, therefore poor coherence is more likely to be a problem on large aperture arrays, such as bottom mounted sensors, than on small aperture arrays such as towed arrays and portable fixed arrays. Low coherence of sperm whale clicks on widely spaced sensors can be attributed to the directional characteristics of sperm whale vocalisations potentially causing the received signals to differ significantly [14, 16, 22]. Sperm whale clicks are also regular, without being exactly periodic, so multiple peaks can occur in the cross-correlation function and determining the correct peak may not be a trivial task. This problem may be compounded if the animal is significantly closer to one sensor than the other so that the click at time $k+1$ arrives at the near sensor before the click at time k arrives at the far sensor. The problem becomes even more involved in the presence of multi-path arrivals via surface or sea-floor reflections.

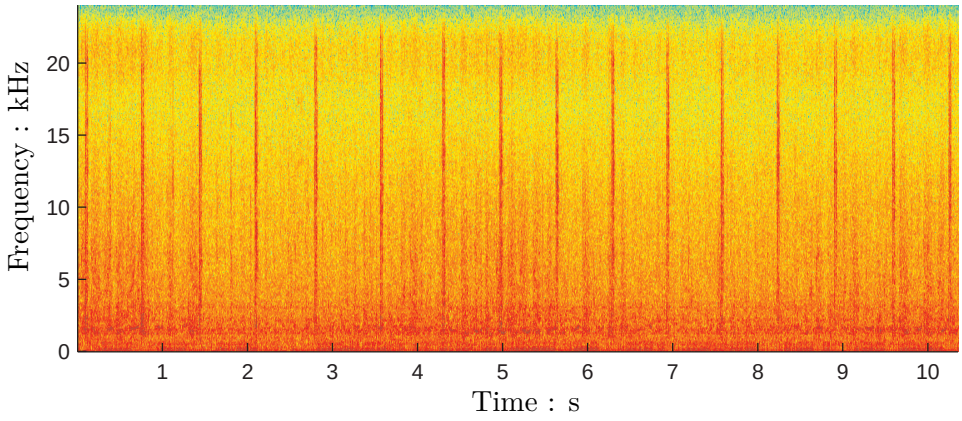

Figure 2.4: The spectrogram of a sperm whale click train. Clicks are visible as short duration wide-band impulses

2.2.3 Cross-correlation of Low Coherence Signals

Where it is not possible to extract robust cross-correlations using the received time domain signals it may be possible to cross-correlate transformed signals or evaluate time-delays based on a statistical analysis of the signals. One alternative to cross-correlating acoustic signals is to cross-correlate the signal envelopes. Typical sperm whale echo-location clicks have a duration of approximately 20 ms [13], therefore 20 ms is the logical window size for computing the power of the signals. An example of a click train envelope is shown in figure 2.3. If the cross-correlation function of the signal envelopes still includes multiple peaks then it is possible to compute a histogram of the correlation within a time-window [22]. The peak value of the histogram is taken to represent the correct delay. Further estimation is then possible by taking the mean of the delay values falling into the peak bin.

Time-delays can be computed by cross-correlating the spectrograms of the received signals or frequency contour maps derived from the spectrograms. The echo-location clicks are clearly visible in the spectrogram of figure 2.4 as short duration wide-band impulses. In the case of sperm whale clicks a click map can be produced from the spectrogram on each channel, essentially a binary string where '1' represents the presence of a click, these strings can then be cross-correlated. This is the system used by the United States Navy's Marine Mammal Monitoring on Navy Ranges (M3R) project [24]. When an acoustic signal includes multi-path arrivals it is typically useful to determine which correlation peak corresponds to the direct arrivals. In such cases the direct arrivals can be identified using an 'augmented-template correlation function' (ATCF) which is a cross-correlation of the non-negative lags of an auto-correlation function with the lags from a cross-correlation function [66, 67].

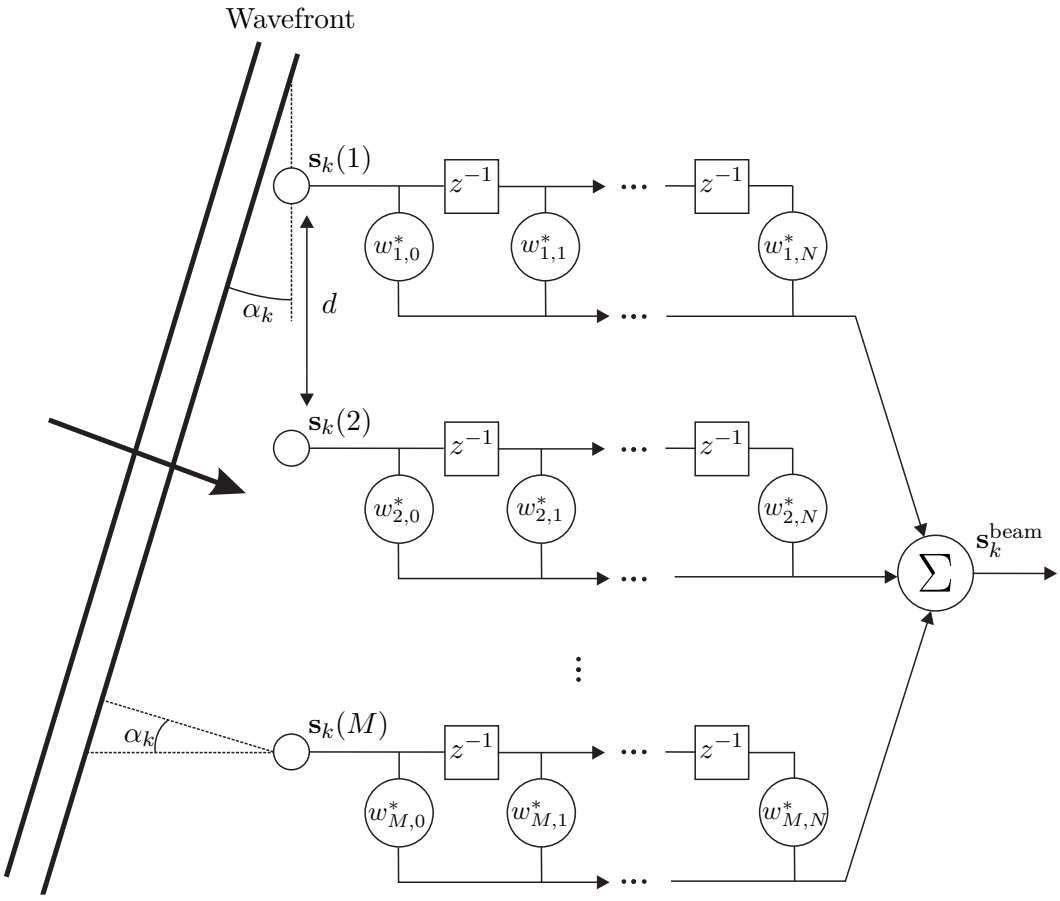

Figure 2.5: The sensor and filtering arrangement for beamforming with a planar wavefront approaching the sensor array at angle α_k.

2.3 Beamforming

The arrival time-delay estimation discussed in section 2.2 works on the principle of detecting an acoustic event and computing the direction from which it was received, beamforming utilises the opposite approach of listening in specific directions and then detecting any acoustic events that may be present [68, 69]. Beamforming on linear arrays is achieved using an array of sensors and spatially processing the planar waves received across the array for specified angles of incidence.

Figure 2.5 shows a planar wavefront propagating across a sensor array at angle α_k. Each signal feeds into an FIR filter, the coefficients of which are set to implement a variable time-delay line used to control the angle of the beam. Using:

$$\tau_k = \frac{d}{c} \sin \alpha_k \tag{2.16}$$

the time-delay of the wavefront arriving on adjacent sensors can be calculated, where a time-delay of 0 is an arrival at 0 rads (broadside)[1]. The wavefront arriving on sensors 1 and 2

[1]This is a deviation from the standard used in section 2.2 and elsewhere, however treating a bearing of 0 rads as broadside simplifies derivation of the beamforming equations and conforms to the accepted standard for beamforming.

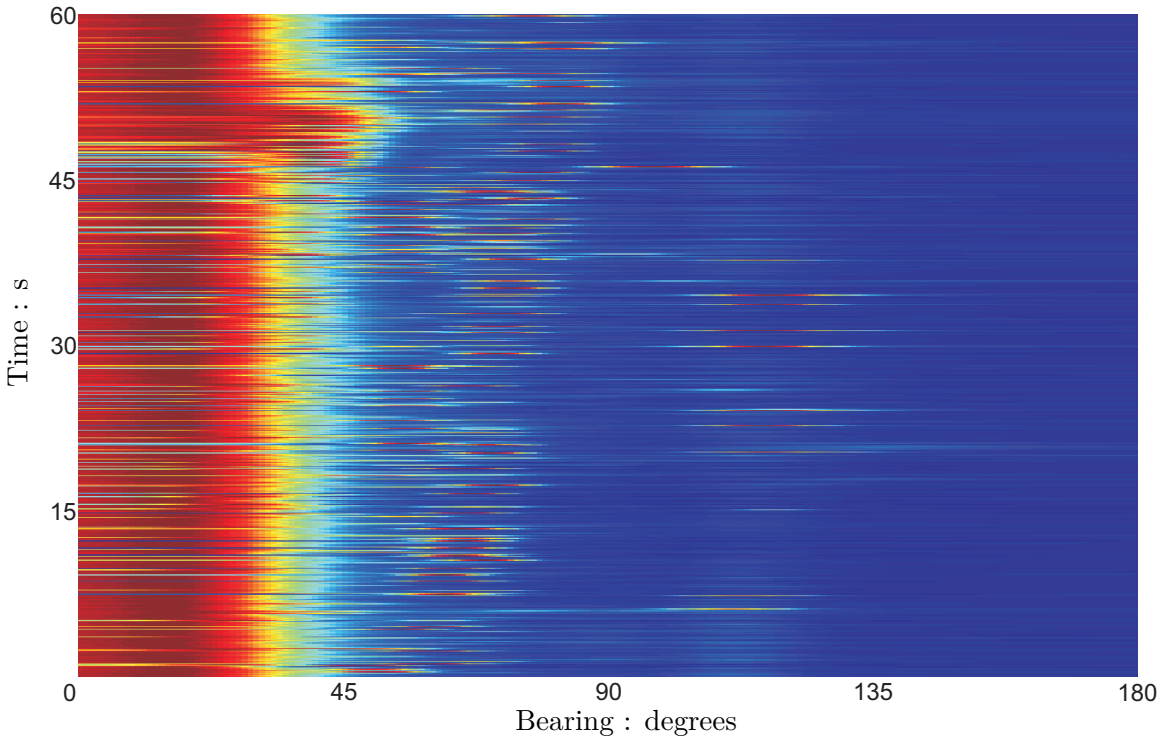

Figure 2.6: Time-bearing display showing beams formed between forward end-fire 0° and rear end-fire 180°. The energy between 0° and 40° is boat noise. Energy from sperm whale clicks can also be observed.

arrives with delay τ, at a delay of 2τ between sensors 1 and 3 and with a delay of $(M-1)\tau$ between sensors 1 and M. The beam is formed by spatially summing over the delayed signals:

$$\mathbf{s}_k^{\text{beam}} = \sum_{m=1}^{M} \mathbf{s}_{k-(m-1)\tau}(m) \tag{2.17}$$

The result, $\mathbf{s}_k^{\text{beam}}$, is the beam signal in the direction α_k with acoustic signals from sources at other angles filtered out. A more efficient method of implementation is to utilise the phase difference of the arriving wavefront at each sensor in place of the time-delay line, so that:

$$\mathbf{s}_k^{\text{beam}} = \sum_{m=1}^{M} A^{\text{amp}} \exp\left\{-j\left(2\pi\omega_0\left(k-(m-1)\tau\right) - \boldsymbol{\rho}\cdot[(m-1)d, 0]\right)\right\} \tag{2.18}$$

$$= A^{\text{amp}} \exp\left\{2\pi j\omega_0 k\right\} \sum_{m=1}^{M} \exp\left\{-j\left(2\pi\omega_0(m-1)\tau + \boldsymbol{\rho}\cdot[(m-1)d, 0]\right)\right\} \tag{2.19}$$

where A^{amp} is amplitude, ω_0 is the temporal frequency of the wave, $[(m-1)l, 0]$ is the position of the mth sensor and $\boldsymbol{\rho}$ is the wave number vector given the wavelength λ and sound propagation speed:

$$\boldsymbol{\rho} = \left[\frac{\omega}{c}\sin\alpha, \frac{\omega}{c}\cos\alpha\right] \tag{2.20}$$

where $\omega/c = 2\pi/\lambda$. A time-bearing display using beamforming for detecting sperm whale clicks over a 1 minute period is shown in figure 2.6. Forward end-fire is at 0° and rear end-fire is at 180°. The band of energy between 0° and 40° is noise created by the vessel towing the

hydrophone array. Sperm whale clicks can also be observed, one click train can be observed between 50° and 85° between 0 s and 60 s. As is the case for source bearing estimation using time-delay measurements, beamforming on linear arrays results in a source location ambiguity surface for any combination of ϕ and ψ that satisfies (2.9) and is unable to determine range. Beamforming is used to detect and track marine mammals in [70] where left-right information is inferred from the known snaking of the array (acquired using heading sensors) as it is towed through the water. TNO's Delphinus array, designed for marine mammal research, is equipped with 16 low frequency elements for beamforming [37, 47]. Further discussion of beamforming is beyond the scope of this work as it is not utilised, however more information is available in [68, 69].

2.4 Hydrophone Array Configurations

Hydrophone arrays for marine mammal research can be divided into two categories, towed arrays and fixed arrays. Towed arrays are linear arrays towed behind a boat or ship, whereas fixed arrays maintain a fixed position. The most common hydrophone configuration used in marine mammal studies are towed hydrophone arrays. Such arrays comprise of a length of towing cable followed by the hydrophone elements towed behind a boat or ship. Towed arrays often consist of only two hydrophone elements which can be used to compute arrival time-delay measurements across the array aperture [3]. The inclusion of more elements within the array allows for beamforming [37, 47]. Although the computed source direction is one dimensional, and therefore results in a source ambiguity hyperboloid, towed arrays are very popular because the costs of construction and deployment are relatively low. Towed arrays can also be used in population surveys over large areas [3,4] and for tracking specific individual animals through a dive cycle [47].

When utilising a towed hydrophone array comprising of a single hydrophone pair, time-delay measurements are extracted as described in section 2.2. The time-delays are then used to approximate the bearing of the source animal and, over time, establish range and whether the animal is to the left or right of the towing vessel. A more detailed discussion of localisation using towed arrays is presented in section 2.7. Towed arrays can be extended to include a second hydrophone pair which can be used with the first to triangulate the range of a vocalising animal [28, 29]. The two hydrophone pairs are separated by some distance so there is a technical challenge in associating the clicks received on each hydrophone pair from the same source animal.

Fixed arrays can be either large aperture or small aperture. Small aperture arrays can be deployed temporarily or permanently, however large aperture arrays, such as bottom mounted sensors, tend to be long term deployments due to cost. An example of a large aperture array is the US Navy's Atlantic Underwater Test and Evaluation Centre (AUTEC) range where the hydrophones are mounted on the sea-floor and spread over distances of several kilometres [71]. Arrays such as the AUTEC range are very expensive to deploy and maintain. Finfer et al.

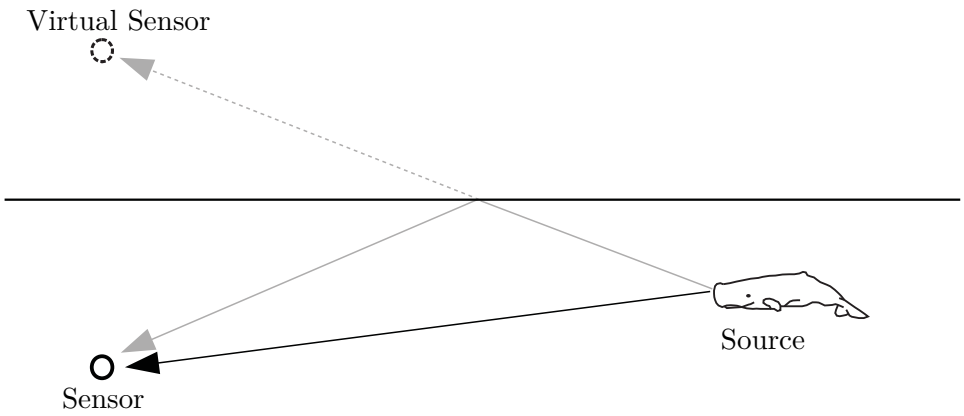

Figure 2.7: An acoustic source and the direct and reflected acoustic propagation paths. The reflected path can be used to establish a virtual receiver

utilised a small aperture fixed array lowered over the side of a sailing boat to localise clicking sounds in British coastal waters [72]. Small fixed arrays can easily be lowered over the side of a boat, raised again and relocated, however it would take considerably more time to acoustically survey the same area than if using a towed array.

The benefit of fixed arrays over towed arrays is that they do not have to be linear and therefore the elements can be separated over three dimensions thereby allowing three dimensional localisation. Three dimensional localisation is possible with only four elements separated over the three dimensions, however this can lead to ambiguous source localisations so ideally a minimum of five elements should be utilised [73]. Localisation methods for fixed arrays are presented in section 2.6.

2.5 Surface Reflections and Virtual Sensors

Sperm whale clicks are often received on hydrophones via more than one propagation path through the ocean. The first arrival is direct but the second is reflected via either the surface or the sea floor. Reflected waves propagate via a longer path so are received after the direct arrival, if detected and associated with the correct direct arrival they can be used to establish virtual sensors and provide additional localising information [22, 23, 28, 29, 63, 74].

The propagation paths of the direct and reflected receptions are shown in figure 2.7. Cross-correlating the direct and reflected arrivals on a single sensor yields the delay between the direct arrival and the reflection in a similar manner as is achieved by cross-correlating the signals received on two separate sensors. If a reflection can be detected then the additional time-delay measurement can be defined as being between the real sensor below the surface and a virtual sensor an equal distance above the surface.

Nosal and Frazer propose using only the time-delays between direct and reflected arrivals rather than measuring the time-delays of direct arrivals between sensors, for localising on large aperture fixed arrays [23]. The direct-reflected time-delays are used to establish an

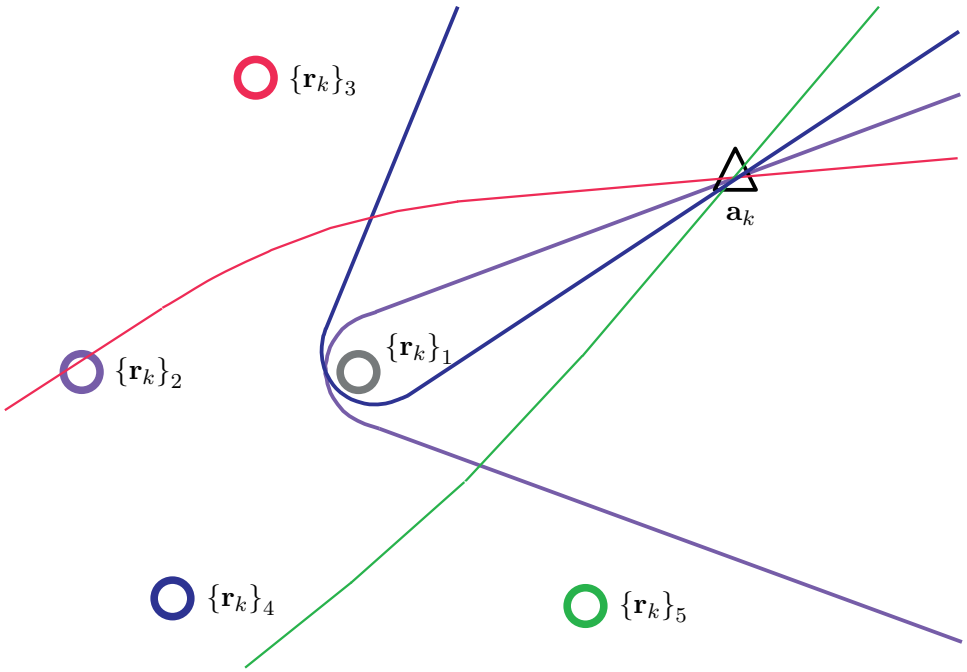

Figure 2.8: A 2D illustration of four hyperbolas and the acoustic source at the point at which they intersect

ambiguity surface around each individual sensor where the source is located at the point at which the ambiguity surfaces around each sensor intersect. To account for error in the cross-correlations and the eventuality that all the surfaces do not uniquely intersect at a specific point, a radial-basis function is applied to each of the ambiguity surfaces. Each point on the ambiguity surface has a high probability which reduces for points away for the ambiguity surface. The source location is the point in 3D space at which the product probability is greatest.

Surface reflections can be utilised for source depth estimation on towed arrays [28, 29] and improving depth estimation for fixed arrays [22]. For algorithms using surface reflections in localisation to be robust detection of reflections and association with the correct direct arrival must be reliable. In many cases, especially for sources at longer ranges, reflections are not necessarily detectable or distinguishable from the direct arrival, consequently techniques utilising surface reflections are not always practical.

2.6 Fixed Array Localisation

The time-delays on a fixed array are measured between a reference sensor and each of the $N_{\mathbf{r}} - 1$ additional sensors. Each of the $N_{\mathbf{r}} - 1$ time-delays defines a hyperboloid centred on the sensor pair axis, the point at which each of these hyperboloids intersect represents the source location, shown in figure 2.8.

Having acquired the time-delays it remains to solve (2.3). Three-dimensional resolution is possible given appropriate sensor separations and can be achieved via a weighted least squares or

an analytical approach. The weighted least squares approach involves searching for the source location parameters that, when substituted into (2.1), match the time-delay measurements. An analytical approach requires calculating the propagation time for the acoustic wavefront to propagate from the source to the reference sensor and combining the result with the measured time-delays to find the source location. Both these methods are presented in the following sections.

2.6.1 Weighted Least Squares Localisation

If $\boldsymbol{h}(\,)$ is entirely accurate and $\hat{\boldsymbol{\Theta}}_k = \boldsymbol{\Theta}_k$ then the maximum likelihood of the source location is obtained by minimising the weighted least squares function [22]:

$$\Psi(\mathbf{a}_k) = \sum_{n=2}^{N} \frac{(\tau(1,n) - \boldsymbol{h}(\mathbf{a}_k; \boldsymbol{\Theta}_k))^2}{\text{var}\{\tau(1,n)\}} \tag{2.21}$$

where $\tau(1,n)$ is the time-delay between receivers 1 and n. The measurement noise variance $\text{var}\{\tau(1,n)\}$ between sensors 1 and n is derived from spectral analysis of the delay estimates. Assuming low frequency components relate to animal movement, the noise variance can be estimated from higher frequency components. The source location is the minimum of the squared error surface where the value of $\mathbf{a}_k$ minimises $\Psi(\mathbf{a}_k)$. The minimum is found using a gradient descent algorithm such as the Nelder-Mead simplex algorithm [75].

2.6.2 Analytical Localisation

Given an array of acoustic sensors at time k at known positions $\{\mathbf{r}_k\}_{1:N_\mathbf{r}}$, a vector of known arrival times between the reference sensor and other sensors and a known constant sound speed c, then the source location $\mathbf{a}_k$ can be determined analytically [73, 76]. The distance between the source location and the nth sensor $\{\mathbf{r}_k\}_n$ is:

$$||\{\mathbf{r}_k\}_n - \mathbf{a}_k|| = ct(n) \tag{2.22}$$

$$= c(\tau(1,n) + t(1)) \tag{2.23}$$

where $t(1)$ is the propagation time from source to reference receiver, $t(n)$ is the propagation time from source to the nth sensor and c is the sound propagation speed. When squared this expression becomes:

$$||\{\mathbf{r}_k\}_n - \mathbf{a}_k||^2 = c^2(\tau(1,n) + t(1))^2 \tag{2.24}$$

If the reference sensor $\{\mathbf{r}_k\}_1$ is positioned at the origin of the coordinate system then the propagation time, $t(1)$, from source to the reference sensor can be calculated. If the source

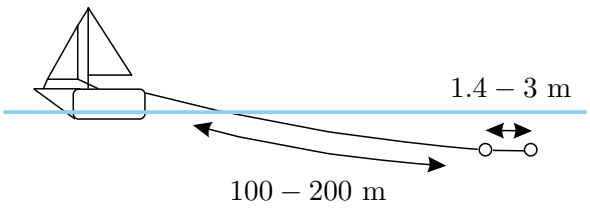

Figure 2.9: Side projection of a two element towed hydrophone configuration with typical cable length and aperture for tracking sperm whales

location is[2]:

$$\mathbf{a}_k = \mathbf{R}^{-1}\frac{\boldsymbol{\iota}}{2} - c^2 t(1)\mathbf{R}^{-1}\boldsymbol{\tau} \tag{2.25}$$

where:

$$\mathbf{R} = \begin{bmatrix} \{r_k(1)\}_2 & \{r_k(2)\}_2 & \{r_k(3)\}_2 \\ \{r_k(1)\}_3 & \{r_k(2)\}_3 & \{r_k(3)\}_3 \\ \{r_k(1)\}_4 & \{r_k(2)\}_4 & \{r_k(3)\}_4 \\ \{r_k(1)\}_5 & \{r_k(2)\}_5 & \{r_k(3)\}_5 \end{bmatrix} \tag{2.26}$$

$$\boldsymbol{\tau} = \begin{bmatrix} \tau(1,2) \\ \tau(1,3) \\ \tau(1,4) \\ \tau(1,5) \end{bmatrix} \tag{2.27}$$

$$\boldsymbol{\iota} = \begin{bmatrix} ||\{\mathbf{r}_k\}_2||^2 - c^2\tau^2(1,2) \\ ||\{\mathbf{r}_k\}_3||^2 - c^2\tau^2(1,3) \\ ||\{\mathbf{r}_k\}_4||^2 - c^2\tau^2(1,4) \\ ||\{\mathbf{r}_k\}_5||^2 - c^2\tau^2(1,5) \end{bmatrix} \tag{2.28}$$

then solving:

$$t(1) = \frac{c\rho_2 \pm \sqrt{c^2\rho_2^2 - (c^2\rho_3 - 1)\,\rho_1}}{2c\,(c^2\rho_3 - 1)} \tag{2.29}$$

yields the propagation time from $\mathbf{a}_k$ to $\{\mathbf{r}_k\}_1$, where:

$$\rho_1 = \left(\left\{\mathbf{r}^{-1}\right\}_{1:5}\boldsymbol{\iota}\right)^T\left(\left\{\mathbf{r}^{-1}\right\}_{1:5}\boldsymbol{\iota}\right) \tag{2.30}$$

$$\rho_2 = \left(\left\{\mathbf{r}^{-1}\right\}_{1:5}\boldsymbol{\tau}\right)^T\left(\left\{\mathbf{r}^{-1}\right\}_{1:5}\boldsymbol{\iota}\right) \tag{2.31}$$

$$\rho_3 = \left(\left\{\mathbf{r}^{-1}\right\}_{1:5}\boldsymbol{\tau}\right)^T\left(\left\{\mathbf{r}^{-1}\right\}_{1:5}\boldsymbol{\tau}\right) \tag{2.32}$$

Where the effective sound speed between $\mathbf{a}_k$ and each sensor $\{\mathbf{r}_k\}_{1:5}$ is not equal $t(1)$ becomes the root of a quartic, details of this case and the necessary equations are presented in [76].

2.7 Towed Array Localisation

A typical towed hydrophone array with a single element pair yields a single time-delay measurement that results in a hyperboloid shaped ambiguity surface centred on the array axis, as described in section 2.2. The configuration of a two element towed hydrophone array is shown in figure 2.9 along with typical cable length, 100 - 200 m, and aperture, 1.4 - 3 m, for tracking sperm whales. Although a single measurement alone yields a source ambiguity it is possible to use multiple measurements to approximate the position of an animal.

Estimates of the animal's bearing to the hydrophone array can be made by negating the fact that the received time-delay is a function of both the bearing and elevation of the animal and assuming it is simply a function of the bearing. Making this assumption reduces the ambiguity surface to an ambiguity curve and it remains to resolve the range of the animal and whether the animal lies to the left or right of the hydrophone pair.

Towed arrays may be equipped with array positioning instrumentation such as depth sensors, heading sensors, inclinometers and speed sensors. Such instrumentation provides information on the position and motion of the array elements relative to the boat which will be different to the boat itself due to the cable length. The information from the positioning instruments can be used in conjunction with the acoustic data to improve location estimation accuracy and are important for use of the localisation methods described by Thode [28, 29].

2.7.1 Range Estimation

Range estimation aims to establish the distance of the animal from the hydrophone array. Range can be subdivided into horizontal range, depth and slant range which is the magnitude of the horizontal range and depth. A very crude method of range estimation is to use the received sound pressure level [20]. This method assumes the equipment is accurately calibrated, good knowledge of the environmental parameters is available and the animals' vocalisations are omni-directional which, for sperm whales, is not the case [16].

If time-delay measurements are acquired from the array in two different positions, the source is stationary and the hydrophones and source are in the same horizontal plane, so that $\alpha = \phi$ then the horizontal range can be estimated using multi-view geometry [77]. The necessary multi-view geometry is shown in figure 2.10. The position of the source $\mathbf{r}_k$ at time k and $k+n$ can be independently defined as the sum of the hydrophone array position and the relative source position:

$$\mathbf{a}_k = \mathbf{r}_k + r_k \left[\cos\phi_k, \sin\phi_k\right]' \tag{2.33}$$

$$\mathbf{a}_{k+n} = \mathbf{r}_{k+n} + r_{k+n} \left[\cos\phi_{k+n}, \sin\phi_{k+n}\right]' \tag{2.34}$$

[2] $\mathbf{R}$ is used here as a matrix of sensor position row vectors, as defined in (2.26), and should not be confused with the use of $\mathbf{R}$ with subscript (of the variables the covariance is taken of) as a notation for covariance matrices in following chapters.

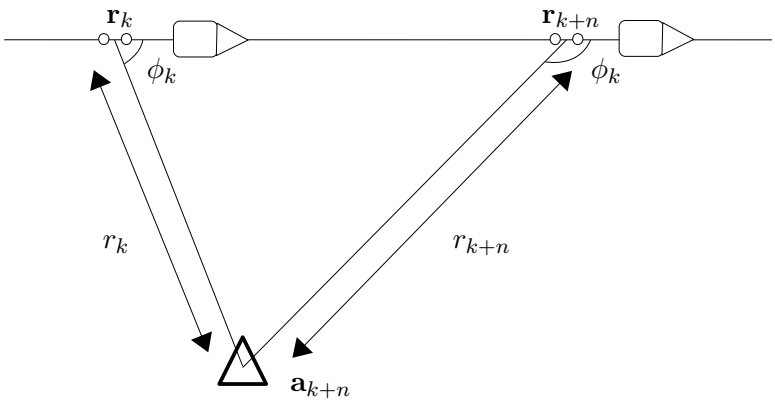

Figure 2.10: Multi-view geometry for calculating the range of and localising a stationary target using bearings measured at k and $k+n$ from positions $\mathbf{r}_k$ and $\mathbf{r}_{k+n}$

where ${r_k}^3$ is the unknown horizontal range at time k and $\mathbf{a}_k = \mathbf{a}_{k+n}$. The difference in the relative positions of the source at each measurement is the same as the difference in the position of the array:

$$\mathbf{r}_{k+n} - \mathbf{r}_k = r_{k+n} \begin{bmatrix} \cos\phi_{k+n} \\ \sin\phi_{k+n} \end{bmatrix} - r_k \begin{bmatrix} \cos\phi_k \\ \sin\phi_k \end{bmatrix} \tag{2.35}$$

Re-formulating in matrix-vector form gives:

$$\mathbf{r}_{k+n} - \mathbf{r}_k = \begin{bmatrix} \cos\phi_k & -\cos\phi_{k+n} \\ \sin\phi_k & -\sin\phi_{k+n} \end{bmatrix}^{-1} \begin{bmatrix} r_{k+n} \\ r_k \end{bmatrix} \tag{2.36}$$

which, when re-arranged to make the ranges the subject is:

$$\begin{bmatrix} r_k \\ r_{k+n} \end{bmatrix} = \begin{bmatrix} \cos\phi_k & -\cos\phi_{k+n} \\ \sin\phi_k & -\sin\phi_{k+n} \end{bmatrix}^{-1} [\mathbf{r}_{k+n} - \mathbf{r}_k] \tag{2.37}$$

Substituting the calculated ranges back into (2.33) and (2.34) yields the position of the source. In practice it is the range at time $k+n$ which is of interest as this is the most recent position of the array.

The multi-view geometric approach relies on the target being stationary. If the animal is moving in the same direction as the array the range will be over-estimated, if the animal is travelling in the opposite direction the range will be under-estimated as shown in figures 2.11(a) and 2.11(b). The extent of the error is dependent on the magnitude of the speed difference. For the stationary assumptions to hold the array must be moving significantly quicker than the animal. Although this method of range estimation can be described analytically it is typically performed using computer software whereby the operator plots bearing lines, derived from the time-delay measurements, on a chart and looks for the point at which they intersect.

Reconfiguring a towed hydrophone array to consist of two hydrophone element pairs as shown in figure 2.12 allows slant range to be computed using multi-view geometry because time-delay

[3]It should be noted that $\mathbf{r}_k$ is the position vector of the receiving sensor pair and r_k is the target range.

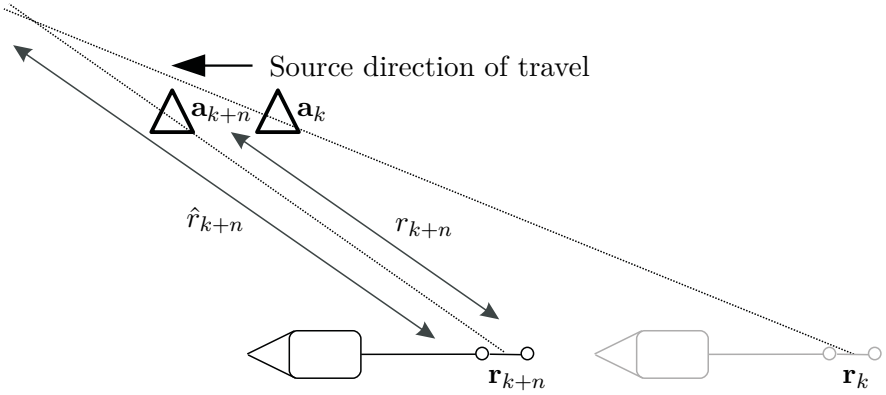

(a) Source travelling in the same direction as boat results in an over-estimate of the range

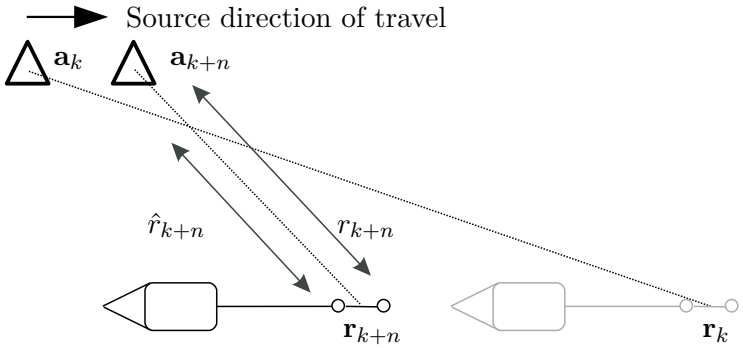

(b) Source travelling in the opposite direction as boat results in an under-estimate of the range

Figure 2.11: Examples of how source motion causes error in range estimation when the source is travelling (a) the same direction as the boat and (b) the opposite direction to the boat.

measurements are received on both hydrophone pairs from the same vocalisation. In such cases the source location ambiguity surface is reduced to circular shape at a range determined by the time-delay received at each sensor pair.

Using Surface Reflections to Improve Range Estimation and Estimate Depth

Using surface reflections and knowledge of the global inclination of the array and local inclination of the hydrophone pairs depth and horizontal range estimation becomes possible [28, 29]. Figure 2.12 shows the geometry of a two sensor pair array. Two additional array geometry elements are introduced here, the local inclination angle at the rear element pair, ν^{local}, and the global inclination angle between the front and rear sensor pairs, ν^{global}. Exploiting the geometries shown in figure 2.12 the slant range of the animal to the rear hydrophone pair, $r_{\text{direct,rear}}$, can be calculated as:

$$r^{\text{direct,rear}} = r^{\text{front,rear}} + \frac{d^{\text{front,rear}} r^{\text{front,rear}} \cos\alpha^{\text{direct,rear}} - \left(\left(d^{\text{front,rear}}\right)^2 + \left(r^{\text{front,rear}}\right)^2\right)/2}{d^{\text{front,rear}} - r^{\text{front,rear}} \cos\alpha^{\text{direct,rear}}} \tag{2.38}$$

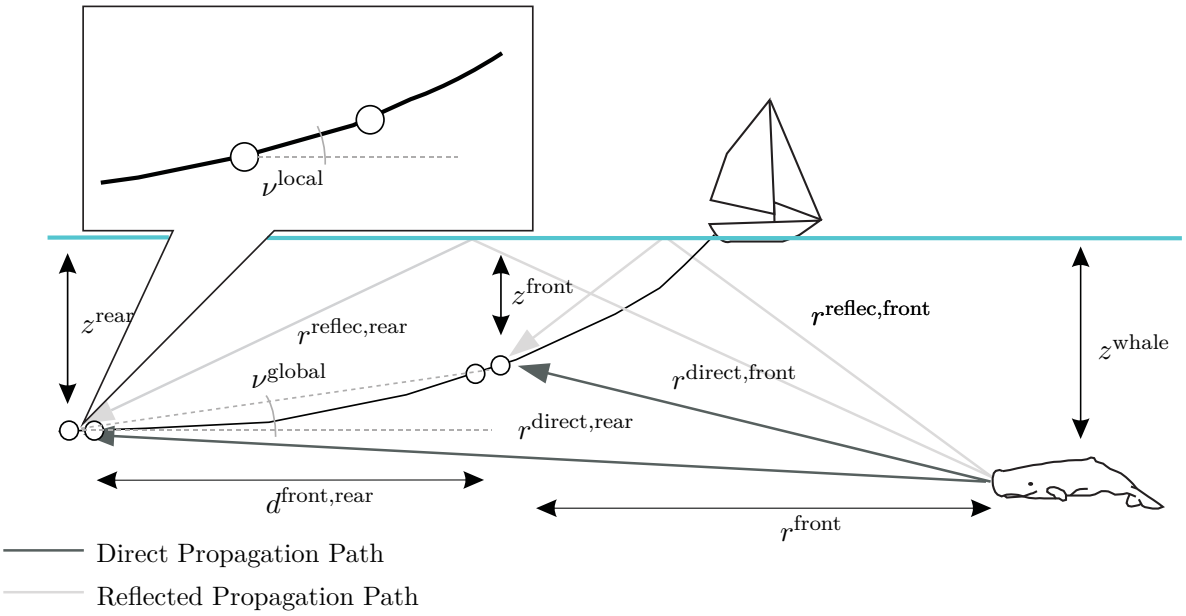

Figure 2.12: The geometries of direct and surface reflected arrivals of sperm vocalisations to the hydrophones pairs on a two hydrophone pair array (after Thode 2005 [29])

where $r^{\text{front,rear}}$ is the difference in slant range of direct arrivals to the front and rear hydrophone pairs, $d^{\text{front,rear}}$ is the distance between the front and rear hydrophone pairs and $\alpha^{\text{direct,rear}}$ is the received angle of the direct arrival on the rear hydrophone pair. Equation (2.38) assumes that $\nu^{\text{local}} = \nu^{\text{global}}$, i.e. the array cable is straight. If $\nu^{\text{local}} \neq \nu^{\text{global}}$ then:

$$r^{\text{direct,rear}} = r^{\text{front,rear}} + \frac{A_1 - A_2}{A_3 - A_4 - A_5} \tag{2.39}$$

where:

$$A_1 = d^{\text{front,rear}} r^{\text{front,rear}} \cos\nu^{\text{global}} \cos\nu^{\text{local}} \frac{\left(d^{\text{front,rear}}\right)^2 + \left(r^{\text{front,rear}}\right)^2}{2} \tag{2.40}$$

$$A_2 = d^{\text{front,rear}} \sin\left(\nu^{\text{local}} - \nu^{\text{global}}\right) \ldots$$
$$\ldots \left[z^{\text{rear}} - r^{\text{direct-rear,reflec-rear}} \frac{2r^{\text{front,rear}} + r^{\text{direct-rear,reflec-rear}}}{4z^{\text{rear}}} \right] \tag{2.41}$$

$$A_3 = \cos\nu^{\text{local}} r^{\text{front,rear}} \tag{2.42}$$

$$A_4 = d^{\text{front,rear}} \cos\alpha^{\text{direct,rear}} \cos\nu^{\text{global}} \tag{2.43}$$

$$A_5 = d^{\text{front,rear}} r^{\text{direct-rear,reflec-rear}} \sin\frac{\nu^{\text{local}} - \nu^{\text{global}}}{z^{\text{rear}}} \tag{2.44}$$

where z^{rear} is the depth of the rear element pair. The propagation distances for the direct arrivals (also the slant range) and reflected arrivals can be defined as:

$$r^{\text{direct,rear}} = \sqrt{\left(r^{\text{horiz,rear}}\right)^2 + \left(z^{\text{whale}} - z^{\text{rear}}\right)^2} \tag{2.45}$$

$$r^{\text{reflec,rear}} = \sqrt{\left(r^{\text{horiz,rear}}\right)^2 + \left(z^{\text{whale}} + z^{\text{rear}}\right)^2} \tag{2.46}$$

The rear hydrophone pair slant range can be used along with the front hydrophone pair slant range to calculate animal depth. The front hydrophone pair slant range is computed from the rear direct arrival:

$$\left(r^{\text{direct,front}}\right)^2 = \left(d^{\text{front,rear}}\right)^2 + \left(r^{\text{direct,rear}}\right)^2 - 2d^{\text{front,rear}} r^{\text{direct,rear}} \cos\alpha^{\text{global}} \tag{2.47}$$

where α^{global} is the angle of reception from the time-delay between the front and rear hydrophone pairs. The animal depth, z^{whale}, can now be calculated:

$$z^{\text{whale}} = \frac{\left(r^{\text{reflec,rear}} - r^{\text{direct,rear}}\right)\left(2r^{\text{direct,front}} + 2r^{\text{front,rear}} + \left(r^{\text{reflec,rear}} - r^{\text{direct,rear}}\right)\right)}{4z^{\text{rear}}} \tag{2.48}$$

The horizontal range of the animal from the rear hydrophone pair and depth can now be calculated using (2.45) and (2.48) and used to calculate the horizontal bearing of the animal. As well as this analytic method it is also possible to compute the source location of the animal via this geometry using a numerical method [29].

Although this method provides three dimensional localisation once the left-right ambiguity has been resolved (see section 2.7.2) it relies on being able to robustly detect surface reflections. The appropriate instrumentation on the array to enable knowledge of the array depth and inclination at both the front and rear hydrophone pairs and the appropriate element arrangement is also necessary.

2.7.2 Left-Right Resolution

When tracking a sperm whale using a single-hydrophone pair towed array it is common to assume that the animal is in the same horizontal plane as the hydrophone pair so that $\alpha = \phi$. In this case the three-dimensional hyperboloid ambiguity surface collapses to a two-dimensional ambiguity hyperbola, as illustrated in figure 2.2. One implication of this assumption is, in the two-dimensional case, it is unknown whether the animal is to the left or right of the array and is referred to as the left-right ambiguity.

A left-right ambiguity can be resolved by manoeuvring the towed array and monitoring the change in received time-delay. If after turning the towing vessel and array to port the clicks are received from a more forward direction then the animal is to the left, if the click receptions move towards the rear then then animal is to the right. This process is shown in figure 2.13. This method can fail to produce a clear resolution of the ambiguity if the horizontal range is relatively short in comparison to the animal's depth as the elevation component of the received measurement will be significant. As for range estimation using a hydrophone pair, left-right ambiguity resolution is typically performed by a human operator plotting bearing lines, derived from the time-delay measurements, on a digital chart and deciding to which side of the boat the animal is situated.

An alternative method of resolving left-right ambiguity is to tow an additional hydrophone with some horizontal separation to the standard hydrophone pair [29]. The time-delay between

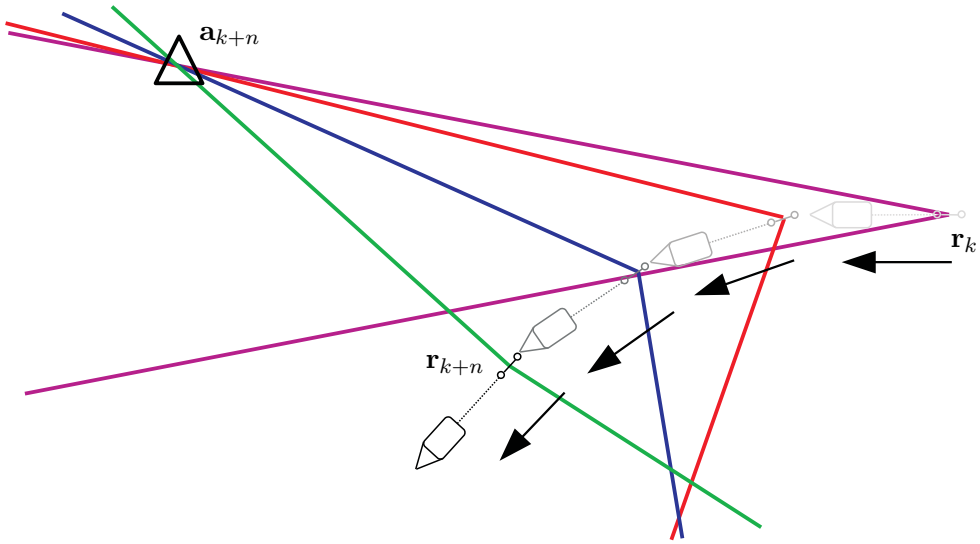

Figure 2.13: To resolve the left-right ambiguity the vessel manoeuvres to the left and the measurements move rearwards indicating the animal is to the right

the additional hydrophone and the standard hydrophone pair can then be used to determine on which side of the array the animal is situated. Practicality is limited because of the difficulties involved in maintaining independent hydrophones in the correct relative positions due to differing cable lengths and tow depths that are dependent on hydrophone array buoyancy characteristics.

2.8 Proposed Localisation and Tracking Solution

Several methods for localising vocalising sperm whales for different configurations of array have been reviewed. The most common array configuration is the towed array utilising a hydrophone pair, therefore development of improved localisation and tracking methods for these types of arrays and their associated measurements is warranted. It is desirable to avoid the use of additional equipment, received sound pressure level measurements and detection of surface reflections. Methods that can be implemented purely in software are likely to bring the most far-reaching benefits because NGOs and academic institutions can upgrade their tracking systems without the cost of purchasing additional hardware or replacement hydrophone arrays.

Hydrophone pair towed array systems have been utilised successfully and effectively for many years, however they require a human operator to decide on the position of the animal. Although the assumptions required for the associated tracking, range and left-right estimation methods are crude and results are subjective to the skills of the operator, they utilise only the time-delay measurements of directly arriving clicks. If the assumptions that the hydrophones and animal are in the same plane and that the animal is stationary can be relaxed then improved localisation, including depth estimation, would be possible. Additionally it is also desirable to automate the localisation and tracking process. Methods that have been proposed for this purpose require either additional hardware, in the form of more hydrophone

elements and positioning instruments, or robust surface reflection detection.

As discussed, there are many possible positions in which the animal could be situated to produce a given time-delay measurement. It is proposed that if the source location ambiguity is modelled as a probability density function (PDF) then the source can be estimated as the mean of the PDF via a minimum mean squared error (MMSE) estimate. The PDF modelling the ambiguity can then be updated whenever a new measurement is received and a new estimate made. Initially the PDF can be uniform over the source ambiguity hyperboloid. As more measurements are acquired the PDF will change shape to favour a particular range interval and, as the towing vessel and array manoeuvre, a bearing and elevation interval.

Given the source location $\mathbf{a}_k$, it is a relatively simple process using (2.1) to calculate the delay τ_k. As discussed in section 2.2.1 the measurement process is noisy so it is appropriate to represent τ_k in terms of a PDF:

$$p\left(\mathbf{b}_k|\mathbf{a}_k\right) \tag{2.49}$$

where $\mathbf{b}_k = \tau_k$, the mean of PDF (2.49) is given by (2.1) when $\mathbf{v}_k = 0$ and the variance is defined by the noise process $\mathbf{v}_k$, itself dependent on the resolution of the cross-correlation. Inversion of (2.49) requires Bayes's theorem [78] so that $\mathbf{a}_k$ is derived from the posterior distribution dependent on all the previously measured time-delays, known as the measurement history:

$$p\left(\mathbf{a}_k|\mathbf{b}_{1:k}\right) = \frac{p\left(\mathbf{b}_k|\mathbf{a}_k\right)p\left(\mathbf{a}_k|\mathbf{b}_{1:k-1}\right)}{p\left(\mathbf{b}_k|\mathbf{b}_{1:k-1}\right)} \tag{2.50}$$

The derivation of this posterior distribution is presented in section 3.2. A further advantage of a Bayesian approach to tracking is that should a second hydrophone pair be available the additional time-delay measurement is simply augmented to the measurement vector $\mathbf{b}_k$ and the information is incorporated into constructing the posterior PDF representing the animal's position.

Tracking filters, such as the Kalman filter and particle filter, are recursive Bayesian estimators and the particle filter has been reported as successfully tracking a target from passive bearing measurements where range is a parameter to be estimated [54, 55, 58, 59, 79–82]. Typically bearings tracking scenarios track only range and bearing from a bearing measurement or track range, bearing and elevation from both bearing and elevation measurements. The proposition here is novel because the target to be tracked is a sperm whale, the equipment available is relatively simple and bearing, elevation and range are to be estimated from a measurement that is a function of the bearing and elevation of the whale to the array.

2.9 Summary and Conclusion

An acoustic wavefront propagating through the ocean from an acoustic source to a set of sensors arrives on each receiver at a different time. The delays in the arrival time can be computed using cross-correlation. Using these time-delays it is possible to localise the acoustic source.

Both fixed and towed hydrophone array configurations are utilised in acoustic based marine mammal research. Fixed arrays separate the hydrophones over three dimensions to enable three dimensional source localisation. Towed arrays are by far the most widely used because of the relatively low cost of construction, deployment, re-deployment and the volume of ocean they can be used to survey. Towed array elements are arranged in a linear configuration so are unable to unambiguously resolve source location from a single acoustic arrival. Furthermore, in marine mammal research typically only a single hydrophone pair is used resulting in a hyperboloid shaped source location ambiguity surface. Methods have been developed to infer animal range and resolve whether the animal is to the left or right of the observing vessel, however these methods are somewhat crude and subjective.

Alternative towed array tracking methods have been proposed, however these often rely on robust detection of surface reflections or additional equipment. Here it has been proposed that the location of the vocalising sperm whale should be represented as a PDF constructed from the received time-delay measurements. This would allow multiple hypotheses of the animal's position, along with the likelihood that an animal is in that position, to be maintained. This PDF can then be updated whenever a new measurement is received. This is achievable if the PDF of the animal's position is a posterior PDF as defined by Bayes's theorem.

Tracking filters can be utilised to implement the proposed tracking solution and are discussed in chapter 3. Chapter 4 then builds on some of the specificities required for the application of tracking filters to sperm whale tracking. Tracking filters are then applied to simulated data for testing in chapter 5 before being applied to track a real sperm whale in chapter 7.

Chapter 3

Tracking Filters

After reviewing acoustic localisation methods for both fixed and towed hydrophone array configurations in chapter 2, section 2.8 proposed representing the location of an acoustic source as a probability density function (PDF). Such a formulation of the localisation problem allows information on the source animal's location to be inferred from time-delay measurements that individually contain very limited and non-specific information. It was proposed that by taking several such measurements over time as the tracking vessel and array manoeuvre the information can collectively be used to infer the relative range, bearing and elevation of the animal from the hydrophone array.

This chapter formulates a source location PDF as the posterior PDF given by Bayes's theorem. In section 3.1 the tracking problem is conceptualised as a recursive state estimation problem. Section 3.2 formulates a recursive state estimation solution using Bayes's theorem. The first implementable version of the conceptual solution is the Kalman filter, presented in section 3.3, which is then extended to non-linear and non-Gaussian systems in section 3.4. Particle filtering, which utilises Monte-Carlo simulations to model the posterior PDF instead of using parametric modelling, is discussed in sections 3.5 and 3.6. Finally application of the subjects covered in sections 3.1 to 3.6 to acoustic sperm whale tracking is described in section 3.7, including discussion on the appropriate choice of tracking filter.

3.1 Conceptual Tracking Problem

The change in parameters of many systems, such as the position of a whale, can be characterised in a recursive form, whereby the current system parameters are a function of the previous system parameters. In reality the system is likely to function in a continuous fashion, however measurement acquisition and tracking are likely to be performed in the digital domain so a discrete representation is likely to be more useful. In discrete form the system function is characterised as a recursive Markov process [53, 54, 83–85]:

$$\mathbf{a}_k = \boldsymbol{f}_{k-1}\left(\mathbf{a}_{k-1}, \mathbf{e}_{k-1}\right) \tag{3.1}$$

where $\mathbf{a}_k$ is the system state parameter vector at time k and $\mathbf{a}_k \in \mathbb{R}^{N_\mathbf{a}}$, $\boldsymbol{f}_{k-1}(\,)$ is the time dynamic system function defining the transformation of the system parameters between time $k-1$ and k and $\mathbf{e}_{k-1}$ is a noise term that accounts for system components not modelled by $\boldsymbol{f}_{k-1}(\,)$.

The transformation of the system parameters to measurement data, such as from whale position to a time delay measurement, can be defined as the function [53, 54, 83–85]:

$$\mathbf{b}_k = \boldsymbol{h}_k(\mathbf{a}_k, \mathbf{v}_k) \tag{3.2}$$

where $\mathbf{b}_k$ is the measurement data vector at time k and $\mathbf{b}_k \in \mathbb{R}^{N_\mathbf{b}}$, $\boldsymbol{h}_k(\,)$ is the time dynamic measurement function defining the transformation between the system parameters and measurement data and $\mathbf{v}_k$ is a noise term that accounts for measurement components not modelled by $\boldsymbol{h}_k(\,)$.

Using the functions defined in (3.1) and (3.2), PDFs for the system update process and the measurement process can be constructed. The transitional prior PDF, characterising the transition of the previous system parameters to the current system parameters, is defined as [54]:

$$p(\mathbf{a}_k|\mathbf{a}_{k-1}) \tag{3.3}$$

The transitional prior could be expanded to include previous system parameters because each parameter is dependent on the one before:

$$\begin{aligned} p(\mathbf{a}_k|\mathbf{a}_{k-1}) &= p(\mathbf{a}_k|\mathbf{a}_{k-1}, \mathbf{a}_{1:k-2}) \\ &= p(\mathbf{a}_k|\mathbf{a}_{1:k-1}) \end{aligned} \tag{3.4}$$

however, if the system is assumed to be a first order Markov process then $\mathbf{a}_k$ is only dependent on $\mathbf{a}_{k-1}$, therefore (3.4) is assumed to be the same as (3.3).

The PDF characterising the evidential data given the system parameters, referred to as the likelihood, is defined as:

$$p(\mathbf{b}_k|\mathbf{a}_k) \tag{3.5}$$

The likelihood density may also be expanded to include previous system parameters:

$$p(\mathbf{b}_k|\mathbf{a}_k) = p(\mathbf{b}_k|\mathbf{a}_k, \mathbf{a}_{1:k-1}) \tag{3.6}$$

however, making the Markovian assumption, the term $\mathbf{a}_{1:k-1}$ can be omitted and (3.5) is sufficient.

Where the noise components do not exist these PDFs are simply delta functions centred on the result of the function, as shown for (3.1) in figure 3.1(a). Where there is a noise term the shape of the PDF is defined by the distribution of the noise, as shown in figure 3.1(b) where the noise is normally distributed.

Typically it is not the system parameters that are known but the measurement data. The

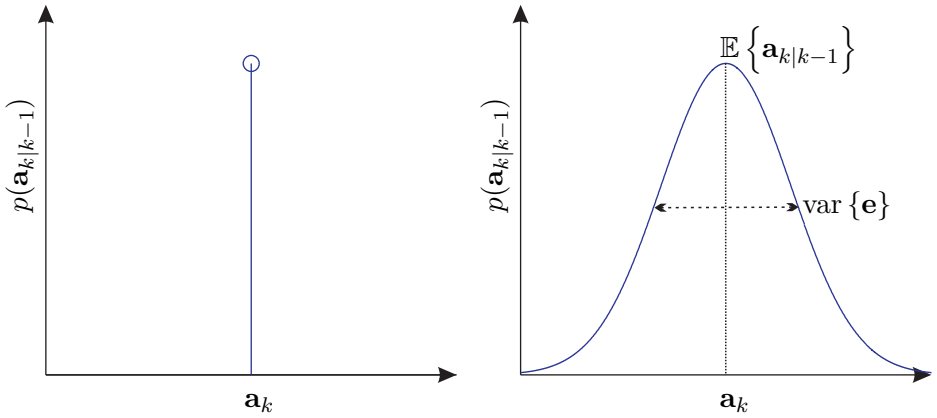

(a) PDF of system function output with no noise

(b) PDF of system function output with normally distributed noise

Figure 3.1: The PDFs of the system function output with (a) no system noise and (b) normally distributed system noise

tracking problem is to recursively estimate the target system parameters using (3.3) and (3.5).

3.2 Conceptual Tracking Solution

Estimation of the system parameters from the measurement data can be described as an inversion of the forward function (3.2). Inversion of the model is often not possible as information may have been lost in the measurement transformation which can lead to an ambiguous solution, such as the loss of range information in the computation of a time-delay between two hydrophone elements. As the solution to (3.2) is ambiguous it is more appropriate to formulate a PDF representing $\mathbf{a}_k$ dependent on the measurement history $\mathbf{b}_{1:k} = \{\mathbf{b}_1, \ldots, \mathbf{b}_k\}$. In order to obtain this distribution it is necessary to derive the posterior distribution from the expanded evidence density (3.6):

$$p\left(\mathbf{a}_k|\mathbf{b}_{1:k}\right) \tag{3.7}$$

which can be constructed using Bayes's theorem.

Bayes's theorem describes how to find the distribution of the system parameter X given the measurement data Y:

$$p\left(X|Y\right) = \frac{p\left(Y|X\right)p\left(X\right)}{p\left(Y\right)} \tag{3.8}$$

where the term $p\left(X\right)$ and $p\left(Y|X\right)$ are the prior and likelihood respectively, $p\left(Y\right)$ is a normalising factor and $p\left(X|Y\right)$ is the resulting posterior distribution. Formulating the tracking problem in a recursive manner using Bayes's theorem requires expressions for the prior and normalising densities.

The transitional prior defines the current system parameter, $\mathbf{a}_k$, as dependent on the previous, $\mathbf{a}_{k-1}$, however the information needed to construct the previous posterior density, from which $\mathbf{a}_{k-1}$ is derived, is the measurement data history, $\mathbf{b}_{1:k-1}$. At initialisation the poste-

rior density is $p(\mathbf{a}_0 | \mathbf{b}_0)$ which is recursively updated using the measurement data history, $\mathbf{b}_{1:k}$ to construct the posterior density $p(\mathbf{a}_k|\mathbf{b}_{1:k})$. Therefore, the prediction of the target state using the measurements $\mathbf{b}_{1:k-1}$, referred to as the dynamic prior, is dependent on the previous posterior and the transitional prior and is obtained via the Chapman-Kolmogorov equation [53, 54]:

$$p(\mathbf{a}_k|\mathbf{b}_{1:k-1}) = \int p(\mathbf{a}_k|\mathbf{a}_{k-1})\, p(\mathbf{a}_{k-1}|\mathbf{b}_{1:k-1}) d\mathbf{a}_{k-1} \tag{3.9}$$

Updating the prediction to include the current measurement, $\mathbf{b}_k$, to obtain $p(\mathbf{a}_k|\mathbf{b}_{1:k})$ requires deriving the normalising factor, obtained by integrating the product of the likelihood and dynamic prior with respect to $\mathbf{a}_k$:

$$p(\mathbf{b}_k|\mathbf{b}_{1:k-1}) = \int p(\mathbf{b}_k|\mathbf{a}_k)\, p(\mathbf{a}_k|\mathbf{b}_{1:k-1}) d\mathbf{a}_k \tag{3.10}$$

By substituting (3.5), (3.9) and (3.10) into (3.8) the posterior density is obtained:

$$\begin{aligned} p(\mathbf{a}_k|\mathbf{b}_{1:k}) &= p(\mathbf{a}_k|\mathbf{b}_k, \mathbf{b}_{1:k-1}) \\ &= \frac{p(\mathbf{b}_k|\mathbf{a}_k)\, p(\mathbf{a}_k|\mathbf{b}_{1:k-1})}{p(\mathbf{b}_k|\mathbf{b}_{1:k-1})} \end{aligned} \tag{3.11}$$

The distribution (3.11) is computed from the transitional prior distribution, (3.9), and the likelihood distribution, $p(\mathbf{b}_k|\mathbf{a}_k)$. Computation of $p(\mathbf{a}_k|\mathbf{b}_{1:k})$ can be described as a two stage process, the first stage being computation of the transitional prior, (3.9), and the second stage being computation of the posterior, (3.11). This two stage process forms the basis of the tracking filter methods discussed in the following sections of this chapter.

Once the posterior density has been obtained it can be used to estimate the system parameters $\mathbf{a}_k$ as the distribution mean, via a minimum mean squared error (MMSE) estimate, or as the distribution peak, via a maximum a-priori (MAP) estimate:

$$\hat{\mathbf{a}}_{k|k}^{\text{MMSE}} \equiv \mathbb{E}\{\mathbf{a}_k|\mathbf{b}_{1:k}\} = \int \mathbf{a}_k \cdot p(\mathbf{a}_k|\mathbf{b}_{1:k}) \partial \mathbf{a}_k \tag{3.12}$$

$$\hat{\mathbf{a}}_{k|k}^{\text{MAP}} \equiv \arg\max_{\mathbf{a}_k} p(\mathbf{a}_k|\mathbf{b}_{1:k}) \tag{3.13}$$

The different estimation methods may result in a different parameter estimate from the same posterior PDF. In the case of a symmetric density the estimates are the same, as shown in figure 3.2(a). If the density is asymmetric the estimates will most likely be different, as shown in figure 3.2(b).

3.2.1 Tracking Filters as a Solution to the Tracking Problem

As shown by (3.9) and (3.11) the conceptual solution for obtaining the posterior density is a recursive process so a recursive estimator is an obvious solution to a practical implementation of (3.11). In practice a recursive estimator has a fixed memory requirement - as only the evidence, transitional prior, dynamic prior and normalising distributions need to be retained

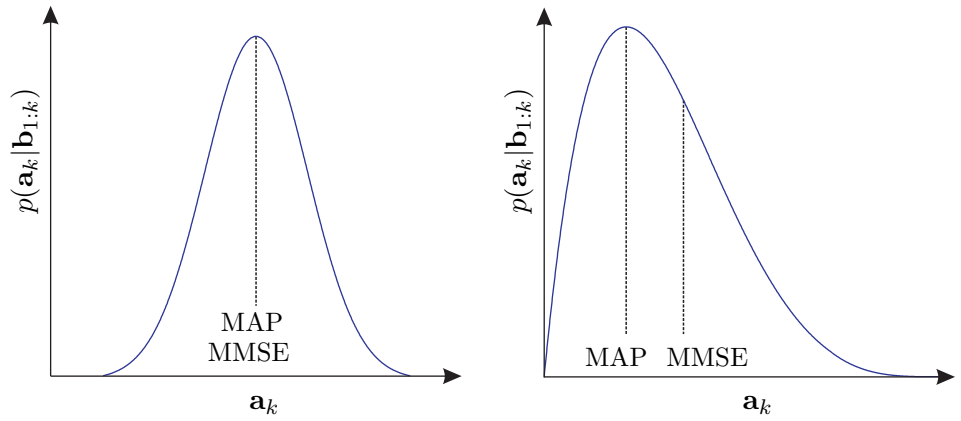

(a) MAP and MMSE yield the same estimates

(b) MAP and MMSE yield the different estimates

Figure 3.2: Differences in MMSE and MAP estimates for (a) a normal PDF and (b) a beta PDF

- and so is suitable for real-time implementation.

Unfortunately storage of the necessary distributions is not necessarily a trivial matter. In the case of normal PDFs the mean and covariance provide a complete description of the density. If the distribution is non-Gaussian there is a potentially infinite memory requirement to store enough information for a complete description. Gaussianity in all densities involved is dependent on the functions (3.1) and (3.2) being linear and the noise processes $\mathbf{e}_k$ and $\mathbf{v}_k$ being normally distributed and additive. If such conditions for the densities are met then the Kalman filter, reviewed in section 3.3, is the optimal recursive estimator [53, 54, 84–86]. If these conditions are not met then either a Gaussian distribution will have to be fitted to the non-Gaussian densities so they can be applied to the Kalman filter framework, as they are in the extended and unscented Kalman filters, or modelled discretely, as they are in particle filtering.

3.3 The Kalman Filter

First proposed in 1960 as a more practical alternative to the Wiener filter [50], the Kalman filter is a Bayesian estimator where the optimality criterion is the minimum mean squared error:

$$\mathbb{E}\left\{\left(\mathbf{a}_k - \hat{\mathbf{a}}_{k|k}\right)^2\right\} \tag{3.14}$$

which lies at the mean of a normal posterior distribution. The Kalman filter recursively computes the optimal Bayesian solution for non-stationary processes as opposed to the N-block adaptation of the Wiener filter, which assumes the system is stationary over a block of N samples.

To adequately describe the posterior density parametrically it must be accurately described by a mean and covariance, i.e. normally distributed, which means the system and measurement

noise processes must both be Gaussian. For the posterior to remain normally distributed the system and measurement functions must both be linear. If both these criteria are met then the Kalman filter is the optimal recursive estimator [54].

The Kalman filter implements the two step approach to parameter estimation described by (3.9) and (3.11), a prediction stage followed by a prediction update stage via an MMSE estimate. Firstly the system and measurement equations are linearised, the prediction stage is derived, then the MMSE estimator is presented and finally the Kalman update is derived. The discussions in this section draw largely from [54, 84, 86].

3.3.1 Linear System and Measurement Functions

Re-stating the system (3.1) and measurement (3.2) functions to assume linearity allows them to be expressed in matrix vector form:

$$\mathbf{a}_k = \mathbf{F}\mathbf{a}_{k-1} + \mathbf{e}_{k-1} \tag{3.15}$$

$$\mathbf{b}_k = \mathbf{H}\mathbf{a}_k + \mathbf{v}_k \tag{3.16}$$

where $\mathbf{F}$ and $\mathbf{H}$ are the system and measurement matrices characterising $\boldsymbol{f}_k(\,)$ and $\boldsymbol{h}_k(\,)$ respectively[1] and $\mathbf{e}_k$ and $\mathbf{v}_k$ are additive system and measurement noise processes.

3.3.2 Target State Prediction

The transitional prior density, necessary to compute the posterior distribution, is acquired by predicting the current target state from the target state at $k-1$. If $\mathbf{a}_{k-1}$ is known then, assuming ignorance of the measurement noise, $\mathbf{a}_k$ can be predicted using:

$$\hat{\mathbf{a}}_{k|k-1} = \mathbb{E}\left\{\mathbf{a}_k|\mathbf{b}_{1:k-1}\right\} \tag{3.17}$$

$$= \mathbb{E}\left\{\mathbf{F}\mathbf{a}_{k-1} + \mathbf{e}_{k-1}|\mathbf{b}_{1:k-1}\right\} \tag{3.18}$$

$$= \mathbf{F}\mathbb{E}\left\{\mathbf{a}_{k-1}|\mathbf{b}_{1:k-1}\right\} \tag{3.19}$$

where $\hat{\mathbf{a}}_{k|k-1}$ is the prediction of system parameters at k given the information available at $k-1$. The noise term $\mathbf{e}_k$ is dropped from the prediction because it is independent sample-to-sample and zero mean so $\mathbb{E}\left\{\mathbf{e}_k\right\} = 0$, furthermore $\mathbf{b}_{k-1}$ and $\mathbf{e}_k$ are orthogonal so $\mathbb{E}\left\{\mathbf{e}_k|\mathbf{b}_{1:k-1}\right\} = 0$. Therefore, the prediction step is:

$$\hat{\mathbf{a}}_{k|k-1} = \mathbf{F}\hat{\mathbf{a}}_{k-1|k-1} \tag{3.20}$$

The target state prediction (3.20) will be updated using the Kalman update to obtain the final state estimate in section 3.3.4.

[1] The matrices $\mathbf{F}$ and $\mathbf{H}$ have been set time-invariant by not maintaining the time subscript, k, from $\boldsymbol{f}_k(\,)$ and $\boldsymbol{h}_k(\,)$ for clarity of notation; simply re-instating the time subscript would restore the time variability.

3.3.3 The MMSE Estimator

If $\mathbf{e}_k$ and $\mathbf{v}_k$ are assumed to be zero-mean white Gaussian processes with auto-covariance matrices $\mathbf{R_{ee}}$ and $\mathbf{R_{vv}}$ respectively:

$$\mathbb{E}\{\mathbf{e}_{1:k}\} = 0 \qquad \mathbb{E}\{\mathbf{e}_k\mathbf{e}_m\} = \begin{cases} 0 & k \neq m \\ \mathbf{R_{ee}} & k = m \end{cases}$$

$$\mathbb{E}\{\mathbf{v}_{1:k}\} = 0 \qquad \mathbb{E}\{\mathbf{v}_k\mathbf{v}_m\} = \begin{cases} 0 & k \neq m \\ \mathbf{R_{vv}} & k = m \end{cases}$$

then $\mathbf{a}_k$ and $\mathbf{b}_k$ are assumed to be Gaussian random variables with covariance matrix:

$$\mathbf{R} = \begin{bmatrix} \mathbf{R_{aa}} & \mathbf{R_{ab}} \\ \mathbf{R_{ba}} & \mathbf{R_{bb}} \end{bmatrix} \tag{3.21}$$

so the joint probability of the Gaussian distribution of $\mathbf{a}$ and $\mathbf{b}$ can be described as [86]:

$$p(\mathbf{a},\mathbf{b}) = \frac{1}{\sqrt{2\pi\,|\mathbf{R_{ab}}|}} \exp\left\{ -\frac{1}{2} \begin{bmatrix} \mathbf{a}-\mathbb{E}\{\mathbf{a}\} \\ \mathbf{b}-\mathbb{E}\{\mathbf{b}\} \end{bmatrix}' \mathbf{R_{ab}^{-1}} \begin{bmatrix} \mathbf{a}-\mathbb{E}\{\mathbf{a}\} \\ \mathbf{b}-\mathbb{E}\{\mathbf{b}\} \end{bmatrix} \right\} \tag{3.22}$$

which means the conditional probability, $p(\mathbf{a}|\mathbf{b})$, is also Gaussian [86]:

$$\mathbb{E}\{\mathbf{a}|\mathbf{b}\} = \mathbb{E}\{\mathbf{a}\} + \mathbf{R_{ab}}\mathbf{R_{bb}^{-1}}(\mathbf{b}-\mathbb{E}\{\mathbf{b}\}) \tag{3.23}$$

The MMSE estimate is the mean of the posterior distribution, as stated in (3.12), and the parameter estimate is conditional on the measurement history:

$$\hat{\mathbf{a}}_{k|k} = \mathbb{E}\{\mathbf{a}_k|\mathbf{b}_{1:k}\} \tag{3.24}$$

Given zero means to eliminate the terms $\mathbb{E}\{\mathbf{a}\}$ and $\mathbb{E}\{\mathbf{b}\}$ and applying (3.23), the MMSE estimate conditional on the measurement history is:

$$\hat{\mathbf{a}}_{k|k}^{\mathrm{MMSE}} = \mathbf{R_{ab}}\mathbf{R_{bb}^{-1}}\mathbf{b}_{1:k} \tag{3.25}$$

The parameters $\mathbf{a}_k$ are correlated sample to sample and therefore the data samples $\mathbf{b}_k$ are also correlated sample to sample. For linear MMSE estimation to be optimal the estimation error must be orthogonal to each data sample [86, 87]. These estimation errors represent the measurement noise and unpredictable parts of the signal and are found by subtracting the predicted data from the actual data:

$$\tilde{\mathbf{b}}_k = \mathbf{b}_k - \hat{\mathbf{b}}_{k|k-1} \tag{3.26}$$

where the measurement data prediction is:

$$\hat{\mathbf{b}}_{k|k-1} = \mathbf{H}\hat{\mathbf{a}}_{k|k-1} \tag{3.27}$$

Incorporating the innovation into (3.24) gives:

$$\hat{\mathbf{a}}_{k|k} = \mathbb{E}\left\{\mathbf{a}_k|\mathbf{b}_{1:k-1}, \tilde{\mathbf{b}}_k\right\} \tag{3.28}$$

which using (3.17) can be expanded to:

$$\hat{\mathbf{a}}_{k|k} = \mathbb{E}\left\{\mathbf{a}_k|\mathbf{b}_{1:k-1}\right\} + \mathbb{E}\left\{\mathbf{a}_k|\tilde{\mathbf{b}}_k\right\} \tag{3.29}$$

$$= \hat{\mathbf{a}}_{k|k-1} + \mathbb{E}\left\{\mathbf{a}_k|\tilde{\mathbf{b}}_k\right\} \tag{3.30}$$

This establishes the predict-update form of the Kalman filter. It now remains to derive the update expression for the estimator $\mathbb{E}\left\{\mathbf{a}_k|\tilde{\mathbf{b}}_k\right\}$.

3.3.4 The Kalman Update

Given the predicted system parameters, $\hat{\mathbf{a}}_{k|k-1}$, the unpredictable parameter components are estimated by an MMSE estimate. Expanding $\mathbb{E}\left\{\mathbf{a}_k|\tilde{\mathbf{b}}_k\right\}$ gives:

$$\mathbb{E}\left\{\mathbf{a}_k|\tilde{\mathbf{b}}_k\right\} = \mathbf{R}_{\mathbf{a}\tilde{\mathbf{b}}}\mathbf{R}_{\tilde{\mathbf{b}}\tilde{\mathbf{b}}}^{-1}\tilde{\mathbf{b}}_k \tag{3.31}$$

$$= \mathbb{E}\left\{\mathbf{a}_k\tilde{\mathbf{b}}_k\right\}\mathbb{E}\left\{\tilde{\mathbf{b}}_k\tilde{\mathbf{b}}_k\right\}^{-1}\tilde{\mathbf{b}}_k \tag{3.32}$$

$$= \mathbb{E}\left\{\mathbf{a}_k\tilde{\mathbf{b}}_k\right\}\mathbb{E}\left\{\tilde{\mathbf{b}}_k\tilde{\mathbf{b}}_k\right\}^{-1}\left(\mathbf{b}_k - \hat{\mathbf{b}}_{k|k-1}\right) \tag{3.33}$$

where $\mathbb{E}\{\mathbf{a}_k\} = 0$. If the covariance matrix product is combined to a single representation $\mathbf{K}_k$, known as the Kalman gain, so that:

$$\mathbf{K}_k = \mathbf{R}_{\mathbf{a}\tilde{\mathbf{b}}}\mathbf{R}_{\tilde{\mathbf{b}}\tilde{\mathbf{b}}}^{-1} \tag{3.34}$$

$$= \mathbb{E}\left\{\mathbf{a}_k\tilde{\mathbf{b}}_k\right\}\mathbb{E}\left\{\tilde{\mathbf{b}}_k\tilde{\mathbf{b}}_k\right\}^{-1} \tag{3.35}$$

then (3.30) can be expressed as:

$$\hat{\mathbf{a}}_{k|k} = \hat{\mathbf{a}}_{k|k-1} + \mathbf{K}_k\left(\mathbf{b}_k - \hat{\mathbf{b}}_{k|k-1}\right) \tag{3.36}$$

Further expansion of the $\tilde{\mathbf{b}}_k$ terms in (3.35) gives $\mathbf{K}_k$ in terms of $\mathbf{a}_k$, $\hat{\mathbf{a}}_{k|k-1}$ and $\mathbf{b}_k$:

$$\mathbf{K}_k = \mathbb{E}\left\{\mathbf{a}_k\left(\mathbf{b}_k - \mathbf{H}\hat{\mathbf{a}}_{k|k-1}\right)'\right\}\mathbb{E}\left\{\left(\mathbf{b}_k - \mathbf{H}\mathbf{a}_{k|k-1}\right)\left(\mathbf{b}_k - \mathbf{H}\mathbf{a}_{k|k-1}\right)'\right\}^{-1} \tag{3.37}$$

This expansion still leaves an $\mathbf{a}_k$ term in the first expectation, which is unknown and therefore needs eliminating. Using the fact that the system parameter prediction and innovation terms are uncorrelated so that $\mathbb{E}\left\{\hat{\mathbf{a}}_{k|k-1}\tilde{\mathbf{b}}_k\right\} = 0$ then:

$$\mathbb{E}\left\{\left(\mathbf{a}_k - \hat{\mathbf{a}}_{k|k-1}\right)\right\} = \mathbb{E}\left\{\mathbf{a}_k\tilde{\mathbf{b}}_k\right\} - \mathbb{E}\left\{\hat{\mathbf{a}}_{k|k-1}\tilde{\mathbf{b}}_k\right\} \tag{3.38}$$

$$= \mathbb{E}\left\{\mathbf{a}_k|\tilde{\mathbf{b}}_k\right\} \tag{3.39}$$

Using this property the covariance matrix $\mathbf{R}_{\mathbf{a}\tilde{\mathbf{b}}}$ can be derived:

$$\mathbf{R}_{\mathbf{a}\tilde{\mathbf{b}}} = \mathbb{E}\left\{\mathbf{a}_k\left(\mathbf{b}_k - \mathbf{H}\hat{\mathbf{a}}_{k|k-1}\right)'\right\} \tag{3.40}$$

$$= \mathbb{E}\left\{\left(\mathbf{a}_k - \hat{\mathbf{a}}_{k|k-1}\right)\left(\mathbf{b}_k - \mathbf{H}\hat{\mathbf{a}}_{k|k-1}\right)'\right\} \tag{3.41}$$

$$= \mathbb{E}\left\{\left(\mathbf{a}_k - \hat{\mathbf{a}}_{k|k-1}\right)\left(\mathbf{H}\mathbf{a}_k - \mathbf{H}\hat{\mathbf{a}}_{k|k-1} + \mathbf{v}_k\right)'\right\} \tag{3.42}$$

$$= \mathbb{E}\left\{\left(\mathbf{F}\mathbf{a}_{k-1} - \mathbf{F}\hat{\mathbf{a}}_{k-1|k-1} + \mathbf{e}_{k-1}\right)\left(\mathbf{H}\mathbf{F}\hat{\mathbf{a}}_{k-1|k-1} - \mathbf{H}\mathbf{F}\hat{\mathbf{a}}_{k-1|k-1} + \mathbf{H}\mathbf{e}_k + \mathbf{v}_k\right)'\right\} \tag{3.43}$$

$$= \mathbf{H}\mathbb{E}\left\{\mathbf{F}\left(\mathbf{a}_{k-1} - \hat{\mathbf{a}}_{k-1|k-1}\right)\left(\mathbf{a}_{k-1} - \hat{\mathbf{a}}_{k-1|k-1}\right)'\mathbf{F}' + \mathbf{R}_{\mathbf{ee}}\right\} \tag{3.44}$$

$$= \mathbf{H}\left(\mathbf{F}\mathbf{P}_{k-1|k-1}\mathbf{F}' + \mathbf{R}_{\mathbf{ee}}\right) \tag{3.45}$$

where $\mathbf{P}_{k-1|k-1} = \left(\mathbf{a}_{k-1} - \hat{\mathbf{a}}_{k-1|k-1}\right)\left(\mathbf{a}_{k-1} - \hat{\mathbf{a}}_{k-1|k-1}\right)'$ is the mean squared error (MSE) matrix from the previous estimate. The auto-covariance matrix $\mathbf{R}_{\tilde{\mathbf{b}}\tilde{\mathbf{b}}}$, the inverse of which is used in the computation of MMSE estimator, is derived by expanding to terms of the system parameters, system matrix, measurement matrix and noise covariance matrices:

$$\mathbf{R}_{\tilde{\mathbf{b}}\tilde{\mathbf{b}}} = \mathbb{E}\left\{\left(\mathbf{b}_k - \mathbf{H}\hat{\mathbf{a}}_{k|k-1}\right)\left(\mathbf{b}_k - \mathbf{H}\hat{\mathbf{a}}_{k|k-1}\right)'\right\} \tag{3.46}$$

$$= \mathbb{E}\left\{\left(\mathbf{H}\mathbf{a}_k - \mathbf{H}\hat{\mathbf{a}}_{k|k-1} + \mathbf{v}_k\right)\left(\mathbf{H}\mathbf{a}_k - \mathbf{H}\hat{\mathbf{a}}_{k|k-1} + \mathbf{v}_k\right)'\right\} \tag{3.47}$$

$$= \mathbb{E}\left\{\left(\mathbf{H}\mathbf{F}\mathbf{a}_{k-1} - \mathbf{H}\mathbf{F}\hat{\mathbf{a}}_{k-1|k-1} + \mathbf{H}\mathbf{e}_k + \mathbf{v}_k\right)\left(\mathbf{H}\mathbf{F}\mathbf{a}_{k-1} - \mathbf{H}\mathbf{F}\hat{\mathbf{a}}_{k-1|k-1} + \mathbf{H}\mathbf{e}_k + \mathbf{v}_k\right)'\right\} \tag{3.48}$$

$$= \mathbf{H}\mathbb{E}\left\{\mathbf{F}\left(\mathbf{a}_{k-1} - \hat{\mathbf{a}}_{k-1|k-1}\right)\left(\mathbf{a}_{k-1} - \hat{\mathbf{a}}_{k-1|k-1}\right)'\mathbf{F}' + \mathbf{R}_{\mathbf{ee}}\right\}\mathbf{H}' + \mathbf{R}_{\mathbf{vv}} \tag{3.49}$$

$$= \mathbf{H}\left(\mathbf{F}\mathbf{P}_{k-1|k-1}\mathbf{F}' + \mathbf{R}_{\mathbf{ee}}\right)\mathbf{H}' + \mathbf{R}_{\mathbf{vv}} \tag{3.50}$$

Now the Kalman gain can be expressed in terms of MSE and covariance matrices:

$$\mathbf{K}_k = \mathbf{R}_{\mathbf{a}\tilde{\mathbf{b}}}\mathbf{R}_{\tilde{\mathbf{b}}\tilde{\mathbf{b}}}^{-1} \tag{3.51}$$

$$= \left[\mathbf{H}\left(\mathbf{F}\mathbf{P}_{k-1|k-1}\mathbf{F}' + \mathbf{R}_{\mathbf{ee}}\right)\right]\left[\mathbf{H}\left(\mathbf{F}\mathbf{P}_{k-1|k-1}\mathbf{F}' + \mathbf{R}_{\mathbf{ee}}\right)\mathbf{H}' + \mathbf{R}_{\mathbf{vv}}\right]^{-1} \tag{3.52}$$

The MSE of the prediction, $\mathbf{P}_{k|k-1}$, is given by:

$$\mathbf{P}_{k|k-1} = \mathbb{E}\left\{\left(\mathbf{a}_k - \hat{\mathbf{a}}_{k|k-1}\right)\left(\mathbf{a}_k - \hat{\mathbf{a}}_{k|k-1}\right)'\right\} \tag{3.53}$$

$$= \mathbb{E}\left\{\left(\mathbf{a}_k - \mathbf{F}\hat{\mathbf{a}}_{k-1|k-1}\right)\left(\mathbf{a}_k - \mathbf{F}\hat{\mathbf{a}}_{k-1|k-1}\right)'\right\} \tag{3.54}$$

$$= \mathbf{F}\mathbf{P}_{k-1|k-1}\mathbf{F}' + \mathbf{R}_{\mathbf{ee}} \tag{3.55}$$

Algorithm 3.1 $\left[\hat{\mathbf{a}}_{k|k}, \mathbf{P}_{k|k}\right]$ = Kalman Filter $\left(\hat{\mathbf{a}}_{k-1|k-1}, \mathbf{P}_{k-1|k-1}\right)$

Predict the state at k from $\hat{\mathbf{a}}_{k-1|k-1}$:

$$\hat{\mathbf{a}}_{k|k-1} = \mathbf{F}\hat{\mathbf{a}}_{k-1|k-1}$$

Predict the MSE:

$$\mathbf{P}_{k|k-1} = \mathbf{F}\mathbf{P}_{k-1|k-1}\mathbf{F}' + \mathbf{R}_{\mathbf{ee}}$$

Calculate the Kalman gain matrix:

$$\mathbf{K}_k = \left[\mathbf{P}_{k|k-1}\mathbf{H}_k'\right]\left[\mathbf{H}\mathbf{P}_{k|k-1}\mathbf{H}' + \mathbf{R}_{\mathbf{vv}}\right]^{-1}$$

Apply update to prediction:

$$\hat{\mathbf{a}}_{k|k} = \hat{\mathbf{a}}_{k|k-1} + \mathbf{K}_k\left(\mathbf{b}_k - \mathbf{H}\hat{\mathbf{a}}_{k|k-1}\right)$$

Update the MSE:

$$\mathbf{P}_{k|k} = \left(\mathbf{I} - \mathbf{K}_k\mathbf{H}\right)\mathbf{P}_{k|k-1}$$

It is now necessary to derive a recursive expression for $\mathbf{P}_{k|k}$:

$$\begin{aligned}
\mathbf{P}_{k|k} &= \mathbb{E}\left\{\left(\mathbf{a}_k - \hat{\mathbf{a}}_{k|k-1}\right)\left(\mathbf{a}_k - \hat{\mathbf{a}}_{k|k-1}\right)'\right\} && (3.56)\\
&= \mathbb{E}\left\{\left(\mathbf{a}_k\hat{\mathbf{a}}_{k|k-1} - \mathbf{K}_k\left(\mathbf{b}_k - \mathbf{H}\hat{\mathbf{a}}_{k|k-1}\right)\right)\left(\mathbf{a}_k\hat{\mathbf{a}}_{k|k-1} - \mathbf{K}_k\left(\mathbf{b}_k - \mathbf{H}\hat{\mathbf{a}}_{k|k-1}\right)\right)'\right\} && (3.57)\\
&= \mathbb{E}\left\{\left(\mathbf{a}_k - \hat{\mathbf{a}}_{k|k-1}\right)\left(\mathbf{a}_k - \hat{\mathbf{a}}_{k|k-1}\right)'\right\} - \mathbb{E}\left\{\left(\mathbf{a}_k - \hat{\mathbf{a}}_{k|k-1}\right)\left(\mathbf{b}_k - \mathbf{H}\hat{\mathbf{a}}_{k|k-1}\right)'\mathbf{K}_k'\right\}\ldots\\
&\quad\cdots - \mathbb{E}\left\{\mathbf{K}_k\left(\mathbf{b}_k - \mathbf{H}\hat{\mathbf{a}}_{k|k-1}\right)\left(\mathbf{a}_k - \hat{\mathbf{a}}_{k|k-1}\right)'\right\}\ldots\\
&\quad\cdots + \mathbb{E}\left\{\mathbf{K}_k\left(\mathbf{b}_k - \mathbf{H}\hat{\mathbf{a}}_{k|k-1}\right)\left(\mathbf{b}_k - \mathbf{H}\hat{\mathbf{a}}_{k|k-1}\right)'\mathbf{K}_k'\right\} && (3.58)
\end{aligned}$$

Substituting $\mathbf{P}_{k|k-1}$ into the first expectation of (3.58), $\mathbf{R}_{\mathbf{a}\tilde{\mathbf{b}}}$ into the second and third and $\mathbf{R}_{\tilde{\mathbf{b}}\tilde{\mathbf{b}}}$ into the fourth the error correlation matrix, $\mathbf{P}_{k|k}$, becomes:

$$\begin{aligned}
\mathbf{P}_{k|k} &= \mathbf{P}_{k|k-1} - \mathbf{R}_{\mathbf{a}\tilde{\mathbf{b}}}\mathbf{K}_k' - \mathbf{K}_k\mathbf{R}_{\mathbf{a}\tilde{\mathbf{b}}}' + \mathbf{K}_k\mathbf{R}_{\tilde{\mathbf{b}}\tilde{\mathbf{b}}}\mathbf{K}_k' && (3.59)\\
&= \mathbf{P}_{k|k-1} - \mathbf{R}_{\mathbf{a}\tilde{\mathbf{b}}}\left[\mathbf{R}_{\mathbf{a}\tilde{\mathbf{b}}}\mathbf{R}_{\tilde{\mathbf{b}}\tilde{\mathbf{b}}}^{-1}\right]' - \left[\mathbf{R}_{\mathbf{a}\tilde{\mathbf{b}}}\mathbf{R}_{\tilde{\mathbf{b}}\tilde{\mathbf{b}}}^{-1}\right]\mathbf{R}_{\mathbf{a}\tilde{\mathbf{b}}}' + \left[\mathbf{R}_{\mathbf{a}\tilde{\mathbf{b}}}\mathbf{R}_{\tilde{\mathbf{b}}\tilde{\mathbf{b}}}^{-1}\right]\mathbf{R}_{\tilde{\mathbf{b}}\tilde{\mathbf{b}}}\left[\mathbf{R}_{\mathbf{a}\tilde{\mathbf{b}}}\mathbf{R}_{\tilde{\mathbf{b}}\tilde{\mathbf{b}}}^{-1}\right]' && (3.60)\\
&= \mathbf{P}_{k|k-1} - \mathbf{K}_k\mathbf{R}_{\mathbf{a}\tilde{\mathbf{b}}}' && (3.61)
\end{aligned}$$

An implementable form of the recursive expression for the MSE is finally derived by substituting $\mathbf{R}_{\mathbf{a}\tilde{\mathbf{b}}} = \mathbf{P}_{k|k-1}\mathbf{H}'$:

$$\mathbf{P}_{k|k} = \left(\mathbf{I} - \mathbf{K}_k\mathbf{H}\right)\mathbf{P}_{k|k-1} \quad (3.62)$$

In practice this requires an expression for $\mathbf{P}_{0|-1}$. If the actual error value is unknown then $\mathbf{P}_{k|k-1}$ is usually initialised with large values on the diagonal. The final Kalman filter algorithm is summarised in Algorithm 3.1.

The Kalman filter has been derived and will be applied within a multiple hypothesis tracking (MHT) framework in chapter 6 to identify which clicks came from which animals based on time-delay history. Adaptations of the Kalman filter for tracking non-linear and non-Gaussian problems are presented in the next section.

3.4 Sub-Optimal Extensions to the Kalman Filter

Two of the most widely considered adaptations of the Kalman filter for non-linear and non-Gaussian tracking problems are the extended Kalman filter (EKF) and the unscented Kalman filter (UKF) [54, 85, 86, 88–90]. Both algorithms are sub-optimal but have been successfully applied, notably the EKF has been used extensively in angle-only tracking applications [79, 91–93]. Neither algorithm is utilised in this work but both are included for completeness and are briefly discussed.

3.4.1 Extended Kalman Filter

The EKF achieves non-linear estimation by approximating the non-linear system and measurement functions as linear for the error matrix and Kalman gain calculations. The system and measurement equations, (3.1) and (3.2), are re-stated as non-linear with additive noise processes so that:

$$\mathbf{a}_k = \boldsymbol{f}\left(\mathbf{a}_{k-1}\right) + \mathbf{e}_{k-1} \tag{3.63}$$

$$\mathbf{b}_k = \boldsymbol{h}\left(\mathbf{a}_k\right) + \mathbf{v}_k \tag{3.64}$$

where $\boldsymbol{f}(\,)$ and $\boldsymbol{h}(\,)$ have been assumed to be time-invariant so that the time subscript can be dropped for clarity of notation. A linearisation of (3.63) is derived via a first-order Taylor series expansion around the last state estimate, $\hat{\mathbf{a}}_{k-1|k-1}$:

$$\boldsymbol{f}\left(\mathbf{a}_{k-1}\right) \approx \boldsymbol{f}\left(\hat{\mathbf{a}}_{k-1|k-1}\right) + \left.\frac{\partial \boldsymbol{f}}{\partial \mathbf{a}_{k-1}}\right|_{\mathbf{a}_{k-1}=\hat{\mathbf{a}}_{k-1|k-1}} \left(\mathbf{a}_{k-1} - \hat{\mathbf{a}}_{k-1|k-1}\right) \tag{3.65}$$

where the linear estimate of the system function is represented by the Jacobian matrix:

$$\hat{\mathbf{F}}_{k-1} = \left.\frac{\partial \boldsymbol{f}}{\partial \mathbf{a}_{k-1}}\right|_{\mathbf{a}_{k-1}=\hat{\mathbf{a}}_{k-1|k-1}} \tag{3.66}$$

The linear system function estimate $\hat{\mathbf{F}}_{k-1}$ is time indexed to allow for variation in the previous parameter estimate $\hat{\mathbf{a}}_{k-1|k-1}$. Similarly the linearised estimate of the measurement function (3.64) is:

$$\boldsymbol{h}\left(\mathbf{a}_k\right) \approx \boldsymbol{h}\left(\mathbf{a}_{k|k-1}\right) + \left.\frac{\partial \boldsymbol{h}}{\partial \mathbf{a}_k}\right|_{\mathbf{a}_k=\hat{\mathbf{a}}_{k|k-1}} \left(\mathbf{a}_k - \hat{\mathbf{a}}_{k|k-1}\right) \tag{3.67}$$

where the linear estimate of the measurement function is represented by the Jacobian matrix:

$$\hat{\mathbf{H}}_k = \left.\frac{\partial \boldsymbol{h}}{\partial \mathbf{a}_k}\right|_{\mathbf{a}_k=\hat{\mathbf{a}}_{k|k-1}} \tag{3.68}$$

Algorithm 3.2 $\left[\hat{\mathbf{a}}_{k|k}, \mathbf{P}_{k|k}\right] = \text{EFK}\left(\hat{\mathbf{a}}_{k-1|k-1}, \mathbf{P}_{k-1|k-1}\right)$

Predict system state at k from $\hat{\mathbf{a}}_{k-1|k-1}$:

$$\hat{\mathbf{a}}_{k|k-1} = \boldsymbol{f}\left(\hat{\mathbf{a}}_{k-1|k-1}\right)$$

Compute the Jacobian matrix $\hat{\mathbf{F}}_{k-1}$:

$$\hat{\mathbf{F}}_{k-1} = \frac{\partial \boldsymbol{f}}{\partial \mathbf{a}_{k-1}}\Big|_{\mathbf{a}_{k-1}=\hat{\mathbf{a}}_{k-1|k-1}}$$

Predict the MSE:

$$\mathbf{P}_{k|k-1} = \hat{\mathbf{F}}_{k-1}\mathbf{P}_{k-1|k-1}\hat{\mathbf{F}}'_{k-1} + \mathbf{R}_{\mathbf{ee}}$$

Compute the Jacobian matrix $\hat{\mathbf{H}}_k$:

$$\hat{\mathbf{H}}_k = \frac{\partial \boldsymbol{h}}{\partial \mathbf{a}_k}\Big|_{\mathbf{a}_k=\hat{\mathbf{a}}_{k|k-1}}$$

Calculate the Kalman gain matrix:

$$\mathbf{K}_k = \left[\mathbf{P}_{k|k-1}\hat{\mathbf{H}}'_k\right]\left[\hat{\mathbf{H}}_k\mathbf{P}_{k-1|k-1}\hat{\mathbf{H}}'_k + \mathbf{R}_{\mathbf{vv}}\right]^{-1}$$

Apply update to prediction:

$$\hat{\mathbf{a}}_{k|k} = \hat{\mathbf{a}}_{k|k-1} + \mathbf{K}_k\left(\mathbf{b}_k - \boldsymbol{h}\left(\hat{\mathbf{a}}_{k|k-1}\right)\right)$$

Update the MSE:

$$\mathbf{P}_{k|k} = \left(\mathbf{I} - \mathbf{K}_k\hat{\mathbf{H}}_k\right)\mathbf{P}_{k|k-1}$$

The linearised system and measurement functions can now be respectively defined as:

$$\mathbf{a}_k = \hat{\mathbf{F}}_{k-1}\mathbf{a}_{k-1} + \mathbf{e}_{k-1} + \left(\boldsymbol{f}\left(\hat{\mathbf{a}}_{k-1|k-1}\right) - \hat{\mathbf{F}}_{k-1}\hat{\mathbf{a}}_{k-1|k-1}\right) \tag{3.69}$$

$$\mathbf{b}_k = \hat{\mathbf{H}}_k\mathbf{a}_k + \mathbf{v}_k + \left(\boldsymbol{h}\left(\hat{\mathbf{a}}_{k|k-1}\right) - \hat{\mathbf{H}}_k\hat{\mathbf{a}}_{k|k-1}\right) \tag{3.70}$$

The EKF algorithm is obtained by substituting $\hat{\mathbf{F}}_{k-1}$ and $\hat{\mathbf{H}}_k$ into the error equations (3.55) and (3.62) and the Kalman gain equation (3.52). The complete EKF algorithm is shown in Algorithm 3.2. Although the EKF addresses the linearity constraints of the Kalman filter it is only reliable for non-linear systems that update at regular intervals and do not violate the assumptions of local linearity [88, 89]. EKF convergence relies on the propagation of the deterministic component $\boldsymbol{f}\left(\hat{\mathbf{a}}_{k-1|k-1} - \hat{\mathbf{F}}_{k-1}\hat{\mathbf{a}}_{k-1|k-1}\right)$ through the system, however this can introduce large errors and consequently the filter may diverge [90]. Implementation issues also arise due to the non-trivial requirement of computing the Jacobian matrices (3.66) and (3.68) [88, 90].

3.4.2 Unscented Kalman Filter

Julier and Uhlman proposed applying the unscented transform to the Kalman filter framework as an alternative to the EKF [88] under the premise that it's simpler to model an arbitrary distribution as a Gaussian than to linearise an arbitrary non-linear function [90]. The distributions are represented by a set of strategically drawn samples known as sigma points. Implementation of the UKF is, in general, simpler than for the EKF because the UKF does not require the computation of Jacobian matrices.

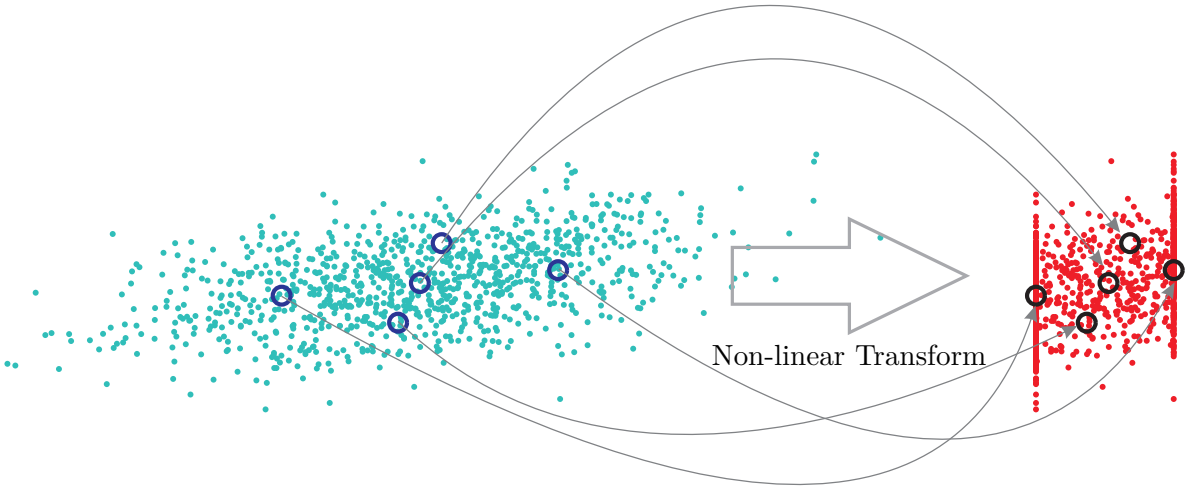

Figure 3.3: Randomly drawn samples and the strategically drawn sigma points drawn from the distribution at $k-1$. The random samples and sigma points are propagated through a non-linear function to give the non-Gaussian distribution at k.

Unscented Transform

The set of $2N_{\mathcal{A}}+1$ sigma points, $\mathcal{A}$, are chosen so that they represent the mean and covariance of the system distribution. Each of the $2N_{\mathcal{A}}+1$ points is assigned a respective weight, $\mathcal{W}$:

$$\{\mathcal{A}\}_0 = \bar{\mathbf{a}} \qquad \{\mathcal{W}\}_0 = \frac{\kappa}{(N_{\mathcal{A}}+\kappa)} \tag{3.71}$$

$$\{\mathcal{A}\}_{1:N_{\mathcal{A}}} = \bar{\mathbf{a}} + \left\{\left(\sqrt{(N_{\mathcal{A}}+\kappa)\,\mathbf{R_{aa}}}\right)\right\}_{1:N_{\mathcal{A}}} \qquad \{\mathcal{W}\}_{1:N_{\mathcal{A}}} = \frac{1}{2\,(N_{\mathcal{A}}+\kappa)} \tag{3.72}$$

$$\{\mathcal{A}\}_{N_{\mathcal{A}}+1:2N_{\mathcal{A}}} = \bar{\mathbf{a}} - \left\{\left(\sqrt{(N_{\mathcal{A}}+\kappa)\,\mathbf{R_{aa}}}\right)\right\}_{1:N_{\mathcal{A}}} \qquad \{\mathcal{W}\}_{N_{\mathcal{A}}+1:2N_{\mathcal{A}}} = \frac{1}{2\,(N_{\mathcal{A}}+\kappa)} \tag{3.73}$$

where $\kappa \in \mathbb{R}$, $\left\{\left(\sqrt{(N_{\mathcal{A}}+\kappa)\,\mathbf{R_{aa}}}\right)\right\}_n$ is the nth column of the matrix square root of $(n+\kappa)\,\mathbf{R_{aa}}$ and $\mathcal{W}$ is the set of weights associated with the sigma points. The parameter κ is a positive value that controls the distance from the central sigma point at which the sigma points representing the variance are drawn. A useful heuristic for Gaussian distributions is $N_{\mathcal{A}}+\kappa = 3$ [88].

The prior distribution parameters are obtained by propagating the sigma points through the non-linear system function, so that:

$$\mathcal{A}_k = \boldsymbol{f}\left(\mathcal{A}_{k-1}\right) \tag{3.74}$$

A mean and covariance are then calculated from the transformed sigma points:

$$\bar{\mathbf{a}}_k = \sum_{n=0}^{2N_{\mathcal{A}}} \{\mathcal{W}\}_n \{\mathcal{A}_k\}_n \tag{3.75}$$

$$\mathbf{R_{aa}} = \sum_{n=0}^{2N_{\mathcal{A}}} \{\mathcal{W}\}_n \left(\{\mathcal{A}_k\}_n - \bar{\mathbf{a}}_k\right)\left(\{\mathcal{A}_k\}_n - \bar{\mathbf{a}}_k\right)' \tag{3.76}$$

The left side distribution shown in figure 3.3 shows a set of randomly drawn samples from

a normal distribution and the representative strategically drawn sigma points. The random samples and sigma points are propagated through a non-linear function resulting in the right side non-Gaussian distribution which the sigma points still model as normal. The resulting distribution estimate is accurate up to the third-order Taylor series expansion and estimation of non-Gaussian distributions is accurate up to the second order. It can be shown that the unscented transform is able to partially include information from higher orders [88, 90].

UKF Algorithm

The UKF algorithm is shown in algorithm 3.3 based on the UKF algorithm presented in [94]. The algorithm replaces the auto-covariance matrix $\mathbf{R_{aa}}$ in equations 3.71 to 3.73 with the MSE matrix $\mathbf{P}_{k-1|k-1}$. At initialisation $\mathbf{P}_{0|0}$ can be defined as $\mathbf{P}_{0|0} = \mathbb{E}\left\{(\mathbf{a}_0 - \hat{\mathbf{a}}_0)(\mathbf{a}_0 - \hat{\mathbf{a}}_0)'\right\}$, however this requires knowledge of $\mathbf{a}_0$, as an alternative the diagonal of matrix $\mathbf{P}_{0|0}$ can be set to large values.

Square Root Unscented Kalman Filter

A modification of the UKF is the square root UKF which attempts to reduce processing time and improve filter stability by updating the covariance matrices at each time step instead of re-calculating them [61, 94]. This is made possible by calculating the Cholesky factors of the initial error matrix and then updating them via a QR decomposition and Cholesky update at each time step.

3.4.3 Summary

For linear Gaussian tracking problems the Kalman filter is the optimal recursive estimator. If the necessary restrictions of the Kalman filter can not be met then the EKF and UKF provide alternative, although sub-optimal, tracking algorithms. The UKF is simpler to implement than the EKF since there is no need to compute the necessary Jacobian matrices. The UKF also provides better higher order statistical modelling than the EKF [88].

The EKF and UKF may still prove to be inadequate, in this case it may be necessary to adopt a Monte-Carlo approach, whereby the non-Gaussian posterior distribution is modelled as a set of discrete points. This is the approach taken in particle filtering which is presented in the following sections.

3.5 Conceptual Particle Filtering Solution

Particle filtering methods were first suggested in the 1960s but the lack of available computing power made them impractical [54]. In the early 1990s they re-emerged as a solution to non-linear non-Gaussian tracking problems using sequential Monte-Carlo simulations to model

Algorithm 3.3 $\left[\hat{\mathbf{a}}_{k|k}, \mathbf{P}_{k|k}\right] = \text{UKF}\left(\hat{\mathbf{a}}_{k-1|k-1}, \mathbf{P}_{k-1|k-1}\right)$

Calculate sigma points $\{\mathcal{A}_{k-1}\}_{1:N_{\mathcal{A}}}$ and weights $\{\mathcal{W}\}_{1:N_{\mathcal{A}}}$ using equations 3.71 to 3.73 substituting $\mathbf{R_{aa}}$ for $\mathbf{P}_{k-1|k-1}$
Transform sigma points via system function:

$$\{\mathcal{A}_k\}_{1:N_{\mathcal{A}}} = \boldsymbol{f}\left(\{\mathcal{A}_{k-1}\}_{1:N_{\mathcal{A}}}\right)$$

Calculate statistics of the sigma points:

$$\hat{\mathbf{a}}_{k|k-1} = \sum_{n=0}^{2N_{\mathcal{A}}} \{\mathcal{W}\}_n \{\mathcal{A}_k\}_n$$

$$\mathbf{R_{aa}} = \sum_{n=0}^{2N_{\mathcal{A}}} \{\mathcal{W}\}_n \left(\{\mathcal{A}_k\}_n - \hat{\mathbf{a}}_{k|k-1}\right)\left(\{\mathcal{A}_k\}_n - \hat{\mathbf{a}}_{k|k-1}\right)' + \mathbf{R_{ee}}$$

Transform parameter sigma points to measurement sigma points:

$$\mathcal{B}_k = \boldsymbol{h}\left(\mathcal{A}_k\right)$$

Calculate the statistics for the measurement and innovation:

$$\hat{\mathbf{b}}_k = \sum_{n=0}^{2N_{\mathcal{A}}} \{\mathcal{W}\}_n \{\mathcal{B}_k\}_n$$

$$\mathbf{R}_{\tilde{\mathbf{b}}\tilde{\mathbf{b}}} = \sum_{n=0}^{2N_{\mathcal{A}}} \{\mathcal{W}\}_n \left(\{\mathcal{B}_k\}_n - \hat{\mathbf{b}}_k\right)\left(\{\mathcal{B}_k\}_n - \hat{\mathbf{b}}_k\right)' + \mathbf{R_{vv}}$$

Calculate the covariance of the system parameters and the innovation:

$$\mathbf{R}_{\mathbf{a}\tilde{\mathbf{b}}} = \sum_{n=0}^{2n_{\mathcal{A}}} \{\mathcal{W}\}_n \left(\{\mathcal{A}_k\}_n - \hat{\mathbf{a}}_k\right)\left(\{\mathcal{B}_k\}_n - \hat{\mathbf{b}}_k\right)'$$

Calculate the Kalman gain:

$$\mathbf{K}_k = \mathbf{R}_{\mathbf{a}\tilde{\mathbf{b}}}\mathbf{R}_{\tilde{\mathbf{b}}\tilde{\mathbf{b}}}$$

Update the prediction

$$\hat{\mathbf{a}}_{k|k} = \hat{\mathbf{a}}_{k|k-1} + \mathbf{K}_k\left(\mathbf{b}_k - \hat{\mathbf{b}}_k\right)$$

Update the MSE matrix:

$$\mathbf{P}_{k|k} = \mathbf{R_{aa}} - \mathbf{K}_k\mathbf{R}_{\tilde{\mathbf{b}}\tilde{\mathbf{b}}}\mathbf{K}_k'$$

the posterior distribution as a set of discrete points in the parameter space with a set of supporting weights [51]. The Kalman filter and its derivatives model the posterior distribution parametrically as Gaussian and then make a MMSE estimate, however a Gaussian model may fail to accurately represent the underlying statistics of the system and measurement processes. Using a set of discrete points in the parameter space modelling of non-Gaussian distributions is possible. This section presents a conceptual particle filtering solution to the tracking problem and discusses Monte-Carlo integration, importance sampling, sequential importance sampling, re-sampling and finally a theoretical generic particle filter. Practical particle filters are presented in section 3.6.

3.5.1 Monte-Carlo Integration

Particle filtering approximates the posterior distribution $p(\mathbf{a}_k|\mathbf{b}_{1:k})$ as a set of 'particles' consisting of discrete points and supporting weights. This is achieved through Monte-Carlo estimation which approximates the integral I of a function as the mean of a set of samples drawn from the posterior PDF.

The integral of the function $\boldsymbol{g}(\mathbf{a})$:

$$I = \int \boldsymbol{g}(\mathbf{a}) d\mathbf{a} \tag{3.77}$$

can be factorised so that:

$$I = \int \digamma(\mathbf{a})\, p(\mathbf{a}) d\mathbf{a} \tag{3.78}$$

where $\digamma(\mathbf{a})$ and $p(\mathbf{a})$ are factors of $\boldsymbol{g}(\mathbf{a})$ and $p(\mathbf{a})$ is a PDF, so that $\int p(\mathbf{a}) d\mathbf{a} = 1$. An estimate of the integral can be obtained from the sample mean as:

$$\hat{I} = \frac{1}{N_a} \sum_{n=1}^{N_a} \digamma\left(\{\mathbf{a}\}_n\right) \tag{3.79}$$

where $N_a \gg 1$ and $\{\mathbf{a}\}_{1:N_a}$ are samples drawn from the PDF $p(\mathbf{a})$[2]. Figure 3.4 shows a continuous distribution and a Monte-Carlo point-wise approximation.

The law of large numbers states that $\hat{I}$ will converge to I if the samples $\{\mathbf{a}\}_{1:N_a}$ are independent [54]. If the variance of $\digamma(\mathbf{a})$:

$$\text{var}\{\digamma\} = \int \left(\digamma(\mathbf{a}) - I\right)^2 p(\mathbf{a}) d\mathbf{a} \tag{3.80}$$

is finite then the central limit theorem holds and the estimation error converges in distribution to [54]:

$$\lim_{N_a \to \infty} \sqrt{N_a} \left(\hat{I} - I\right) \sim \mathcal{N}\left(0, \text{var}\{\digamma\}\right) \tag{3.81}$$

The rate of convergence of the estimation error, $\tilde{I} = \hat{I} - I$, is dependent on the number of samples N_a, specifically the convergence rate is of order $\mathcal{O}\left(N_a^{1/2}\right)$ [54].

[2] In section 3.1 $N_{\mathbf{a}}$ referred to the dimensionality of vector $\mathbf{a}$, here - and elsewhere - N_a denotes the number of Monte-Carlo samples so that a complete set is $\{\mathbf{a}\}_{1:N_a}$

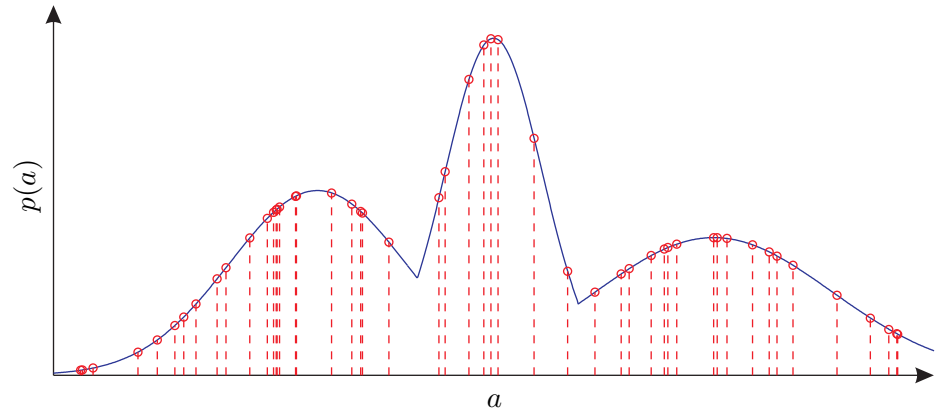

Figure 3.4: A continuous distribution (blue) and the Monte-Carlo point-wise approximation (red)

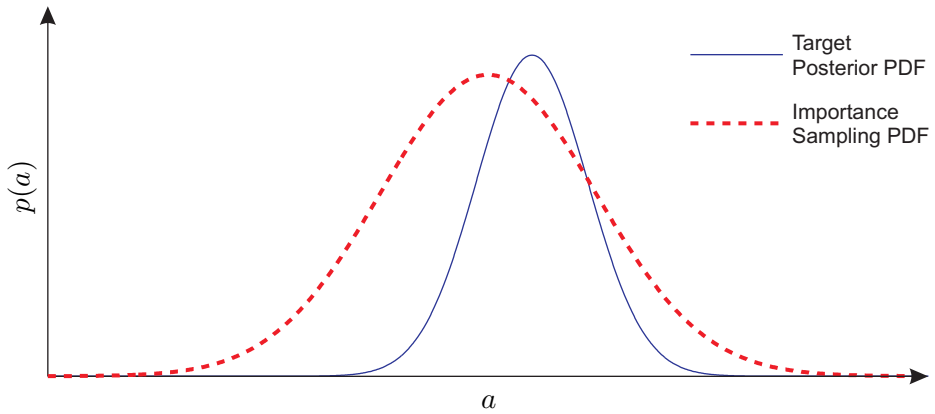

Figure 3.5: The target posterior PDF and an importance sampling approximation

When applying Monte-Carlo integration to a Bayesian context the PDF, $p(\mathbf{a})$, corresponds to the posterior distribution. It is usually not possible to sample from the posterior distribution because it is often multivariate, non-standard and only known up to a proportionality constant. This problem is overcome by importance sampling.

3.5.2 Importance Sampling

As it is not usually possible to sample directly from the posterior PDF, $p(\mathbf{a})$, samples are drawn from an importance density, $q(\mathbf{a}_k)$, which is related to the posterior, such that:

$$p(\mathbf{a}) = \tilde{w}(\mathbf{a})\, q(\mathbf{a}) \tag{3.82}$$

The concept of an importance density is illustrated in figure 3.5. The solid blue line represents the true posterior, or target, PDF and the dotted red line represents the importance PDF.

Rearranging (3.82) and substituting into (3.78) gives:

$$I = \int F(\mathbf{a}) \frac{p(\mathbf{a})}{q(\mathbf{a})} q(\mathbf{a}) d\mathbf{a} \tag{3.83}$$

$$= \int F(\mathbf{a}) \tilde{w}(\mathbf{a}) q(\mathbf{a}) d\mathbf{a} \tag{3.84}$$

Using (3.79) and the samples $\{\mathbf{a}\}_{1:N_a}$ drawn from $F(\mathbf{a})$ and $\tilde{w}(\mathbf{a})$, the Monte-Carlo estimate of (3.84) is:

$$\hat{I} = \frac{1}{N_a} \sum_{n=1}^{N_a} F(\{\mathbf{a}\}_n) \tilde{w}(\{\mathbf{a}\}_n) \tag{3.85}$$

If the normalising constant of the posterior density is unknown then the importance weights must be normalised so that they sum to unity. In this case the Monte-Carlo estimate of $\hat{I}$ is:

$$\hat{I} = \sum_{n=1}^{N_a} F(\{\mathbf{a}\}_n) w(\{\mathbf{a}\}_n) \tag{3.86}$$

where the normalised weight for particle n is:

$$w(\{\mathbf{a}\}_n) = \frac{\tilde{w}(\{\mathbf{a}\}_n)}{\sum_{m=1}^{N_a} \tilde{w}(\{\mathbf{a}\}_m)} \tag{3.87}$$

The final Monte-Carlo estimate using the importance distribution is given by equation (3.86). It is now convenient to formulate importance sampling as a recursive process so that it can be incorporated into a recursive tracking filter.

3.5.3 Sequential Importance Sampling

Sequential importance sampling is the recursive formulation of importance sampling as presented in section 3.5.2. If the weights are proportional to the joint posterior and importance densities then:

$$\{w\}_n \propto \frac{p(\{\mathbf{a}_{0:k}\}_n | \mathbf{b}_{1:k})}{q(\{\mathbf{a}_{0:k}\}_n | \mathbf{b}_{1:k})} \tag{3.88}$$

where $\{\mathbf{a}_{0:k}\}_n$ is the nth particle and $\{w\}_n$ is the nth supporting weight. This allows the joint posterior to be characterised as $\{\{\mathbf{a}_{0:k}\}_{1:N}, \{w_k\}_{1:N}\}$ [53]. Using this property the joint posterior can be discretely approximated from an importance density as:

$$p(\mathbf{a}_{0:k}|\mathbf{b}_{1:k}) \approx \sum_{n=1}^{N_a} \{w_k\}_n \delta(\mathbf{a}_{0:k} - \{\mathbf{a}_{0:k}\}_n) \tag{3.89}$$

To fit this approximation into the recursive conceptual solution presented in section 3.2 the current joint posterior $p(\mathbf{a}_{0:k}|\mathbf{b}_{1:k})$ - which incorporates all states up until time k - needs to be calculable from the previous joint posterior $p(\mathbf{a}_{0:k-1}|\mathbf{b}_{1:k-1})$. This approximation can be made through the joint importance density approximation so that the previous importance

density is updated using the marginal importance density:

$$q\left(\mathbf{a}_{0:k}|\mathbf{b}_{1:k}\right) \triangleq q\left(\mathbf{a}_k|\mathbf{a}_{0:k-1},\mathbf{b}_{1:k}\right) q\left(\mathbf{a}_{0:k-1}|\mathbf{b}_{1:k-1}\right) \tag{3.90}$$

This provides the joint importance density at k. For $p\left(\mathbf{a}_{0:k}|\mathbf{b}_{1:k}\right)$ to be approximated it is also necessary to obtain the weight update. Expanding $p\left(\mathbf{a}_{0:k}|\mathbf{b}_{1:k}\right)$ in terms of $p\left(\mathbf{a}_{0:k-1}|\mathbf{b}_{1:k-1}\right)$, $p\left(\mathbf{b}_k|\mathbf{a}_k\right)$ and $p\left(\mathbf{a}_k|\mathbf{a}_{k-1}\right)$:

$$p\left(\mathbf{a}_{0:k}|\mathbf{b}_{1:k}\right) = \frac{p\left(\mathbf{b}_k|\mathbf{a}_{0:k},\mathbf{b}_{1:k-1}\right) p\left(\mathbf{a}_{0:k}|\mathbf{b}_{1:k-1}\right)}{p\left(\mathbf{b}_k|\mathbf{b}_{1:k-1}\right)} \tag{3.91}$$

$$= \frac{p\left(\mathbf{b}_k|\mathbf{a}_{0:k},\mathbf{b}_{1:k-1}\right) p\left(\mathbf{a}_k|\mathbf{a}_{0:k-1},\mathbf{b}_{1:k-1}\right) p\left(\mathbf{a}_{0:k-1}|\mathbf{b}_{1:k-1}\right)}{p\left(\mathbf{b}_k|\mathbf{b}_{1:k-1}\right)} \tag{3.92}$$

$$= \frac{p\left(\mathbf{b}_k\right) p\left(\mathbf{a}_k|\mathbf{a}_{0:k-1}\right)}{p\left(\mathbf{b}_k|\mathbf{b}_{1:k-1}\right)} p\left(\mathbf{a}_{0:k-1}|\mathbf{b}_{1:k-1}\right) \tag{3.93}$$

$$\propto p\left(\mathbf{b}_k|\mathbf{a}_k\right) p\left(\mathbf{a}_k|\mathbf{a}_{k-1}\right) p\left(\mathbf{a}_{0:k-1}|\mathbf{b}_{1:k-1}\right) \tag{3.94}$$

Note the similarity of (3.91) with (3.11), the difference being the expansion of the previous state and measurement terms to include the full state and measurement history. Substituting (3.90) and (3.94) into (3.88) gives a recursive expression for the weight update:

$$\left\{w_k\right\}_n \propto \frac{p\left(\mathbf{b}_k|\left\{\mathbf{a}_k\right\}_n\right) p\left(\left\{\mathbf{a}_k\right\}_n|\left\{\mathbf{a}_{k-1}\right\}_n\right) p\left(\left\{\mathbf{a}_{0:k-1}\right\}|\mathbf{b}_{1:k-1}\right)}{q\left(\left\{\mathbf{a}_k\right\}_n|\mathbf{a}_{0:k-1},\mathbf{b}_{1:k}\right) q\left(\left\{\mathbf{a}_{0:k-1}\right\}_n|\mathbf{b}_{1:k-1}\right)} \tag{3.95}$$

$$= \left\{w_{k-1}\right\}_n \frac{p\left(\mathbf{b}_k|\left\{\mathbf{a}_k\right\}_n\right) p\left(\left\{\mathbf{a}_k\right\}_n|\left\{\mathbf{a}_{k-1}\right\}_n\right)}{q\left(\left\{\mathbf{a}_k\right\}_n|\left\{\mathbf{a}_{0:k-1}\right\}_n,\mathbf{b}_{1:k}\right)} \tag{3.96}$$

If $q\left(\mathbf{a}_k|\mathbf{a}_{0:k-1},\mathbf{b}_{1:k}\right) = q\left(\mathbf{a}_k|\mathbf{a}_{k-1},\mathbf{b}_k\right)$ then the importance density is only dependent on $\mathbf{a}_{k-1}$ and $\mathbf{b}_k$ and the result is an estimate of the posterior $p\left(\mathbf{a}_k|\mathbf{b}_{1:k}\right)$. The updated weight can now be expressed as:

$$\left\{w_k\right\}_n \propto \left\{w_{k-1}\right\}_n \frac{p\left(\mathbf{b}_k|\left\{\mathbf{a}\right\}_n\right) p\left(\left\{\mathbf{a}_k\right\}_n|\left\{\mathbf{a}_{k-1}\right\}_n\right)}{q\left(\left\{\mathbf{a}_k\right\}_n|\left\{\mathbf{a}_{k-1}\right\}_n,\mathbf{b}_k\right)} \tag{3.97}$$

so that the posterior estimate is:

$$p\left(\mathbf{a}_k|\mathbf{b}_{1:k}\right) \approx \sum_{n=1}^{N_a} \left\{w_k\right\}_n \delta\left(\mathbf{a}_k - \left\{\mathbf{a}_k\right\}_n\right) \tag{3.98}$$

It can be shown that as $N_a \to \infty$ (3.98) approaches the true posterior density $p\left(\mathbf{a}_k|\mathbf{b}_{1:k}\right)$ [53, 54, 95].

3.5.4 The SIS Particle Filter

The SIS particle filter is an implementation of the recursive posterior estimate derived in section 3.5.3, represents the simplest form of particle filter and provides the basis for practical versions of the particle filter. The complete SIS particle filter procedure is shown in algorithm 3.4. The SIS particle filter itself has practical issues because it suffers from sample degeneracy whereby variance of the particles increases over time and all but one of the weights becomes

Algorithm 3.4 $\left[\{\mathbf{a}_k, w_k\}_{1:N_a}\right]$ = SIS Particle Filter $\left(\{\mathbf{a}_{k-1}, w_{k-1}\}_{1:N_a}, \mathbf{b}_k\right)$

For all particles:
for $n = 1 : N_a$ **do**
Draw particle:
$\{\mathbf{a}_k\}_n \sim q\left(\mathbf{a}_k | \{\mathbf{a}_{k-1}\}_n, \mathbf{b}_k\right)$
Assign a weight:
$\{w_k\}_n \propto \{w_{k-1}\}_n \frac{p\left(\mathbf{b}_k | \{\mathbf{a}_k\}_n\right) p\left(\{\mathbf{a}_k\}_n | \{\mathbf{a}_{k-1}\}_n\right)}{q\left(\{\mathbf{a}_k\}_n | \{\mathbf{a}_{k-1}\}_n, \mathbf{b}_k\right)}$
end for
return $\left(\{\mathbf{a}_k, w_k\}_{1:N_a}\right)$

negligible [53,83]. The algorithm suggests particles are sampled from the optimal importance distribution, which is the true posterior, an operation that is typically not possible or very difficult [54]. Both these issues are addressed in the following sections and lead to a practical particle filter.

3.5.5 Particle Re-Sampling

Sample degeneracy can be quantified as the number of effective particles:

$$N_{\text{eff}} = \frac{N_a}{1 + \text{var}\left\{\tilde{w}_k\right\}} \tag{3.99}$$

where $\tilde{w}_k = p\left(\{\mathbf{a}_k\}_n | \mathbf{b}_{1:k}\right) / q\left(\{\mathbf{a}_k\}_n | \{\mathbf{a}_{k-1}\}_n, \mathbf{b}_k\right)$ is the 'true' weight which can not be exactly evaluated [53,54]. An approximation of the number of effective weights can be calculated by:

$$\widehat{N}_{\text{eff}} = \frac{1}{\sum_{n=1}^{N} \left\{w_k^2\right\}_n} \tag{3.100}$$

where $\widehat{N}_{\text{eff}} \leq N_a$ indicates degeneracy and $\widehat{N}_{\text{eff}} \ll N_a$ indicates severe degeneracy.

Three options are available to maintain sufficient sample variance and prevent degeneracy: brute force, whereby enough particles are utilised to postpone degeneration until tracking is complete; optimally selecting the importance distribution to minimise particle variance or re-sampling of the particles based on the assigned weights or re-sampling the particle set. The most common method of overcoming degeneracy is re-sampling. There are three common types of re-sampling: multi-nomial re-sampling; systematic re-sampling and residual re-sampling which may be applied systematically or adaptively [83]. All three re-sampling schemes are based on removing particles of low probability, i.e. a low weight, and replacing them with duplicates of those with a higher probability whilst allowing through a small quantity of low weight particles to maintain diversity in the filter. Multi-nomial re-sampling randomly selects particles from the current particle set and assigns them to a new particle set whereby particles of higher probability are more likely to be selected. Systematic re-sampling is based on an 'ordered' technique and residual re-sampling is based on estimating the number of times each particle should be replicated [83]. Multi-nomial re-sampling is the most commonly described

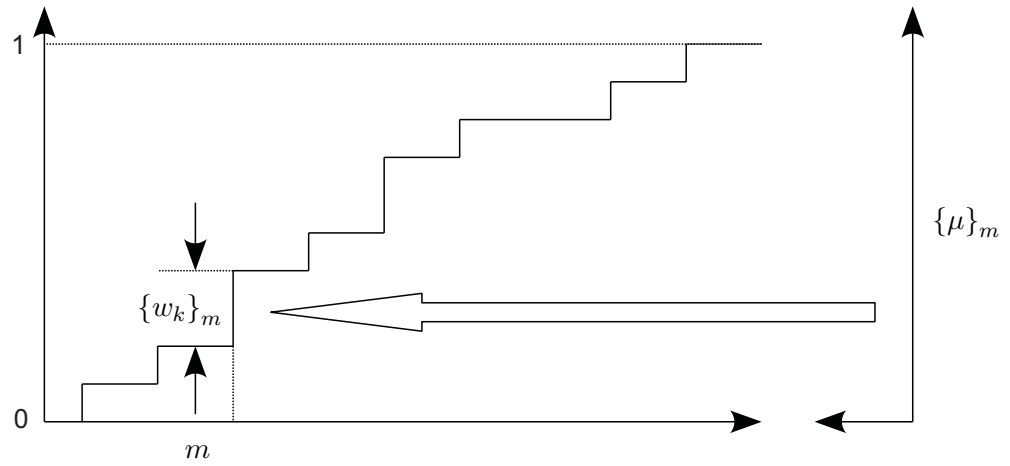

Figure 3.6: The process of re-sampling, $\{\mu\}_m \sim \mathcal{U}[0,1]$ maps to particle $\{\mathbf{a}_k\}_m$. The selected particle has a higher chance of being selected and multiplied because of its high value of $\{w_k\}_m$.

method in the tracking filter literature so is the method that will be used in this work. Although the particle sets before and after re-sampling are different they approximate the same distribution. A graphical representation of the re-sampling algorithm is shown in figure 3.6; particles for re-sampling are chosen randomly by drawing a random value from a uniform distribution $\{\mu\}_m \sim \mathcal{U}[1,0]$ and mapping to particle index m. In figure 3.6 the sample $\{\mathbf{a}_k\}_m$ has been selected for re-sampling; this particle has a higher probability of being re-sampled because it has a higher weight $\{w_k\}_m$.

The re-sampling algorithm is shown in algorithm 3.5 in a generalised version which returns the re-sampled particle set, the weights of the re-sampled particle set and the indices of the particles in the previous particle set that were re-sampled. Differing combinations of these returned variables are utilised by different particle filter implementations. Although re-sampling is designed to overcome the problem of sample degeneracy it can lead to the opposite problem of sample impoverishment, whereby the variance of the weights greatly decreases and the particles collapse to a single point [53, 54, 83]. Sample impoverishment is most likely to occur in applications where system noise is particularly low.

3.5.6 The Generic Particle Filter

The generic particle filter bridges the gap between the SIS particle filter in section 3.5.4 and the practical particle filters presented in section 3.6 and incorporates the re-sampling algorithm into the SIS particle filter. The generic particle filter algorithm is shown in algorithm 3.6.

The generic particle filter states the importance density to be $q(\mathbf{a}_k | \{\mathbf{a}_{k-1}\}_n, \mathbf{b}_k)$ but still leaves it undefined.

Algorithm 3.5 $\left[\{\mathbf{a}_k, w_k, n\}_{1:N_a}\right] = \text{Re-sample}\left(\{\mathbf{a}_k, w_k\}_{1:N_a}\right)$

Initialise the CDF: $\epsilon_1 = 0$
Construct the CDF:
for $n = 2 : N_a$ **do**
  $\{\epsilon\}_n = \{\epsilon\}_{n-1} + \{w_k\}_n$
end for
Start at the bottom of the CDF: $n = 1$
Draw starting point: $\{\mu\}_1 \sim \mathcal{U}\left[0, N_a^{-1}\right]$
For the whole CDF:
for $m = 1 : N_a$ **do**
  Move Along the CDF:
  $\{\mu\}_m = \{\mu\}_1 + N_a^{-1}(m-1)$
  while $\{\mu\}_m > \{\epsilon\}_n$ **do**
    Move along the CDF: $n = n + 1$
  end while
  Assign sample: $\{\mathbf{a}_k\}_m = \{\mathbf{a}_k\}_n$
  Assign weight: $\{w_k\}_m = N_a^{-1}$
  Assign parent: $\{n\}_m = n$
end for
return $\left(\{\mathbf{a}_k, w_k, n\}_{1:N_a}\right)$

3.5.7 The Optimal Importance Density

The optimal choice of importance density is the density that minimises sample impoverishment through minimisation of the weight variance so that:

$$\text{var}\left\{\{w_{1:k}\}_n\right\} = \left\{w_{1:k}^2\right\}_n \left[\int \frac{\left(p\left(\mathbf{b}_k|\mathbf{a}_k, \{\mathbf{a}_{k-1}\}_n\right)\left(\mathbf{a}_k|\{\mathbf{a}_{k-1}\}_n\right)\right)^2}{q\left(\mathbf{a}_k|\{\mathbf{a}_{k-1}\}_n, \mathbf{b}_k\right)} d\mathbf{a}_k - p\left(\mathbf{b}_k|\{\mathbf{a}_{k-1}\}_n\right)^2\right] \tag{3.101}$$

is minimised. The distribution that minimises the weight variance is the posterior distribution [54, 83]:

$$q\left(\mathbf{a}_k|\{\mathbf{a}_{k-1}\}_n, \mathbf{b}_k\right)_{\text{opt}} = p\left(\mathbf{a}_k|\{\mathbf{a}_{k-1}\}_n, \mathbf{b}_k\right) \tag{3.102}$$

$$= \frac{p\left(\mathbf{b}_k|\mathbf{a}_k\{\mathbf{a}_{k-1}\}_n\right) p\left(\mathbf{a}_k|\{\mathbf{a}_{k-1}\}_n\right)}{p\left(\mathbf{b}_k|\mathbf{a}_{k-1}\right)} \tag{3.103}$$

Substituting (3.103) into (3.97) gives:

$$\{w_k\}_n \propto \{w_{k-1}\}_n p\left(\mathbf{b}_k|\{\mathbf{a}_{k-1}\}_n\right) \tag{3.104}$$

which implies the weights at time k can be computed before the particles are propagated. To use this optimal importance density it is necessary to be able to sample from $p\left(\mathbf{a}_k|\{\mathbf{a}_{k-1}\}_n, \mathbf{b}_k\right)$ and evaluate:

$$p\left(\mathbf{b}_k|\{\mathbf{a}_{k-1}\}_n\right) = \int p\left(\mathbf{b}_k|\mathbf{a}_k\right) p\left(\mathbf{a}_k|\{\mathbf{a}_{k-1}\}_n\right) d\mathbf{a}_k \tag{3.105}$$

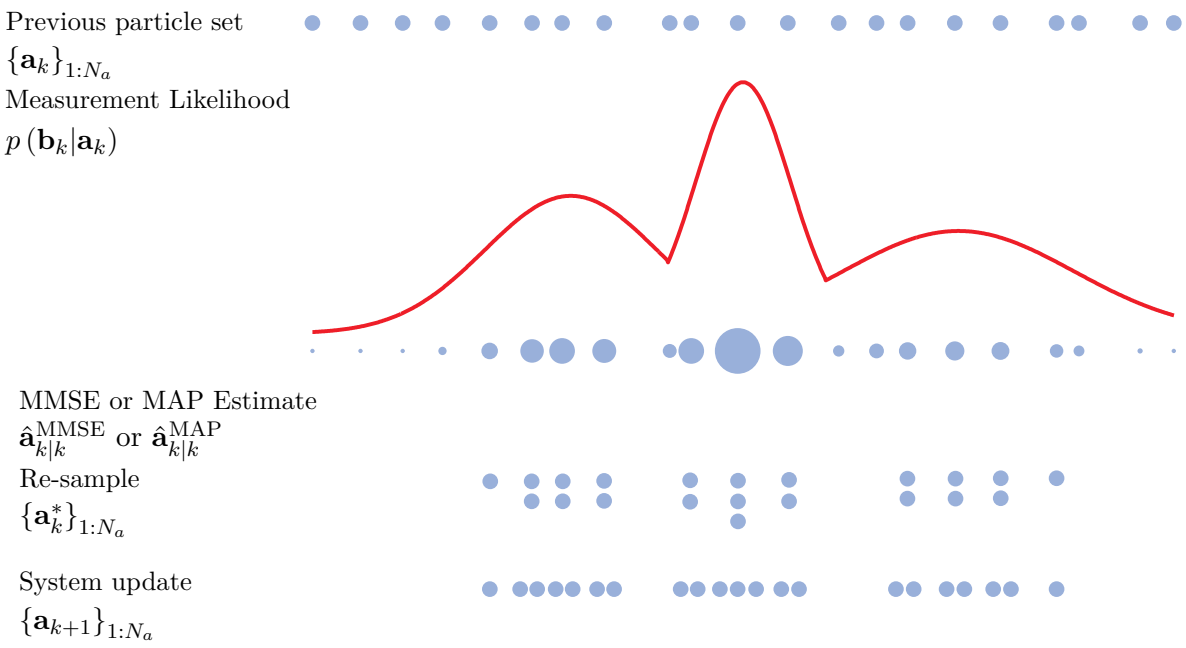

Figure 3.7: A single iteration of a particle filter, the prior samples are weighted, an estimate is computed, the particles are re-sampled and propagated for the next iteration

up to a normalising constant [54]. Neither of these may possible unless $p(\mathbf{a}_k|\{\mathbf{a}_{k-1}\}_n, \mathbf{b}_k)$ is Gaussian or the possible states of $\{\mathbf{a}_k\}$ are limited to a discrete set, so this optimal choice is often unusable. Further information on the optimal importance density can be found in [54,83].

The choice of importance density is the most critical component in the design of a particle filter and the next section presents practical particle filtering solutions based on alternative importance densities.

3.6 Practical Particle Filters

The particle filtering solution proposed in section 3.5 makes use of an abstract importance density, the optimal choice of which is the posterior density, however this is often unavailable. This section presents the sampling importance re-sampling particle filter and discusses several other practical particle filtering algorithms [3].

3.6.1 SIR Particle Filter

The sampling importance re-sampling (SIR) particle filter, also known as the bootstrap filter or condensation filter, was presented by Gordon, Salmond and Smith in 1993 as a method for overcoming the limitations of the EKF [51]. The SIR particle filter uses the transitional prior as the importance density. Computation of the importance weights from the transitional prior is relatively simple and has lead to the SIR particle filter being widely adopted.

[3] In this sense the term 'practical' describes particle filtering algorithms regarded as being readily implementable.

Algorithm 3.6 $\left[\{\mathbf{a}_k, w_k\}_{1:N_a}\right]$ = Generic Particle Filter $\left(\{\mathbf{a}_{k-1}, w_{k-1}\}_{1:N_a}, \mathbf{b}_k\right)$

Draw samples from importance distribution:
for $n = 1 : N_a$ **do**
  Draw particle: $\{\mathbf{a}_k\}_n \sim q\left(\mathbf{a}_k | \{\mathbf{a}_{k-1}\}_n, \mathbf{b}_k\right)$
  Assign a weight: $\{w_k\}_n \propto \{w_{k-1}\}_n \frac{p\left(\mathbf{b}_k | \{\mathbf{a}_k\}_n\right) p\left(\{\mathbf{a}_k\}_n | \{\mathbf{a}_{k-1}\}_n\right)}{q\left(\{\mathbf{a}_k\}_n | \{\mathbf{a}_{k-1}\}_n, \mathbf{b}_k\right)}$
end for
Normalise weights: $\{w_k\}_{1:N_a} = \frac{\{w\}_{1:N_a}}{\sum_{n=1}^{N_a} \{w_k\}^n}$
Calculate the number of effective particles: $\widehat{N}_{\text{eff}} = \frac{1}{\sum_{n=1}^{N_a} \{w_k^2\}^n}$
If the number of effective particles is below a threshold re-sample:
if $\widehat{N}_{\text{eff}} < N_{\text{thresh}}$ **then**
  $\left[\{\mathbf{a}_k, w_k, -\}_{1:N_a}\right]$ = Re-sample $\left(\{\mathbf{a}_k, w_k\}_{1:N_a}\right)$
end if
return $\left(\{\mathbf{a}_k, w_k\}_{1:N_a}\right)$

The Transitional Prior Importance Density

If the transitional prior importance density is defined as:

$$q\left(\mathbf{a}_k | \{\mathbf{a}_{k-1}\}_n, \mathbf{b}_k\right)_{\text{prior}} = p\left(\mathbf{a}_k | \{\mathbf{a}_{k-1}\}_n\right) \tag{3.106}$$

then substituting (3.106) into (3.96) gives:

$$\{w_k\}_n \propto \{w_{k-1}\}_n p\left(\mathbf{b}_k | \{\mathbf{a}_k\}_n\right) \tag{3.107}$$

because the priors cancel. Using this weighting, based on the likelihood, the importance weights can not be evaluated before the particles are propagated as they can be with the optimal importance density. Furthermore, if the weight is entirely dependent on the likelihood, sequential updating becomes unnecessary because re-sampling is performed at every time step whereby the weights of the re-sampled particles are $\{w_k\}_n = {}^1/_{N_a}$ [83].

The SIR Algorithm

The SIR particle filter algorithm is given in algorithm 3.7. Although re-sampling is required at every iteration to ensure convergence, it is possible to reduce computational load by carrying the weights from the previous iteration and only re-sampling if $\widehat{N}_{\text{eff}} < N_{\text{thresh}}$ [60,83,96], which is the form of the SIR algorithm described here. If re-sampling is employed at every iteration the effective particle test can be dropped and there is no need to store the importance weights from the previous iteration.

As well as utilising easily realisable importance samples, the assumptions and additional information needed are also limited. The requirements are that the following be known: the initial density at $k = 0$, $\{\mathbf{a}_0\}_n \sim p\left(\mathbf{a}_0\right)$; the system function $\boldsymbol{f}_{k-1}\left(\mathbf{a}_{k-1}, \mathbf{e}_{k-1}\right)$ and noise distribution $p\left(\mathbf{e}\right)$ and the measurement function $\boldsymbol{h}_k\left(\mathbf{a}_k, \mathbf{v}_k\right)$ and noise distribution $p\left(\mathbf{v}\right)$.

Algorithm 3.7 $\left[\{\mathbf{a}_k, w_k\}_{1:N_a}\right] = \text{SIR}\left(\{\mathbf{a}_{k-1}, w_{k-1}\}_{1:N_a}\right)$

Draw particles from transitional prior density:
for $n = 1 : N_a$ **do**
  Draw Particle: $\{\mathbf{a}_k\}_n \sim p\left(\mathbf{a}_k | \{\mathbf{a}_{k-1}\}_n\right)$
  Assign a weight: $\{\tilde{w}_k\}_n = \{w_{k-1}\}_n p\left(\mathbf{b}_k | \{\mathbf{a}_k\}_n\right)$
end for
Normalise weights: $\{w_k\}_n = \frac{\{\tilde{w}_k\}_n}{\sum_{n=1}^{N_a} \{\tilde{w}_k^2\}_n}$
Make a re-sampling decision:
$\widehat{N}_{\text{eff}} \frac{1}{\sum_{1:n}^{N_a} \{w_k^2\}_n}$
if $\widehat{N}_{\text{eff}} \leq N_{\text{thresh}}$ **then**
  Re-sample: $\left[\{\mathbf{a}_k, -, -\}_{1:N_a}\right] = \text{Re-sample}\left(\{\mathbf{a}_k, w_k\}_{1:N_a}\right)$
end if
return $\left(\{\mathbf{a}_k, w_k\}_{1:N_a}\right)$

Although relatively simple to implement there are drawbacks to the SIR filter. Firstly, approximation of the tails of $p\left(\mathbf{a}_k | \mathbf{b}_{1:k-1}\right)$ is poor and when outliers occur there is also poor approximation of (3.11) [83, 97]. Secondly, although re-sampling is utilised, sufficient system variance is still required to prevent sample degeneracy [53, 83]. Finally, the latest measurement $\mathbf{b}_k$ is not utilised in the importance density as it is in the generic particle filter, therefore searching of the state space is relatively inefficient [53, 54, 97].

3.6.2 Other Particle Filters

Other particle filtering algorithms are based on alternative importance distributions. This section reviews two other particle filtering algorithms, the auxiliary SIR (ASIR) particle filter and the locally linearised particle filter (LLPF) which have both been proposed for angle-only target tracking [61, 97]. The SIR particle filter will be utilised in chapters 5 and 7 so the full algorithm has been given in this chapter; the ASIR and LLPF algorithms are not utilised in later chapters so only the key parts of them are discussed in this section, however full algorithm listings can be found in appendix A (algorithms A.1 and A.2).

Auxiliary SIR Particle Filter

The ASIR particle filter attempts to include information from the latest measurement into the importance density to improve posterior modelling of outlying particles and tail modelling performance. Pitt and Shepherd proposed using the latest measurement by performing the re-sampling step at $k-1$ after the measurement at k has been acquired but before the particles are propagated [54, 83, 97]. Samples are drawn from the joint density $p\left(\mathbf{a}_k, n | \mathbf{b}_{1:k}\right)$, which is

derived from:

$$p(\mathbf{a}_k, n|\mathbf{b}_{1:k}) \propto p(\mathbf{b}_k|\mathbf{a}_k)\, p(\mathbf{a}_k, n|\mathbf{b}_{1:k-1}) \tag{3.108}$$

$$= p(\mathbf{b}_k|\mathbf{a}_k)\, p(\mathbf{a}|n, \mathbf{b}_{1:k-1})\, p(n|\mathbf{b}_{1:k-1}) \tag{3.109}$$

$$= p(\mathbf{b}_k|\mathbf{a}_k)\, p(\mathbf{a}_k|\{\mathbf{b}_{k-1}\}_n)\, \{w_{k-1}\}_n \tag{3.110}$$

This results in particles drawn from the pair $\{\mathbf{a}_k, n\}_{1:M_a}$, where M_a represents a different set of indices to N_a but is still the same length [53, 54]. Dropping n from (3.110) results in the density $p(\mathbf{a}_k|\mathbf{b}_{1:k})$. The importance density is defined as:

$$q(\mathbf{a}_k, n|\mathbf{b}_{1:k}) \propto p(\mathbf{b}_k|\{\check{\mathbf{a}}_k\}_n)\, p(\mathbf{a}_k|\{\mathbf{a}_{k-1}\}_n) \tag{3.111}$$

where $\{\check{\mathbf{a}}_k\}_n$ is a term in some way related to $\mathbf{a}_k$ given $\{\mathbf{a}_{k-1}\}_n$, for example it may be the mean or a sample drawn from the transitional prior. The weight update for the ASIR filter is:

$$\{w_k\}_m \propto \{w_{k-1}\}_{\{n\}_m} \frac{p(\mathbf{b}_k|\{\mathbf{a}_k\}_m)\, p\left(\{\mathbf{a}_k\}_m | \{\mathbf{a}_{k-1}\}_{\{n\}_m}\right)}{q(\{\mathbf{a}_k\}_m, \{n\}_m | \mathbf{b}_{1:k})} \tag{3.112}$$

$$= \frac{p(\mathbf{b}_k|\{\mathbf{b}_k\}_m)}{p\left(\mathbf{b}_k|\{\check{\mathbf{a}}_k\}_{\{n\}_m}\right)} \tag{3.113}$$

The complete ASIR particle filtering algorithm is given in algorithm A.1 in appendix A. The advantage of the ASIR particle filter over the SIR filter is that samples are more likely to be drawn from areas of high likelihood which makes the ASIR filter less sensitive to outliers when system variance is low. However, in cases where system noise variance is high the ASIR may provide inferior performance compared to the SIR filter [54].

Locally Linearised Particle Filters

The LLPF models each sample point as a local Gaussian with a mean and covariance so that each particle represents a local normal PDF rather than a discrete point (as in the SIR and ASIR) so that:

$$q(\{\mathbf{a}_k\}_n | \{\mathbf{a}_{k-1}\}_n, \mathbf{b}_k)_{\text{LLPF}} = \mathcal{N}\left(\left\{\mathbf{a}_k; \hat{\mathbf{a}}_k, \hat{\mathbf{P}}_k\right\}_n\right) \tag{3.114}$$

The Gaussian parameters $\{\hat{\mathbf{a}}_k\}_n$ and $\left\{\hat{\mathbf{P}}_k\right\}_n$ are acquired by propagating each of the previous particle set and respective covariances through an iteration of an EKF or UKF. Importance samples are drawn from the updated mean and covariance values. Weights are computed as:

$$\{\tilde{w}_k\}_n = \frac{p(\mathbf{b}_k|\{\mathbf{a}_k\}_n)\, p(\{\mathbf{a}_k\}_n | \{\mathbf{a}_{k-1}\}_n)}{q(\{\mathbf{a}_k\}_n | \{\mathbf{a}_{k-1}\}_n, \mathbf{b}_k)_{\text{LLPF}}} \tag{3.115}$$

The complete LLPF algorithm is given in algorithm A.2 in appendix A. Due to the reasons discussed in section 3.4 there is little reason to use the EKF over the UKF to obtain $\{\hat{\mathbf{a}}_k\}_n$ and $\left\{\hat{\mathbf{P}}_k\right\}_n$. This method of approximating the importance density propagates the particles

towards the likelihood function, consequently the LLPF can be expected to perform better than the SIR particle filter [54]. Yu et al. suggest that a variation of the LLPF based on the square root UKF provides better angle-only tracking than the SIR particle filter [61].

There are a large number of other types of particle filters, some of the more common being regularised particle filters [98, 99], multiple model-particle filters [54] and Rao-Blackwellised particle filters [100].

3.7 Application of Particle Filters to Sperm Whale Tracking

The sperm whale towed array tracking problem described in chapter 1 and formulated in section 2.8, whereby the source location ambiguity is represented as a PDF, is an application of the conceptual tracking problem defined in section 3.1 and can be solved using the solution defined in section 3.2. It follows that a spatial sperm whale tracking solution can be developed from one of the tracking filters presented in sections 3.3, 3.4 and 3.6. This section discusses the system and measurement components of the specific application and the requirements that must be satisfied by the choice of tracking filter. Appropriate system functions are discussed in chapter 4.

3.7.1 System State, System Function and System Noise

The system parameters, function and noise components represent the animal's spatial position and motion relative to the tracking array. Position is most intuitively represented in a Cartesian coordinate system, for which there are linear system models, however alternative coordinate systems, such as polar coordinates may provide improved tracking performance. A more extensive review of coordinate systems and motion modelling is presented in chapter 4 where the specific choices of motion model and coordinate system are defined. Kalman filter can be used in conjunction with polar coordinate systems when bearing, elevation and range measurements are available. If range measurements are not available, as is the case in many passive tracking applications, the tracking problem becomes a bearings only problem whereby the measurement function is non-linear thereby eliminating the Kalman filter as a tracking option and reducing the choice of tracking filter to an EKF, UKF or particle filter which can operate when the system and measurement functions are non-linear [59, 79].

Depending on the order of the motion model chosen the system noise process will account for changes in animal position, velocity, acceleration or possibly higher order motion statistics. Taking a conventional constant velocity motion model [101] the system noise will be the changes in animal velocity, i. e. representative of acceleration. Data for animal motion whilst dived is presented in chapter 4 but collection of such information is not a medial task and requires a degree of estimation. It remains however that there is a limit to how fast the animal can travel and there may be limits to the length of time for which some speeds may be maintained. This may lead to instances where the animal is more likely to slow down than

accelerate and therefore a normally distributed noise density may not be sufficiently accurate. In such cases the Kalman filter will again not be applicable and possibly would also make the EKF and the UKF impractical.

3.7.2 Measurement, Measurement Function and Measurement Noise

In towed array tracking with a single hydrophone pair the measurement is a single time-delay, τ, measured across the array aperture. Using (2.8) and (2.9), the time delay can be defined as:

$$\tau = (\cos\phi \cos\psi)\, dc^{-1} \tag{3.116}$$

where ϕ and ψ are the horizontal and vertical angles of the target to the array respectively, d is the array aperture and c is the sound propagation speed. As the measurement at k is the time-delay:

$$\mathbf{b}_k = \tau \tag{3.117}$$

then the measurement function is:

$$\mathbf{h}\left(\mathbf{a}_k\right) + \mathbf{v}_k \equiv (\cos\phi \cos\psi)\, dc^{-1} \tag{3.118}$$

The measurement noise component, $\mathbf{v}_k$, of the time-delay measurement originates in the cross-correlation stage of the time-delay estimation process. The resolution of the time-delay estimate is dependent on the digital sampling rate of the data acquisition and the array aperture size. The cross-correlation computes the delay to an integer number of samples and therefore the process suffers from quantisation. Due to the reasons discussed in section 2.2.1, this error will not be normally distributed and will depend on the direction of arrival, whereby broadside arrivals will suffer less quantisation than end-fire receptions, so whilst at the whale is at broadside linear assumptions my be valid, however at end-fire these assumptions may not hold.

3.7.3 Choice of Tracking Filter for Sperm Whale Tracking

The shape of the PDFs required to represent the source animal's position are unlikely to be normal and may be multi-modal, uniform or a variety of other shapes. Disregarding other click receptions, for a single click reception the PDF over the ambiguity hyperbola will be uniform. This limits the effectiveness of the Kalman filter and its derivatives as tracking filter options because such distributions can not be adequately modelled using first and second order statistics. Furthermore, the measurement function is non-linear and the integer value quantisation error of the measurements prevent the EKF or UKF assumptions holding true. Depending on the choice of system function and noise distribution these components may also be non-linear and non-Gaussian and therefore may not be adequately modelled by the EKF and UKF. Particle filters are capable of modelling the non-linear functions and non-Gaussian distributions necessary for this application and are therefore the tracking filter of choice.

The SIR particle filter has previously been applied to angle-only target tracking with high rates of success in several applications [55, 58, 59, 80, 81]. The ASIR particle filter and LLPF have been shown to offer improved performance over the SIR particle filter in some angle-only tracking applications [61,97]. The specifics of the current tracking application differ in that the system noise is comparatively high and the time-delay measurement being used is a function of both the bearing and elevation of the animal to the array. Use of this measurement feature is somewhat novel. The simplicity and versatility of the SIR particle filter make it the ideal tracking filter choice for this application.

3.8 Summary and Conclusion

This chapter has presented a target tracking and state-estimation problem whereby the objective is to estimate a target state given a related measurement. This concept has been developed into several practical tracking filters with the particle filter being selected as the most appropriate for tracking sperm whales from time-delay measurements acquired from a towed hydrophone array. This section summarises this chapter and how what has been presented relates to what is presented in the following chapters.

Given a measurement which is related in some way to a set of target parameters it is desirable to estimate those parameters. In this case the parameters are the whale's position and velocity and the measurement is the time-delay in reception of the vocalisation across two hydrophones. The process by which the parameters change and measurements are acquired can be separated into separate processes whereby the current parameters are a recursive function of the previous parameters and the measurement is a function that transforms the parameters to the received measurement. The system process comprises a known system function, describing the whale's motion, and a noise component which accounts for unknown processes in the system function, such as the animal's accelerations. The measurement process comprises a known measurement function and a noise term to account for errors in the acquisition process.

Given the target state it is a relatively simple process to estimate the measurement that would be received. The inverse process requires Bayes's theorem, which states that the PDF of a target parameter set given a measurement is the product of the likelihood of the measurement given the parameters and prior probability that the target parameters occurred. Assuming the target state can be modelled as a Markovian process, a recursive formulation of Bayes's theorem is possible, in this instance the probability of the target state is made dependent on the previous measurements using the Chapman-Kolmogorov equation. The resulting posterior distribution can then be used to compute MMSE or MAP estimates of the target state.

If the noise process driving the system process and the measurement noise are both normally distributed and the system and measurement functions are both linear then the statistics of the system measurement processes can be described parametrically as a mean and variance. This enables an MMSE estimate of the system state to be made from the measurements. If the linear and Gaussian assumptions can not be made then an alternative to the Kalman

filter is necessary. Two adaptations of the Kalman filter, the EKF and UKF, have been discussed which attempt to fit the non-linear and non-Gaussian systems into the Kalman filter framework.

Although the Kalman filter does not have the non-linear capabilities necessary for the spatial tracking problem of tracking sperm whale positions from time-delay measurements it will be utilised as part of a multi-hypothesis tracker (MHT) in chapter 6. This will enable the association of clicks with a source animal based on the time-delay history of click receptions. In this application the predict-update nature of the Kalman filter forms an essential part of the MHT's operation.

Particle filters model the likelihood and prior PDFs using Monte-Carlo estimates so that the densities are approximated as a set of discrete points and respective support weights. This is in contrast to the Kalman filter which models the distributions parametrically. The major benefit of particle filters over Kalman filters is that they're capable of tracking where the system and measurement functions are non-linear and the noise distributions are non-Gaussian. A MAP or MMSE estimate can be made from the particles at each iteration depending on the nature of the tracking problem.

Particle filters offer the best tracking filter solution for tracking sperm whales from towed hydrophone arrays because the measurement function is non-linear and measurement noise is non-Gaussian. The particle filter allows complete freedom of choice for the system and measurement functions and respective distributions. The particle filter is also easily adapted to tracking for other configurations of array by changing the system and measurement functions.

Further development of the particle filter for the subject application requires development of the system function and the system noise statistics, presented in chapter 4. The tracking filter also requires testing with simulations, chapter 5, before being used to track the position of an animal based on real data, chapter 7. Kalman filters are utilised in multiple hypothesis tracking in chapter 6.

Chapter 4

Motion Modelling

Chapter 3 presented a conceptual tracking filter solution for target state estimation and several practical tracking filter implementations. Central to each of these is the concept of a system function, which in spatial target tracking describes the position and motion of the target. In addition to selecting an appropriate system function an appropriate coordinate system is required along with a noise distribution which adequately represents the un-modelled changes in the target motion. This chapter presents several motion models and coordinate systems, discusses the known characteristics of sperm whale swimming motion and finally presents the selected coordinate system, system function and system noise distribution.

4.1 Motion Models

Many generalised motion models have been suggested in the target tracking literature and it is necessary in this work to identify which of these is the most appropriate and any modifications that may be required for sperm whale motion modelling. A comprehensive survey of target motion models is presented by Li and Jilkov [101], this section presents an overview of the models reported by Li and Jilkov and as such draws largely from their work. Even though coordinate systems are presented and discussed in section 4.2, these models are presented in Cartesian form and in the case of an alternative coordinate system being utilised then conversion of the state parameters between coordinate systems is possible.

4.1.1 Conceptual Motion Modelling Solution

In the physical world a moving target is an object occupying a volume of space, however in target tracking it is typically easier to identify the target as a point such as the centre of volume or centre of mass. The position of this point can be modelled in continual time as [101]:

$$\mathbf{a}\left(t_k\right) = \boldsymbol{f}\left(\mathbf{a}\left(t_{k-1}\right), \mathbf{u}\left(t_{k-1}\right), \mathbf{e}\left(t_{k-1}\right), \left(t_k - t_{k-1}\right)\right), \quad \mathbf{a}\left(t_0\right) = \mathbf{a}_0 \tag{4.1}$$

where $\mathbf{u}$ is a known control vector representing the deterministic control input to the target or of the observing platform and t_k is time at discrete time index k. Tracking is to be performed in discrete time so it is convenient to re-phrase (4.1) as:

$$\mathbf{a}_k = \boldsymbol{f}_{k-1}\left(\mathbf{a}_{k-1}, \mathbf{u}_{k-1}, \mathbf{e}_{k-1}\right) \tag{4.2}$$

where $\mathbf{a}_k = \mathbf{a}\left(t_k\right)$, $\mathbf{u}_k = \mathbf{u}\left(t_k\right)$ and $\mathbf{e}_k = \mathbf{e}\left(t_k\right)$. If the control process $\mathbf{u}_k$ and noise process $\mathbf{e}_k$ are additive then (4.2) becomes:

$$\mathbf{a}_k = \boldsymbol{f}_{k-1}\left(\mathbf{a}_{k-1}\right) + \mathbf{u}_{k-1} + \mathbf{e}_{k-1} \tag{4.3}$$

Although deterministic manoeuvring motion modelling methods exist [102–104] the control process is typically unknown and modelled as a random process [101]. As such, $\mathbf{u}_k$ will be omitted from the following sections - and reinstated later to represent the deterministic component of the observing boat manoeuvres - so that (4.3) becomes:

$$\mathbf{a}_k = \boldsymbol{f}_{k-1}\left(\mathbf{a}_{k-1}\right) + \mathbf{e}_{k-1} \tag{4.4}$$

If $\boldsymbol{f}_{k-1}$ is a linear function, as could be assumed if motion is modelled in a Cartesian coordinate system, (4.4) can be re-phrased in matrix-vector form:

$$\mathbf{a}_k = \mathbf{F}_{k-1}\mathbf{a}_{k-1} + \mathbf{G}_{k-1}\mathbf{e}_{k-1} \tag{4.5}$$

where $\mathbf{F}_k$ and $\mathbf{G}_k$ are defined in the following sections as both are dependent on the order of the model utilised.

4.1.2 Random Walk

Random walk motion models present a very simple motion modelling solution. The lowest possible order of system state vector is the three dimensional target position vector:

$$\mathbf{a}_k = \begin{bmatrix} x_k \\ y_k \\ z_k \end{bmatrix} \tag{4.6}$$

The noise process $\mathbf{e}_{k-1}$ represents the displacement in target position between $k-1$ and k, so that:

$$\mathbf{a}_k = \mathbf{a}_{k-1} + \mathbf{e}_{k-1} \tag{4.7}$$

Although random walks can be applied to the Kalman filter and its derivatives they typically fail to model the target state dynamics sufficiently and the target state prediction $\hat{\mathbf{a}}_{k|k-1} = \hat{\mathbf{a}}_{k-1|k-1}$. Random walks can be useful in conjunction with particle filters if the system function is unknown but a system noise distribution can be established through statistical analysis of the

target state parameters. In this case system noise samples can be drawn from the distribution:

$$\mathbf{e}_{k-1} \sim \mathcal{N}(0, \mathbf{R}_{\mathbf{ee}}) \tag{4.8}$$

where $\mathcal{N}$ is a normal distribution (which can be substituted for any desired distribution) and applied to particles using (4.7).

4.1.3 Constant Velocity Motion Models

Constant velocity motion models are utilised to model the motion of a target travelling at near constant velocity in a near constant direction, also described as non-manoeuvring. In a constant velocity motion model the system state vector is comprised of the position and velocity in x, y and z dimensions:

$$\mathbf{a}_k = [x, \dot{x}, y, \dot{y}, z, \dot{z}]' \tag{4.9}$$

where $\dot{x}$, $\dot{y}$, $\dot{z}$ are velocities. The system state update is defined as:

$$\mathbf{a}_k = \mathbf{F}\mathbf{a}_{k-1} + \mathbf{G}\mathbf{e}_{k-1} \tag{4.10}$$

where:

$$\mathbf{F} = \begin{bmatrix} 1 & T & 0 & 0 & 0 & 0 \\ 0 & 1 & 0 & 0 & 0 & 0 \\ 0 & 0 & 1 & T & 0 & 0 \\ 0 & 0 & 0 & 1 & 0 & 0 \\ 0 & 0 & 0 & 0 & 1 & T \\ 0 & 0 & 0 & 0 & 0 & 1 \end{bmatrix} \quad \mathbf{G} = \begin{bmatrix} T^2/2 & 0 & 0 \\ T & 0 & 0 \\ 0 & T^2/2 & 0 \\ 0 & T & 0 \\ 0 & 0 & T^2/2 \\ 0 & 0 & T \end{bmatrix} \quad \mathbf{e}_k = \begin{bmatrix} e_{\dot{x}} \\ e_{\dot{y}} \\ e_{\dot{z}} \end{bmatrix} \tag{4.11}$$

The noise process $\mathbf{e}_k$ represents noise on the target velocities. The time subscript k has been dropped from $\mathbf{F}$ and $\mathbf{G}$ for clarity of notation under the assumption that the measurement period, T, is constant. In practice sperm whale clicks are a-periodic and therefore the measurements and target updates are applied a-periodically and the non-constant period between measurements and updates will be denoted as T_k. Where necessary the time subscripts will be restored to $\mathbf{F}_k$ and $\mathbf{G}_k$.

Under this model the components of $\mathbf{e}_k$ are uncoupled across the three dimensions so that the covariance of $\mathbf{G}\mathbf{e}_k$ is given by:

$$\mathbf{R}_{\mathbf{ee}} = \text{diag}\left[\text{var}\left\{e_{\dot{x}}\right\}\mathbf{Q}, \text{var}\left\{e_{\dot{y}}\right\}\mathbf{Q}, \text{var}\left\{e_{\dot{z}}\right\}\mathbf{Q}\right] \tag{4.12}$$

where:

$$\mathbf{Q} = \begin{bmatrix} T^4/4 & T^3/2 \\ T^3/2 & T^2 \end{bmatrix} \tag{4.13}$$

4.1.4 Coordinate-Uncoupled Manoeuvre Models

A target that is changing speed and direction is described as a manoeuvring target whereby accurate motion modelling requires an appropriate motion model. Manoeuvring target motion models can be divided into two categories, coordinate-uncoupled and coordinate-coupled. The coordinate-uncoupled motion models reviewed in this section model acceleration, which is independent across the x, y and z dimensions, as independent white noise processes. Each of the three models discussed - white noise acceleration, Wiener sequence and polynomial - are differentiated by the model order. Coordinate-coupled motion models, which maintain dependence on changes in target motion across the dimensions, are discussed in section 4.1.5.

White Noise Acceleration Model

The white noise acceleration model represents the simplest form of manoeuvring target motion model. The vectors $\mathbf{a}_k$ and $\mathbf{e}_k$ and matrices $\mathbf{F}$ and $\mathbf{G}$ remain the same order and the update equations remain the same as for the constant velocity motion model, the difference being that the system noise covariance matrix $\mathbf{R_{ee}}$ values are much higher to allow a greater freedom of variation in the changes affecting $\dot{x}_k$, $\dot{y}_k$ and $\dot{z}_k$. This model is attractive for its simplicity and is useful when manoeuvring is small or random [101].

Wiener Sequence

A manoeuvring target's trajectory, such as an aircraft's, is typically governed by the deterministic control input vector defining the rate of acceleration of the target in each dimension. The target accelerations are incorporated into the target state vector as additional dimensions:

$$\mathbf{a}_k = [x_k, \dot{x}_k, \ddot{x}_k, y_k, \dot{y}_k, \ddot{y}_k, z_k, \dot{z}_k, \ddot{z}_k]' \tag{4.14}$$

where $\ddot{x}_k$, $\ddot{y}_k$ and $\ddot{z}_k$ are the acceleration parameters across the three dimensions of the coordinate system.

In the physical world acceleration is a continuous process which, when sampled, can be described as a process that increments or decrements independently between $k-1$ and k. As such acceleration can be modelled as a Wiener sequence and the motion model can be expressed in matrix-vector form as:

$$\mathbf{a}_k = \mathbf{F}\mathbf{a}_{k-1} + \mathbf{G}\mathbf{e}_{k-1} \tag{4.15}$$

where:

$$\mathbf{F} = \text{diag}\left[\mathbf{F}_3, \mathbf{F}_3, \mathbf{F}_3\right] \qquad \mathbf{F}_3 = \begin{bmatrix} 1 & T & T^2/2 \\ 0 & 1 & T \\ 0 & 0 & 1 \end{bmatrix} \tag{4.16}$$

$$\mathbf{G} = \text{diag}\left[\mathbf{G}_3, \mathbf{G}_3, \mathbf{G}_3\right] \qquad \mathbf{G}_3 = \begin{bmatrix} T^2/2 \\ T \\ 1 \end{bmatrix} \tag{4.17}$$

In this model the covariance matrix of $\mathbf{e}_k$ is:

$$\mathbf{R}_{\mathbf{ee}} = \text{diag}\left[\text{var}\left\{\mathbf{e}_{\ddot{x}}\right\}\mathbf{Q}_3, \text{var}\left\{\mathbf{e}_{\ddot{y}}\right\}\mathbf{Q}_3, \text{var}\left\{\mathbf{e}_{\ddot{z}}\right\}\mathbf{Q}_3\right] \tag{4.18}$$

where:

$$\mathbf{Q}_3 = \begin{bmatrix} T^4/4 & T^3/2 & T^2/2 \\ T^3/2 & T^2 & T \\ T^2/2 & T & 1 \end{bmatrix} \tag{4.19}$$

The Wiener model is in some ways unrealistic, most manoeuvring targets are unlikely to manoeuvre with constant acceleration uncoupled across x, y and z, however like the white noise model, the Wiener model is attractive because it remains relatively simple.

Polynomial

The constant velocity motion model in section 4.1.3, the white noise acceleration model and the Wiener acceleration motion model can be regarded as specific 1st and 2nd order polynomial motion models. Generalising these models yields a polynomial motion model expression:

$$\mathbf{a}_k = \mathbf{F}\mathbf{a}_k + \mathbf{G}\begin{bmatrix} e_x \\ e_y \\ e_z \end{bmatrix} \tag{4.20}$$

where:

$$\mathbf{a}_k = \left[x_k, \ldots, x_k^n/n!, y_k, \ldots, y_k^n/n!, z_k, \ldots, z_k^n/n!\right]' \tag{4.21}$$

$$\mathbf{F} = \text{diag}\left[\mathbf{F}_n, \mathbf{F}_n, \mathbf{F}_n\right] \qquad \mathbf{F}_n = \begin{bmatrix} 1 & T & \ldots & T^n/n \\ 0 & 1 & \ldots & T^{n-1}/n-1 \\ \vdots & \vdots & \ddots & \vdots \\ 0 & 0 & \ldots & 1 \end{bmatrix} \tag{4.22}$$

$$\mathbf{G} = \text{diag}\left[\mathbf{G}_n, \mathbf{G}_n, \mathbf{G}_n\right] \qquad \mathbf{G}_n = \begin{bmatrix} T^n/n \\ \vdots \\ T \\ 1 \end{bmatrix} \tag{4.23}$$

The order, n, of the model is the model derivative that is assumed to be near-constant. Like the other motion models reviewed in this section this model is coordinate uncoupled. Although polynomial models are generally useful for fitting data and solving smoothing problems, tracking is however a prediction and filtering problem. Regardless of this many special polynomial motion modelling methods have been developed for target tracking [101].

4.1.5 Coordinate Coupled Manoeuvre Models

Although in the literature many angle-only tracking problems use either constant velocity or coordinate uncoupled acceleration motion models [58, 59, 61, 79, 96, 105], other more sophisticated motion models have been proposed [101, 106, 107]; the following sections provide a brief overview of two of these methods.

Singer Model

Singer proposed modelling acceleration as a first order Markov process instead of as a Wiener sequence, whereby the acceleration increment is dependent on the previous [101, 106]. Acceleration, $\ddot{\mathbf{a}}_k$, can be described as:

$$\ddot{\mathbf{a}}_k = \zeta \ddot{\mathbf{a}}_{k-1} + \ddot{\mathbf{e}}_{k-1} \tag{4.24}$$

where $\ddot{\mathbf{a}}_k = [\ddot{x}_k, \ddot{y}_k, \ddot{z}_k]'$ is the acceleration vector in each dimension, $\ddot{\mathbf{e}}_k$ is a zero-mean white noise process, $\zeta = \exp\{-\eta T\}$, $\eta = 1/\mathcal{T}$ and $\mathcal{T}$ is the manoeuvre time constant. The Markov process assumed by the Singer model is a zero-mean, first order, stationary process. The resulting system update equation is:

$$\mathbf{a}_k = \mathbf{F}\mathbf{a}_{k-1} + \mathbf{G}\mathbf{e}_k \tag{4.25}$$

where:

$$\mathbf{F} = \operatorname{diag}[\mathbf{F}_\eta, \mathbf{F}_\eta, \mathbf{F}_\eta] \tag{4.26}$$

$$\mathbf{F}_\eta = \begin{bmatrix} 1 & T & (\eta T - 1 + \exp\{-\eta T\})/\eta^2 \\ 0 & 1 & (1 - \exp\{-\eta T)\}/\eta \\ 0 & 0 & \exp\{-\eta T\} \end{bmatrix} \tag{4.27}$$

Singer also proposes that the variance parameters, $\operatorname{var}\{\ddot{x}_k\}$, $\operatorname{var}\{\ddot{y}_k\}$ and $\operatorname{var}\{\ddot{z}_k\}$, model tenerary-uniform distributions for each dimension [106], shown in figure 4.1. This distribution allows the target to manoeuvre with zero acceleration with probability $p(0)$; accelerate or decelerate at rate $\ddot{\mathbf{a}}^{\max}$ with probability $p(\ddot{\mathbf{a}}^{\max})$ or accelerate or decelerate at a rate with uniform probability distributed between $\pm\ddot{\mathbf{a}}^{\max}$ where $p(\ddot{\mathbf{a}}^{\max})$, $p(0)$ and $\ddot{\mathbf{a}}^{\max}$ are design parameters.

The Singer model does not make use of online information about the target manoeuvre so,

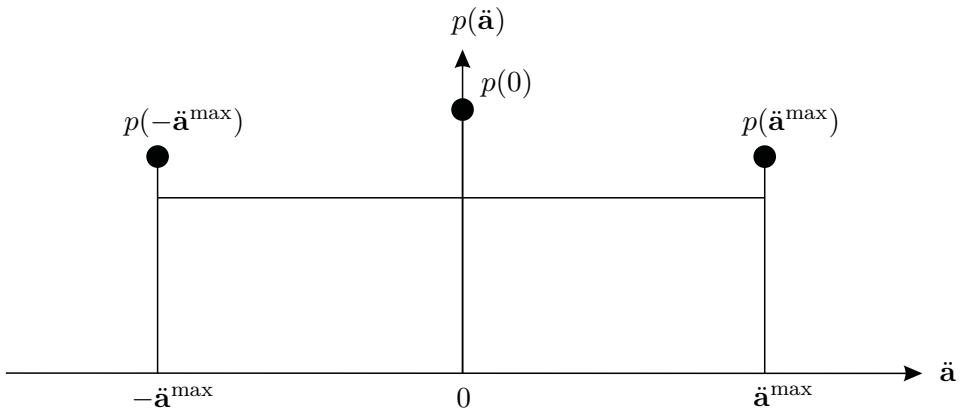

Figure 4.1: Tenerary-uniform mixture PDF used in the Singer motion model

like the other models discussed here, can be regarded as an a-priori motion model, however adaptation of parameters η, $p\left(\ddot{\mathbf{a}}^{\max}\right)$, $p\left(0\right)$, T and $\ddot{\mathbf{a}}^{\max}$ based on online data, if available, is possible [101]. The Singer model is limited in that it is symmetric with zero-mean which implies that the average target acceleration is also zero and acceleration is as probable as deceleration.

Mean Adaptive Model

The mean adaptive acceleration model is a Singer model modified so that the mean acceleration can be adapted to non-zero values [101]:

$$\ddot{\mathbf{a}}_k = \tilde{\mathbf{a}}_k + \bar{\mathbf{a}}_k \tag{4.28}$$

where $\tilde{\mathbf{a}}_k$ is the zero-mean Singer acceleration process and $\bar{\mathbf{a}}_k$ is the mean of the acceleration assumed constant over each sampling interval. The acceleration estimate, $\hat{\mathbf{a}}_{k-1}$, of the true acceleration, $\ddot{\mathbf{a}}_{k-1}$, from all available information (the measurements $\mathbf{b}_{1:k}$) is taken to be the current value of the mean acceleration, $\bar{\mathbf{a}}_k$, recursively updated from time 1 to k, so that $\bar{\mathbf{a}}_k = \hat{\mathbf{a}}_{k-1}$. The resulting system update expression is:

$$\mathbf{a}_k = \mathbf{F}\mathbf{a}_{k-1} + \mathbf{J}\bar{\mathbf{a}}_k + \mathbf{G}\mathbf{e}_k \tag{4.29}$$

where:

$$\mathbf{F} = \mathrm{diag}\left[\mathbf{F}_\eta, \mathbf{F}_\eta, \mathbf{F}_\eta\right] \tag{4.30}$$

and:

$$\mathbf{J} = \mathrm{diag}\left[\mathbf{J}_\eta, \mathbf{J}_\eta, \mathbf{J}_\eta\right] \tag{4.31}$$

$$\mathbf{J}_\eta = \left[\begin{bmatrix} T^2/2 \\ T \\ 1 \end{bmatrix} - \begin{bmatrix} \left(\eta T - 1 + \exp\left\{-\eta T\right\}\right)/\eta^2 \\ \left(1 - \exp\left\{-\eta T\right\}\right)/\eta \\ \exp\left\{-\eta T\right\} \end{bmatrix}\right] \tag{4.32}$$

and $\mathbf{G}$ is defined in (4.17).

4.2 Coordinate Systems

The motion models presented in section 4.1 are derived in the Cartesian Coordinate system, however alternative coordinate systems have been proposed in the literature, notably the 2 dimensional modified polar coordinate (MPC) system [79] and its three dimensional equivalent the modified spherical coordinate (MSC) system [59,91,92]. This section reviews and compares the Cartesian coordinate and MSC systems.

Cartesian coordinate systems can be used in tracking applications where measurements acquired from sensors with three dimensional separation are available [108]. If tracking acoustically using bottom mounted sensors or other fixed hydrophone array, as discussed in chapter 2, then a Cartesian coordinate system is suitable because the sensors are spread over three dimensions [22–24]. Often in single observer tracking scenarios measurements are acquired in polar or spherical coordinate form relative to the observer's own position [55, 84]. In passive tracking applications, such as passive sonar and infra-red heat signature tracking, range is often un-measurable until the observing platform performs a manoeuvre, this is a classical tracking problem known as angle-only (or bearings-only[1]) tracking in which range is a parameter to be estimated [55, 59]. The necessary observer manoeuvring information is incorporated via the inclusion of the detereministic control vector $\mathbf{u}_k$ in the system function.

Cartesian and spherical coordinate systems are illustrated in figure 4.2. In the horizontal plane, figures 4.2(a) and 4.2(b), the x-axis of the Cartesian system lies along the centreline of the boat and indicates a bearing of 0 rads and the y-axis is perpendicular to the centreline of the boat, if the boat changes heading the coordinate system rotates with the boat. Bearing is measured in radians, where bearings to the left are between 0 and π and bearings to the right are between 0 and $-\pi$; if the animal is behind the boat it will be represented by a bearing greater than $\pi/2$ or less than $-\pi/2$. In the vertical (x-z) plane, figures 4.2(c) and 4.2(d), the elevation is measured between 0 and $-\pi/2$ rads. The elevation angle is only given as between $-\pi/2$ and 0 because it is reasonable to assume the animal is below the boat and positioning behind the boat is signified by bearing.

Early solutions to the angle-only tracking problem relied on time motion analysis methods until the EKF was proposed as a tracking solution, however the estimator displays stability issues primarily due to ill-conditioning of the covariance matrix [109]. These issues arise because the x and y components (x, y and z in 3 dimensions) of the state vector are coupled to both the observable angle and un-observable range. Introduction of the modified polar coordinate (MPC) system provides a method that automatically decouples the observable angle and un-observable nearness (range reciprocal) components [79]. The MPC state vector

[1] 'Bearings-only' tracking is the most commonly used term in the literature, however here it will be referred to as 'angle-only' tracking to differentiate between the arrival angle of the application specific measurement and relative horizontal bearing of the animal's position.

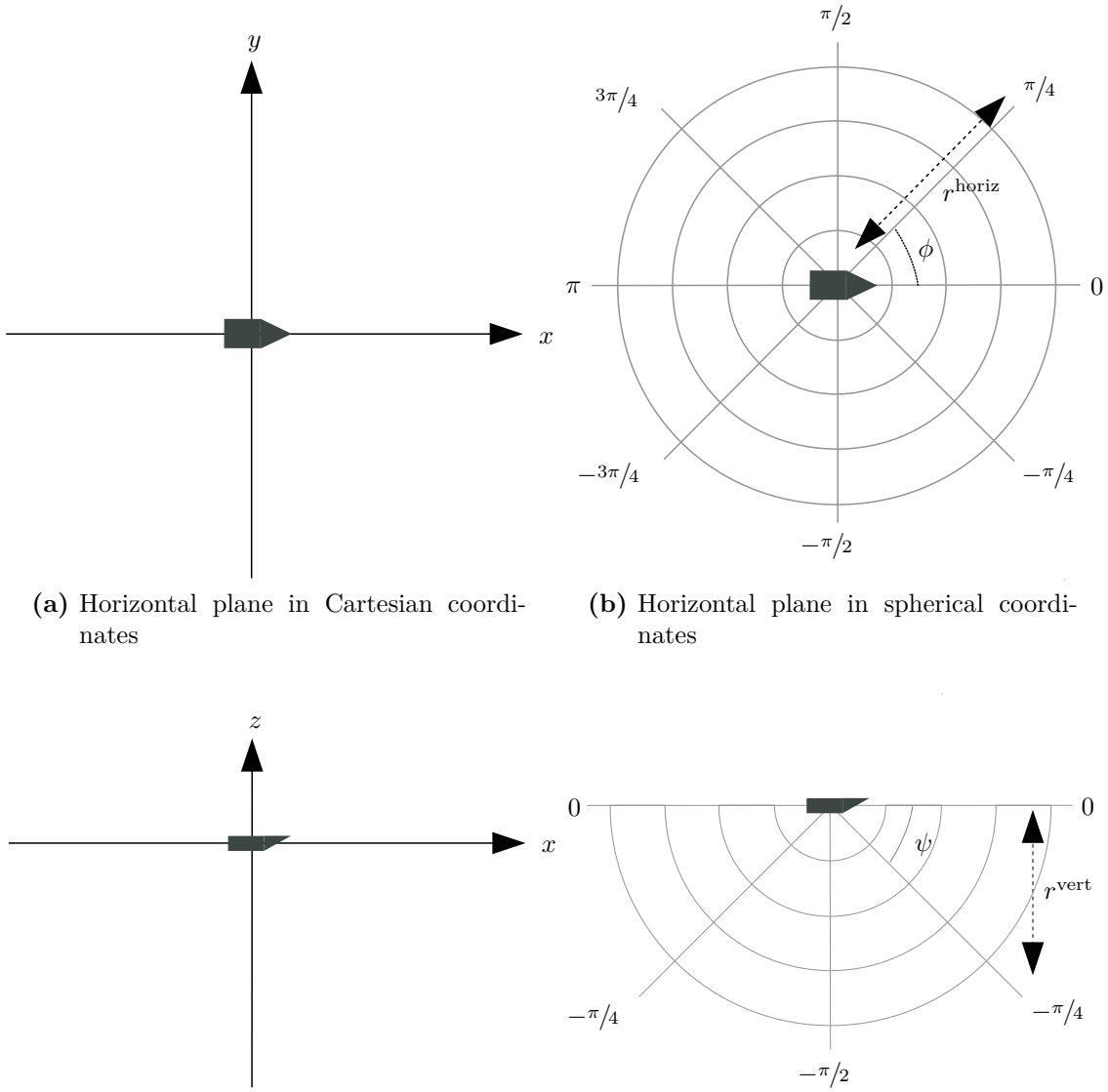

(a) Horizontal plane in Cartesian coordinates

(b) Horizontal plane in spherical coordinates

(c) Vertical plane in Cartesian coordinates

(d) Vertical plane in spherical coordinates

Figure 4.2: Cartesian and spherical coordinate systems illustrated in the horizontal and vertical planes. Bearings are measured in radians, positive to the left and negative to the right. Elevation is measured between 0 and $-\pi/2$ rads because the animal will never be higher than sea level.

is[2]:

$$\mathbf{a}_k^{\text{MPC}} = \begin{bmatrix} 1/r_k \\ \dot{r}_k/r_k \\ \phi_k \\ \dot{\phi}_k \end{bmatrix} = \begin{bmatrix} \frac{1}{\sqrt{x^2+y^2}} \\ \frac{\dot{x}x+\dot{y}y}{x^2+y^2} \\ \tan^{-1}\frac{y}{x} \\ \frac{\dot{y}x-\dot{x}y}{x^2+y^2} \end{bmatrix} \tag{4.33}$$

Nearness is utilised in place of range so that as the range of the target increases the respective components of the covariance matrix decrease instead of increase, which would cause filter instability. The component $\dot{r}_k/r_k$ is the inverse of the 'time-to-go', often used as a measure of track priority [91]. Three of the state components, $a_k^{\text{MPC}}(2)$, $a_k^{\text{MPC}}(3)$ and $a_k^{\text{MPC}}(4)$ are measurable using angle-only information as shown by the state differentials:

$$\dot{\mathbf{a}}_k^{\text{MPC}} = \begin{bmatrix} -\left(\dot{r}/r\right)\left(1/r\right) \\ \dot{\phi}^2 - \left(\dot{r}/r\right) + \left(1/r\right)\left(\dot{x}\sin\phi + \dot{y}\cos\phi\right) \\ \dot{\phi} \\ -2\dot{\phi}\left(\dot{r}/r\right) + \left(1/r\right)\left(\dot{x}\cos\phi - \dot{y}\sin\phi\right) \end{bmatrix} \tag{4.34}$$

The transformation from MPC back to Cartesian is:

$$\mathbf{a}_k^{\text{car}} = \begin{bmatrix} r\cos\phi \\ r\dot{r}\cos\phi - r\dot{\phi}\sin\phi \\ r\sin\phi \\ r\dot{r}\sin\phi + r\dot{\phi}\cos\phi \end{bmatrix} \tag{4.35}$$

The MPC system can be extended to three dimensions as the modified spherical coordinate (MSC) system [59, 91–93], where the state vector is expanded to include the vertical angle (elevation) and vertical angular velocity components:

$$\mathbf{a}_k^{\text{MSC}} = \begin{bmatrix} 1/r \\ \dot{r}/r \\ \phi \\ \dot{\phi} \\ \psi \\ \dot{\psi} \end{bmatrix} = \begin{bmatrix} \frac{1}{\sqrt{x^2+y^2+z^2}} \\ \frac{\dot{x}x+\dot{y}y+\dot{z}z}{x^2+y^2+z^2} \\ \tan^{-1}\frac{y}{x} \\ \frac{\dot{y}x-\dot{x}y}{x^2+y^2}\cos\left(\tan^{-1}\frac{-z}{\sqrt{x^2+y^2}}\right) \\ \tan^{-1}\frac{-z}{\sqrt{x^2+y^2}} \\ \frac{-\dot{z}\left(x^2+y^2\right)+z(\dot{x}x+\dot{y}y)}{(x^2+y^2+z^2)\sqrt{x^2+y^2}} \end{bmatrix} \tag{4.36}$$

[2]Time indices have been dropped from vector elements for clarity

Transformation from MSC back to Cartesian is achieved using the following:

$$\mathbf{a}_k^{\text{car}} = \begin{bmatrix} x \\ \dot{x} \\ y \\ \dot{y} \\ z \\ \dot{z} \end{bmatrix} = \begin{bmatrix} r\cos\psi\cos\phi \\ \dot{r}\cos\psi\cos\phi - r\dot{\psi}\sin\psi\cos\phi - r\dot{\phi}\cos\psi\sin\phi \\ r\cos\psi\sin\phi \\ \dot{r}\cos\psi\sin\phi - r\dot{\psi}\sin\psi\sin\phi + r\dot{\phi}\cos\psi\cos\phi \\ -r\sin\psi \\ -\dot{r}\sin\psi - r\dot{\psi}\cos\psi \end{bmatrix} \tag{4.37}$$

More discussion and presentation of the MSC system is given in [59, 91–93]. Due to the non-linearities involved in the transformation between Cartesian coordinates and received bearings and the resultant ill-conditioning of the covariance matrices, MPC and MSC systems are widely accepted as the optimal coordinate systems for bearings-only tracking using EKFs. Although most particle filters can handle the non-linearities and don't suffer from covariance matrix ill-conditioning problems, it has been shown that particle filter tracking performance improves when an MSC system state is utilised [59]. Matrix ill-conditioning problems may occur in locally-linearised particle filters. This category of particle filter uses an EKF or UKF to update the state of each particle, part of this process involves updating covariance matrices that are utilised in the next filter iteration. A discussion of the appropriateness of the Cartesian, MPC and MSC coordinate systems for sperm whale tracking from a single time-delay measurement is presented in section 4.5.

4.3 Sperm Whale Dive Motion

Developing an appropriate motion model and selecting an appropriate parameter for the system variance requires an analysis of information available on sperm whale motion. This section presents an overview of the sperm whale's dive cycle and profile followed by a dive reconstruction from a data acquisition tag (DTAG) and a discussion of swimming speeds determined from various sources.

4.3.1 Dive Profile

A dive cycle consists of three stages, descent, foraging and ascent [13, 110, 111], which yields an approximately U-shaped dive profile. Figure 4.3 shows a single dive profile recorded by the depth sensor on a DTAG - incorporating a depth sensor, acoustic sensor, a three-dimensional accelerometer and a three-dimensional magnetometer [112] - attached to the animal using suction cups. The data shown in figure 4.3 was acquired as part of the 3S 2009 project [47], data from the same tag deployment will be utilised in chapters 6 and 7.

A dive initiates with the animal performing a 'fluke up' whereby the animal pitches down from a horizontal position on the surface for the descent to depth. Fluking is visually observable from the sea surface as the animal raises its tail fluke and descends [13]. The fluke up sighting

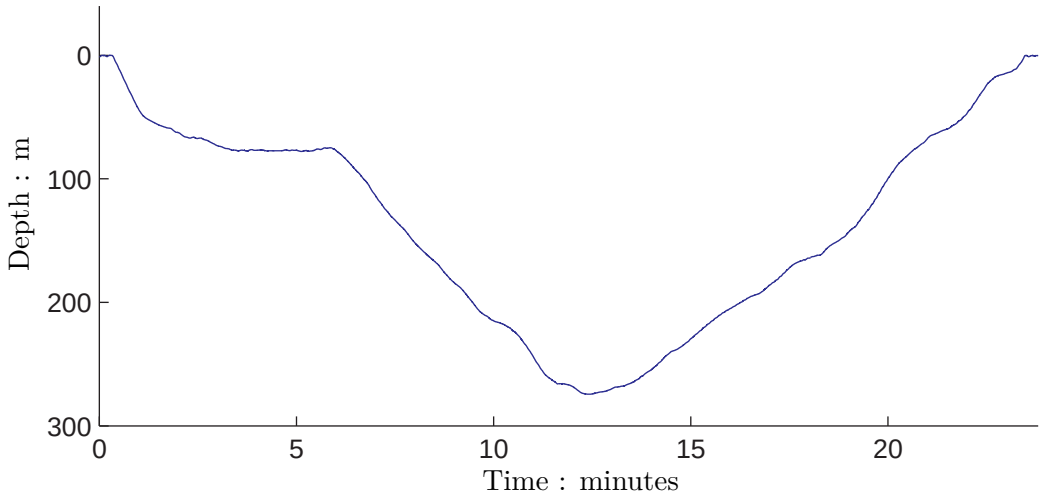

Figure 4.3: An example sperm whale dive profile

provides the last opportunity to obtain a fix on the animal's position until it surfaces. DTAG data shows descent angles are between 40° and 60° with a vertical velocity between 1 and 1.5 ms^{-1} [110]. These figures are consistent with those acquired using acoustic localisation methods of between 0.8 and 1.4 ms^{-1} [9]. Vocalisations can start soon after the dive has commenced or may be delayed for several minutes until the animal reaches a preferred foraging depth layer [10]. Vocalisations are produced for approximately 2/3 of the descent phase. The dive continues to depths typically between 300 and 800 m, however dives may reach depths of 1 - 2 km and, in some cases, be as shallow as 200 m [13].

The foraging phase occurs after the descent and within favoured depth layers [10]. Sperm whales are believed to travel at similar speeds during the horizontal foraging stage of the dive as they do at the surface, specifically between 0.55 ms^{-1} and 1.39 ms^{-1}, derived from displacement measurements over periods of 30 minutes to 2 hours [13]. Acoustic localisation measurements estimate horizontal swim speeds of between 0.2 and 2.6 ms^{-1} depending on if the animal is swimming with or against the current [9]. Foraging times are typically 15 to 30 minutes for a typical 30 to 45 minute dive [13].

During the ascent phase vertical velocities vary from 1.1 to 1.56 ms^{-1} at a pitch between 43° and 75° [110]. Vocalisation typically stops at the end of the foraging stage with the animal quiet during the ascent to the surface.

4.3.2 DTAG Dive and Track Reconstruction

Figures 4.4(a) and 4.4(b) show the profile of a dive and the corresponding reconstruction of the horizontal movements of the animal between the sightings at fluke up and surfacing. The horizontal track is reconstructed using the accelerometer and magnetometer recordings and then fitted to the sighting locations. No speed over ground or positioning sensors are available on the DTAG so the reconstruction is prone to error and may give the position of the animal as different to the sighting. Transforming the reconstruction to match the sighting positions

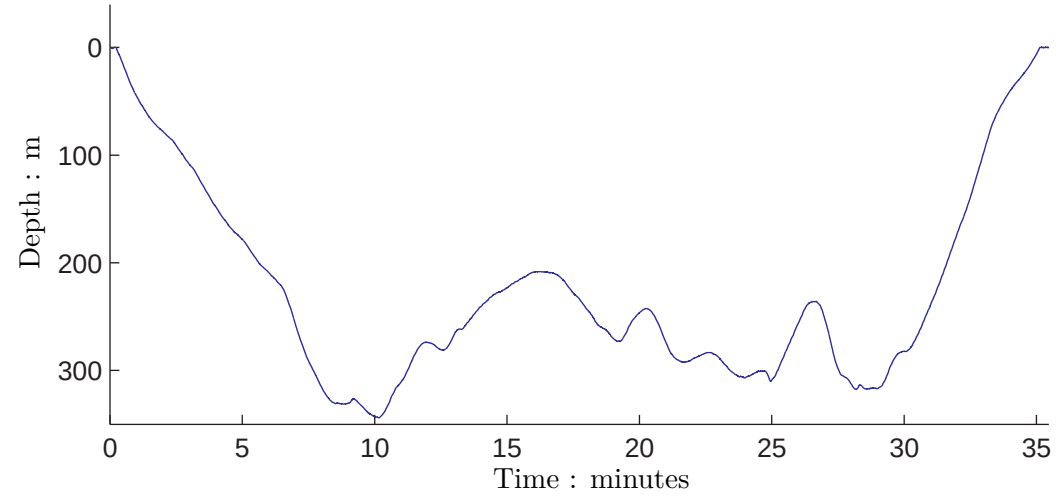

(a) Dive profile

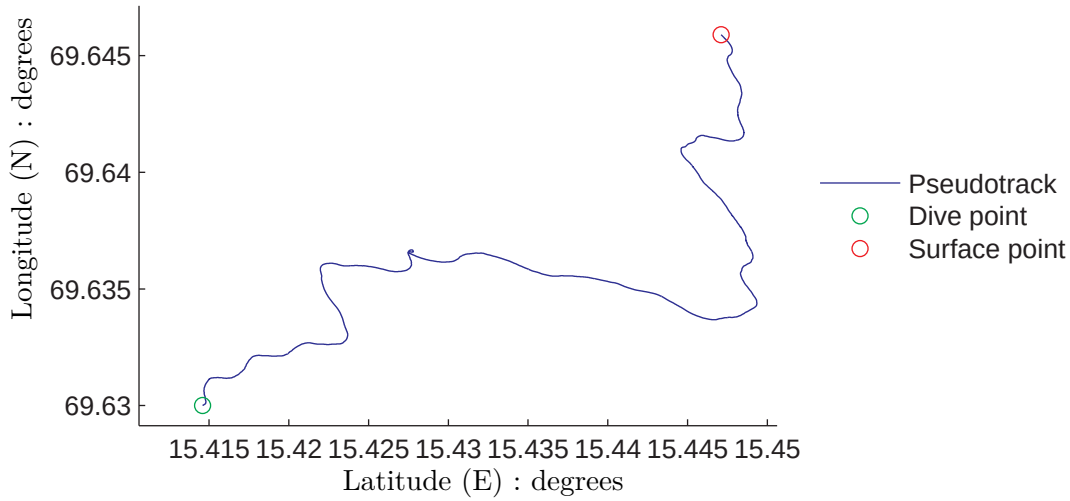

(b) Reconstruction of the horizontal dive track

Figure 4.4: The dive profile (a) and horizontal pseudotrack reconstruction from DTAG data (b) for a sperm whale

can be justified as compensating for current flow which is not detected by the accelerometers. In such cases the direction and magnitude of the transformation should be checked against preceding and succeeding dives, if the directions and magnitudes are significant then the current compensation argument is not valid as there are physical limits to how rapidly the current speed and direction can change.

Although the DTAG itself includes accelerometers there is a lack of information on the variations in the absolute speed of the animal. Although it is known that the animal must have to manoeuvre to catch prey [10], there is also a lack of available information regarding the rate of change of heading and pitch.

The next section establishes a distribution from which noise samples representing changes in acceleration can be drawn, however appropriate values may need to be established through experimentation.

4.4 System Noise for Sperm Whale Tracking

Development of the motion model requires developing an appropriate distribution from which to draw system noise samples. Since no ranging information is available in the measurements, filter stability depends on the accuracy of the representation of the system function and noise distribution, otherwise a solution may be found that fits the measurements but with an unrealistic range estimate. Firstly this section looks at the limitations of drawing samples from a normal distribution in terms of realistic representation of animal acceleration and deceleration. Following this an alternative sampling method is proposed that incorporates a rejection function of speed samples that are unrealistic.

4.4.1 Insufficiencies in Gaussian Modelling

The exact shape of the system noise distribution depends on whether noise samples are drawn from a distribution representing the speed or acceleration of the animal, however the need to maintain realism in the statistical representation of the animal's motion remains. The discussion in this section is applicable whether the noise samples represent velocity or acceleration.

If using a Cartesian coordinate system for tracking then simply drawing velocity or acceleration samples from a normal distribution uncouples the motion model across the three dimensions, which may also lead to unrealistic speeds being modelled. This can be overcome by modelling speed and direction using a spherical coordinate system so that only a single speed sample needs to be drawn. Speed is a measure of magnitude so can only be positive, this can be overcome when drawing values from a normal distribution by taking the absolute value of drawn negative samples.

Figure 4.5 shows two normal distributions, where the curve is centred at the speed at time k. The curve represents the distribution from which a sample for the speed at time $k+1$ can

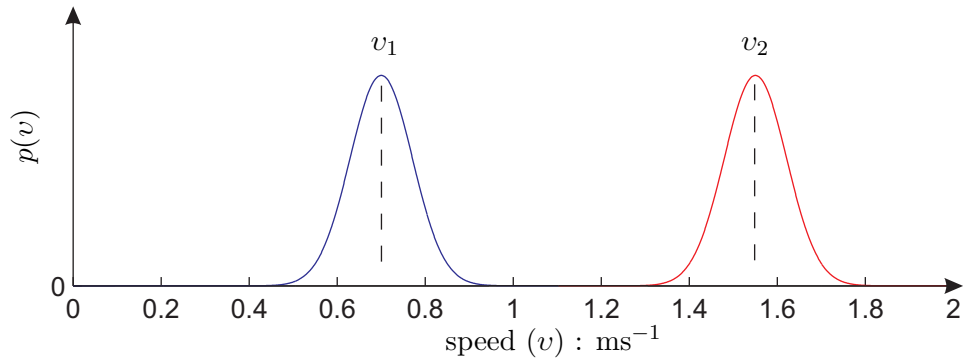

Figure 4.5: The distribution from which speed samples will be drawn for two different current speeds

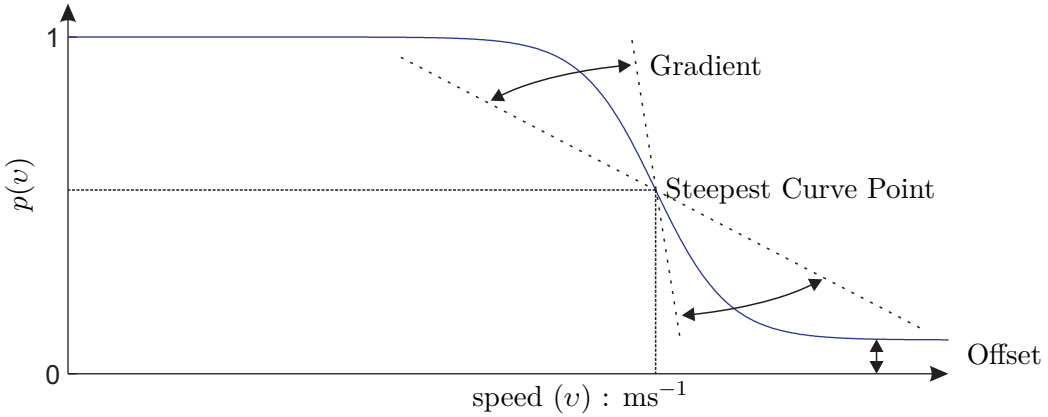

Figure 4.6: A hyperbolic tangent function used to reduce the probability of samples that would cause unrealistic speed in the motion model

be drawn (this may be achieved by drawing a new speed sample or drawing and adding an acceleration sample to the current speed). As discussed in section 4.3, typical travel speeds for a sperm whale are between 0.55 ms^{-1} and 1.39 ms^{-1}, however the mean of the red curve shows the animal to be travelling slightly faster at 1.55 ms^{-1}. The normal distribution of the red curve allows samples to be drawn that would cause the animal's speed to increase even further. This mechanism allows the model to represent the animal's speed as a process which increases without bound.

4.4.2 Overcoming Limitations of a Gaussian System Noise Distribution

The limitations presented by using a system noise distribution that is independent of current speed, such as a normal distribution, can be overcome by drawing samples from an alternative distribution, however formulating the necessary distribution is not a trivial task. Further complications in formulating an appropriate distribution may be presented by the order of the motion model. An alternative is to simulate a non-Gaussian distribution by rejecting system noise samples drawn from a normal distribution that do not conform to the model, this approach is discussed in this section.

The difficulties of drawing system samples from a distribution independent of the current

speed, v_k, and limiting the modelled maximum speed, $v^{\max}$, of the animal can be overcome using a second distribution as the basis for rejecting samples using the speed at k and what the speed would be at $k+1$ given the drawn sample. After a system noise sample is drawn the updated target speed is calculated followed by calculation of an acceptance criteria using the hyperbolic tangent function:

$$\boldsymbol{\chi}\left(v_{k-1}+\dot{v}_k\right) = (1-C)\left(\frac{\tanh\left(AB - A(v_{k-1}+\dot{v}_k) - 1\right) + 1}{2}\right) + C \tag{4.38}$$

which forms the curve shown in figure 4.6 where A is the maximum gradient of the curve, B is the speed at the steepest point of the curve and C is the offset from the speed axis. The resulting probability is compared against a sample drawn from the uniform distribution $\mu \sim \mathcal{U}(0,1)$, acceptance of the system noise sample is given by:

$$v_k = \begin{cases} v_{k-1}+\dot{v}_k & \text{if } \mu < \boldsymbol{\chi}\left(v_{k-1}+\dot{v}_k\right) \\ v_{k-1} & \text{otherwise} \end{cases} \tag{4.39}$$

If the test is failed the system sample can be either rejected, and the old speed sample used, or the process can be repeated until a sample is drawn that is accepted. The shape of the rejection function can be controlled using the gradient, A, curve mid-point, B, and offset, C, parameters. The curve mid-point parameter controls the speed at which a sample has a 50% chance of being rejected (assuming no offset) and the gradient controls the rate of transition from automatic acceptance to automatic rejection (again assuming no offset). The offset parameter allows a small proportion of system samples that would cause high speeds to be accepted, this may be necessary to maintain diversity in the particle filter. Use of the offset parameter will however cause changes in the midpoint and gradient parameters. A benefit of this system is system samples can be rejected based on the resulting speed regardless of the order of the motion model.

4.5 Motion Model and Coordinate System for Sperm Whale Tracking

Sections 4.1, 4.2 and 4.4 have discussed the design elements necessary to formulate a motion model for target tracking and section 4.3 has discussed sperm whale swimming motion. This section develops and presents a complete system function for updating particle states.

4.5.1 Coordinate System

For the purpose of tracking an animal from a boat it makes sense to present results in a spherical coordinate system centred over the boat. This will provide intuitive measurements relative to the boat and conform with the polar coordinate system typically used to record visual sightings.

The MSC system could be utilised even though the use of a SIR particle filter negates the necessity of maintaining filter stability by selection of a coordinate system that reduces matrix ill-conditioning. If a locally-linearised particle filter were to be utilised it may be necessary to use an MSC system because matrix ill-conditioning may be a problem in the locally-linearised particle propagation stage. The MSC system does however provide a coordinate system which includes bearing, elevation and range related parameters.

For the MSE estimate of the animal position the state of each particle will be transformed to Cartesian coordinates. This is necessary because if the particles are spread across the x-axis to the rear of the boat then the resulting estimate will place the animal in front of the boat, for example the mean of $-3\pi/4$ and $3\pi/4$, both bearings to the rear of the boat, is 0, directly ahead of the boat; the estimate should be to the rear of the boat at π rads. Computing the MSE estimate in Cartesian space alleviates this problem.

4.5.2 Motion Model

As discussed in section 4.3, there is considerable understanding of the sperm whales's dive cycle, however there is not enough knowledge about the instantaneous motion, such as accelerations and manoeuvring, to enable a sophisticated motion model to be developed. Furthermore a normal distribution noise model is not adequately representative of the changes in speed sperm whale motion is realistically subjected to. Appropriate modelling of the system noise distribution is necessary to avoid the estimated range increasing exponentially and causing the filter to effectively behave in an unstable manner so the draw and accept/reject system discussed in section 4.4 will be used.

Since there is insufficient understanding of instantaneous sperm whale accelerations and manoeuvring a random walk may be applicable, however there are drawbacks to a random walk model in Cartesian space. Firstly such a model in Cartesian form is uncoupled across dimensions so changes of velocity in one direction do not affect changes of velocity in the other two and lead to unrealistic overall speeds. A normal system noise distribution in this application should have a mean of 0 to avoid bias towards motion in a particular direction. The sample most likely to be drawn from a normal distribution with a mean of 0 is 0, effectively meaning no movement. Alternatively a uniform distribution could be utilised which would increase the likelihood of non-zero samples being drawn, however this puts hard minimum and maximum limits on the samples that may be drawn and the mean remains as zero. Secondly, drawing samples in Cartesian form complicates the accept/reject method of drawing system noise samples because, although calculating speed is trivial, deciding what to do with rejected samples yet still allow changes in direction is less so. Finally a random walk could yield particles manoeuvring in a unrealistic way because the particle would not include any velocity or trajectory information. It is proposed that system samples be drawn independently for changes in target speed, heading and pitch. This uncouples sample drawing for direction and speed into separate processes so that samples for change in speed can be rejected while

samples for change in heading and pitch can be maintained, so that:

$$e_k^{\upsilon} \sim \mathcal{N}\left(0, \text{var}\left\{\upsilon\right\}\right) \tag{4.40}$$

$$e_k^{\gamma} \sim \mathcal{N}\left(0, \text{var}\left\{\gamma\right\}\right) \tag{4.41}$$

$$e_k^{\beta} \sim \mathcal{N}\left(0, \text{var}\left\{\beta\right\}\right) \tag{4.42}$$

where γ_k and β_k are change in target heading and pitch respectively. In general terms the direction a target is facing may not be the direction in which it is travelling in this case 'pitch' is taken to be the angle relative to horizontal at which the target is ascending or descending. The transformation between Cartesian velocities and speed and angular velocities is:

$$\upsilon_k = \sqrt{\dot{x}_k^2 + \dot{y}_k^2 + \dot{z}_k^2} \tag{4.43}$$

$$\gamma_k = \tan^{-1} \frac{\dot{y}_k}{\dot{x}_k} \tag{4.44}$$

$$\beta_k = \tan^{-1} \frac{-\dot{z}}{\sqrt{\dot{x}_k^2 + \dot{y}_k^2}} \tag{4.45}$$

and:

$$\dot{x}_k = \upsilon_k \cos\beta_k \cos\gamma_k \tag{4.46}$$

$$\dot{y}_k = \upsilon_k \cos\beta_k \sin\gamma_k \tag{4.47}$$

$$\dot{z}_k = \upsilon_k \sin\beta_k \tag{4.48}$$

Samples drawn from distributions representative of motion in a spherical coordinate system will be transformed to Cartesian for application of a near-constant velocity motion model as described in section 4.1.3. Should such a coordinate system be used, then there are methods for applying constant velocity motion models directly to MPCs [79] and MSCs using a numerical solver based on the Euler method [113], however it is simpler to transform to Cartesian and perform the update analytically.

As the coordinate system is centred over the boat the velocity of the target is relative to the boat, a fact that is negated in the drawing of speed, heading and pitch samples so needs to be corrected for in the system function. The coordinate system also needs to be rotated with changes in boat heading to represent the relative change in bearing of the target to the boat. Concatenating both these parameters, the change in boat heading, $\dot{\theta}_k^{\text{boat}}$, and boat speed υ_k^{boat}, together yield a control vector of the form:

$$\mathbf{u}_k = \begin{bmatrix} \dot{\theta}_k^{\text{boat}} \\ \upsilon_k^{\text{boat}} \end{bmatrix} \tag{4.49}$$

The x-axis of the coordinate system is aligned with the centreline of the boat, therefore the correction for boat motion only needs to be applied to the x dimension of the target's velocity:

$$\mathbf{a}_k^{\text{car}} = \mathbf{a}_k^{\text{car}} + \mathbf{L}u_k\left(2\right) \tag{4.50}$$

where:

$$\mathbf{L} = \begin{bmatrix} 0 \\ 1 \\ 0 \\ 0 \\ 0 \\ 0 \end{bmatrix} \tag{4.51}$$

The rotation is applied to the heading and position of the target:

$$\mathbf{a}_k^{\text{car}} = \boldsymbol{\Theta}_k \mathbf{a}_k^{\text{car}} \tag{4.52}$$

where:

$$\boldsymbol{\Theta}_k = \begin{bmatrix} \cos u_k(1) & 0 & \sin u_k(1) & 0 & 0 & 0 \\ 0 & \cos u_k(1) & 0 & \sin u_k(1) & 0 & 0 \\ -\sin u_k(1) & 0 & \cos u_k(1) & 0 & 0 & 0 \\ 0 & -\sin u_k(1) & 0 & \cos u_k(1) & 0 & 0 \\ 0 & 0 & 0 & 0 & 0 & 0 \\ 0 & 0 & 0 & 0 & 0 & 0 \end{bmatrix} \tag{4.53}$$

The complete system function which will be used for propagating particles is summarised in algorithm 4.1.

4.6 Conclusion and Summary

This chapter has reviewed motion modelling and coordinate systems commonly used in target tracking and sperm whale motion over a dive cycle. From these reviews coordinate systems, a system noise sampling scheme and a motion model have been developed.

The motion models presented can be categorised as random walk, constant velocity, coordinate un-coupled manoeuvre and coordinate coupled manoeuvre models. A random walk motion model updates the target position by drawing samples for the target displacement from a distribution approximated through statistical analysis of the target state parameters. Random walks are particularly useful when limited knowledge about the target's motion is available. Given suitable information more sophisticated and representative motion models can be developed. By incorporating the first order differential of the target state (the velocity) into the system state vector, the target can be modelled using a constant velocity motion model. In this case the velocity is a noise driven process and the target is modelled as travelling on a near-constant course at a near-constant speed. The modelling that results is more representative of the target's motion mechanics and therefore allows a more efficient searching of the state space than a random walk. Manoeuvring target motion models can be further derived by the inclusion of acceleration, jerk or possibly higher order state differentials. Coordinate coupled manoeuvring motion models prevent acceleration in each dimension changing independently from each other and model constant turn rates.

Algorithm 4.1 $[\mathbf{a}_k^{\text{car}}] = \text{System Function}\left(\mathbf{a}_{k-1}^{\text{car}}, \mathbf{u}_k, [\text{var}\{\upsilon\}, \text{var}\{\gamma\}, \text{var}\{\beta\}]'\right)$

Compute speed, heading and pitch:

$$\upsilon_{k-1} = \sqrt{\left(a_{k-1}^{\text{car}}(2)\right)^2 + \left(a_{k-1}^{\text{car}}(4)\right)^2 + \left(a_{k-1}^{\text{car}}(6)\right)^2}$$

$$\gamma_{k-1} = \tan^{-1}\frac{a_{k-1}^{\text{car}}(4)}{a_{k-1}^{\text{car}}(2)}$$

$$\beta_{k-1} = \tan^{-1}\frac{-a_{k-1}^{\text{car}}(6)}{\sqrt{\left(a_{k-1}^{\text{car}}(2)\right)^2 + \left(a_{k-1}^{\text{car}}(4)\right)^2}}$$

Draw system noise samples using (4.40) to (4.42):

$e_k^{\upsilon} \sim \mathcal{N}(0, \text{var}\{\upsilon\})$

$e_k^{\gamma} \sim \mathcal{N}(0, \text{var}\{\gamma\})$

$e_k^{\beta} \sim \mathcal{N}(0, \text{var}\{\beta\})$

Test for speed update acceptance using (4.38) and (4.39)

if Speed accepted **then**

$\upsilon_k = \upsilon_{k-1} + e_k^{\upsilon}$

else

$\upsilon_k = \upsilon_{k-1}$

end if

Update heading and pitch:

$\gamma_k = \gamma_{k-1} + e_k^{\gamma}$

$\beta_k = \beta_{k-1} + e_k^{\beta}$

Set new Cartesian position and velocities:

$$\mathbf{a}_k^{\text{car}} = \begin{bmatrix} \mathbf{a}_{k-1}^{\text{car}}(1) \\ \upsilon_k \cos\beta \cos\gamma \\ \mathbf{a}_{k-1}^{\text{car}}(3) \\ \upsilon_k \cos\beta \sin\gamma \\ \mathbf{a}_{k-1}^{\text{car}}(5) \\ \upsilon_k \sin\beta \end{bmatrix}$$

Update particle state:

$\mathbf{a}_k^{\text{car}} = \mathbf{F}\left(\boldsymbol{\Theta}\mathbf{a}_k^{\text{car}} - \mathbf{L}u_k(2)\right) + \mathbf{L}u_k(2)$

return $\mathbf{a}_k^{\text{car}}$

Although over the period of a complete dive cycle the animal does manoeuvre and change course a near-constant velocity motion model has been selected as the most appropriate for use in particle filters for tracking sperm whales because of the lack of knowledge of the instantaneous accelerations and manoeuvres. Under these circumstances a lower order motion model prevents 'over-fitting' of the model to the system. A correct system variance allows for changes in direction and speed which will vary over the course of the dive.

The time-delay measurements in sperm whale tracking are a function of the bearing and elevation of the target but not the range. Using a normal system noise distribution could lead to unrealistic speeds in the motion model because speed is un-coupled from the measurements so must be limited by the statistics of the noise distribution. This can be achieved by utilising a system noise distribution whereby the likelihood of particles achieving unrealistic speeds is proportionally reduced as speed increases. This is achieved using a rejection function whereby system noise samples that will put a particle's speed beyond a threshold are increasingly less likely to be accepted.

During visual sighting and tracking an animal's position relative to the boat is recorded in terms of bearing and range and it is logical to extend this polar system to acoustic tracking. Due to matrix ill-conditioning issues that arise in angle-only tracking applications when using a Cartesian coordinate system the MPC system is typically utilised. This coordinate system is extended to three dimensions by the MSC system which includes elevation angle and elevation angular velocity components. The range of the target from the boat is achieved by inverting the range reciprocal component. The coordinate system is centred over the boat so that the x-axis is aligned with the centre-line of the boat, therefore the bearing of the animals is judged relative to the heading of the boat, rather than relative to north. This requires that the position of the particles be rotated within the coordinate system as the boat changes course.

Any particle lying off the starboard quarter has a negative bearing whilst any particle at the equivalent bearing to port has a positive bearing. The estimate should place the target directly to the stern of the boat at $\pm\pi$ rads, however an MMSE estimate of the bearing will result in an estimate at 0 rads, directly ahead of the boat. This issue can be overcome by performing the MMSE estimate in Cartesian coordinates.

System noise samples will be drawn in a spherical coordinate system centred over the particle for two reasons: firstly changes in velocity will be coupled across the three dimensions thereby preventing them varying independently; secondly if the drawn samples result in a high speed which is rejected by the rejection function the horizontal and vertical angular acceleration samples can still be applied.

The subjects reviewed and discussed in this chapter have led to the development of algorithm 4.1 which will be incorporated into the particle propagation stage of the SIR particle filter algorithm to propagate the particles from $\{\mathbf{a}_{k-1}\}_{1:N}$ to $\{\mathbf{a}_k\}_{1:N}$. This concludes the tracking filter development for the simulated dataset results and analysis presented in chapter 5 and real dataset results presented in chapter 7.

Chapter 5

Application to Simulated Datasets

Chapter 3 proposed using an SIR particle filter to track the position of a whale relative to the observing boat from successive time-delay measurements, described in chapter 2, and the boat manoeuvring information. Chapter 4 described various motion models, that can be utilised as the system function, and state space coordinate systems prior to developing a motion model appropriate to tracking sperm whales. This chapter tests and evaluates the tracking capabilities of the proposed methods using simulated data. Utilising simulated data at this stage provides two benefits, firstly the ground truth is available, which is not true for the real datasets, and secondly, the complexity of the tracking problem can be controlled.

Results from several simulated test datasets are presented. The tracking problem complexity is increased between sets of experiments. Firstly a constant speed non-manoeuvring target is simulated, followed by a dataset where the target manoeuvres in the horizontal plane. The complexity is then increased by sequentially introducing manoeuvring in the horizontal and vertical planes, changes in speed and initialising the tracking filter without knowledge of the true initial position of the target.

5.1 Tracking Filter Performance Criteria and Evaluation

Ideally a tracking method should be able to:

1. Estimate position;
2. Estimate speed and direction of travel;
3. Perform both without knowledge of the starting position and direction of whale motion.

The sections of this chapter evaluate the capability of a particle filter to satisfy each of these requirements by incrementally increasing the complexity of the problem. The drawing of noise samples in the system function using a random number generator results in different Monte-Carlo approximations of the prior distribution, therefore results can differ between repeated

tracking runs of the same measurement data. Consistency is evaluated by comparing results over multiple realisations of the algorithm using the same such parameters.

5.1.1 Experimental Methodology

Tracking results for a whale travelling on a constant course at a constant speed are presented in section 5.2. The experiments in sections 5.3, 5.4 and 5.5 follow a consistent structure. For the experiments in each of these sections at least two test datasets are presented. The datasets are generated randomly following function (3.1) and implemented using algorithm 4.1. For each of the parameters - heading, pitch and speed - a data variance is specified for a normal distribution from which samples for changes in each of these parameters are drawn. Samples drawn for the change in speed are subject to the rejection function described in section 4.4. As a Consequence, the variance of the resulting datasets may differ to that specified. Measurement time-delays are calculated for the relative positions of the whale to the observing boat. Where appropriate, multiple datasets may be processed using the same data parameters. This allows testing of the consistency of tracking performance between datasets generated from the same system model. The speed sample rejection function remains the same for all experiments as:

$$\boldsymbol{\chi}\left(\upsilon_{k-1}+\dot{\upsilon}_k\right)=\frac{\tanh\left(2-2\left(\left(\upsilon_{k-1}+\dot{\upsilon}_k\right)-1\right)\right)+1}{2} \tag{5.1}$$

Testing of tracking performance when the initial position of the whale is unknown in section 5.6 utilises a dataset from section 5.5. This allows comparison between cases where the initial location is known and where it is unknown. Many of the developments in this chapter are applicable to any passive acoustic target tracking using time-delay measurements, not just sperm whales, therefore there is some interchanging of the use of the words 'whale' and 'target' where discussion refers specifically to tracking sperm whales then the target is referred to as a whale.

5.1.2 Performance Criteria and Evaluation

Tracking performance is evaluated for a set of motion models using different heading, pitch and speed variances. Results are presented in terms of spherical coordinates relative to the boat and as a Cartesian reconstruction of the path taken by the simulated boat and the true path followed by the simulated whale.

Several performance measurement criteria can be applied in the evaluation and a track may meet some of these better than others, whilst another tracking realisation may better satisfy others, therefore tracking performance criteria are prioritised in the following order:

1. Tracking of the whale for the entire dataset duration;

2. Tracking of the time-delay measurement as a function of the MMSE estimates of bearing and elevation;
3. Tracking of bearing;
4. Tracking of elevation;
5. Tracking of range.

The highest priority of the tracking criteria is the ability to track a whale for all the measurements without the estimator being unable to compute a solution. If the estimator is unable to complete a track its usefulness is limited. The second priority is that the estimated time-delays should fit the measurements. This demonstrates that the estimator has converged to a solution that fits the measurements and therefore is valid. Bearing is the third priority because the boat manoeuvres in the horizontal plane, therefore this dimension of the motion model includes a deterministic component whereby changes in boat heading cause a change in the bearing of the whale. It is this deterministic component that causes range to become observable during a manoeuvre, as discussed in section 4.2. Elevation is the fourth priority because the measurement is a function of bearing and elevation. Range estimation is the lowest priority because range is uncoupled from the time-delay measurement and therefore is the most difficult to estimate.

Results are presented in several ways. Firstly estimated bearing, elevation, slant range and time-delay for one results set at each test variance is shown along with the true bearing, elevation, range and time-delay. Secondly, a plan view of the boat and true whale positions are shown with a Cartesian reconstruction of the track for each test variance. Although the Cartesian reconstructions are limited to two dimensions so do not explicitly show depth estimates, the longitude and latitude reconstruction alone is often useful. Where tracking errors are small it is occasionally difficult to see the difference between results under different test parameters so error plots for bearing, elevation, range and time-delay are presented. It is important to take into consideration the axes scales when considering these plots. Finally, to check performance consistency over multiple results sets under the same parameters a table of mean square error (MSE) values for bearing, elevation, range and time-delay at each test variance is presented. For each estimated system state parameter at each test variance a minimum, mean and maximum MSE computed from five results sets is presented, the smaller the difference between the minimum and maximum the more consistent the performance. A statistical analysis of MSE values was not performed due to the limited number of results sets. Where appropriate multiple results for a single dataset under the same test parameters are presented to provide a visual representation of performance consistency.

The Cramer-Rao lower bound (CRLB), which represents the theoretical minimum variance of an unbiased estimator, is not presented. Although the CRLB has been derived for tracking where passive bearing and elevation measurements are available [54], derivation for tracking where the measurement is a time-delay that is a function of both bearing and elevation is a complex process beyond the scope of this work.

5.2 Non-Manoeuvring Constant Velocity Target Tracking

This section explores the capabilities of a particle filter to track a target, which is not necessarily a whale, with separation from the observer in the x, y and z dimensions travelling at a constant velocity in a constant direction so that there is zero heading variance, $\text{var}\{\gamma\} = 0$, zero pitch variance, $\text{var}\{\beta\} = 0$ and zero speed variance, $\text{var}\{v\} = 0$, at a known starting point using a time-delay measurement.

Figure 5.1(a) shows the simulation dataset with the target travelling at a constant speed in a straight line at 400 m depth. The boat manoeuvres four times to simulate how a tracking vessel might behave when following an animal so that range becomes observable. Figure 5.1(b) shows the relative position of the target to the boat in spherical coordinates and the time-delay received across the array aperture.

Straight line tracking performance is evaluated using particle filters with increasing test variances for $\text{var}\{\gamma\}$. With $\text{var}\{\gamma\}$ set close to zero and correct initialisation, the filter can be expected to track the target accurately as the motion model closely represents the target's motion.

Figure 5.2 shows multiple results for tracking the simulated target in figure 5.1. The target has been tracked several times with the test variance $\text{var}\{\gamma\}$ set to values in the range of 1.7453×10^{-9} rads^2 to 1.2217×10^{-2} rads^2. This does not exploit the knowledge that the target is not manoeuvring, however the filter does use knowledge that speed is constant because the speed variance is set to $\text{var}\{v\} = 0$. The tracks where $\text{var}\{\gamma\}$ is higher show greater deviation from the true track, which is to be expected because the particles effectively have more freedom to diverge to alternative solutions that fit the measurements. Figure 5.2(a) shows the bearing, elevation, range and time-delay estimates of the target from the observer.

For all trialled variances bearing tracking remains accurate. Errors in both the elevation and range estimates increase with test variance as expected, the range more so than the elevation. Both re-converge and the errors decrease at the points where the observer performs a manoeuvre, then diverge again until the next manoeuvre. At all times the estimate of bearing and elevation transform to a time-delay that closely matches the measurement, demonstrating the particle filter has converged to a solution that fits the measurements.

Figure 5.3 shows the estimation error for bearing, elevation, range and time-delay that is obtained for each trialled test variance. As expected, the error is greatest for the results set where the test variance is highest.

In the SIR particle filter algorithm system noise samples are drawn randomly from the system noise distribution, therefore, although the importance density remains the same, the Monte-Carlo point wise approximation of the importance density will differ from realisation to realisation. Consequently, tracking results may differ when re-processing the same data with the same test variances. Performance consistency can be evaluated by re-running the tracking filter with the same measurement dataset and test variances multiple times. Table

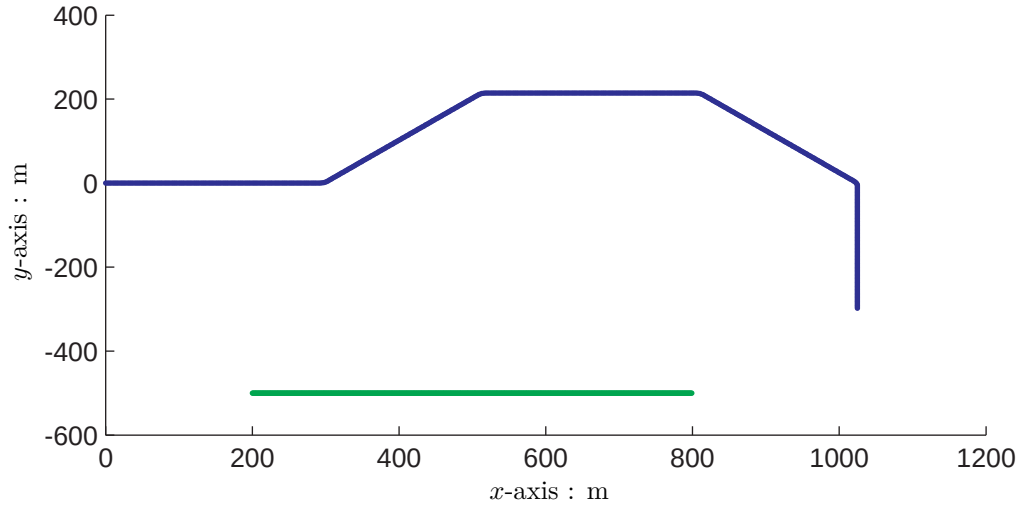

(a) Plan view of true target and boat positions

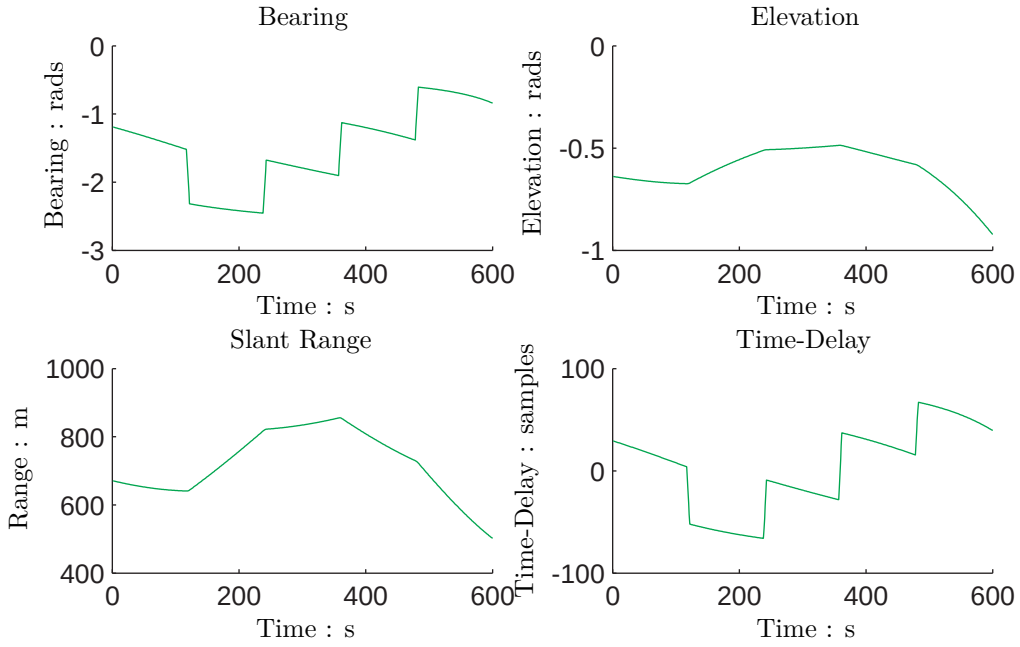

(b) Positions of the target relative to the boat in spherical coordinates and the time-delay received across the array aperture

Figure 5.1: Simulation dataset for a constant velocity non-manoeuvring target, (a) the plan view of the boat and target and (b) the relative positions of the target from the boat in spherical coordinates and the received time-delays.

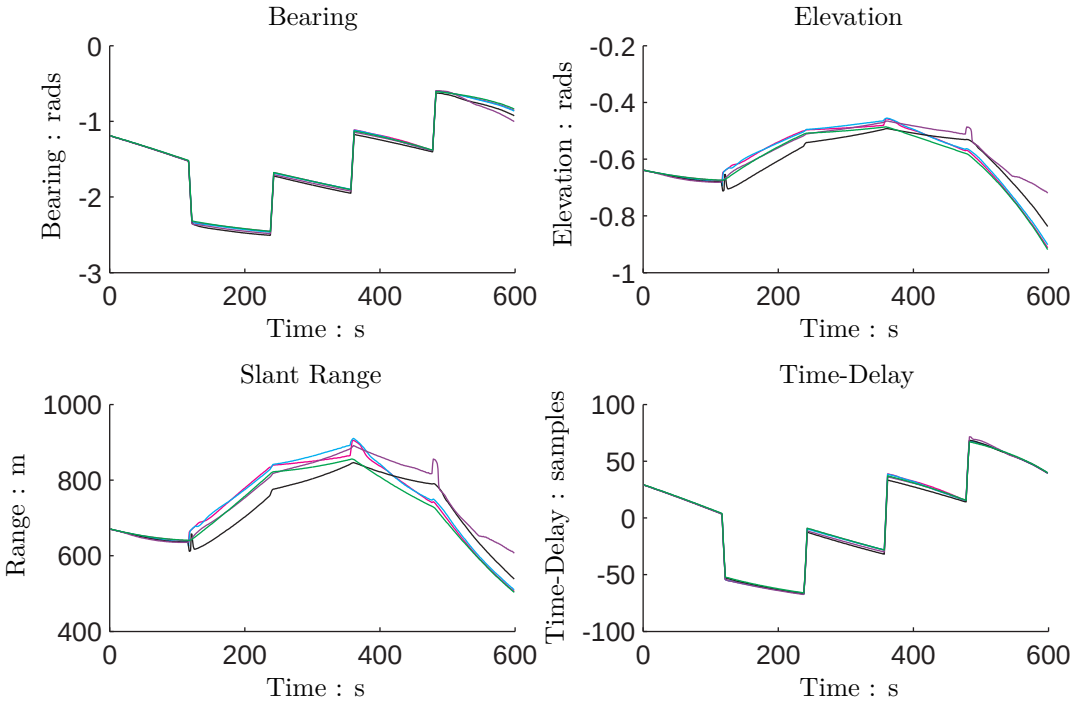

(a) Relative position of target and tracking results relative to boat in spherical form

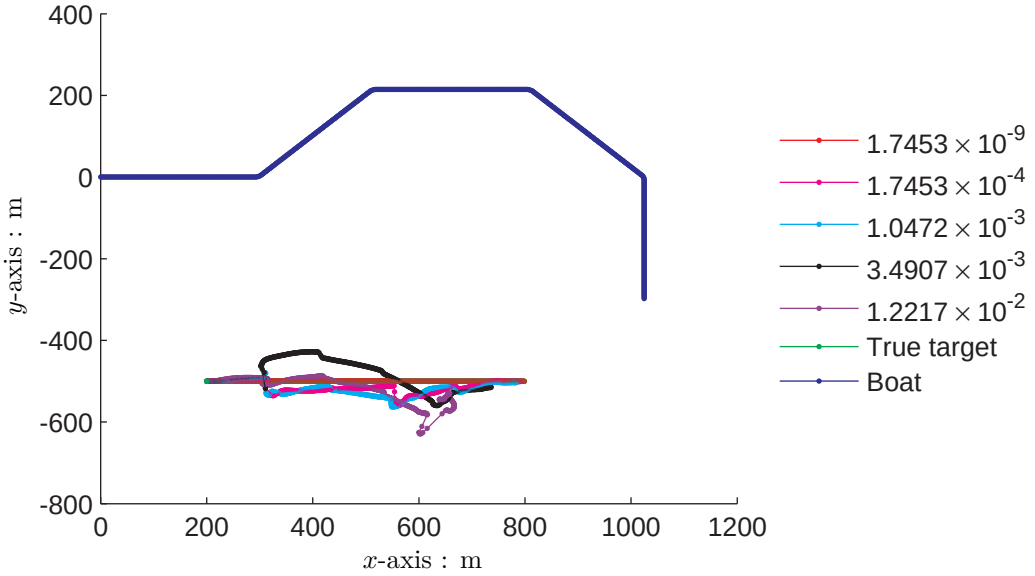

(b) Plan view reconstruction of boat path, target path and tracking results in Cartesian form

Figure 5.2: True target positions and tracking results in (a) spherical coordinates relative to the boat and (b) plan view reconstruction of the boat and true target positions and tracking results for different heading test variances.

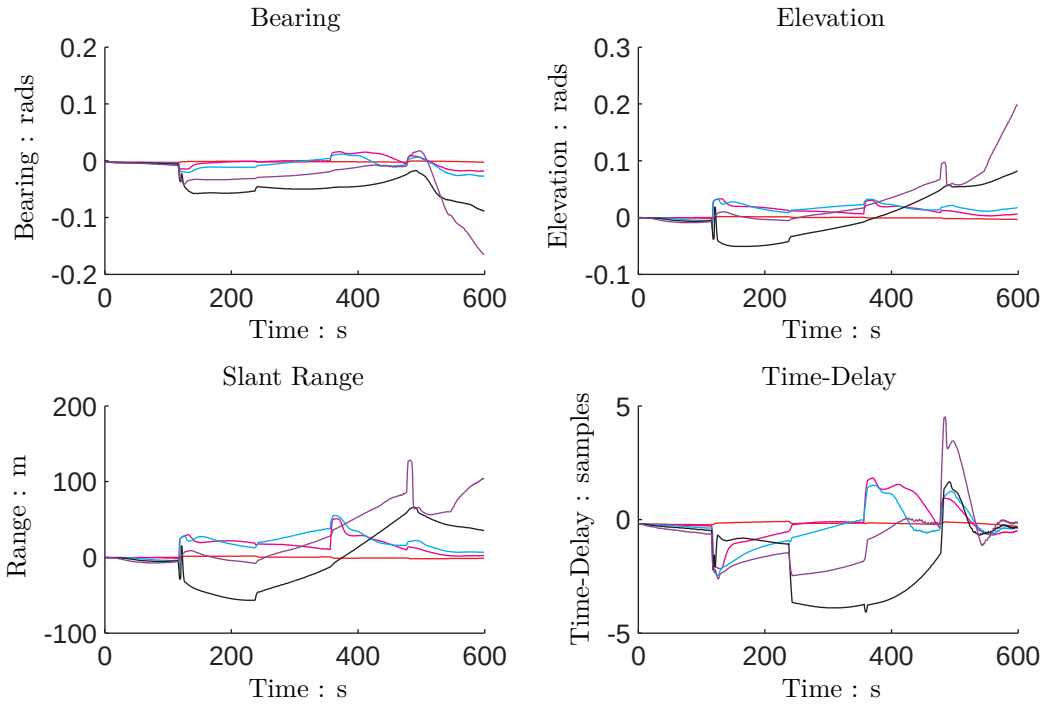

Figure 5.3: Relative position tracking errors for the results in figure 5.2 at each heading test variance. The legend is given in figure 5.2.

Parameter	**System Variance**	**MSE Statistics**		
		min	mean	max
Bearing (rads)	1.7453×10^{-9}	8.2186×10^{-4}	8.2186×10^{-4}	8.2186×10^{-4}
	1.7453×10^{-4}	8.1294×10^{-4}	8.1294×10^{-4}	8.1294×10^{-4}
	1.0472×10^{-3}	9.7711×10^{-4}	9.7711×10^{-4}	9.7711×10^{-4}
	3.4907×10^{-3}	3.0834×10^{-3}	3.0834×10^{-3}	3.0834×10^{-3}
	1.2217×10^{-2}	2.8879×10^{-3}	2.8879×10^{-3}	2.8879×10^{-3}
Elevation (rads)	1.7453×10^{-9}	2.5777×10^{-8}	2.5777×10^{-8}	2.5777×10^{-8}
	1.7453×10^{-4}	1.9192×10^{-4}	1.9192×10^{-4}	1.9192×10^{-4}
	1.0472×10^{-3}	3.0395×10^{-4}	3.0395×10^{-4}	3.0395×10^{-4}
	3.4907×10^{-3}	1.572×10^{-3}	1.572×10^{-3}	1.572×10^{-3}
	1.2217×10^{-2}	3.0227×10^{-3}	3.0227×10^{-3}	3.0227×10^{-3}
Range (m)	1.7453×10^{-9}	1.1455×10^{-2}	1.1455×10^{-2}	1.1455×10^{-2}
	1.7453×10^{-4}	322.61	322.61	322.61
	1.0472×10^{-3}	514.11	514.11	514.11
	3.4907×10^{-3}	1429	1429	1429
	1.2217×10^{-2}	2213	2213	2213
Time Delay (samples)	1.7453×10^{-9}	4.5396	4.5396	4.5396
	1.7453×10^{-4}	4.6507	4.6507	4.6507
	1.0472×10^{-3}	4.8312	4.8312	4.8312
	3.4907×10^{-3}	10.145	10.145	10.145
	1.2217×10^{-2}	6.6559	6.6559	6.6559

Table 5.1: Minimum, mean and maximum MSE values for five tracking results sets at each test variance for the dataset shown in figure 5.1.

5.1 shows minimum, mean and maximum MSE values for bearing, elevation and range and the time-delay derived from the bearing and elevation estimates over five results sets at each test variance. The minimum, mean and maximum MSE scores across results sets in table 5.1 are equal. This demonstrates that over each results set the estimator performed consistently with respect to the overall MSE.

5.2.1 Summary

This section has shown that if the initial position and direction of travel of a constant speed non-manoeuvring target is known then it can be tracked from a time-delay measurement. Results show consistent and accurate performance for bearing, elevation, range and time-delay estimation. In this case range estimation is the component of the target state vector which is most sensitive to changes in $\text{var}\{\gamma\}$.

5.3 Horizontally Manoeuvring Constant Speed Target Tracking

Section 5.2 presented tracking results for a constant speed non-manoeuvring target for different test variances. As expected, optimal tracking performance was obtained utilising the smallest heading test variance because the true motion of the target has zero variance. This section tests tracking filter performance with datasets where the target is manoeuvring in the horizontal plane only.

Figures 5.4 and 5.5 show simulation datasets for a target travelling at a constant velocity at 400 m depth and manoeuvring in the horizontal plane. The generation of the dataset in 5.4 draws samples for the change in target heading from a normal distribution with variance $\text{var}\{\gamma\} = 1.0472 \times 10^{-3}$ and the dataset shown in figure 5.5 draws samples for the change in heading from a normal distribution with variance $\text{var}\{\gamma\} = 1.2217 \times 10^{-2}$.

Tracking results for the dataset generated with $\text{var}\{\gamma\} = 1.0472 \times 10^{-3}$ are shown in figure 5.6 and error plots are shown in figure 5.7. For a test variance of $\text{var}\{\gamma\} = 1.7453 \times 10^{-9}$ the target track is estimated as a straight line because the particles are unable to change heading at a rate high enough to match that of the true target motion. As a consequence bearing estimates fail to converge which also causes a failure of the time-delay estimate track to converge, demonstrating that the estimated track does not match the measurements.

Results in figure 5.6 are surprising because they show the optimal tracking system variance as $\text{var}\{\gamma\} = 1.7453 \times 10^{-4}$, below that at which the data were generated. Figure 5.6 shows all the tracking results follow the correct target positions until the manoeuvre at 120 s, after this point all the tracks diverge from the true position then adjust heading to converge back towards the true track. Between manoeuvres the track at test variance $\text{var}\{\gamma\} = 1.7453 \times 10^{-4}$ is more bound to a straight line assumption. Consequently, the track is more fixed on the

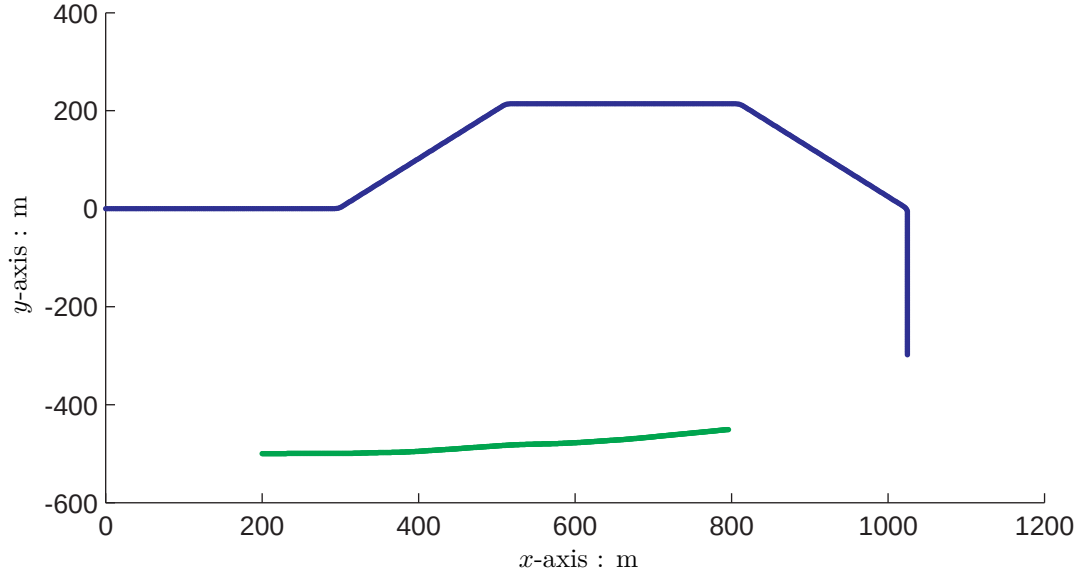

(a) Plan view of true target and boat positions

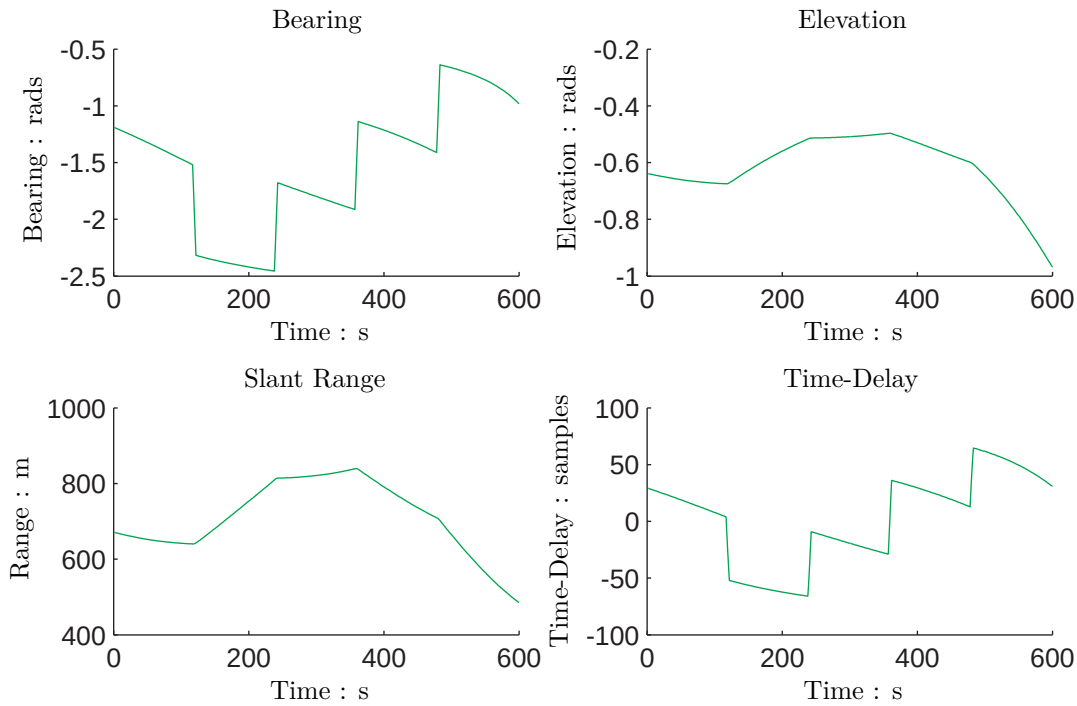

(b) Positions of the target relative to the boat in spherical coordinates and the time-delay received across the array aperture

Figure 5.4: Simulation dataset for a constant velocity manoeuvring target where changes in target heading a drawn from a normal distribution with variance $\text{var}\{\gamma\} = 1.0472 \times 10^{-3}$, shown in (a) plan view and (b) relative positions of the target from the boat in spherical coordinates and the received time-delays.

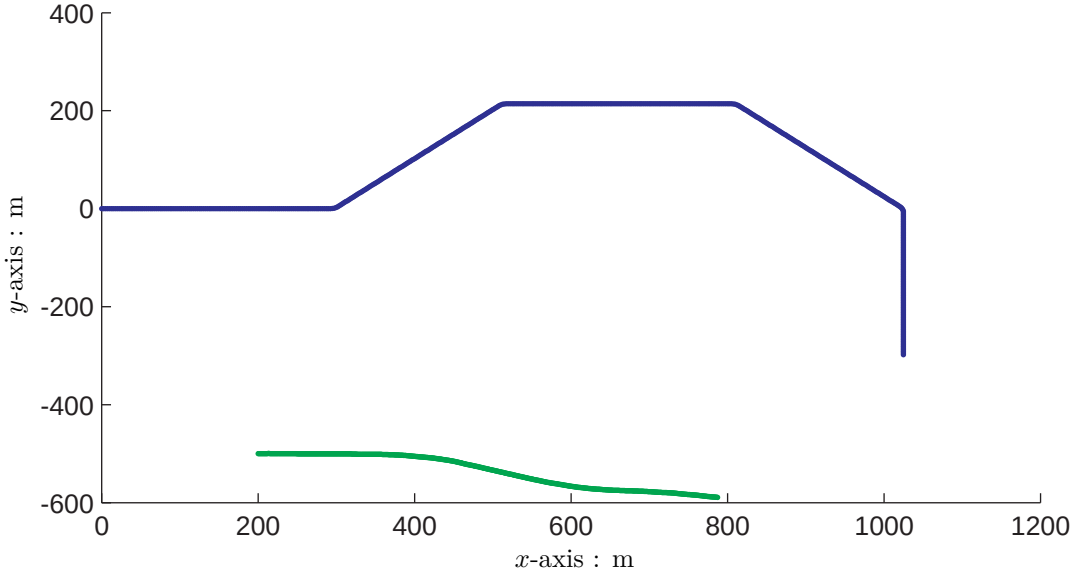

(a) Plan view of true target and boat positions

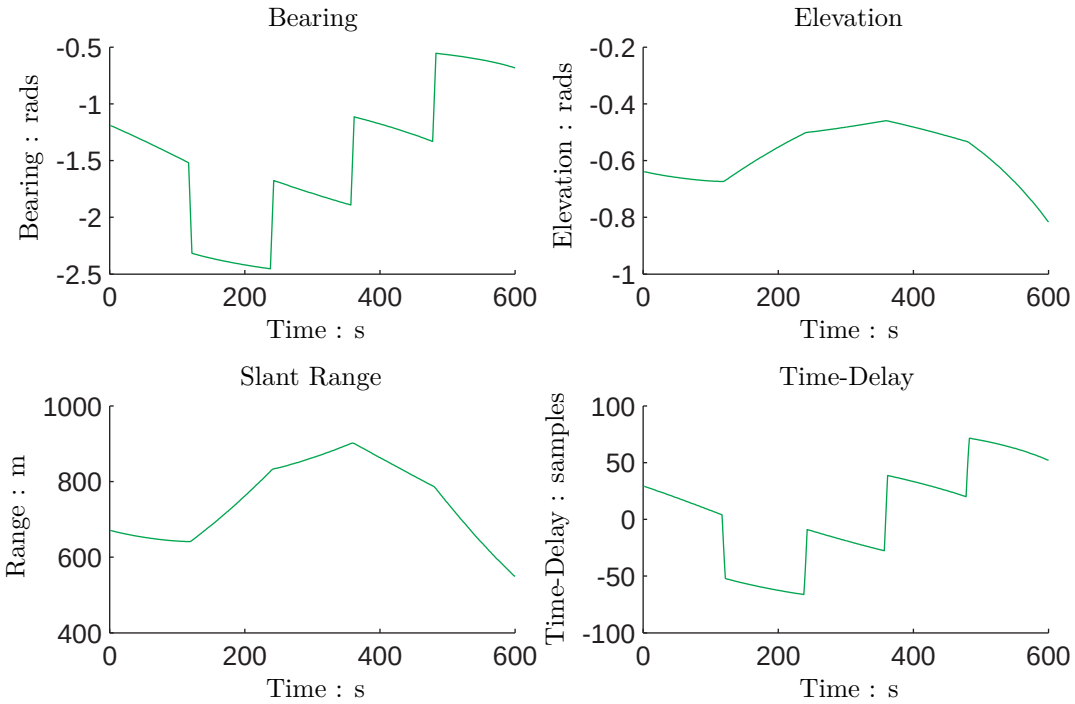

(b) Positions of the target relative to the boat in spherical coordinates and the time-delay received across the array aperture

Figure 5.5: Simulation dataset for a constant velocity manoeuvring target where changes in target heading a drawn from a normal distribution with variance $\text{var}\{\gamma\} = 1.2217 \times 10^{-3}$, shown in (a) plan view and (b) relative positions of the target from the boat in spherical coordinates and the received time-delays.

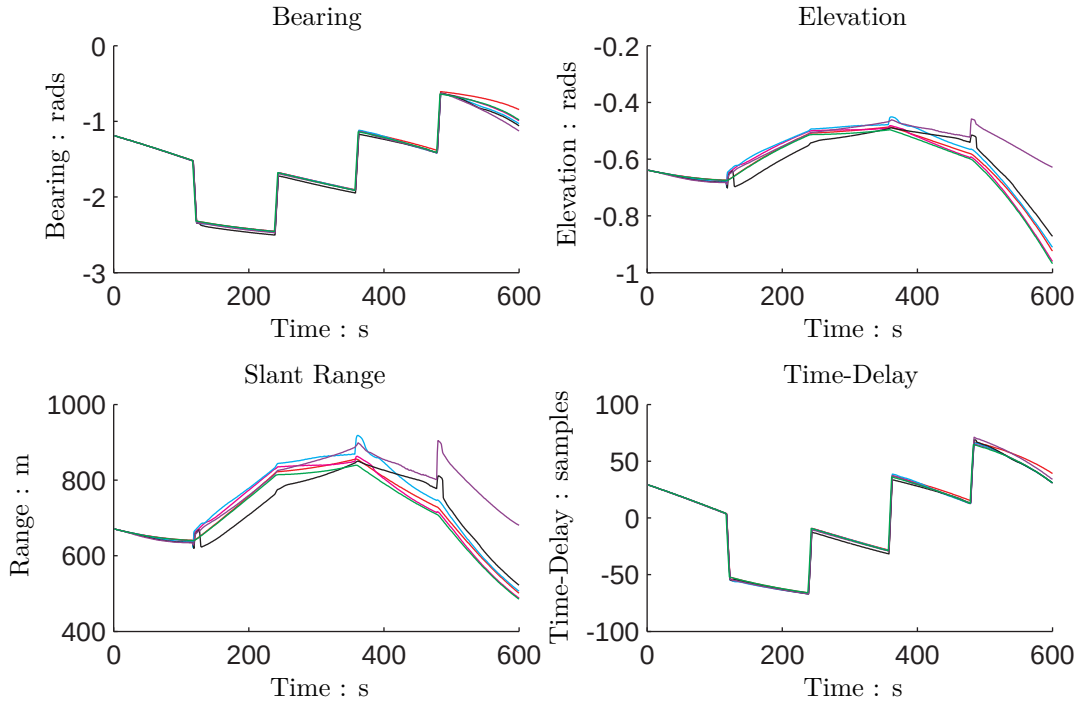

(a) Relative position of target and tracking results relative to boat in spherical form

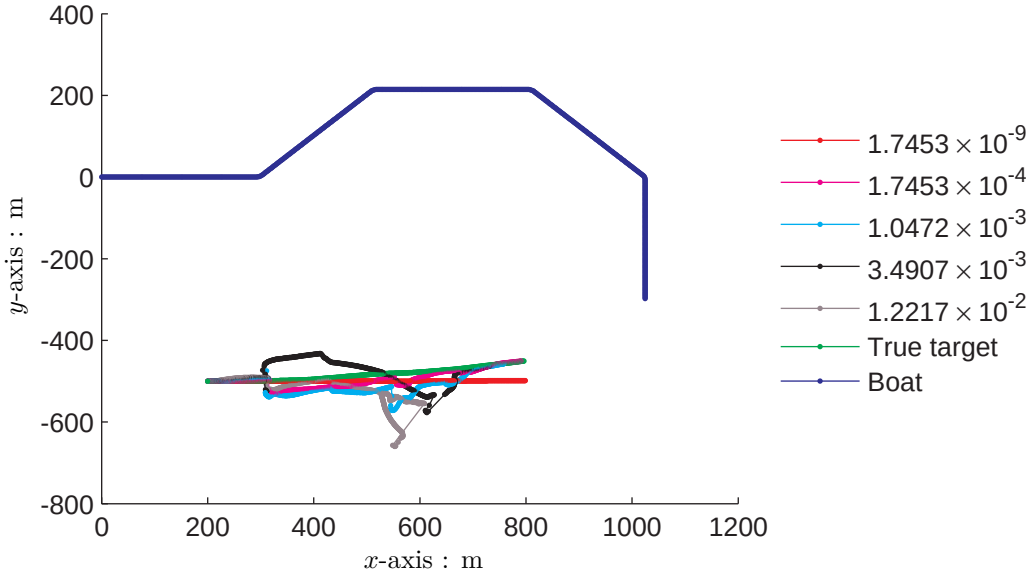

(b) Plan view reconstruction of boat path, target path and tracking results in Cartesian form

Figure 5.6: True target positions and tracking results for the dataset shown in figure 5.4 in (a) spherical coordinates relative to the boat and (b) plan view reconstruction of the boat and true target positions and tracking results for different heading test variances.

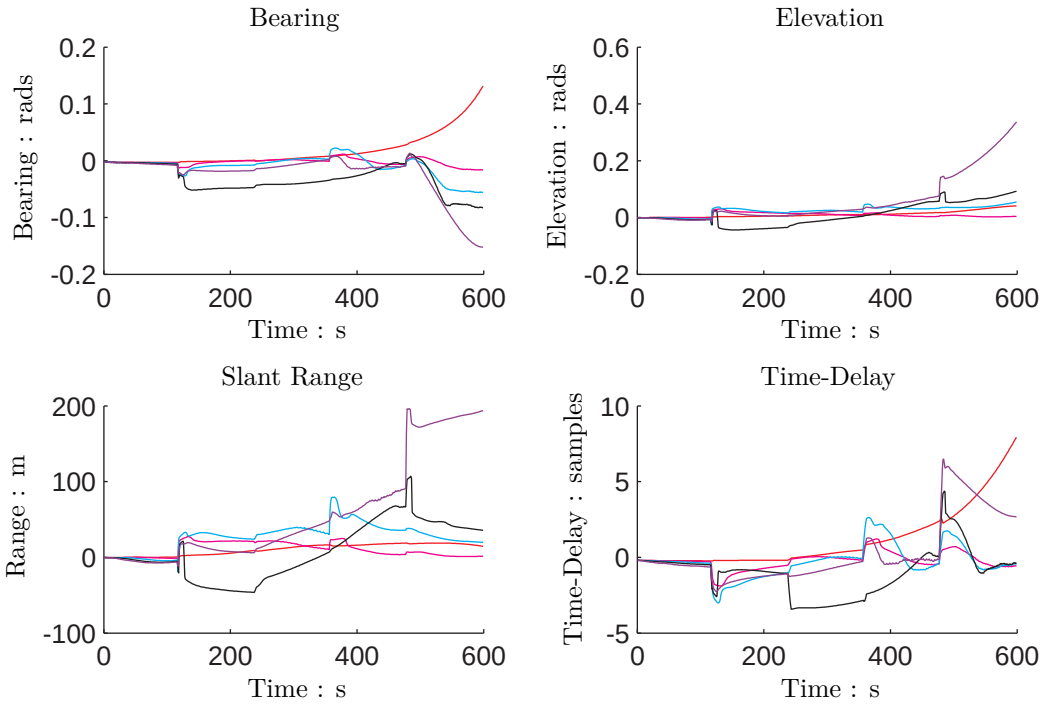

Figure 5.7: Relative position tracking errors for the results in figure 5.6 at each heading test variance. The legend is given in figure 5.6.

Parameter	**System Variance**	**MSE Statistics**		
		min	mean	max
Bearing (rads)	1.7453×10^{-9}	1.9353×10^{-3}	1.9353×10^{-3}	1.9353×10^{-3}
	1.7453×10^{-4}	7.8927×10^{-4}	7.8927×10^{-4}	7.8927×10^{-4}
	1.0472×10^{-3}	1.0907×10^{-3}	1.0907×10^{-3}	1.0907×10^{-3}
	3.4907×10^{-3}	2.4023×10^{-3}	2.4023×10^{-3}	2.4023×10^{-3}
	1.2217×10^{-2}	2.5596×10^{-3}	2.5596×10^{-3}	2.5596×10^{-3}
Elevation (rads)	1.7453×10^{-9}	2.759×10^{-4}	2.759×10^{-4}	2.759×10^{-4}
	1.7453×10^{-4}	1.3328×10^{-4}	1.3328×10^{-4}	1.3328×10^{-4}
	1.0472×10^{-3}	8.6259×10^{-4}	8.6259×10^{-4}	8.6259×10^{-4}
	3.4907×10^{-3}	1.7386×10^{-3}	1.7386×10^{-3}	1.7386×10^{-3}
	1.2217×10^{-2}	1.0945×10^{-2}	1.0945×10^{-2}	1.0945×10^{-2}
Range (m)	1.7453×10^{-9}	180.42	180.42	180.42
	1.7453×10^{-4}	194.21	194.21	194.21
	1.0472×10^{-3}	1078.4	1078.4	1078.4
	3.4907×10^{-3}	1464.2	1464.2	1464.2
	1.2217×10^{-2}	8229.4	8229.4	8229.4
Time Delay (samples)	1.7453×10^{-9}	9.8273	9.8273	9.8273
	1.7453×10^{-4}	4.4592	4.4592	4.4592
	1.0472×10^{-3}	4.9634	4.9634	4.9634
	3.4907×10^{-3}	7.6746	7.6746	7.6746
	1.2217×10^{-2}	8.3811	8.3811	8.3811

Table 5.2: Minimum, mean and maximum MSE values for five tracking results sets at each test variance for the dataset shown in figure 5.4

Parameter	**System Variance**	**MSE Statistics**		
		min	mean	max
Bearing (rads)	1.7453×10^{-9}	2.8491×10^{-3}	2.8654×10^{-3}	2.8812×10^{-3}
	1.7453×10^{-4}	7.9174×10^{-4}	8.1027×10^{-4}	8.2317×10^{-4}
	1.0472×10^{-3}	9.3581×10^{-4}	3.3934×10^{-3}	7.8765×10^{-3}
	3.4907×10^{-3}	3.6923×10^{-3}	4.9657×10^{-3}	6.6152×10^{-3}
	1.2217×10^{-2}	1.2919×10^{-3}	1.869×10^{-3}	3.2808×10^{-3}
Elevation (rads)	1.7453×10^{-9}	1.4857×10^{-3}	1.493×10^{-3}	1.5002×10^{-3}
	1.7453×10^{-4}	9.7451×10^{-5}	1.1284×10^{-4}	1.2274×10^{-4}
	1.0472×10^{-3}	2.684×10^{-4}	1.2267×10^{-3}	2.533×10^{-3}
	3.4907×10^{-3}	1.5528×10^{-3}	1.7386×10^{-3}	1.7386×10^{-3}
	1.2217×10^{-2}	2.7633×10^{-4}	5.829×10^{-4}	1.4632×10^{-3}
Range (m)	1.7453×10^{-9}	1380.3	1384.5	1388.7
	1.7453×10^{-4}	141.34	151.13	164.82
	1.0472×10^{-3}	339.42	1521.8	3214.1
	3.4907×10^{-3}	1911.7	2047.9	2227.2
	1.2217×10^{-2}	289.03	608.8	1509.6
Time Delay (samples)	1.7453×10^{-9}	19.879	19.983	20.085
	1.7453×10^{-4}	4.5894	4.6935	4.7722
	1.0472×10^{-3}	5.1663	13.657	29.711
	3.4907×10^{-3}	14.62	19.035	25.154
	1.2217×10^{-2}	5.6753	7.6052	11.711

Table 5.3: Minimum, mean and maximum MSE values for five tracking results sets at each test variance for the dataset shown in figure 5.5

heading established after the manoeuvre to converge back to the true track than the other tracks with a greater heading variance.

The equal minimum, mean and maximum MSE values in table 5.2 for each test variance are a consequence of the limited number of solutions that fit the measurements. Target pitch and speed variances are both 0, therefore the only varying system parameter affecting how well the particles fit the measurement is the target heading. Assuming the heading of the particles is normally distributed around the true heading of the target the MMSE estimate of the range will not match that of the true target. By the time the manoeuvre occurs the particles will have diverged from the true target track. When the manoeuvre occurs the particles at a greater range are more likely to provide a closer match to the measurements and the lower weighted particles re-sampled out, which explains why the majority of the tracking results in figure 5.6(b) over-estimate range after the first manoeuvre. Due to only one system parameter having a non-zero variance this behaviour is likely to be repeated at each tracking realisation. The matching minimum, mean and maximum MSE values do not indicate that each tracking instance produces either exactly the same results or particle movements, only that the overall error is the same.

Figures 5.8 and 5.9 show tracking results and errors for the dataset shown in figure 5.5. For this dataset the track estimate at test variance $\text{var}\{\gamma\} = 1.7453 \times 10^{-9}$ diverges from the solution in bearing, elevation, range and time-delay. In this case the assumption that the target is moving on a constant course at a constant velocity is not valid. The most accurate

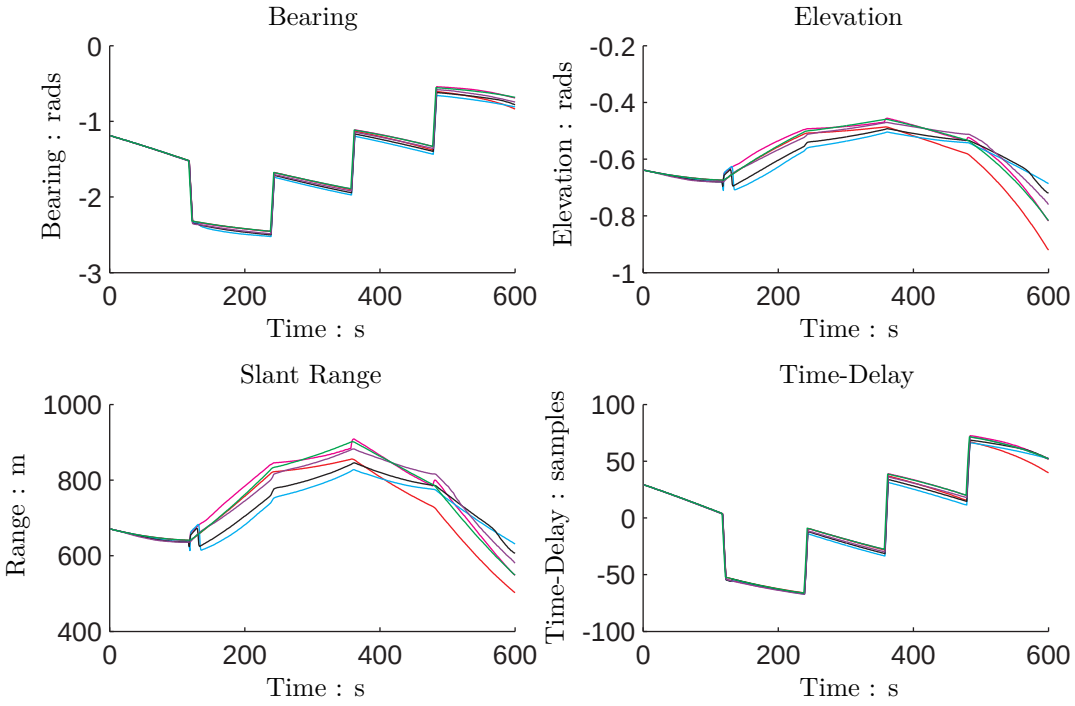

(a) Relative position of target and tracking results relative to boat in spherical form

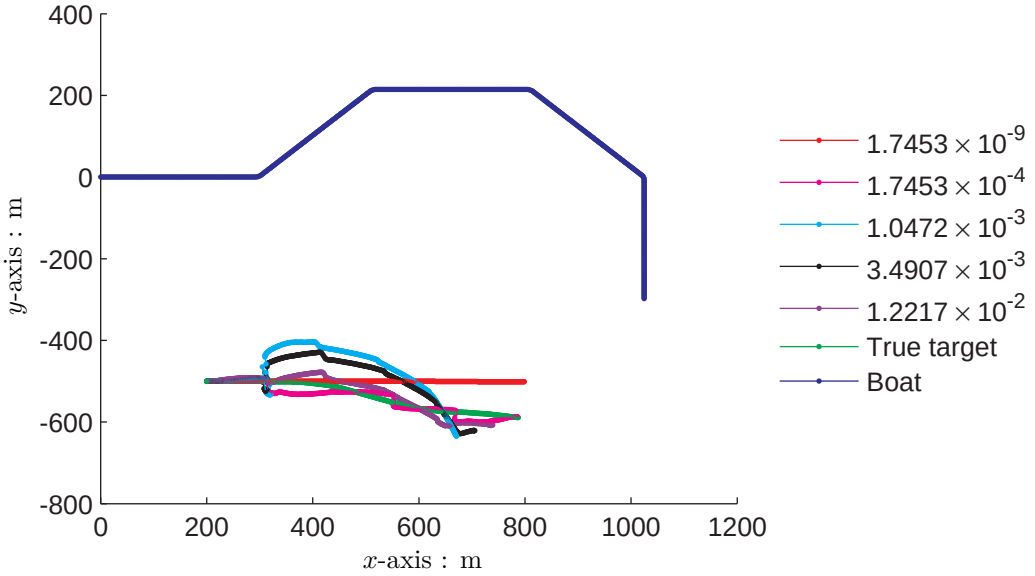

(b) Plan view reconstruction of boat path, target path and tracking results in Cartesian form

Figure 5.8: True target positions and tracking results in (a) spherical coordinates relative to the boat and (b) plan view reconstruction of the boat and target positions for different heading test variances.

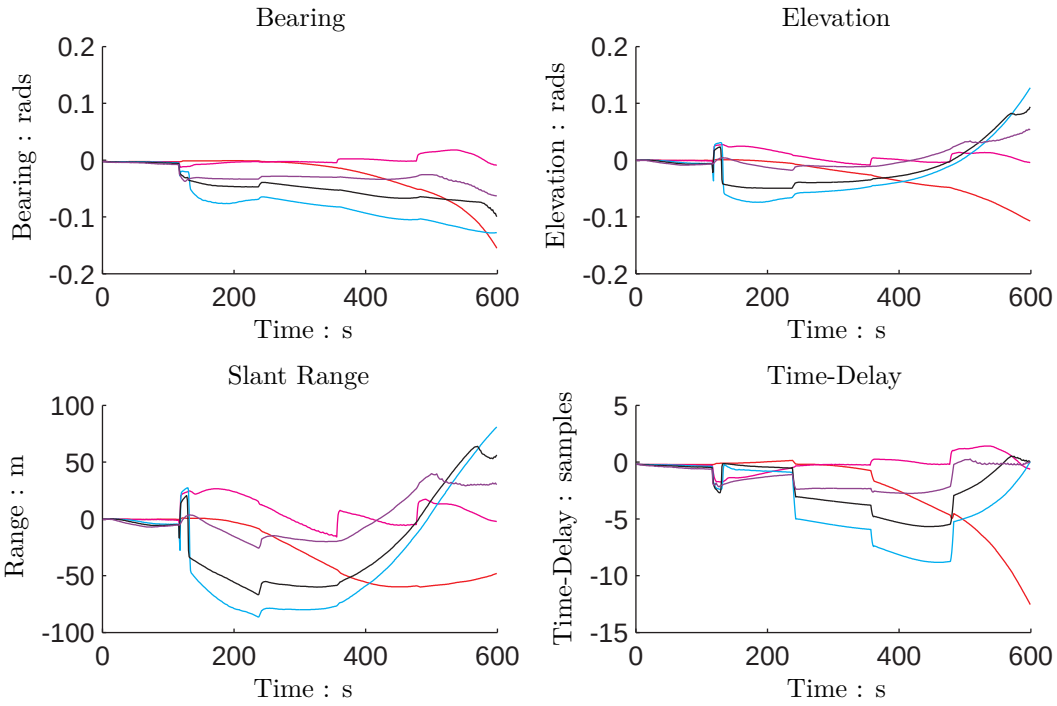

Figure 5.9: Relative position tracking errors for the results shown in figure 5.8 at each heading test variance. The legend is given in figure 5.8.

tracking results are given by a test variance of $\text{var}\{\gamma\} = 1.7453 \times 10^{-4}$. For both datasets tracking results converge across bearing, elevation, range and time-delay. Tracking results for test variances of $\text{var}\{\gamma\} = 1.0472 \times 10^{-3}$ and $\text{var}\{\gamma\} = 3.4907 \times 10^{-3}$ do not track the target as accurately. From figures 5.8 and 5.9 and the MSE values shown in table 5.3 it can be seen that for $\text{var}\{\gamma\} = 1.2217 \times 10^{-2}$ the mean and maximum MSE values are the second lowest for bearing, elevation, range and time-delay. This suggests that the relationship between how the particles spread through the state space, the particle weights and the mean of those particles is non-linear and unpredictable and therefore it may be necessary to find a value for $\text{var}\{\gamma\}$ that gives good performance through experimentation.

Figures 5.10 and 5.11 show true target positions and estimated tracks for a second dataset where samples for change in heading were drawn from a normal distribution with variance $\text{var}\{\gamma\} = 1.2217 \times 10^{-2}$. For this dataset the tracks at test variances $\text{var}\{\gamma\} = 1.7453 \times 10^{-4}$, $\text{var}\{\gamma\} = 1.0472 \times 10^{-3}$ and $\text{var}\{\gamma\} = 3.4907 \times 10^{-3}$ all converge to solutions close to the true target state by the time tracking ceases. For both datasets drawn from a variance $\text{var}\{\gamma\} = 1.2217 \times 10^{-2}$ the range estimates fall short at the first manoeuvre when the test variance is either $\text{var}\{\gamma\} = 1.0472 \times 10^{-3}$ or $\text{var}\{\gamma\} = 3.4907 \times 10^{-3}$. The track estimate using non-manoeuvring constant velocity assumptions in figure 5.10 does not converge to a solution that fits the measurements.

For all three datasets presented in this section, tracking results are accurate until the boat undergoes the first manoeuvre, at which point the track estimates diverge. Until the manoeuvre occurs only particles following the course of the true target, and therefore fit the measurements, receive a high weighting. Particles varying from this course tend to result in

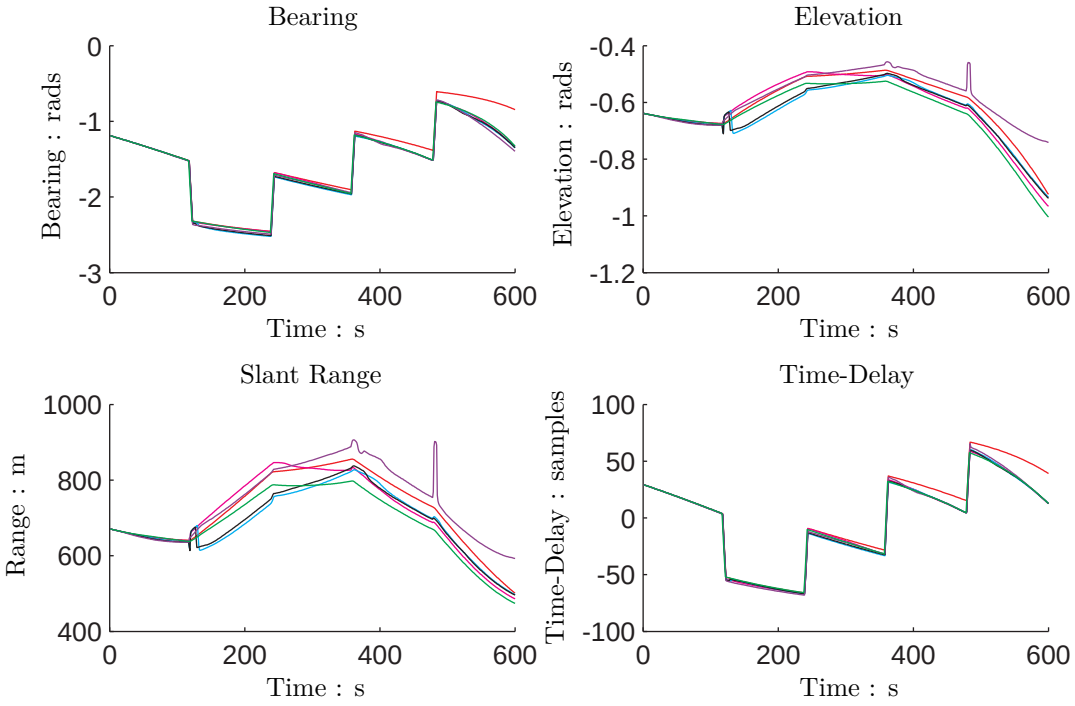

(a) Positions of target and tracking results relative to boat in spherical form

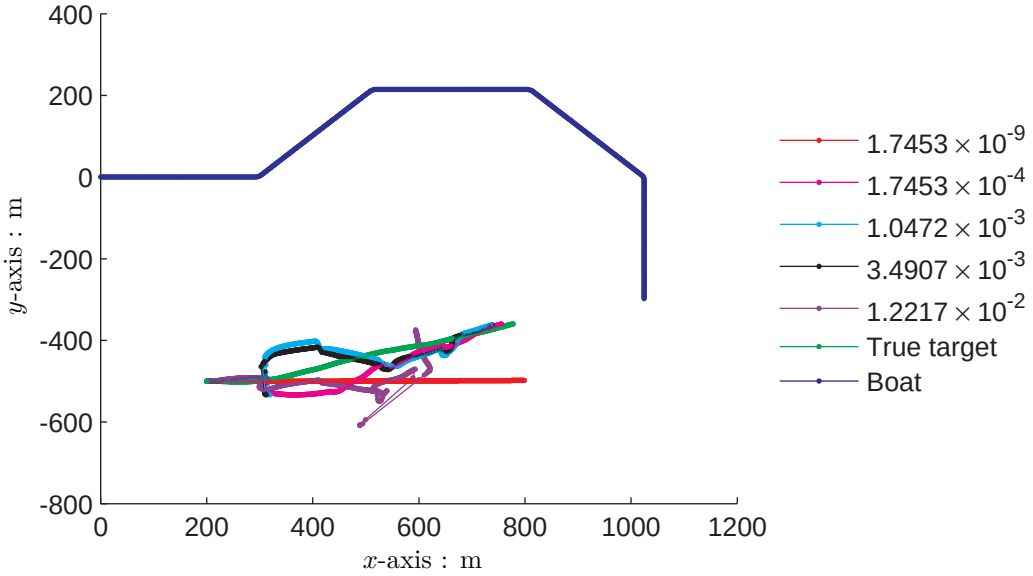

(b) Plan view reconstruction of boat path, target path and tracking results in Cartesian form

Figure 5.10: True target positions and tracking results in (a) spherical coordinates relative to the boat and (b) plan view reconstruction of the boat and target positions for different heading test variances.

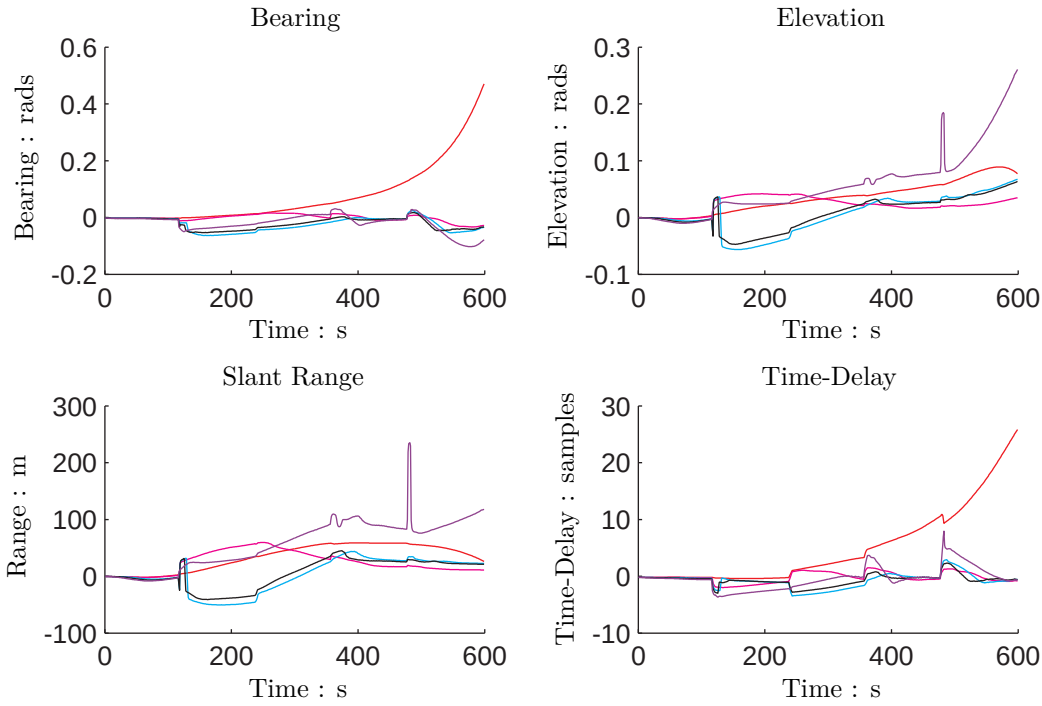

Figure 5.11: Relative position tracking errors for the results shown in figure 5.10 at each heading test variance. The legend is given in figure 5.10.

Parameter	**System Variance**	**MSE Statistics**		
		min	mean	max
Bearing (rads)	1.7453×10^{-9}	1.7701×10^{-2}	1.7754×10^{-2}	1.7775×10^{-2}
	1.7453×10^{-4}	7.8254×10^{-4}	8.0928×10^{-4}	8.3297×10^{-4}
	1.0472×10^{-3}	8.5837×10^{-4}	1.1935×10^{-3}	1.9175×10^{-3}
	3.4907×10^{-3}	9.9084×10^{-4}	1.3608×10^{-3}	1.6352×10^{-3}
	1.2217×10^{-2}	1.303×10^{-3}	1.5769×10^{-3}	2.0774×10^{-3}
Elevation (rads)	1.7453×10^{-9}	2.0878×10^{-3}	2.0973×10^{-3}	2.101×10^{-3}
	1.7453×10^{-4}	2.2091×10^{-4}	4.8345×10^{-4}	7.3201×10^{-4}
	1.0472×10^{-3}	7.1196×10^{-4}	9.6256×10^{-4}	1.224×10^{-3}
	3.4907×10^{-3}	9.5125×10^{-4}	7.5451×10^{-3}	2.0726×10^{-2}
	1.2217×10^{-2}	9.5125×10^{-4}	7.5451×10^{-3}	2.6671×10^{-2}
Range (m)	1.7453×10^{-9}	1725.6	1731.1	1733.3
	1.7453×10^{-4}	272.65	635.37	977.31
	1.0472×10^{-3}	622.35	861.37	1025.9
	3.4907×10^{-3}	703.7	5695.7	16507
	1.2217×10^{-2}	5069	10549	25892
Time Delay (samples)	1.7453×10^{-9}	75.439	75.695	75.796
	1.7453×10^{-4}	4.3925	4.6047	4.7798
	1.0472×10^{-3}	4.6837	5.3128	6.4296
	3.4907×10^{-3}	5.3438	10.889	28.925
	1.2217×10^{-2}	7.0029	16.847	38.412

Table 5.4: Minimum, mean and maximum MSE values for five tracking results sets at each test variance for the dataset shown in figure 5.10

an effective measurement different to the true measurement and receive a low weighting. After the boat manoeuvre occurs the shape of the posterior distribution changes so that particles that have deviated from a continuous course may now fit the measurements while others may not. This effect can be observed in the results as a step change in the estimated track.

5.3.1 Summary

This section has presented three test datasets and tracking results for a target manoeuvring in the horizontal plane. Results show that an assumption that the target is travelling at constant speed and heading is not sufficient for estimating position accurately. More accurate tracking results can be achieved using a white noise process manoeuvring motion model with a variance var $\{\gamma\}$ of magnitude in the order of 10^{-4} even when the data variance is of an order of magnitude of 10^{-3} or 10^{-2}. The next section tests target tracking for a target manoeuvring both horizontally and vertically.

5.4 Horizontal and Vertical Manoeuvring Constant Speed Target Tracking

Section 5.3 presented tracking results for a target manoeuvring in the horizontal plane. It was shown that for both higher and lower data variances a relatively low test variance, var $\{\gamma\}$, produced the most accurate tracking performance. This section expands on developments in the previous section by extending the target's manoeuvring characteristics to include changes in pitch as well as heading.

Figures 5.12 shows a simulation dataset for a target manoeuvring both in the horizontal and vertical planes with samples for changes in heading and pitch drawn from normal distributions with variances var $\{\gamma\} = 1.0472{\times}10^{-3}$ and var $\{\beta\} = 1.0472{\times}10^{-3}$ and 5.13 shows a simulation dataset for a target manoeuvring both in the horizontal and vertical planes with samples for changes in heading and pitch drawn from normal distributions with variances var $\{\gamma\} = 1.2217 \times 10^{-2}$ and var $\{\beta\} = 1.2217 \times 10^{-2}$. Samples for changes in heading and pitch are drawn independently and for both datasets var $\{\upsilon\} = 0$ so that speed remains constant.

Figures 5.14 and 5.15 show tracking results and tracking errors for the dataset shown in figure 5.12. Results show a non-manoeuvring and constant speed motion model provides the most accurate tracking of the system variances trialled. In this case the target is moving on a relatively straight course so the tracking results with a test variance of var $\{\gamma\}$ = var $\{\beta\} = 1.7453 \times 10^{-9}$ diverge least from the true target track, as shown by the MSE scores in table 5.5.

Figures 5.16 and 5.17 show tracking results and errors for the dataset shown in figure 5.13. Results at each test variance match the measurements with exception of var $\{\gamma\}$ = var $\{\beta\} = 1.7453 \times 10^{-9}$. In this case the non-manoeuvring constant speed motion assumptions are

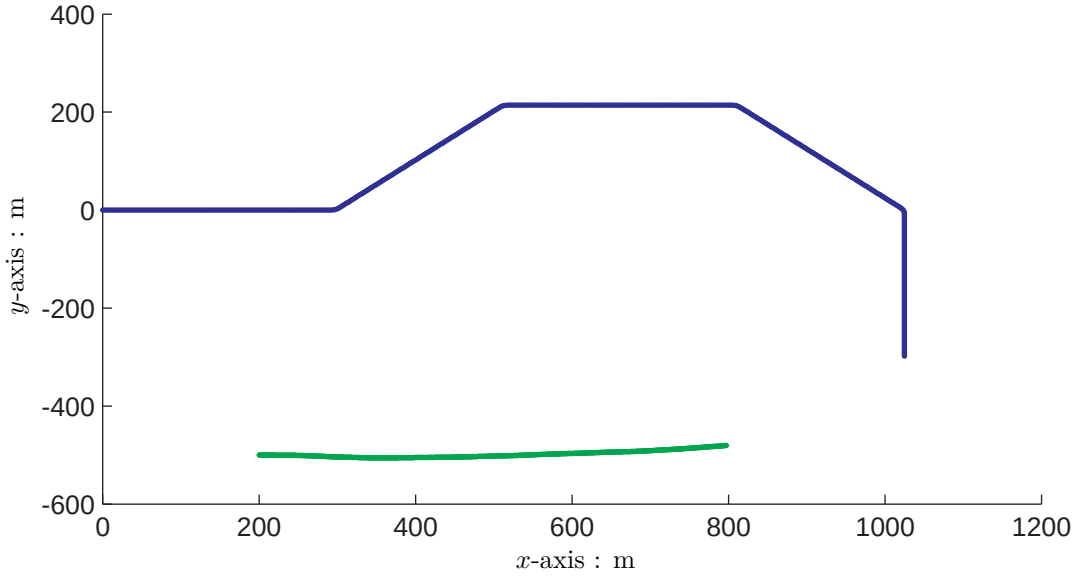

(a) Plan view of true target and boat positions

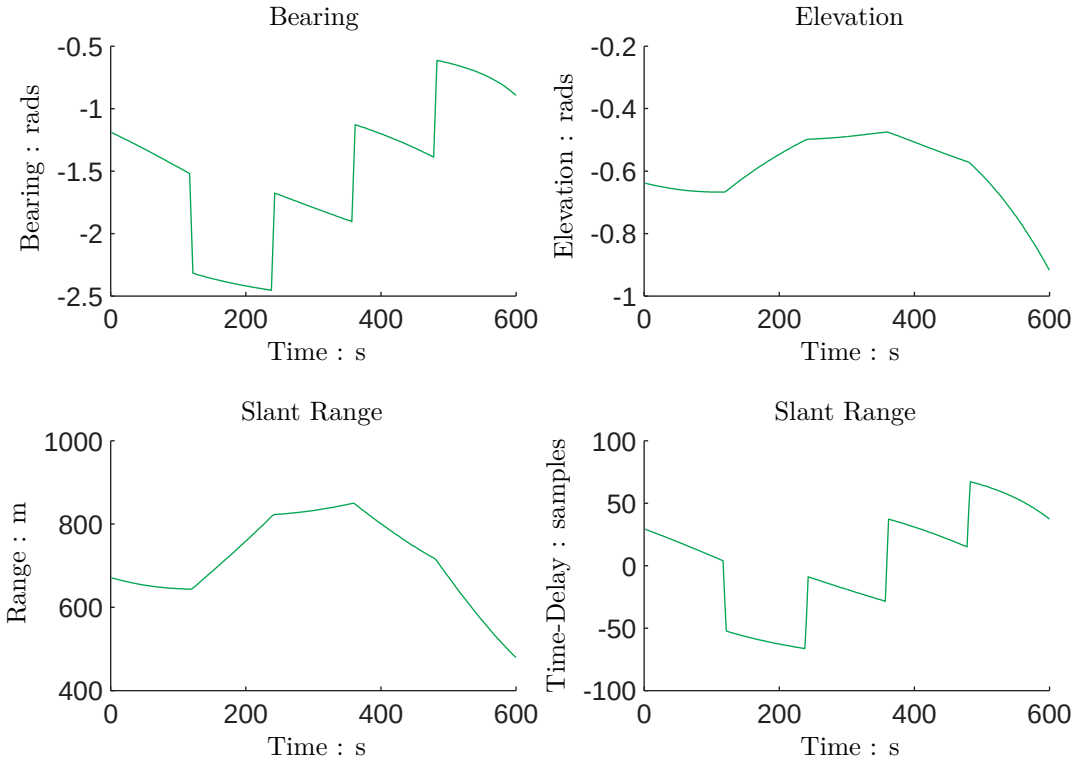

(b) Positions of the target relative to the boat in spherical coordinates and the time-delay received across the array aperture

Figure 5.12: Simulation dataset for a constant velocity manoeuvring target where changes in target heading and pitch are drawn from normal distributions with variances $\text{var}\{\gamma\} = 1.0472 \times 10^{-3}$ and $\text{var}\{\beta\} = 1.0472 \times 10^{-3}$, shown in 5.12a plan view and 5.12b relative positions of the target from the boat in spherical coordinates and the received time-delays.

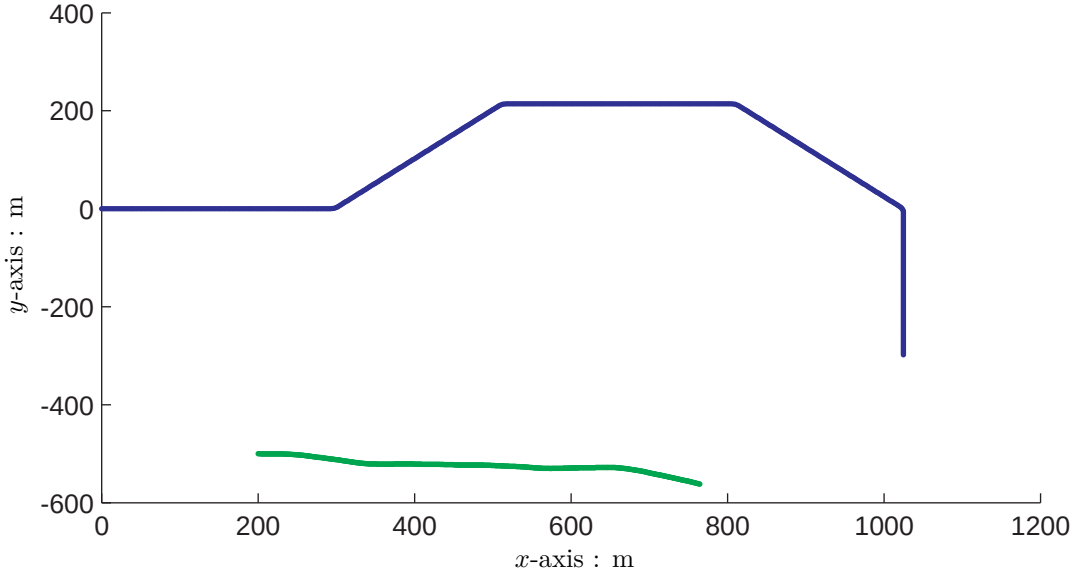

(a) Plan view of true target and boat positions

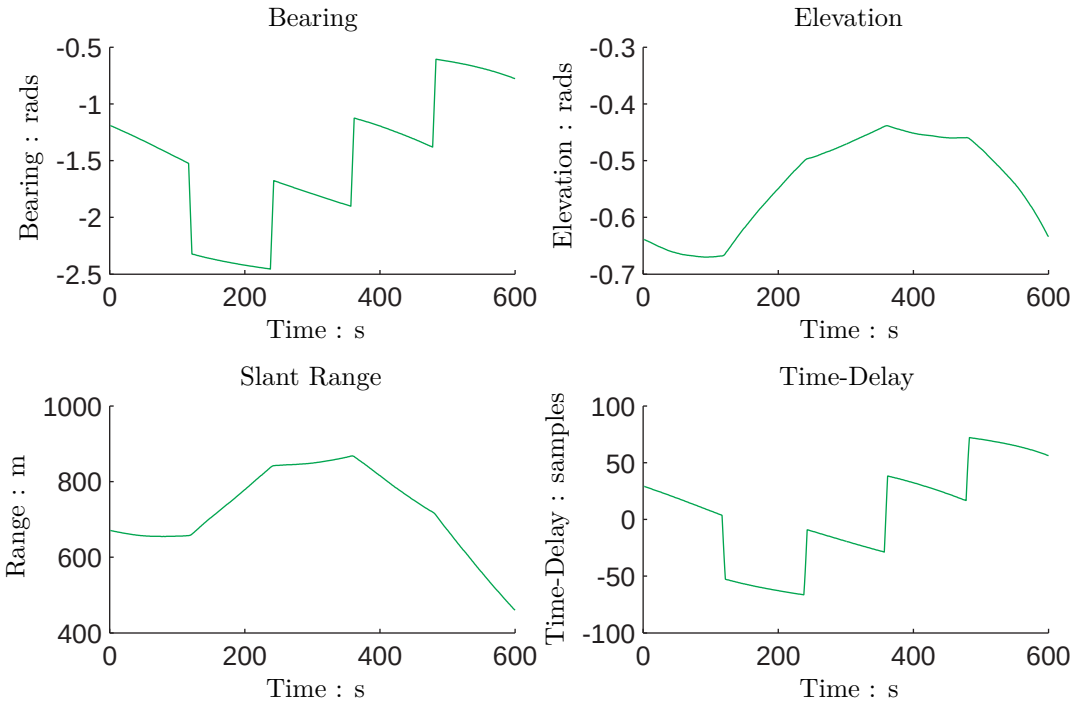

(b) Positions of the target relative to the boat in spherical coordinates and the time-delay received across the array aperture

Figure 5.13: Simulation dataset for a constant velocity manoeuvring target where changes in target heading and pitch are drawn from normal distributions with variances $\text{var}\{\gamma\} = 1.2217 \times 10^{-3}$ and $\text{var}\{\beta\} = 1.2217 \times 10^{-3}$, shown in 5.13a top down view and 5.13b relative positions of the target from the boat in spherical coordinates and the received time-delays.

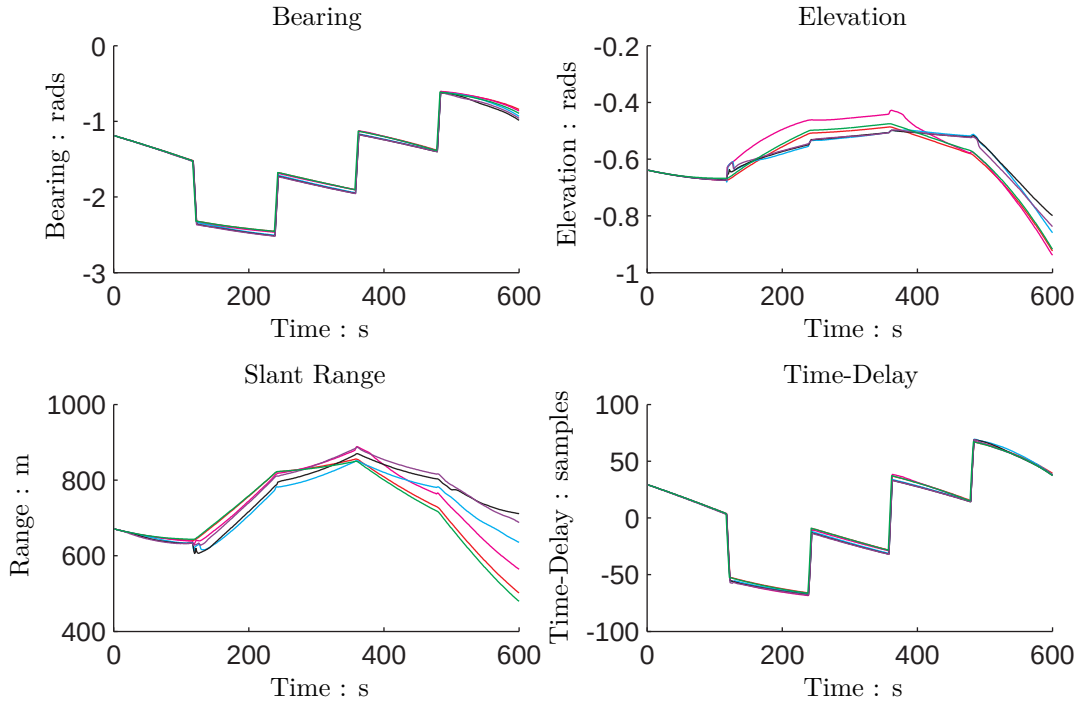

(a) Relative position of target and tracking results relative to boat in spherical form

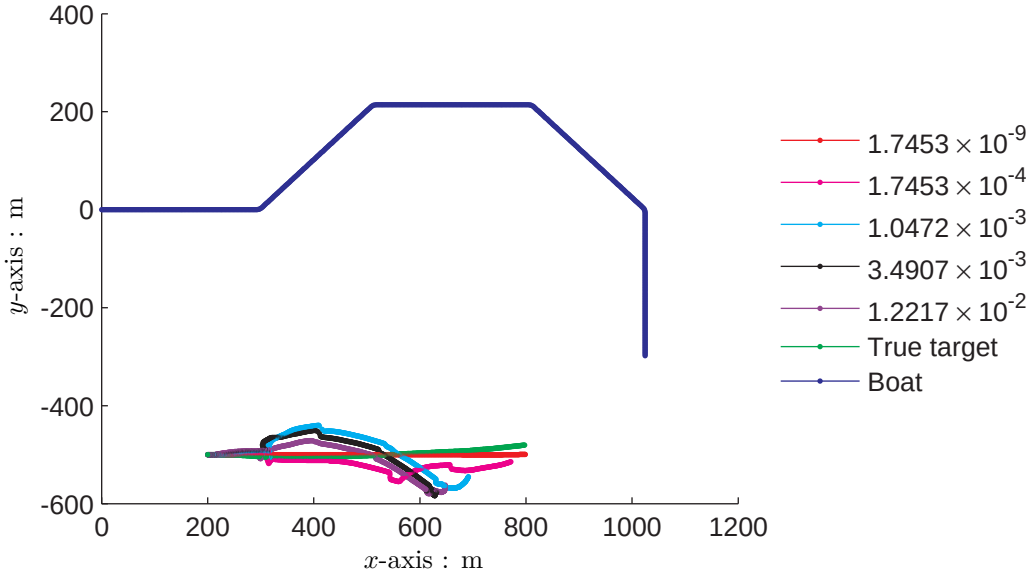

(b) Plan view reconstruction of boat path, target path and tracking results in Cartesian form

Figure 5.14: True target positions and tracking results in (a) spherical coordinates relative to the boat and (b) plan view reconstruction of the boat and target positions for different heading and pitch test variances.

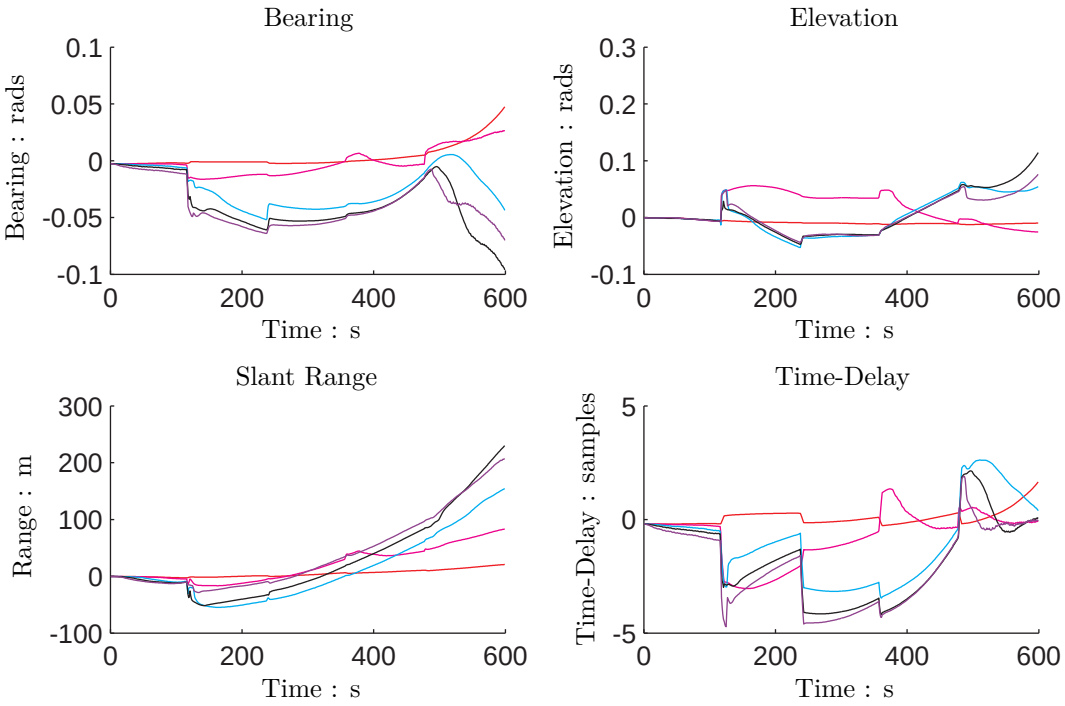

Figure 5.15: Relative position tracking errors for the results shown in figure 5.14 at each heading test variance. The legend is given in figure 5.14.

Parameter	**System Variance**	**MSE Statistics**		
		min	mean	max
Bearing (rads)	1.7453×10^{-9}	9.4278×10^{-4}	9.4435×10^{-4}	9.4529×10^{-4}
	1.7453×10^{-4}	8.6609×10^{-4}	1.0411×10^{-3}	1.283×10^{-3}
	1.0472×10^{-3}	1.224×10^{-3}	1.7428×10^{-3}	2.3021×10^{-3}
	3.4907×10^{-3}	2.4616×10^{-3}	3.3407×10^{-3}	5.6053×10^{-3}
	1.2217×10^{-2}	2.5931×10^{-3}	2.7234×10^{-3}	2.9717×10^{-3}
Elevation (rads)	1.7453×10^{-9}	7.6784×10^{-5}	7.7034×10^{-5}	7.7364×10^{-5}
	1.7453×10^{-4}	3.3029×10^{-4}	6.5085×10^{-4}	1.0421×10^{-3}
	1.0472×10^{-3}	7.8617×10^{-4}	9.9507×10^{-4}	1.1888×10^{-3}
	3.4907×10^{-3}	1.1966×10^{-3}	2.427×10^{-3}	3.5592×10^{-2}
	1.2217×10^{-2}	8.9688×10^{-4}	2.21×10^{-3}	3.3489×10^{-3}
Range (m)	1.7453×10^{-9}	78.242	78.304	78.418
	1.7453×10^{-4}	821.99	1602.3	3530.9
	1.0472×10^{-3}	1446.3	2831.8	3791.2
	3.4907×10^{-3}	3092.4	5121.1	6362.2
	1.2217×10^{-2}	3619.6	5384.1	6381.9
Time Delay (samples)	1.7453×10^{-9}	4.7087	4.7132	4.7164
	1.7453×10^{-4}	4.4163	5.8214	7.9561
	1.0472×10^{-3}	7.3365	9.091	11.167
	3.4907×10^{-3}	9.2148	13.191	21.781
	1.2217×10^{-2}	6.8047	8.5191	11.858

Table 5.5: Minimum, mean and maximum MSE values for five tracking results sets at each test variance for the dataset shown in figure 5.12.

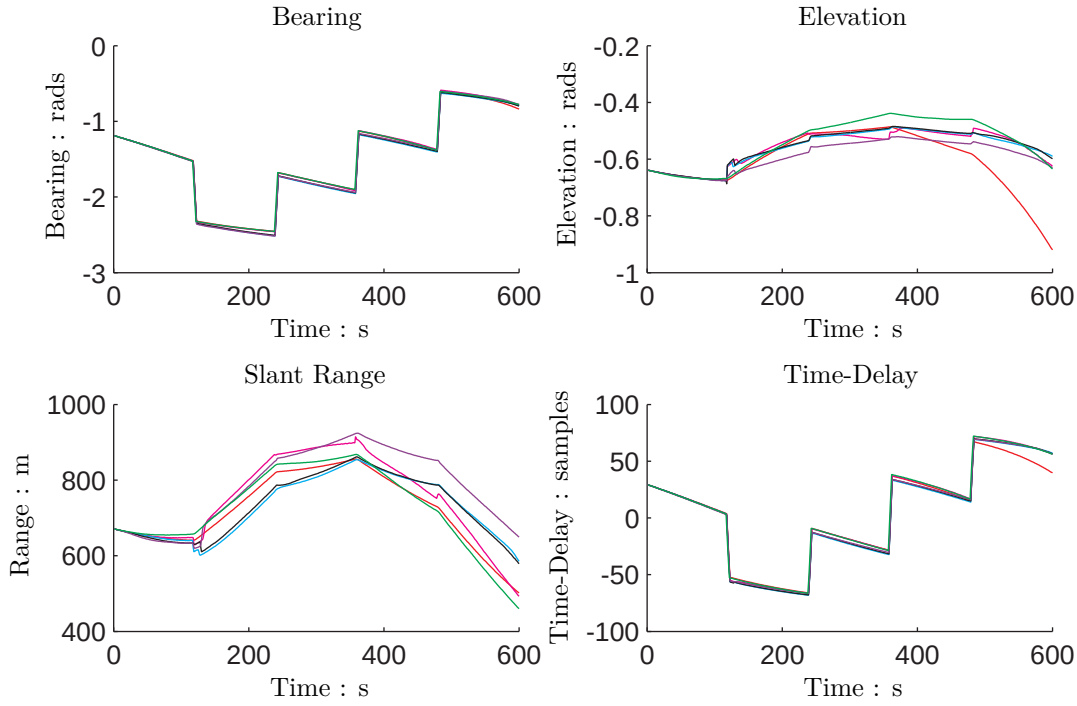

(a) Relative position of target and tracking results relative to boat in spherical form

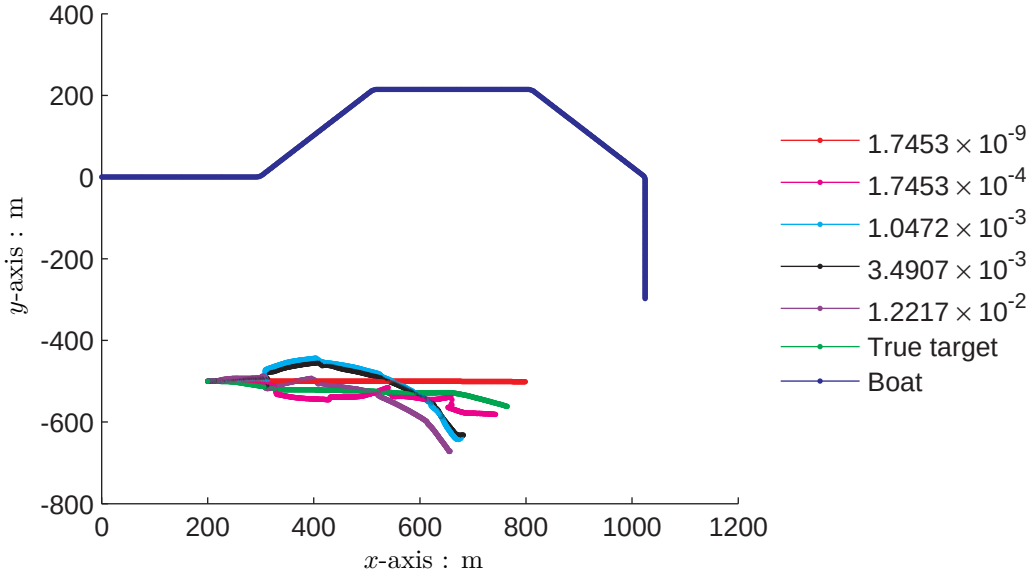

(b) Plan view reconstruction of boat path, target path and tracking results in Cartesian form

Figure 5.16: True target positions and tracking results in (a) spherical coordinates relative to the boat and (b) plan view reconstruction of the boat and target positions for different heading and pitch test variances.

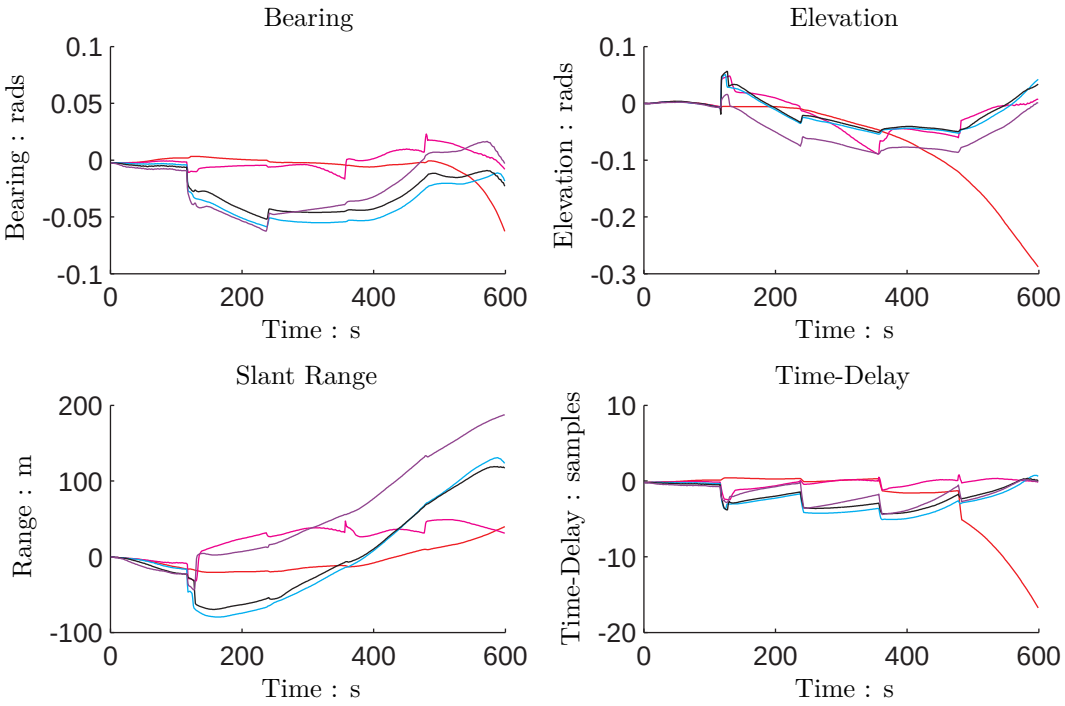

Figure 5.17: Relative position tracking errors for the results in figure 5.6 at each heading test variance. The legend is given in figure 5.6.

not valid, although bearing has been tracked correctly. The divergence of the time-delay estimates for the test variance $\text{var}\{\gamma\} = \text{var}\{\beta\} = 1.7453 \times 10^{-9}$ is caused by errors in the elevation estimate. Large errors occur in range estimates for all the test variances. The test variance resulting in minimal error whilst still producing a solution that fits the measurements is $\text{var}\{\gamma\} = \text{var}\{\beta\} = 1.7453 \times 10^{-4}$.

Figure 5.18 shows the five tracking results sets used for the computation of MSE scores at test variance $\text{var}\{\gamma\} = \text{var}\{\beta\} = 1.7453 \times 10^{-4}$ in table 5.6. Results sets 1, 2, 4 and 5 demonstrate consistent performance, however for results in set 3 range estimates diverge significantly. Bearing estimates remain consistent across all runs but show divergence after the final manoeuvre, which is also shown in the time-delay estimates. Elevation estimates for results sets 2, 3, 4 and 5 are consistent but diverge from the true elevation. Elevation estimates for results set 1 differ to results sets 2, 3, 4 and 5 but do converge.

Figures 5.19 and 5.20 show true positions, tracking results and tracking errors for a second dataset generated with samples for change in heading and pitch drawn from normal distributions with variances $\text{var}\{\gamma\} = \text{var}\{\beta\} = 1.2217 \times 10^{-2}$.

Table 5.7 shows a test variance $\text{var}\{\gamma\} = \text{var}\{\beta\} = 1.7453 \times 10^{-9}$ which provides the most accurate tracking. Examination of figure 5.20 shows a general tracking divergence at test variance $\text{var}\{\gamma\} = \text{var}\{\beta\} = 1.7453 \times 10^{-9}$ across bearing, elevation, range and time-delay. Error in the time-delay estimate increases exponentially, whereas it is relatively steady for other test variances. Taking error distributions over time into account, the most robust tracking is achieved with test variances $\text{var}\{\gamma\} = \text{var}\{\beta\} = 1.7453 \times 10^{-4}$.

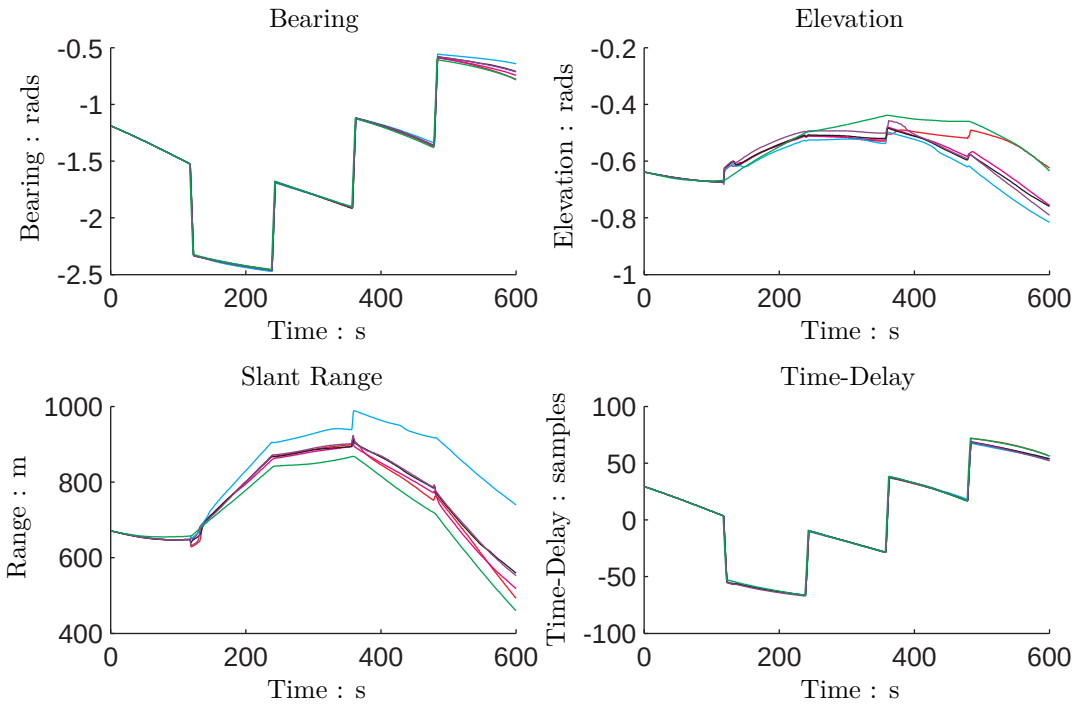

(a) Relative position of target and tracking results relative to boat in spherical form

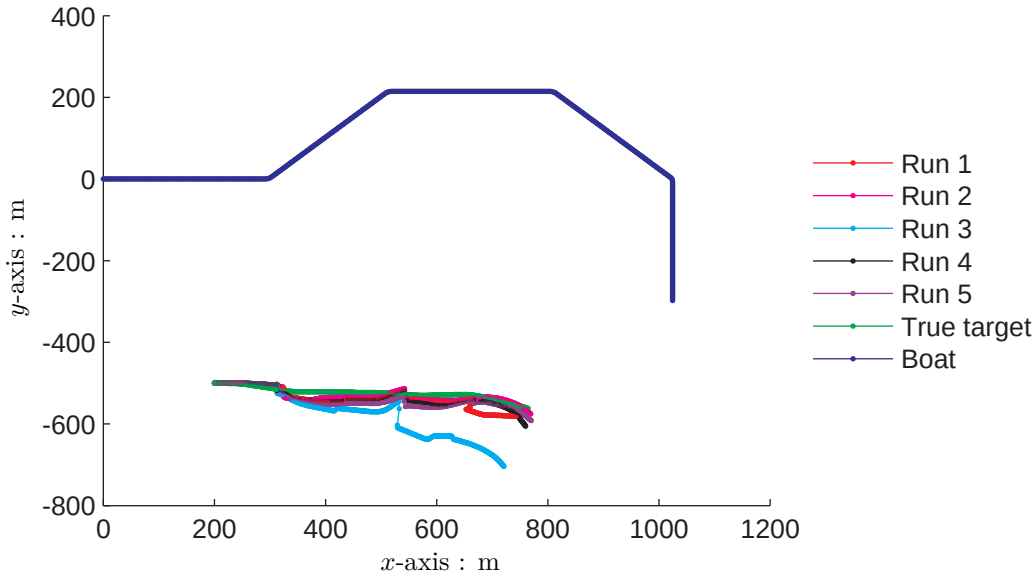

(b) Plan view reconstruction of boat path, target path and tracking results in Cartesian form

Figure 5.18: Multiple results sets for the dataset shown in figure 5.13 at heading and pitch test variances of $\text{var}\{\gamma\} = 1.7453 \times 10^{-4}$ and $\text{var}\{\beta\} = 1.7453 \times 10^{-4}$.

Parameter	System Variance	MSE Statistics		
		min	mean	max
Bearing (rads)	1.7453×10^{-9}	9.5587×10^{-4}	9.5846×10^{-4}	9.636×10^{-4}
	1.7453×10^{-4}	8.1871×10^{-4}	1.3206×10^{-3}	2.4751×10^{-3}
	1.0472×10^{-3}	1.6535×10^{-3}	2.1924×10^{-3}	2.7431×10^{-3}
	3.4907×10^{-3}	1.4446×10^{-3}	1.6798×10^{-3}	1.9764×10^{-3}
	1.2217×10^{-2}	1.9329×10^{-3}	2.376×10^{-3}	3.2511×10^{-3}
Elevation (rads)	1.7453×10^{-9}	9.9219×10^{-3}	9.9382×10^{-3}	9.963×10^{-3}
	1.7453×10^{-4}	1.2465×10^{-3}	5.5836×10^{-3}	1.0024×10^{-2}
	1.0472×10^{-3}	5.5891×10^{-4}	9.8709×10^{-4}	1.4132×10^{-3}
	3.4907×10^{-3}	7.5205×10^{-4}	1.0815×10^{-3}	1.5185×10^{-3}
	1.2217×10^{-2}	1.3313×10^{-3}	2.9017×10^{-3}	5.6577×10^{-3}
Range (m)	1.7453×10^{-9}	289.61	293.4	295.74
	1.7453×10^{-4}	952.76	4938.7	18689
	1.0472×10^{-3}	3204.9	3791.4	4138.5
	3.4907×10^{-3}	3479.6	4242.8	5035.4
	1.2217×10^{-2}	4229.4	5381.9	7584.9
Time Delay (samples)	1.7453×10^{-9}	26.952	27.041	27.148
	1.7453×10^{-4}	4.6931	7.9004	9.5438
	1.0472×10^{-3}	9.2002	12.958	16.001
	3.4907×10^{-3}	6.7214	9.1831	11.759
	1.2217×10^{-2}	9.6174	13.26	17.437

Table 5.6: Minimum, mean and maximum MSE values for five tracking results sets at each test variance for the dataset shown in figure 5.13

Parameter	System Variance	MSE Statistics		
		min	mean	max
Bearing (rads)	1.7453×10^{-9}	8.5369×10^{-4}	8.5425×10^{-4}	8.5469×10^{-4}
	1.7453×10^{-4}	8.0118×10^{-4}	1.0036×10^{-3}	1.2981×10^{-3}
	1.0472×10^{-3}	9.1279×10^{-4}	1.9144×10^{-3}	2.7164×10^{-3}
	3.4907×10^{-3}	1.0303×10^{-3}	1.9566×10^{-3}	2.6323×10^{-3}
	1.2217×10^{-2}	3.0749×10^{-3}	3.6012×10^{-3}	4.0468×10^{-3}
Elevation (rads)	1.7453×10^{-9}	2.1816×10^{-4}	2.1907×10^{-4}	2.2015×10^{-4}
	1.7453×10^{-4}	2.7369×10^{-4}	7.7594×10^{-4}	1.3153×10^{-3}
	1.0472×10^{-3}	2.4112×10^{-4}	1.1317×10^{-3}	1.4725×10^{-3}
	3.4907×10^{-3}	2.2957×10^{-4}	1.9929×10^{-3}	3.4326×10^{-3}
	1.2217×10^{-2}	2.7271×10^{-3}	3.5134×10^{-3}	4.3006×10^{-3}
Range (m)	1.7453×10^{-9}	150.57	151.49	152.3
	1.7453×10^{-4}	508.58	1951	3688.8
	1.0472×10^{-3}	1228.8	2195.1	5067.3
	3.4907×10^{-3}	2129.4	5787.2	10029
	1.2217×10^{-2}	1836.6	5171.5	11765
Time Delay (samples)	1.7453×10^{-9}	4.99272	4.9996	5.0062
	1.7453×10^{-4}	4.3213	5.6361	7.1933
	1.0472×10^{-3}	4.9786	8.2971	11.014
	3.4907×10^{-3}	4.4645	6.9163	8.6988
	1.2217×10^{-2}	7.4165	8.4332	9.7963

Table 5.7: Minimum, mean and maximum MSE values for five tracking results sets at each test variance for the dataset shown in figure 5.19. The legend is given in figure 5.19

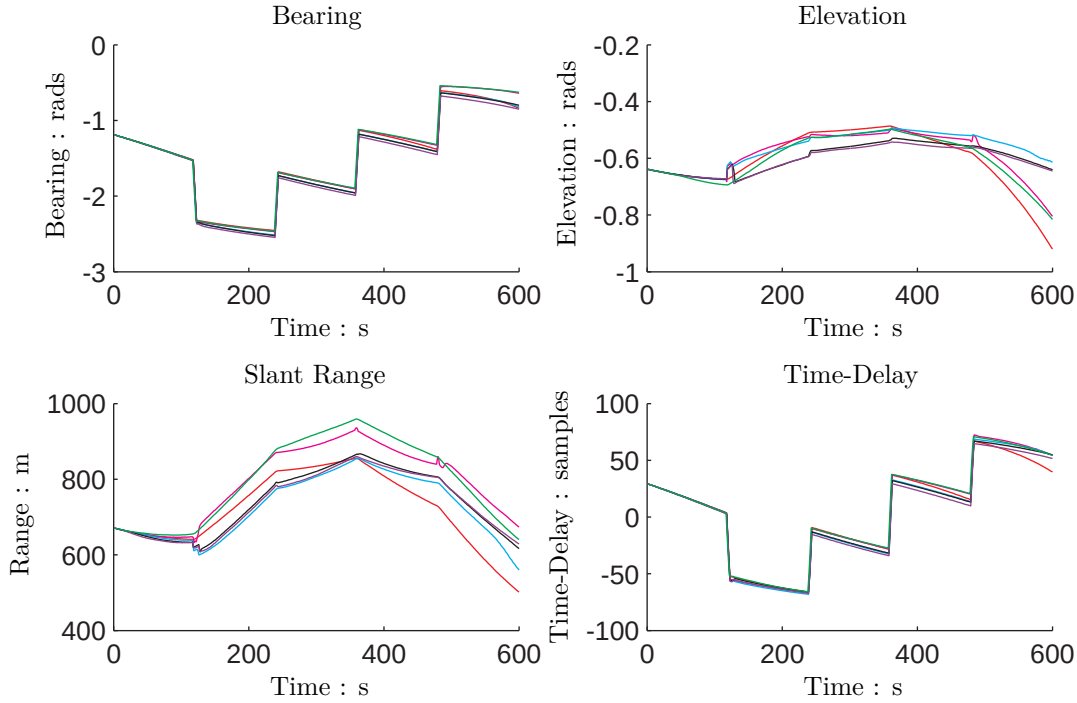

(a) Relative position of target and tracking results relative to boat in spherical form

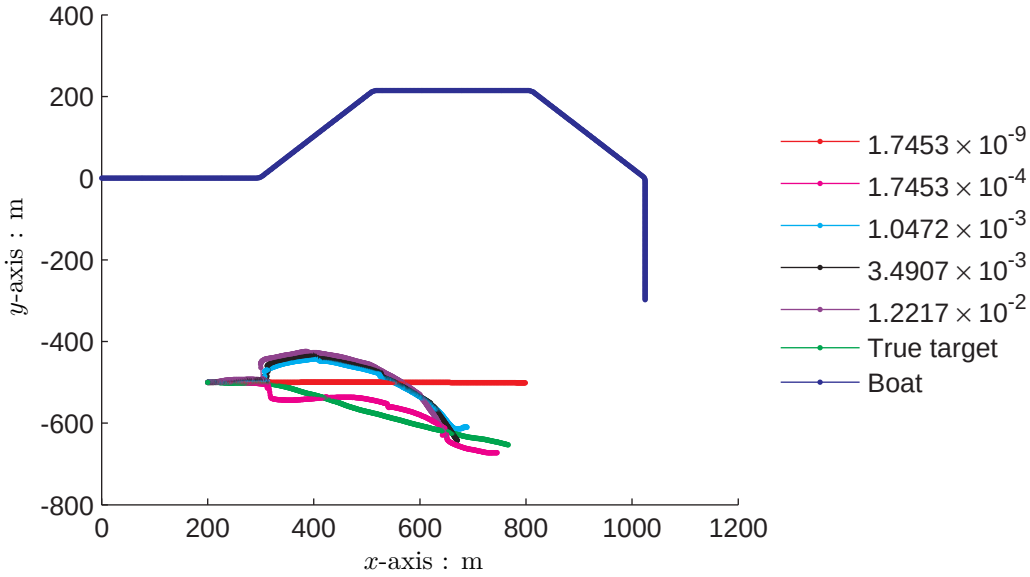

(b) Plan view reconstruction of boat path, target path and tracking results in Cartesian form

Figure 5.19: True target positions and tracking results for a second dataset where change in heading and pitch samples are drawn from normal distributions with variances $\text{var}\{\gamma\} = 1.2217 \times 10^{-2}$ and $\text{var}\{\beta\} = 1.2217 \times 10^{-2}$. Relative true target positions and tracking results are shown in figure (a) and plan view reconstructions of true target positions, boat positions and tracking results are shown in figure (b).

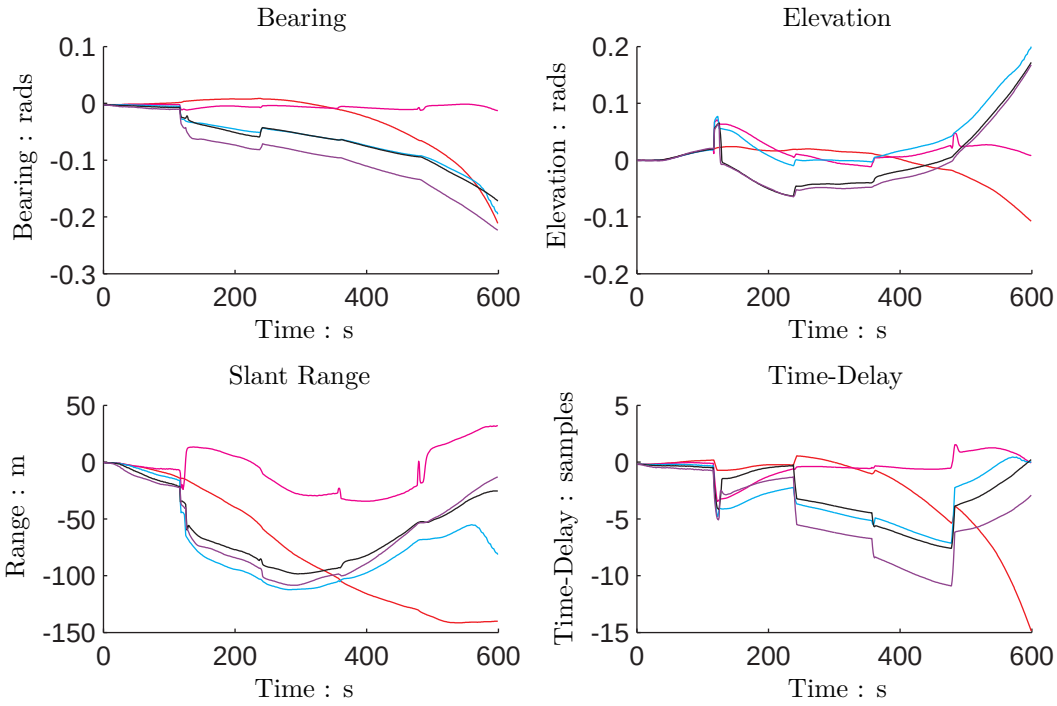

Figure 5.20: Relative position tracking errors for the results in figure 5.19 at each heading test variance. The legend is given in figure 5.19.

5.4.1 Summary

This section has presented tracking results for simulated datasets where the target is manoeuvring in both the horizontal and vertical planes. Bearing and range tracking results for the dataset with a data variance $\text{var}\{\gamma\} = \text{var}\{\beta\} = 1.0472 \times 10^{-4}$ showed optimal tracking performance with a test variance of 1.7453×10^{-9}, essentially providing a straight line assumption. For both datasets with a data variance of 1.2217×10^{-2} the most robust tracking results are provided by a test variance $\text{var}\{\gamma\} = \text{var}\{\beta\} = 1.7453 \times 10^{-4}$. The multiple results sets in figure 5.18 for the dataset shown in figure 5.13 show consistent tracking performance where results fit the measurements in all cases. The same conclusions were found in section 5.3. Section 5.5 further extends the tracking problem to include varying target speed.

5.5 Manoeuvring Varying Speed Target Tracking

Section 5.4 presented tracking results for a simulated target manoeuvring in both the horizontal and vertical planes. This section extends the tracking problem to tracking a manoeuvring target that is also changing speed.

Figure 5.21 shows the positions of the simulated target dataset generated by drawing samples for change in heading and pitch from normal distributions with variances $\text{var}\{\gamma\} = \text{var}\{\beta\} = 1.2217 \times 10^{-2}$ and samples for change in speed drawn from a normal distribution with variance $\text{var}\{v\} = 10^{-6}$ ms^{-1}. Speed samples were subject to the rejection function described in

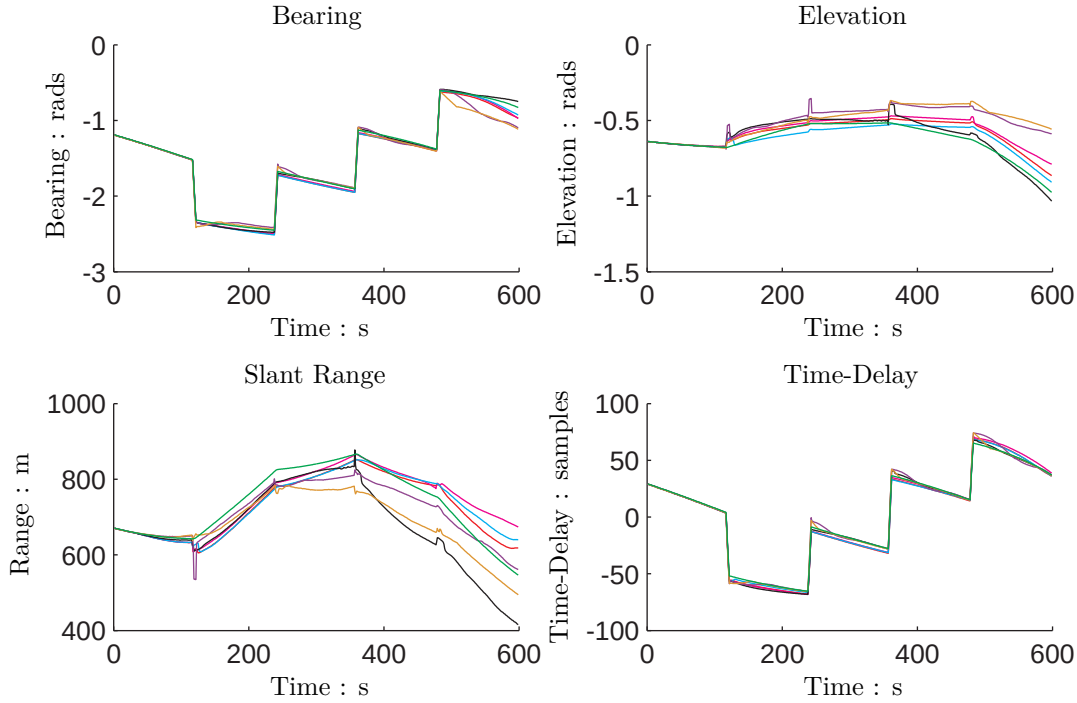

(a) Relative position of target and tracking results relative to boat in spherical form

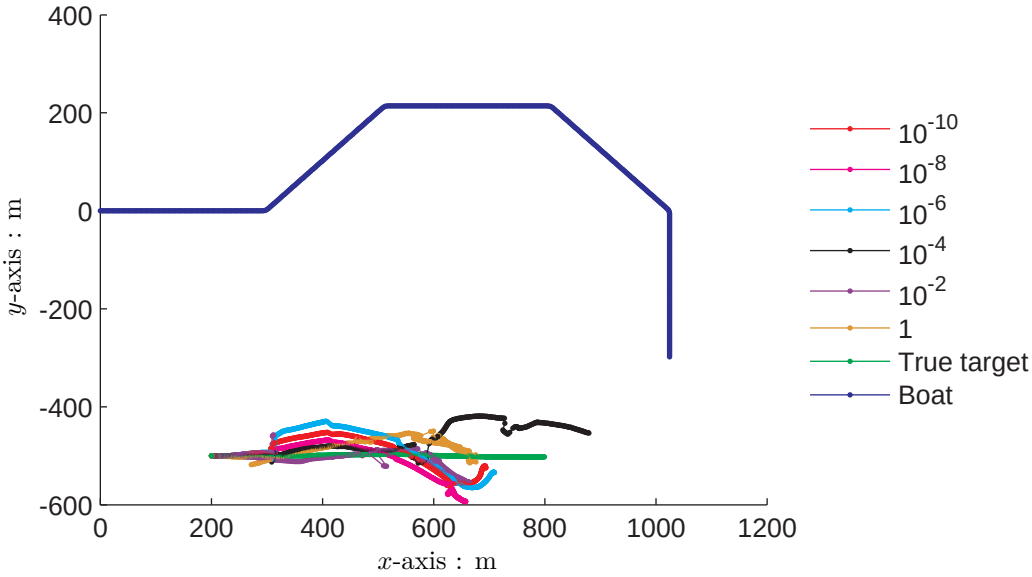

(b) Plan view reconstruction of boat path, target path and tracking results in Cartesian form

Figure 5.21: True target positions and tracking results for a dataset where samples for changes in heading, pitch and speed are drawn from a normal distribution with variances $\text{var}\{\gamma\} = 1.0472 \times 10^{-3}$, $\text{var}\{\beta\} = 1.0472 \times 10^{-3}$ and $\text{var}\{v\} = 10^{-6}$. Relative true target positions and tracking results are shown in (a) plan view reconstructions and true target positions, boat positions and tracking results are shown in figure (b).

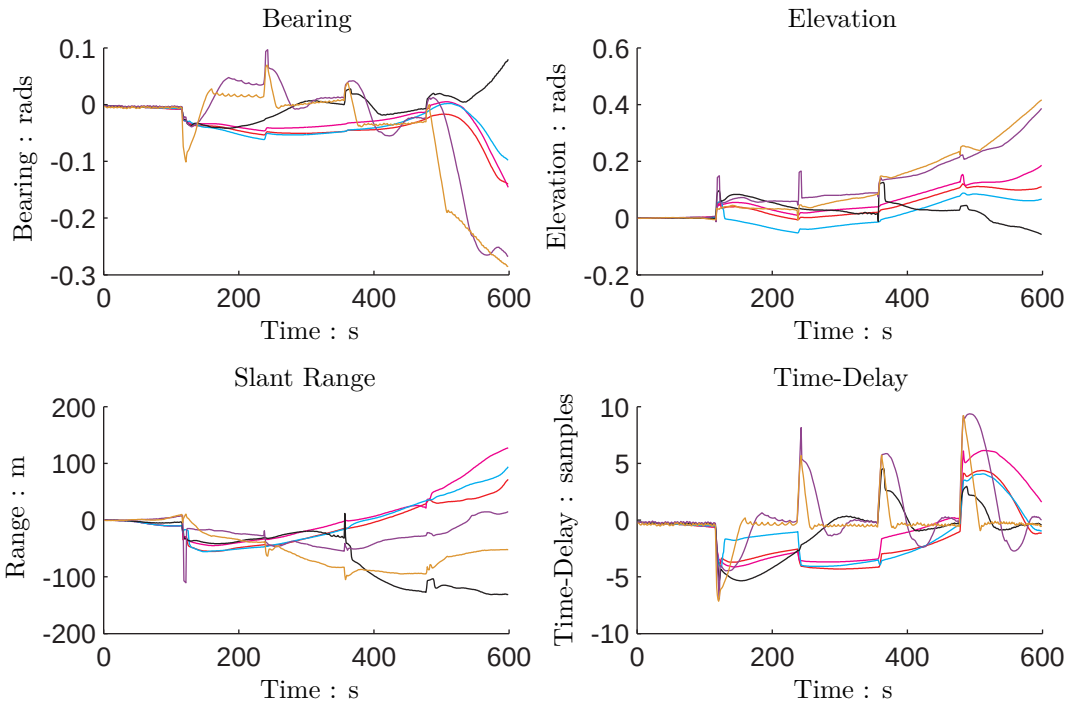

Figure 5.22: Relative position tracking errors for the results in figure 5.21 at each heading and pitch test variance. The legend is given in figure 5.21.

sections 4.4 and 4.5 which limits speeds within the system function.

Figure 5.21 also shows tracking results for the dataset over different speed test variances $\text{var}\{v\}$ between 10^{-10} and 1 and a heading and pitch test variance of $\text{var}\{\gamma\} = \text{var}\{\beta\} = 1.0472 \times 10^{-3}$. Corresponding error plots are shown in figure 5.22. Time-delay estimation results for all test variances follow the trend of the measurements and demonstrate accurate bearing estimation performance until the final manoeuvre where divergence occurs. Elevation results are mixed, the elevation tracking results in figure 5.21(a) show that the best elevation angle tracking performance is obtained with a speed test variance of 10^{-4} whilst least accurate tracking performance results from speed test variances of 10^{-2} and 1 with the other test speed variances providing elevation tracking results in between. Range tracking results are also mixed, up until the manoeuvre at 360 s all range estimates are short of the true range, beyond this time lower test speed variances result in range over-estimation while higher speed test variances result in range under-estimation. Range estimation errors are between ±200 m which, with a true range of 600 m, is an error of up to 33%.

Figure 5.23 shows results over five tracking realisations with the same test parameters where $\text{var}\{\gamma\} = \text{var}\{\beta\} = 1.0472 \times 10^{-3}$ and $\text{var}\{v\} = 10^{-6}$ at test variances $\text{var}\{\gamma\} = \text{var}\{\beta\} = 1.0472 \times 10^{-3}$ and $\text{var}\{v\} = 10^{-8}$. Figure 5.23 shows that four of the five results sets are consistent across the estimation parameters. Range and, to a lesser extent, elevation results for run 4 differ to the other runs. Beyond 120 s run 4 diverges and over-estimates range with a greater error magnitude than the other runs while elevation angle estimation is arguably more accurate after 360 s. These results show performance to be reasonably consistent, however inconsistencies do occur.

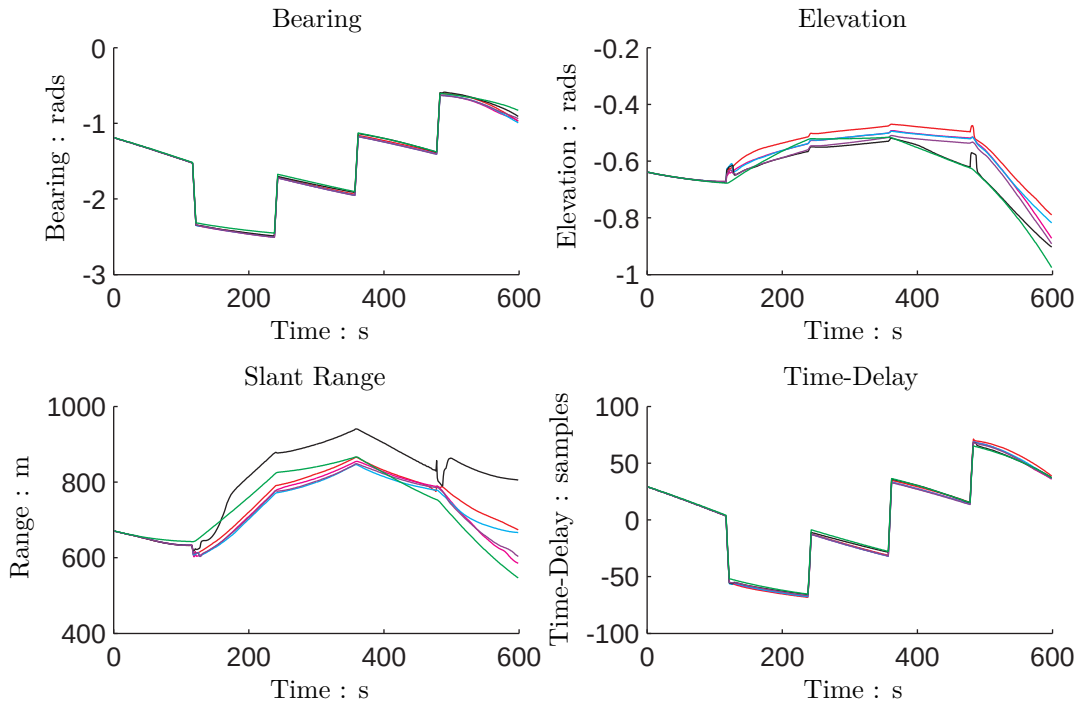

(a) Relative position of target and tracking results relative to boat in spherical form

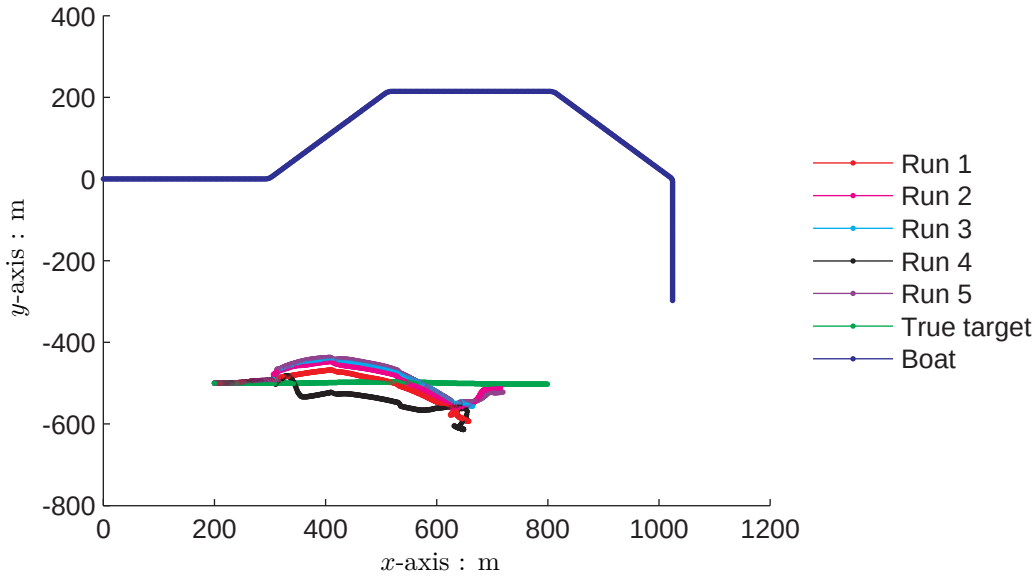

(b) Plan view reconstruction of boat path, target path and tracking results in Cartesian form

Figure 5.23: Multiple results sets for the dataset shown in figure 5.21 for test variances $\mathrm{var}\{\gamma\} = 1.0472 \times 10^{-3}$, $\mathrm{var}\{\beta\} = 1.0472 \times 10^{-3}$ and $\mathrm{var}\{\upsilon\} = 10^{-8}$.

Parameter	**System Variance**	**MSE Statistics**		
		min	mean	max
Bearing (rads)	10^{-10}	2.6428×10^{-3}	3.2226×10^{-3}	4.3823×10^{-3}
	10^{-8}	1.3344×10^{-3}	2.7675×10^{-3}	3.5156×10^{-3}
	10^{-6}	1.284×10^{-3}	2.4396×10^{-3}	3.4185×10^{-3}
	10^{-4}	1.2998×10^{-3}	2.1417×10^{-3}	3.2547×10^{-3}
	10^{-2}	1.2003×10^{-3}	4.198×10^{-3}	8.2985×10^{-3}
	1	2.0636×10^{-3}	6.3491×10^{-3}	9.964×10^{-3}
Elevation (rads)	10^{-10}	2.2838×10^{-3}	3.3021×10^{-3}	4.0799×10^{-3}
	10^{-8}	4.8143×10^{-4}	3.2081×10^{-3}	6.2462×10^{-3}
	10^{-6}	7.5348×10^{-4}	2.2937×10^{-3}	3.7932×10^{-3}
	10^{-4}	8.6084×10^{-4}	2.5813×10^{-3}	4.857×10^{-3}
	10^{-2}	5.5302×10^{-4}	1.1259×10^{-2}	2.3831×10^{-2}
	1	2.0527×10^{-3}	1.5447×10^{-2}	3.1146×10^{-2}
Range (m)	10^{-10}	1114	1718.4	2406.3
	10^{-8}	1117.2	3290.2	9824.8
	10^{-6}	928.71	2335.5	5885.7
	10^{-3}	3057.9	8707.6	22098
	10^{-2}	660.25	5264.6	12123
	1	1530.7	6007.1	11045
Time Delay (samples)	10^{-10}	10.825	12.83	14.735
	10^{-8}	5.1491	11.416	14.916
	10^{-6}	6.8238	10.21	12.272
	10^{-4}	6.7322	7.6761	8.8863
	10^{-2}	4.8841	8.2915	10.873
	1	3.2048	3.9231	5.018

Table 5.8: Minimum, mean and maximum MSE values for five tracking results sets at each test variance for the dataset shown in figure 5.21

The mean MSE values over five runs in table 5.8 for bearing estimation show an optimal speed test variance of 10^{-4}. For elevation angle estimation there is little difference in mean MSE over test variances 10^{-10} and 10^{-4}. The mean range estimation MSE generally increases with speed test variance while mean MSE for time-delay generally decreases as test variance increases. This suggests that for greater speed test variances the particles are able to occupy a greater volume of the state space and re-sample and adapt more quickly when manoeuvres occur. The adaptation is shown on the time-delay plot in figure 5.22, where the time-delay estimate error for $\text{var}\{\upsilon\} = 1$ spikes during manoeuvres but converges back to zero quicker than for lower variances. Although time-delay error quickly reduces after manoeuvres this is not true for bearing and elevation estimation which continue to include errors. This demonstrates the particles are able to diverge from the true target position yet still occupy a volume of the state space that fits the measurements.

Figure 5.24 shows the positions of a second manoeuvring varying speed dataset generated by drawing samples from normal distributions with variances $\text{var}\{\gamma\} = \text{var}\{\beta\} = 1.0472 \times 10^{-3}$ and $\text{var}\{\upsilon\} = 10^{-2}$. Figure 5.24 also shows tracking results for test speed variances between 10^{-10} and 1 and heading and pitch test variances of $\text{var}\{\gamma\} = \text{var}\{\beta\} = 1.0472 \times 10^{-3}$. Results show that if the test speed variance is not sufficiently high then the particle distribution can not achieve a speed high enough to effectively model the motion of the target.

For test speed variances of 10^{-10}, 10^{-8} and 10^{-6} the tracking results presented in figure 5.24 show that tracking fails after the manoeuvre at 200 s. This occurs because the particles are not sufficiently distributed across the state space and all particles receive a zero weighting. If all particles receive a zero weight then the normalisation step of algorithm 3.7 fails due to a divide by zero error. This could be overcome by increasing the measurement variance, however such an increase may result in degraded tracking performance because particles further from the measurement will receive higher weightings. Such a solution can be regarded as an artificial fix for a lack of spreading of the particles through the state space.

Tracking results using speed test variances of 10^{-4}, 10^{-2} and 1 track the target for the duration of the measurements. However, from figures 5.24 and 5.25 it is difficult to draw conclusions as to which test variance provides the most accurate tracking results overall.

Figure 5.26 shows five tracking results sets with test variances $\text{var}\{\gamma\} = \text{var}\{\beta\} = 1.0472 \times 10^{-3}$ and $\text{var}\{\upsilon\} = 10^{-4}$. Tracking results are inconsistent across the results sets. Bearing estimates remain accurate for the majority of all results sets. A boat manoeuvre occurs at 360 seconds, after which results set 4 diverges, mirrored by a divergence in the time-delay estimate. Elevation estimates follow the same trend but results set 5 diverges after the final manoeuvre. Range estimates are generally inconsistent with over 1000 m difference between results sets 4 and 5.

Figure 5.27 shows tracking results for multiple results sets run under the same conditions as the results shown in figure 5.26 but with 10 000 particles instead of 1000. An importance distribution approximated using 10 000 samples more accurately represents the true importance distribution than using 1000 samples. By utilising more samples, approximations of the

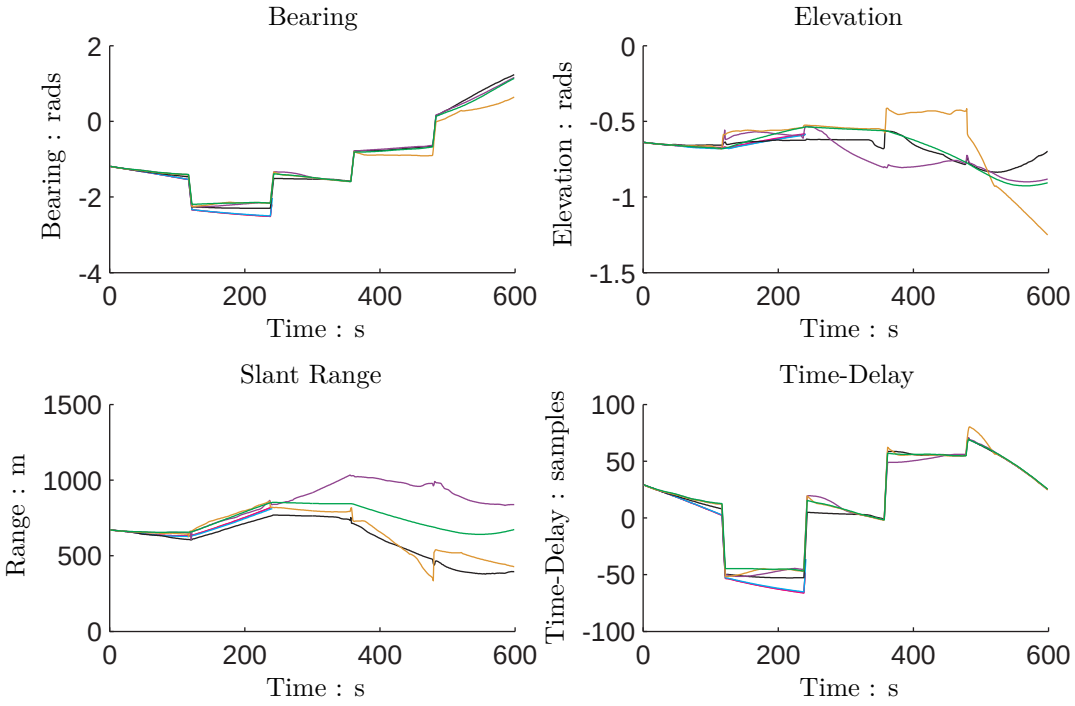

(a) Relative position of target and tracking results relative to boat in spherical form

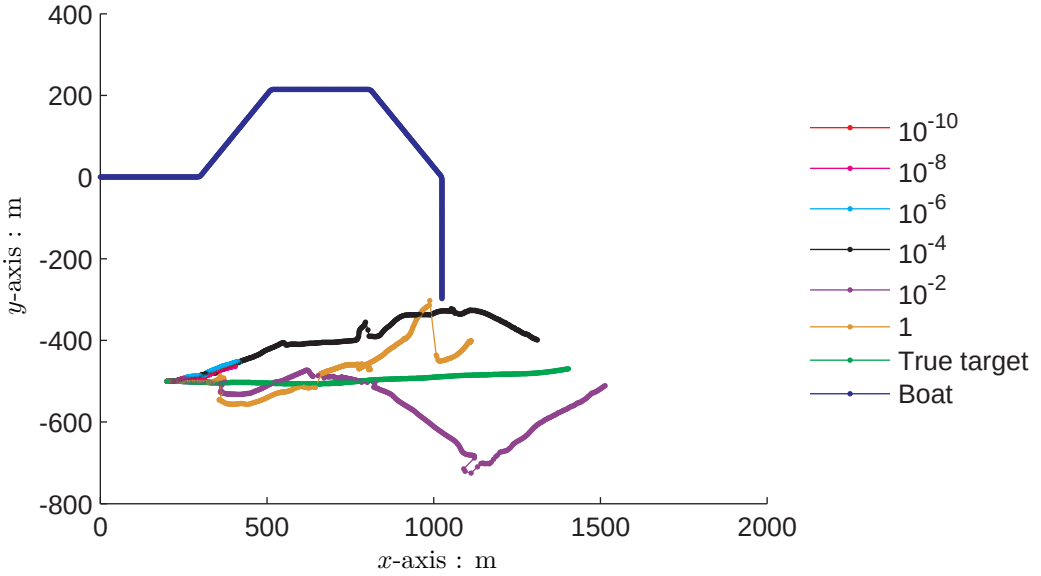

(b) Plan view reconstruction of boat path, target path and tracking results in Cartesian form

Figure 5.24: True target positions and tracking results in (a) relative spherical form and (b) Cartesian reconstructions for data parameters, $\text{var}\{\gamma\} = \text{var}\{\beta\} = 1.0472 \times 10^{-3}$ and $\text{var}\{\upsilon\} = 10^{-2}$

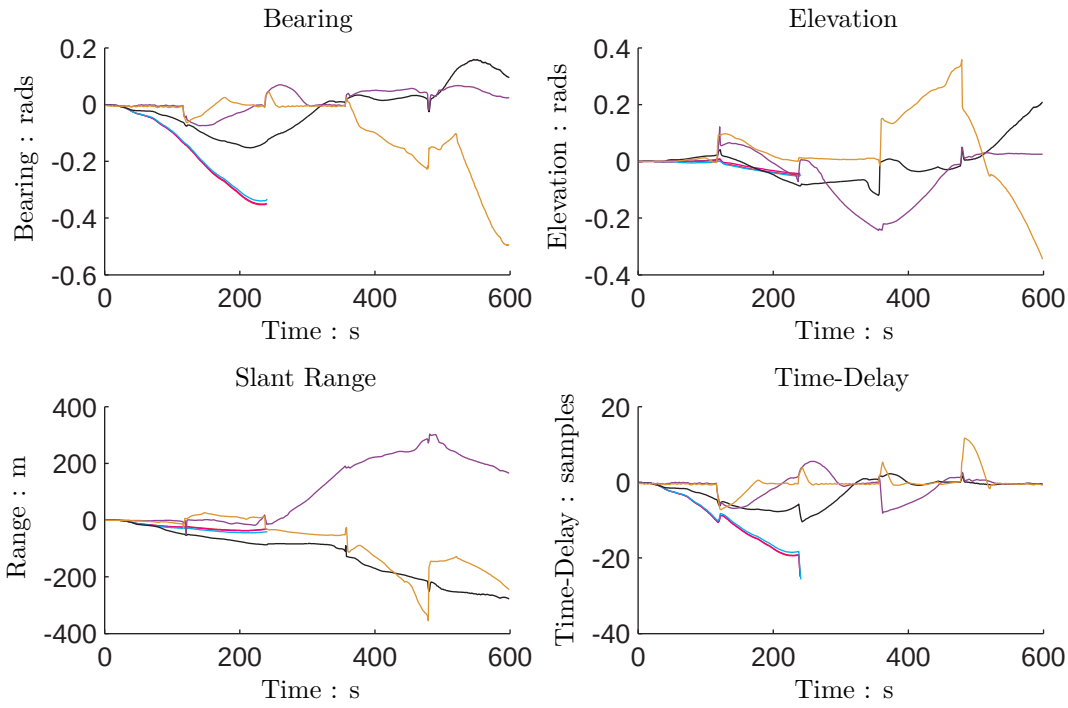

Figure 5.25: Relative position tracking errors for the results shown in figure 5.24 at each speed test variance. The legend is given in figure 5.24.

importance distribution between particle filter realisations with the same data and parameters is more consistent, therefore results are also expected to be more consistent. Results in figure 5.27 show more consistent tracking until the manoeuvre at 360 s. Beyond 360 s range estimates diverge with two results sets showing range over-estimates and three results sets showing consistent range under-estimates. After the manoeuvre at 480 s the three results sets under-estimating the range also diverge from each other, the bearing estimates diverge and the elevation estimates diverge. Compared to the results shown in figure 5.26, bearing, range and time-delay estimates are arguably more consistent and therefore show, when there are more degrees of freedom in the system function, it is necessary to increase the number of particles to maintain performance consistency. However, even with more particles consistency is still lost in comparison to when there are fewer degrees of freedom in the system function and when data variance is lower.

Table 5.9 shows MSE values for the dataset shown in figure 5.24 using 1000 particles. Like table 5.8, table 5.9 shows time-delay tracking improves as speed test variance increases, however bearing and elevation tracking accuracy decreases. It could be argued from the MSE values that range estimation improves as the test variance increases and the mean MSE for test variance 10^{-2} is relatively high compared to the other two test variances because of a large range error in one of the results sets.

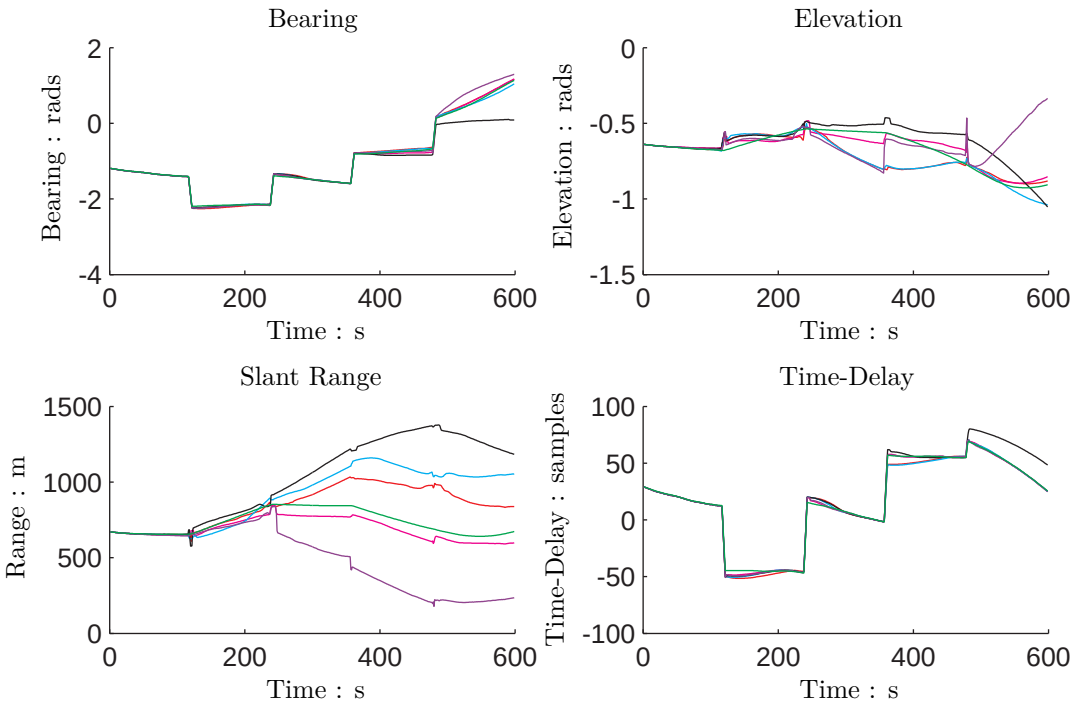

(a) Relative position of target and tracking results relative to boat in spherical form

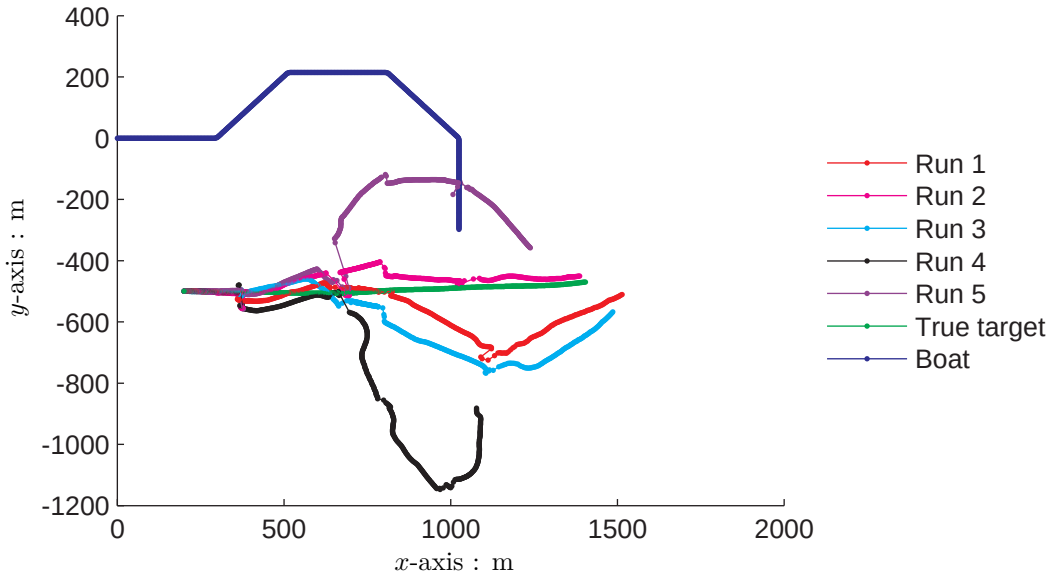

(b) Plan view reconstruction of boat path, target path and tracking results in Cartesian form

Figure 5.26: Multiple results sets for the dataset shown in figure 5.24 for test variances $\text{var}\{\gamma\} = 1.0472 \times 10^{-3}$, $\text{var}\{\beta\} = 1.0472 \times 10^{-3}$ and $\text{var}\{\upsilon\} = 10^{-4}$.

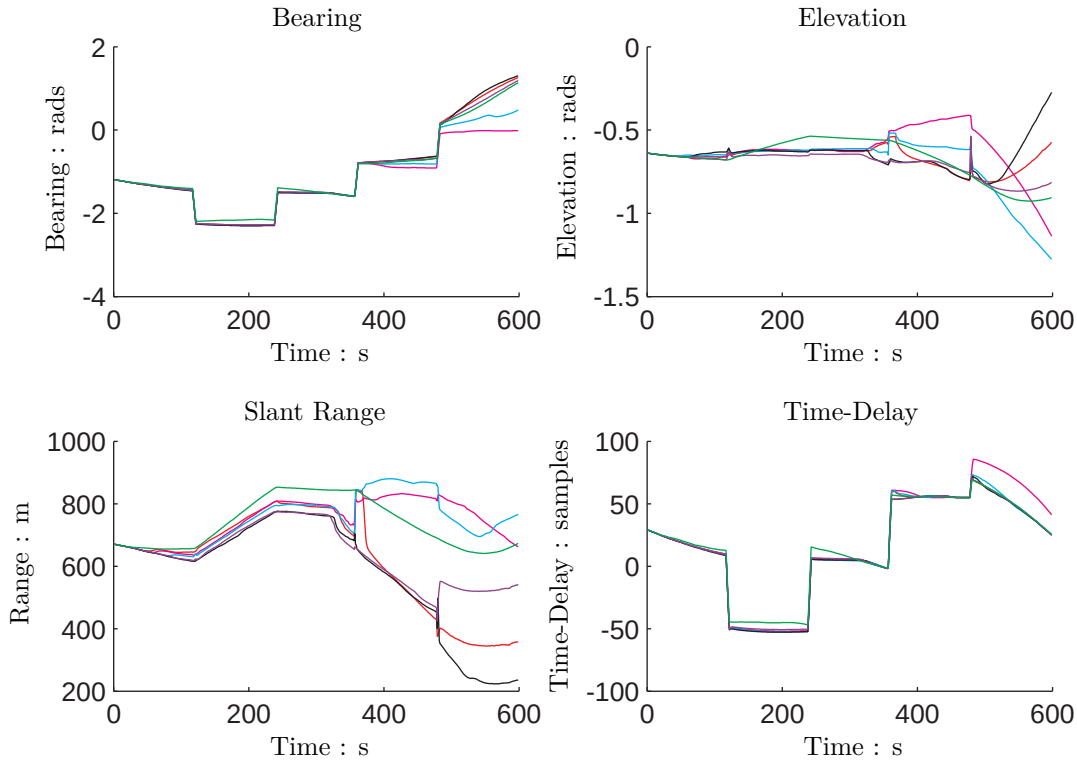

(a) Relative position of target and tracking results relative to boat in spherical form

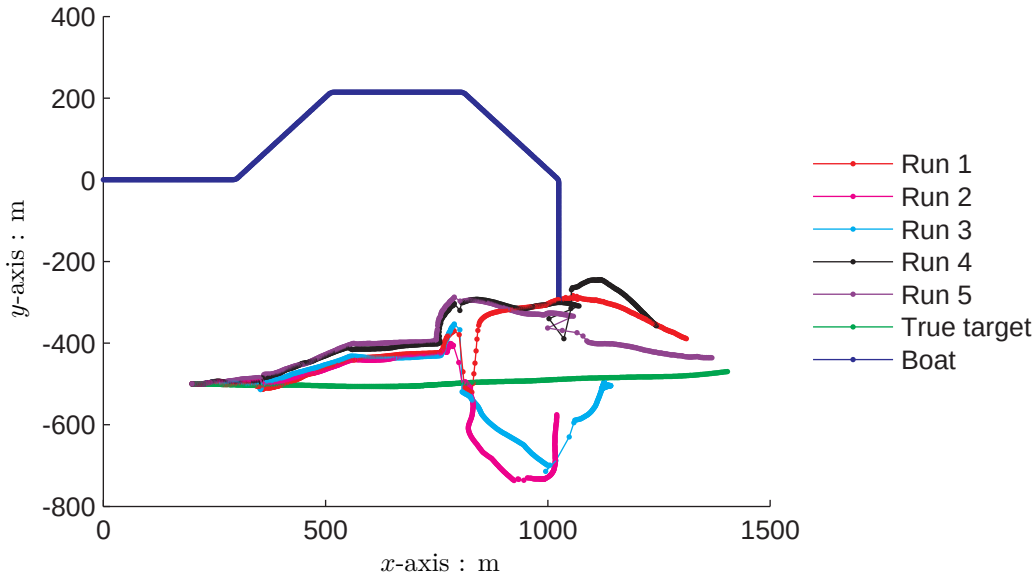

(b) Plan view reconstruction of boat path, target path and tracking results in Cartesian form

Figure 5.27: A repeat of the multiple results sets experiments with fixed test variances shown in figure 5.26 with 10 000 particles rather than 1000 so that the sampled importance distribution better approximates the true importance distribution. Results show more consistent performance until the manoeuvre at 360 seconds.

Parameter	System Variance	MSE Statistics		
		min	mean	max
Bearing (rads)	10^{-4}	7.6697×10^{-3}	1.8057×10^{-2}	4.9025×10^{-2}
	10^{-2}	1.6469×10^{-3}	1.9077×10^{-2}	7.5464×10^{-2}
	1	3.845×10^{-3}	4.0015×10^{-2}	1.3009×10^{-1}
Elevation (rads)	10^{-4}	3.0414×10^{-3}	6.2977×10^{-3}	9.9621×10^{-3}
	10^{-2}	1.4529×10^{-3}	1.1555×10^{-2}	3.0201×10^{-2}
	1	2.548×10^{-3}	1.2036×10^{-2}	1.7166×10^{-2}
Range (m)	10^{-4}	2985.7	11970	23306
	10^{-2}	2650.3	66367	1.5085×10^{5}
	1	2438.5	10581	17032
Time Delay (samples)	10^{-4}	20.726	29.515	50.373
	10^{-2}	3.8214	21.16	72.816
	1	3.938	12.237	33.525

Table 5.9: Minimum, mean and maximum MSE values for five tracking results sets at each test variance for the dataset shown in figure 5.24

5.5.1 Summary

This chapter has presented results for tracking a simulated target which is manoeuvring horizontally and vertically and changing speed. Results show the variance $\text{var}\{\upsilon\}$ must be sufficiently high as to allow the particles to be able to effectively achieve the speeds of the true target. If $\text{var}\{\upsilon\}$ is too high bearing and elevation tracking accuracy will be reduced. The next section discusses tracking performance when the initial position of the target is unknown.

5.6 Manoeuvring Varying Velocity Target Tracking with Unknown Start Position

Sections 5.3 to 5.5 presented tracking results for manoeuvring simulated target datasets initialised at the correct location and with the target travelling in the correct direction. This section discusses tracking performance when the initial target location and direction of travel are unknown. Particles are initialised on an ambiguity hyperboloid derived from the initial time-delay measurement. Results will demonstrate the particle filter's capabilities to resolve the track from an unknown initial starting position.

Figure 5.28 shows tracking results for the dataset tracked in figure 5.21 without initialising at the correct start location with test variances $\text{var}\{\gamma\} = \text{var}\{\beta\} = 1.0472 \times 10^{-3}$ and $\text{var}\{\upsilon\}$ between 10^{-10} and 1. Tracking results shown in figure 5.28 demonstrate how the particles lie on the ambiguity surface and adapt to a solution. Initially MMSE bearing estimates lie on a relative mean bearing of 0 rads, as shown by the bearing estimates in 5.28(a) and the Cartesian track reconstructions shown in figure 5.28(b). Although each particle is in a position that satisfies the measurement it does not necessarily follow that the MMSE estimate derived from these particles will conform to the measured time-delay.

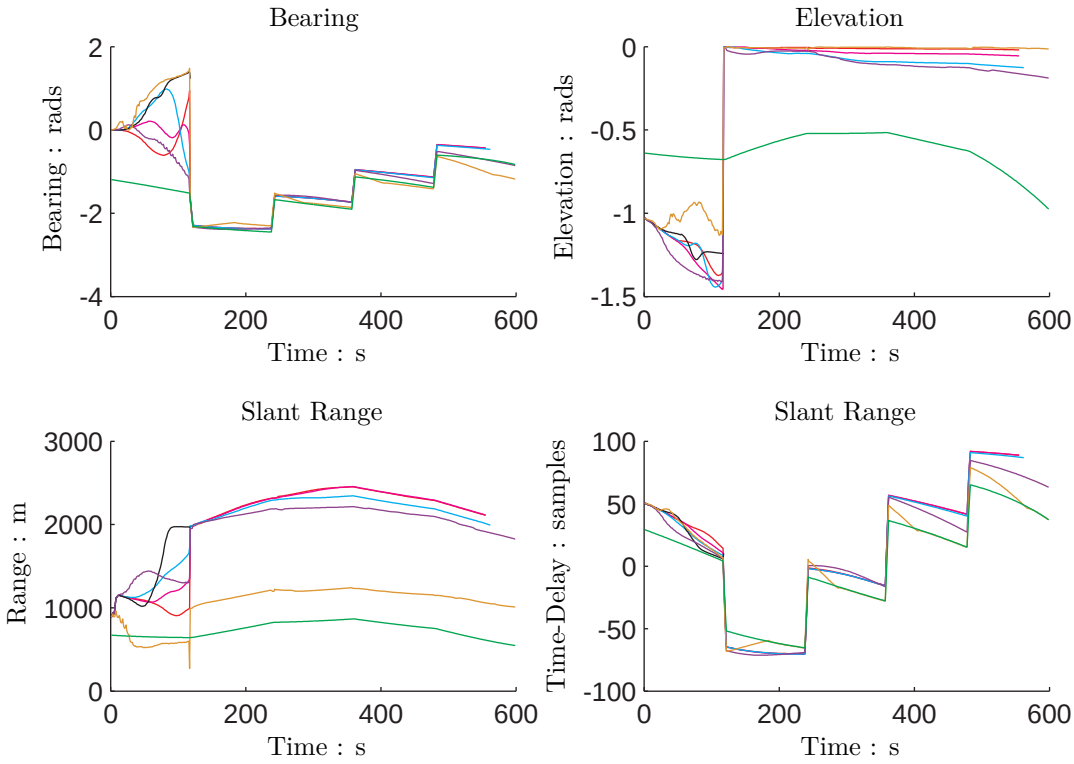

(a) Relative position of target and tracking results relative to boat in spherical form

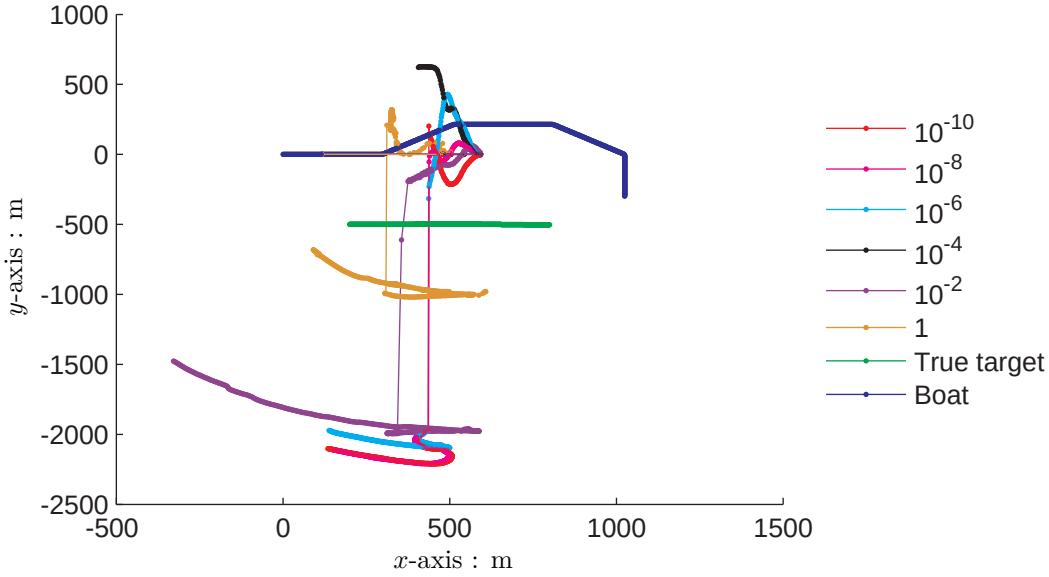

(b) Plan view reconstruction of boat path, target path and tracking results in Cartesian form

Figure 5.28: True target positions and tracking results in (a) relative spherical form and (b) Cartesian reconstructions for data parameters, $\text{var}\{\gamma\} = \text{var}\{\beta\} = 1.0472 \times 10^{-3}$ and $\text{var}\{v\} = 10^{-6}$

As system noise samples are drawn, particles receive varying weightings with the less likely particles tending to be removed by the re-sampling process. Over time the particles converge to a solution whereby the MMSE estimate of the bearing and elevation is expected to match the time-delay measurements. The bearings tracking results in figure 5.28(a) show the tracking filter adapting to a bearing solution, from ahead to one side. For test speed variances $\mathrm{var}\{v\} = 10^{-10}$ and $\mathrm{var}\{v\} = 10^{-4}$ the particle filter adapts to a solution on the incorrect side of the boat which causes tracking to fail at the first manoeuvre. The tracks that converge to the incorrect side fail because, after the manoeuvre, none of the particles are in a position that sufficiently matches the time-delay measurements to receive a non-zero weighting. Furthermore the tracks for test variances 10^{-8} and 10^{-6}, which have converged to the correct side, also fail around 550 s. From 5.28 it can be seen that they both diverge from the true bearing and there is significant error in the time-delay estimation. This is likely caused by the speed test variance being insufficient for the particles to achieve a speed allowing them to maintain a solution that sufficiently fits the measurements. For test speed variances $\mathrm{var}\{v\} = 10^{-8}$, $\mathrm{var}\{v\} = 10^{-6}$, $\mathrm{var}\{v\} = 10^{-2}$ and $\mathrm{var}\{v\} = 1$ bearings are successfully tracked, however tracking for test variances $\mathrm{var}\{v\} = 10^{-8}$ and $\mathrm{var}\{v\} = 10^{-6}$ does eventually fail. All test variances default to an elevation angle of 0 or near 0 rads which results in time-delay estimation error, however the estimated time-delays do follow the measurement trend. Range is also significantly over-estimated, by up to twice the true range.

Results in figure 5.28 demonstrate most accurate tracking results were achieved using a speed test variance of $\mathrm{var}\{v\} = 1$. Figure 5.28 demonstrates a test variance of 1 completed tracking for the complete duration of the data, converged to the correct side and provided the best range estimates. Five results sets are shown in figure 5.29 that demonstrate consistent performance. Although all five results sets initially converge to the incorrect side of the boat, with a test variance of 1 enough diversity is maintained in the filter that it is able to adapt to the correct side once the manoeuvre has occurred. In all cases range is significantly over-estimated and elevation angle estimates default to near 0 for all results sets.

5.6.1 Summary

This section has demonstrated that tracking a manoeuvring varying speed target without initialising at the correct starting location produces unreliable tracking results. In practice this limits the usefulness of the developed tracking method when attempting to track from an initial acoustic detection without a visual sighting and position fix of the animal.

5.7 Conclusions

This chapter has presented tracking results for simulated datasets using the proposed tracking algorithm, system function and noise distribution. The tracking problem complexity has been increased throughout this chapter from a non-manoeuvring constant speed target to a manoeuvring varying speed target with unknown starting position. Results have been presented

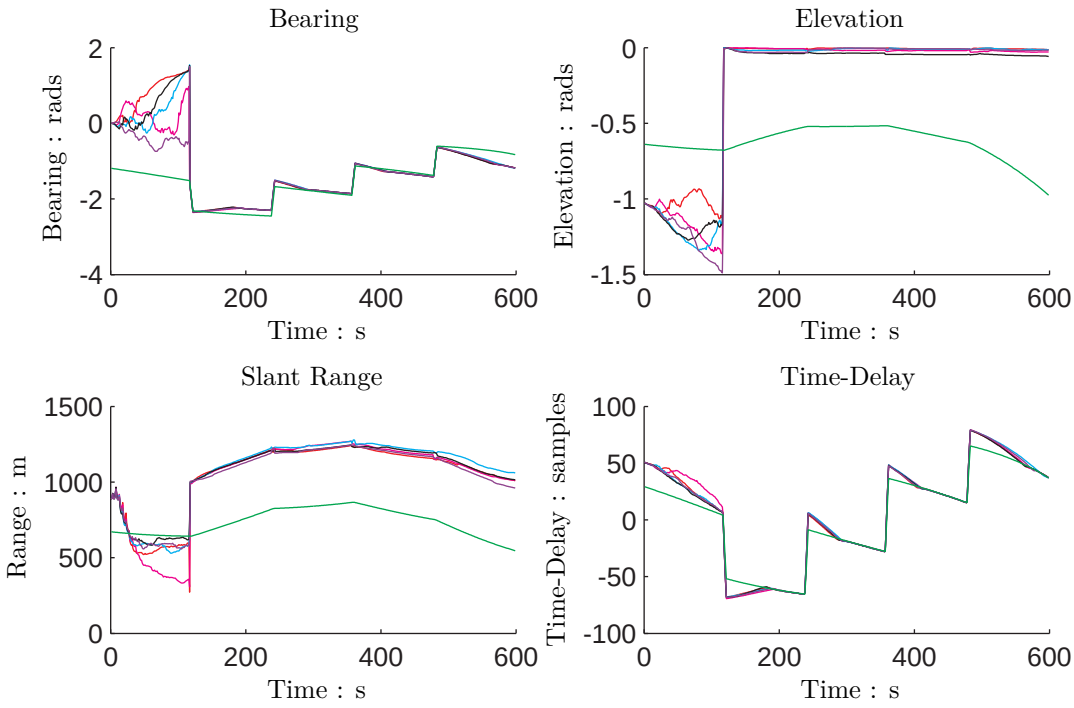

(a) Relative position of target and tracking results relative to boat in spherical form

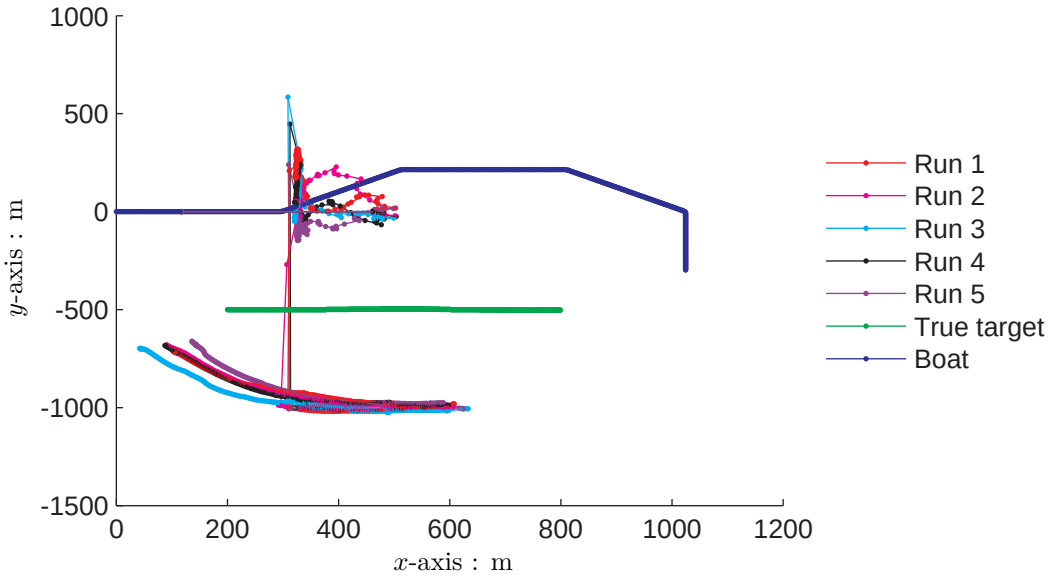

(b) Plan view reconstruction of boat path, target path and tracking results in Cartesian form

Figure 5.29: Multiple results sets for the dataset shown in figure 5.28 with test variances $\text{var}\{\gamma\} = 1.0472 \times 10^{-3}$, $\text{var}\{\beta\} = 1.0472 \times 10^{-3}$ and $\text{var}\{\upsilon\} = 10^{-8}$.

in relative spherical and Cartesian form and as MSE values. This section summarises the results presented in sections 5.2, 5.3, 5.4, 5.5 and 5.6 and discusses the conclusions from these experiments that can be applied to sperm whale tracking in chapter 7.

5.7.1 Results Summary

Section 5.2 presented a dataset for a constant speed non-manoeuvring target initialised at a known location. In this case the target travels in a straight line without any change in speed, therefore the motion model describes the target motion completely. As expected the lowest test heading variance $\text{var}\{\gamma\} = 1.7453 \times 10^{-9}$, provides tracking results with the lowest error. Time-delay estimation error generally increases with test heading variance (the exception being the second highest test variance, 3.4907×10^{-3}). The equal minimum, mean and maximum MSE values for each test variance demonstrate consistent estimator performance across results sets.

Tracking results for a target manoeuvring in the horizontal plane and travelling at a constant speed and at a known starting position are presented in section 5.3, representing the first stage of developing the complexity of the tracking problem. Results for two datasets were presented. One dataset was generated using Monte-Carlo simulations whereby samples for changes in heading were drawn from a normal distribution with variance $\text{var}\{\gamma\} = 1.0472 \times 10^{-3}$ and the other from a normal distribution with variance $\text{var}\{\gamma\} = 1.2217 \times 10^{-2}$. For both datasets the minimum, mean and maximum time-delay MSE values over all five results sets for bearing, elevation, range and time-delay are achieved with test variance $\text{var}\{\gamma\} = 1.7453 \times 10^{-4}$. Consistent MSEs for bearing, elevation, range and time-delay were achieved for all test variances across all results sets for the dataset where $\text{var}\{\gamma\} = 1.0472 \times 10^{-3}$. For the dataset with test variance $\text{var}\{\gamma\} = 1.2217 \times 10^{-2}$ the minimum, mean and maximum MSE values are different, therefore demonstrating inconsistent performance. MSE values for a second dataset where $\text{var}\{\gamma\} = 1.2217 \times 10^{-2}$ shows that performance is not consistent across datasets generated from the same distributions, therefore tracking performance is also dependent on relative target and boat motion. Results also demonstrate that if the target is not travelling in a straight line then, unsurprisingly, a straight line motion model does not yield good tracking results.

Section 5.4 presented tracking results for a target manoeuvring with changes in heading and pitch with known starting location. One dataset was presented where samples for changes in heading and pitch were drawn from normal distributions with variances $\text{var}\{\gamma\} = 1.0472 \times 10^{-3}$ and $\text{var}\{\beta\} = 1.0472 \times 10^{-3}$ and two datasets where samples were drawn from distributions with variances $\text{var}\{\gamma\} = 1.2217 \times 10^{-2}$ and $\text{var}\{\beta\} = 1.2217 \times 10^{-2}$. Samples for changes in heading and changes in pitch were drawn independently.

MSE scores show that minimal tracking errors are achieved for test variances $\text{var}\{\gamma\} = 1.7453 \times 10^{-9}$ and $\text{var}\{\beta\} = 1.7453 \times 10^{-9}$. These scores are misleading because they fail to show the distribution of errors over the duration of the tracking process. Examination of

results and error plots shows that the time-delay estimate, and other estimated parameters, are correct when estimation starts but diverge at an increasing rate. Section 5.1 specifies continual and accurate time-delay estimation as a priority in results evaluation, therefore the test variances that give the lowest MSE scores are not necessarily the optimal choice.

Section 5.5 extends the tracking problem to targets travelling at varying speeds. Two datasets were presented with samples for change in heading and pitch drawn from normal distributions with variances $\text{var}\{\gamma\} = 1.0472 \times 10^{-3}$ and $\text{var}\{\beta\} = 1.0472 \times 10^{-3}$ with samples for change in speed drawn from distributions with variances $\text{var}\{\upsilon\} = 10^{-6}$ and 10^{-2} respectively. The motion model, for both dataset generation and tracking, included the speed rejection function described in section 4.4. Test variances $\text{var}\{\gamma\} = 1.0472 \times 10^{-4}$ and $\text{var}\{\beta\} = 1.0472 \times 10^{-4}$ were fixed while test variances for $\text{var}\{\upsilon\}$ between 10^{-10} and 1 were trialled.

Results showed that higher test speed variances provided the most accurate time-delay estimation whilst tracking of bearing, elevation and range did not demonstrate that any particular test variance performed better than any other. For the dataset with change in speed samples drawn from a distribution with variance $\text{var}\{\upsilon\} = 10^{-2}$, the test variances less than 10^{-4} failed to track for the entire duration of the data. The multiple results set for this dataset demonstrated consistent performance for bearing and time-delay with the exception of results set 4 and range estimation was generally inconsistent.

Section 5.6 utilised the datasets with speed samples drawn from a distribution with variance $\text{var}\{\upsilon\} = 10^{-6}$ from section 5.5 to test the capabilities of the estimator to track a target and resolve the left-right and elevation ambiguity when the starting location is unknown. The particles were initialised on the surface of the ambiguity hyperboloid. Results demonstrated an inability to track elevation angle. Bearing estimates generally diverged, in two cases tracking failed at the first manoeuvre because the estimator was unable to resolve the left-right ambiguity. Range estimation was generally poor, the best range estimates were achieved with a test speed variance of 1. Results demonstrate a sufficient speed variance is required to maintain enough diversity in the filter to prevent range from being greatly over-estimated and delay left-right ambiguity resolution until a boat manoeuvre has occurred.

5.7.2 Experimentally Derived Conclusions

As the tracking problem becomes more complex and the order of the state space increases, accuracy and consistency with which the target can be tracked reduces. Most accurate tracking is also not achieved when the system test variance is the same as that with which the data were created. In the case of a manoeuvring target, relatively low test variances for heading and pitch resulted in the most accurate, and often consistent, tracking performance. When target speed also varied a relatively high test speed variance provided the most accurate and consistent tracking performance. Results suggest that experimentation is required to establish appropriate heading, pitch and speed test variances and that the estimator should be initialised with a sighting location. Testing with real data will be presented in chapter 7.

Chapter 6

Tracking Multiple Animals

The tracking filters presented in chapter 3 are in a form that only allows tracking of a single target. Sperm whales are frequently encountered in groups rather than as isolated individuals, therefore a practical tracking solution needs to be able to track multiple animals simultaneously. Figure 6.1 shows click trains received with different time-delays across the array aperture over a period of 25 minutes. Also present among the click trains are false detections, due to other impulsive sound events in the water, referred to as 'clutter'.

The capability to track multiple animals requires being able to correctly identify the source animal for each received click which can be either an animal already being tracked or an animal that has not been previously detected. The test dataset includes click detections from multiple animals, so to be useful for testing of a spatial tracking system a method to associate received clicks with the individual animal that produced it is necessary. Multiple target tracking (MTT) is a classical tracking problem and considerable effort has been spent on developing MTT methods [114].

6.1 Multiple Target Tracking problem

MTT is a common requirement of many tracking applications [59, 60, 114, 115]. When a measurement or set of measurements are received they need to be associated with a source target, a problem that becomes increasingly difficult when the number of targets is unknown and varying. Each received measurement can be either:

1. from an existing target;
2. a newly detected target;
3. or a false alarm.

A complete MTT system needs to be able to handle all three of these potentials and the termination of a target track [114, 115]. It is particularly important these criteria are met in passive acoustic tracking where very different target states may yield similar measurements

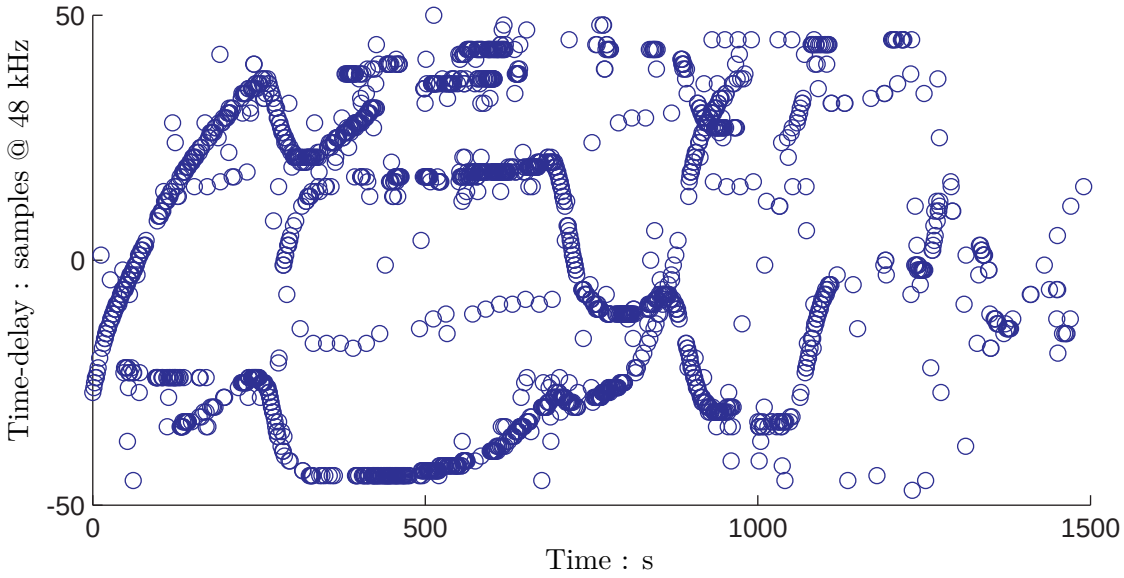

Figure 6.1: An example of click trains received from several vocalising sperm whales at differing source angles and the time-delay of the reception of each click across the hydrophone pair

and new target measurements may emerge having previously been masked by existing target measurements [116]. It is also worth noting that measurement sensors can be classed as either type 1 sensors or type 2 sensors [115]. A type 1 sensor, such as a radar, collects a set of measurements from all targets and associates all measurements collectively. A type 2 sensor associates each measurement as it is received. Passive acoustic tracking utilises a type 2 sensor and therefore type 1 sensors are not considered here.

6.2 Multiple Target Tracking Solutions

The literature presents many solutions to the multiple target tracking problem including nearest neighbour (NN), global nearest neighbour (GNN), joint probability data association (JPDA), incorporation of the data association into the particle filter and multiple hypothesis tracking (MHT).

NN data association associates a received measurement with the target closest matching that observation on an individual basis [59,114]. The influence of false detections can be mitigated by simply applying a gate to the target state, whereby measurements not within the gate of any target are treated as either new targets or noise. NN data association methods allow a single measurement to be used to update multiple targets whilst other measurements may not be utilised at all or multiple measurements may update a single target. The GNN attempts to alleviate this problem by restricting each target to being updated by a single update measurement. Data association decisions are based on the shortest global distance between measurements and targets. In JPDA all targets are updated by a probability weighted sum of all measurements within their gates [59, 114, 117]. A drawback of the JPDA method is it

suffers from a coalescence problem whereby closely spaced targets come together.

Classical data association techniques are typically based around Kalman filter tracking applications, whereby the system and measurement functions are linear and the respective noise processes are Gaussian, however this does not necessarily rule them out from being used with particle filtering methods. It has been suggested that an independent partition particle filter can be used to track multiple targets but this relies on knowledge of how many targets are present [118]. The data association solution for an unknown number of targets can be incorporated into the particle filter using a Gibbs sampler [60, 96, 119, 120]. The Gibbs sampler allows estimation of $p(X)$ given the marginal distributions $p(Y|X)$ and $p(X|Y)$ [120]. In the multi-target tracking case it is the distribution $p(Z, X)$ that is desired where Z is a data association identifier, found by generating samples from the marginal distributions $p(Y|Z, X)$ and $p(Z, X|Y)$ [96, 119]. This can be expanded to include statistical testing as to whether a target has appeared or disappeared [60].

MHT involves deferring the decision as to which target a measurement originated from until more measurements have been collected [114]. Whenever a new measurement is received a hypothesis is formed for each target from which the measurement could have originated, each of these hypotheses are propagated for each new measurement until a point in the future where the uncertainty is resolved by N_{meas} subsequent measurements.

Multiple animal tracking can be formulated into a complete associate and track problem or separated into independent association and tracking problems. The former requires including the association decision into the tracking process. The latter involves identifying which click train each received click is associated with by tracking the time-delay of each click train and then spatially tracking individual animals separately using the time-delay tracks.

Click association is a problem in itself and approaching it separately to spatial tracking means developments can be applied independently of spatial tracking developments. Additionally no modification of the particle filter developments presented so far are required. MHT has been successfully applied to tracking the central frequency of beaked whale clicks for the purposes of linking click trains and detecting odontocete buzzes [7, 32]. The remainder of this chapter develops a method for associating received time-delays with target animals by tracking the time-delay of click trains using an MHT.

6.3 Introduction to MHT

Association of measurements to tracks using a deferred decision process was first presented as a complete algorithm by Reid [115]. The algorithm allowed for measurements to be associated with existing targets, new targets or clutter. For each measurement received new hypotheses are formed whereby the measurement is and is not associated once with each existing target and once with a newly appearing target. In general terms any measurement can be associated with all targets, however to reduce computational load it is common to 'gate'

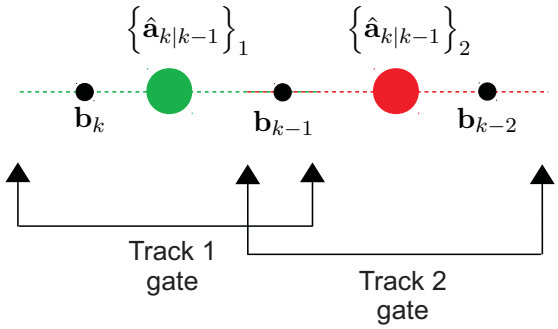

Figure 6.2: An example of measurement to target gating

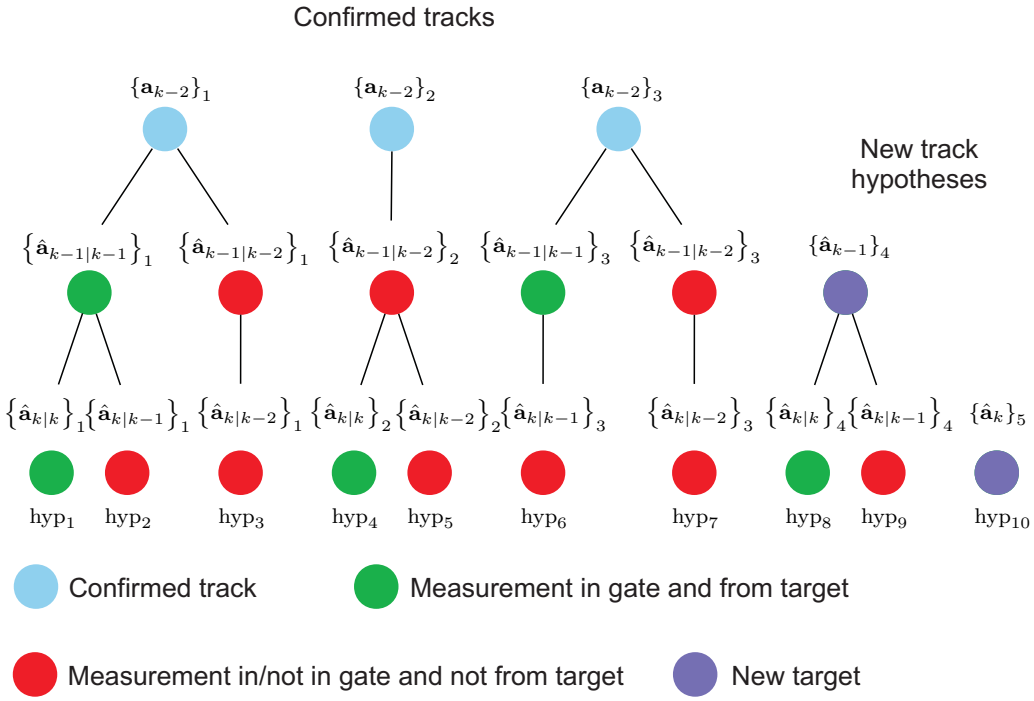

Figure 6.3: A hypothesis tree with 3 confirmed targets and 2 received measurements where $N_{\text{meas}} = 2$

measurements whereby a distance test between each measurement and target state prediction $\hat{\mathbf{a}}_{k|k-1}$ is performed to eliminate the most unlikely tracks [114, 121, 122].

An example of the gating process is shown in figure 6.2. The measurements $\mathbf{b}_k$, $\mathbf{b}_{k-1}$ and $\mathbf{b}_{k-2}$ could all be from previously undetected targets or clutter, however $\mathbf{b}_{k-1}$ lies within the gates of both predicted states of targets $\left\{\hat{\mathbf{a}}_{k|k-1}\right\}_1$ and $\left\{\hat{\mathbf{a}}_{k|k-1}\right\}_2$ so could also be from either of the existing targets while $\mathbf{b}_k$ only lies within the gate of predicted target state $\left\{\hat{\mathbf{a}}_{k|k-1}\right\}_1$ so could be from $\left\{\hat{\mathbf{a}}_{k|k-1}\right\}_1$ or a new target but not from $\left\{\hat{\mathbf{a}}_{k|k-1}\right\}_2$, whilst the measurement $\mathbf{b}_{k-2}$ could have originated from target $\left\{\hat{\mathbf{a}}_{k|k-1}\right\}_2$ or a new target but not from $\left\{\hat{\mathbf{a}}_{k|k-1}\right\}_1$.

After the gating process hypotheses are formed, as illustrated by the tree depicted in figure 6.3, whereby each hypothesis is a potential track of each target. Figure 6.3 shows a measurement association hypothesis tree with three confirmed targets and two received measurements so that $N_{\text{meas}} = 2$. The blue circles represent confirmed tracks for targets $\{\mathbf{a}_{k-2}\}_{1:3}$. For each received measurement there is a hypothesis that the measurement is associated with each

target for which it falls within the gate around that target's state prediction, green circles - e.g. $\left\{\hat{\mathbf{a}}_{k|k}\right\}_1$, that the measurement is not associated with a target state prediction even though it may be within the gate, which therefore remains the current best estimate of target position, red circles - e.g. $\left\{\hat{\mathbf{a}}_{k|k-1}\right\}_1$, and that the received measurement originated from a new target, purple circles - e.g. $\{\hat{\mathbf{a}}_{k-1}\}_4$. For each hypothesis that a measurement is associated with a target a hypothesis exists that the measurement is not associated with that target. Each target can have multiple tracks until the source of each measurement is confirmed, beyond which each target has a single confirmed track, for example hypotheses 1-3 are tracks of the same target. Hypotheses 1, 2 and 3 also demonstrate that if a measurement is associated with a target, and therefore results in the predicted track being updated by the measurement, may affect whether later measurements are within the target gate. Once a track is confirmed the target is classed as confirmed and active.

Each hypothesis is assigned a track score. The track score is formulated recursively as a log likelihood ratio. Initially the track score for confirmed targets is the respective secondary track score (discussed below) and is a large negative value for newly initialised track hypotheses. Each time a measurement is received the track score of each hypothesis may be updated depending on whether that hypothesis utilises the measurement:

$$l_k = \begin{cases} l_{k-1} + \log\left[\exp\{-\sigma T_k\}\, p\left(\mathbf{a}_{k|k-1}, \mathbf{P}_{k|k-1}, \mathbf{b}_k\right)\right] & \text{if measurement utilised} \\ l_{k-1} + \log\left[\exp\{-\sigma T_k\}\right] & \text{if measurement not utilised} \end{cases} \tag{6.1}$$

where l_k is the log likelihood at time k, T_k is the elapsed time since the last time a measurement was associated with that hypothesis, $\exp\{-\sigma T_k\}$ is a track ageing term, where σ is a design parameter, and $p\left(\mathbf{a}_{k|k-1}, \mathbf{P}_{k|k-1}, \mathbf{b}_k\right)$ is the likelihood of a measurement being associated with a specific track [114, 121, 123]. The track scores are compiled into a vector $\mathbf{l}$ of length equal to the current number of hypotheses, N_{hyp}.

The hypotheses are formulated into a binary matrix representation, $\mathbf{C}$, [32, 121–123], the matrix for the hypothesis tree shown in figure 6.3 is:

$$\mathbf{C} = \underbrace{\begin{bmatrix} 1 & 1 & 1 & 0 & 0 & 0 & 0 & 0 & 0 & 0 \\ 0 & 0 & 0 & 1 & 1 & 0 & 0 & 0 & 0 & 0 \\ 0 & 0 & 0 & 0 & 0 & 1 & 1 & 0 & 0 & 0 \\ 1 & 1 & 0 & 0 & 0 & 1 & 0 & 1 & 1 & 0 \\ 1 & 0 & 0 & 1 & 0 & 0 & 0 & 1 & 0 & 1 \end{bmatrix}}_{\text{Track hypotheses}} \begin{matrix} \Big\} \text{Confirmed tracks} \\ \\ \\ \Big\} \text{Measurements and new tracks} \end{matrix} \tag{6.2}$$

Each column of $\mathbf{C}$ represents a track hypothesis. In this example the first three rows account for the confirmed existing targets while the last two rows account for the assignment of the measurements to each track for each hypothesis. The first column represents the hypothesis that both measurements are associated with confirmed target one, the sixth column represents the hypothesis that the first measurement comes from confirmed target three and the last column represents the hypothesis that the second measurement comes from a newly detected

target.

Under the constraint that every measurement must be used once and only once and that each confirmed target can't be terminated (until later in the algorithm) the aim is to find:

$$\max \mathbf{l}'\mathbf{a} \tag{6.3}$$

subject to:

$$\mathbf{C}\mathbf{a} = \mathbf{i} \tag{6.4}$$

where:

$$\mathbf{i} = [1, 1, \ldots, 1]' \tag{6.5}$$

The solution can be found using binary integer programming [121,123] which is similar to linear and integer programming [75] but constrains the solution to only consisting of zeros and ones. The solution is the global hypothesis that has the highest probability under the constraint that each measurement and each confirmed target must be utilised once. When the solution is found the oldest tested measurement, $\mathbf{b}_{k-N_{\text{meas}}}$, is confirmed as assigned to a target then the data association for that measurement is complete. Where a measurement is associated with a new target track that track is regarded as 'active'. If after N_{meas} measurements a measurement is confirmed as having come from a new target then that track's status changes to 'active and confirmed' and the existence of a new target is confirmed.

In addition to the hypothesis related track score, confirmed tracks also have a secondary track score that is reset to zero each time that track is confirmed as updated by a measurement. For each measurement that is confirmed as originating from an individual target all other confirmed target secondary scores are updated to represent the time since they were last updated. The recursive update of the secondary score is [121]:

$$l_k^{\text{2nd}} = l_{k-1}^{\text{2nd}} + \log\left[\left(1 - p\left(DT\right)\right)\exp\left\{-\sigma T_k\right\}\right] \tag{6.6}$$

where $p\left(DT\right)$ is the probability that a target is detected and is set close to 1 [121]. The secondary scores are compared to a termination threshold, when the secondary score for an individual target falls below this threshold that target's status is changed to 'inactive' and the track is no longer updated. This effectively terminates targets that haven't been updated for a predetermined period of time.

6.4 MHT Algorithm

The MHT algorithm is summarised in algorithms 6.1 and 6.2.

Algorithm 6.1

$$\left[\left\{\hat{\mathbf{a}}_{k|k}, \hat{\mathbf{P}}_{k|k}\right\}_{1:M_{\text{hyps}}}, \mathbf{\Phi}_k, \mathbf{l}_k, \mathbf{l}_k^{\text{2nd}}\right] = \text{MHT}\left(\left\{\hat{\mathbf{a}}_{k-1|k-1}, \hat{\mathbf{P}}_{k-1|k-1}\right\}_{1:N_{\text{hyps}}}, \mathbf{\Phi}_{k-1}, \mathbf{l}_{k-1}, \mathbf{l}_{k-1}^{\text{2nd}}, \mathbf{b}_k\right)$$

Predict track states:
for $n = 1 : N_{\text{hyps}}$ **do**
System state:
$\left\{\hat{\mathbf{a}}_{k|k-1}\right\}_n = \mathbf{F}\left\{\hat{\mathbf{a}}_{k-1|k-1}\right\}_n$
MSE matrix:
$\left\{\mathbf{P}_{k|k-1}\right\}_n = \mathbf{F}\left\{\mathbf{P}_{k-1|k-1}\right\}_n \mathbf{F}' + \mathbf{R_{ee}}$
end for
Gate measurement against all active tracks:
$m = N_{\text{hyps}} + 1$
for $n = 1 : N_{\text{hyps}}$ **do**
If in gate
if $\left|\mathbf{b}_k - \mathbf{H}\left\{\hat{\mathbf{a}}_{k|k-1}\right\}_n\right| \leq$ gate **then**
Create associated hypothesis and apply Kalman update:
$\left[\left\{\hat{\mathbf{a}}_{k|k}, \hat{\mathbf{P}}_{k|k}\right\}_m\right] = \text{kalman update}\left(\left\{\hat{\mathbf{a}}_{k|k-1}, \hat{\mathbf{P}}_{k|k-1}\right\}_n\right)$
Assign parent hypothesis:
$\Phi_k(m) = \Phi_k(n)$
Update track score:
$l_k(m) = l_{k-1}(n) + \log\left[\exp\left\{-\sigma T_k\right\} p\left(\left\{\hat{\mathbf{a}}_{k|k-1}, \hat{\mathbf{P}}_{k|k-1}\right\}_n, \mathbf{b}_k\right)\right]$
$m = m + 1$;
end if
Set system state and MSE matrix for non-associated hypothesis:
$\left\{\hat{\mathbf{a}}_{k|k}, \hat{\mathbf{P}}_{k|k}\right\}_n = \left\{\hat{\mathbf{a}}_{k|k-1}, \hat{\mathbf{P}}_{k|k-1}\right\}_n$
Update track Score:
$l_k(n) = l_{k-1}(n) + \log\left[\exp\left\{-\sigma T_k\right\}\right]$
end for
New track hypothesis:
$\left\{\hat{\mathbf{a}}_{k|k}, \hat{\mathbf{P}}_{k|k}\right\}_m = \left\{\mathbf{b}_k, \hat{\mathbf{P}}_0\right\}$
$l_k(m) = l_k^{\text{2nd}}(m) = l_0$
$N = m$
... *Continued in algorithm* 6.2

6.5 Intersection Angle Testing

As shown at 900 s in figure 6.1 time-delays for two click trains can intersect, whereby they cross each other. To be a practical solution the MHT must be capable of tracking individual click trains through such intersections, such a situation is shown by an example in [122]. This section evaluates the performance with which the MHT correctly associates measurements with two targets using two intersecting lines where the measurements - the 0th order derivative - are affected by Gaussian white noise. This will provide an indication as to how well the MHT will be able to associate received clicks with the correct animal when click trains intersect.

The through-intersection tracking performance is evaluated for an acute intersection angle of 18° and an intersection at right angles. For the acute intersection angle the gradients of the two lines, +0.2 and −0.2, will be much closer than for the two lines intersecting at right angles

Algorithm 6.2 MHT continued

... *Continued from algorithm* 6.1
Form hypothesis matrix $\mathbf{C}$ from $\mathbf{\Phi}_k$
Solve binary integer program:
$\xi = \text{bintprog}\left(\mathbf{C}, \mathbf{l}_k, \mathbf{i}\right)$
where ξ is the hypothesis from which the measurement originated at $k - N_{\text{meas}}$
Update secondary track scores:
for $n = 1 : N$ **do**
  if $n = \xi$ **then**
    $l_k^{2\text{nd}}(n) = 0$
  else
    $l_k^{2\text{nd}}(n) = l_{k-1}^{2\text{nd}} + \log\left[\left(1 - p\left(DT\right)\right)\exp\left\{-\sigma T_k\right\}\right]$
  end if
end for
Set track statuses:
$m = 1$
for $1 : N$ **do**
  if $l_k^{2nd}(n) > l_{\text{threshold}}^{2\text{nd}}$ **then**
    $\left[\left\{\hat{\mathbf{a}}_{k|k}, \hat{\mathbf{P}}_{k|k}\right\}_m, \Phi_k(m), l_k(m), l_k^{2\text{nd}}(m)\right] = \left[\left\{\hat{\mathbf{a}}_{k|k}, \hat{\mathbf{P}}_{k|k}\right\}_n, \Phi_k(n), l_k(n), l_k^{2\text{nd}}(n)\right]$
  end if
end for
$M_{\text{hyps}} = m$
return $\left[\left\{\hat{\mathbf{a}}_{k|k}, \hat{\mathbf{P}}_{k|k}\right\}_{1:M_{\text{hyps}}}, \mathbf{\Phi}_k, \mathbf{l}_k, \mathbf{l}_k^{2\text{nd}}\right]$

with gradients of $+1$ and -1. It is the gradient, representative of velocity, that is utilised in the state prediction stage, therefore the greater the difference in the velocities the greater the magnitude of the difference there will be in the state predictions.

For each straight line target the system and measurement variance parameters can affect the measurement association. Setting a higher value for the system variance increases the effect of the measurement in state estimation and the previous state estimate effects how close the target is to the measurement gate. Although not utilised here, the size of the gate may be set proportional to the measurement variance, therefore measurement variance could also affect the gate size.

Using a measurement history of six measurements, performance consistency is tested by repeating each experiment for ten different sets of measurement noise samples. This allows the affect of chance in the drawing of the measurement noise samples on tracking performance to be minimised. For these tests the actual system noise is zero, hence the straight lines, however the system noise parameter of the MHT estimator is varied to simulate a lack of knowledge of the true system noise variance within the filter. The measurement noise variance is set to the value used for drawing the noise samples.

Results in table 6.1 show performance for tracking multiple targets through an intersection, and therefore correct association of measurements, is dependent on the intersection angle, system noise parameter setting in the estimator and the measurement noise variance. For

Intersection angle	System variance	Measurement variance	Performance rate
90°	$\begin{bmatrix} 0.0025 & 0.005 \\ 0.005 & 0.01 \end{bmatrix}$	0.1	10/10
90°	$\begin{bmatrix} 0.25 & 0.5 \\ 0.5 & 1 \end{bmatrix}$	0.1	10/10
90°	$\begin{bmatrix} 0.0025 & 0.005 \\ 0.005 & 0.01 \end{bmatrix}$	1	10/10
90°	$\begin{bmatrix} 0.25 & 0.5 \\ 0.5 & 1 \end{bmatrix}$	1	9/10
18°	$\begin{bmatrix} 0.0025 & 0.005 \\ 0.005 & 0.01 \end{bmatrix}$	0.1	9/10
18°	$\begin{bmatrix} 0.25 & 0.5 \\ 0.5 & 1 \end{bmatrix}$	0.1	5/10
18°	$\begin{bmatrix} 0.0025 & 0.005 \\ 0.005 & 0.01 \end{bmatrix}$	1	8/10
18°	$\begin{bmatrix} 0.25 & 0.5 \\ 0.5 & 1 \end{bmatrix}$	1	2/10

Table 6.1: Rates of correct data association for MHT tracking of intersecting tracks for differing intersection angles, system variances and measurement variances

right-angle intersections at higher and lower system and measurement variances track success rates through intersections are very high. Even though at the point of intersection the statics of the target state are the same, a right-angle intersection represents a greater difference in target state due to the target velocity. This manifests in the estimator through the prediction stage because the target states diverge more rapidly than for a more acute angle and it takes a higher system noise variance to effectively mask the effects of the target velocity in the prediction stage. At shallower angles tracking success rates are lower. Full results plots for each experiment are given in appendix B.

6.6 MHT for Tracking Time-Delays

This section applies the MHT concepts presented in section 6.3 to tracking and associating the time-delays of click trains from individual animals using algorithm 6.1. The system state vector and function and measurement vector and function are developed in section 6.6.1. MHT time-delay tracking results for three datasets are presented and discussed in section 6.6.2.

6.6.1 System State and Measurement for Time-Delay Tracking

Applying the MHT to tracking time-delays requires defining the system and measurement vectors. The system state vector is the measured time-delay and rate of time-delay change:

$$\mathbf{a}_k = \begin{bmatrix} \tau \\ \dot{\tau} \end{bmatrix} \tag{6.7}$$

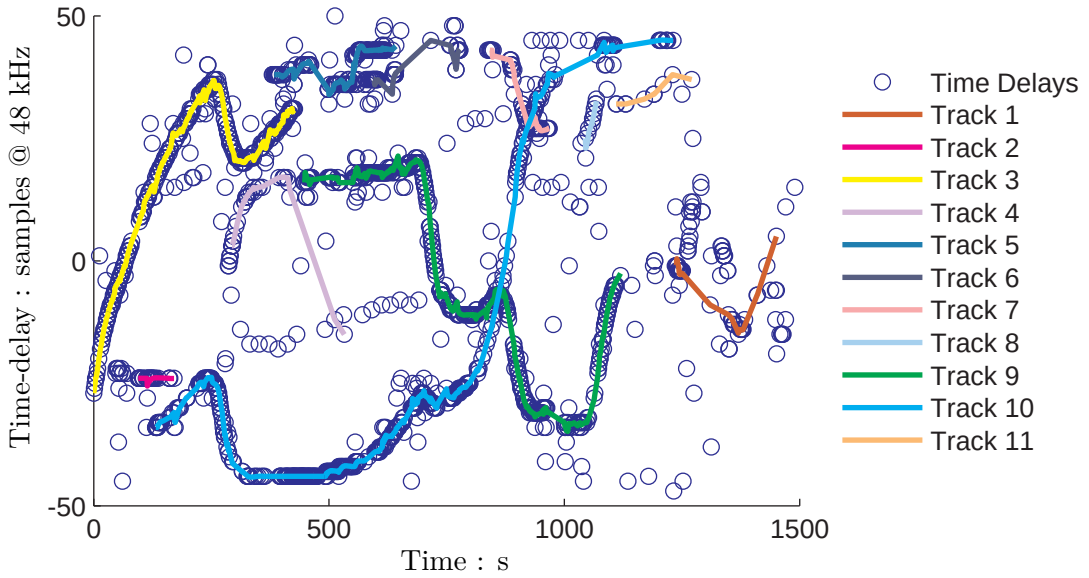

Figure 6.4: MHT tracking results for the clicks trains shown in figure 6.1

where the system update function is:

$$\mathbf{a}_k = \mathbf{F}_k \mathbf{a}_{k-1} + \mathbf{e}_k \tag{6.8}$$

$$= \begin{bmatrix} 1 & T_k \\ 0 & 1 \end{bmatrix} \mathbf{a}_{k-1} + \mathbf{e}_k \tag{6.9}$$

where T_k is the time since the track was updated. The measurement is simply the time-delay:

$$\mathbf{b}_k = \mathbf{H}\mathbf{a}_k + \mathbf{v}_k \tag{6.10}$$

$$= \begin{bmatrix} 1 & 0 \end{bmatrix} \mathbf{a}_k + \mathbf{v}_k \tag{6.11}$$

$$= \tau_k + \mathbf{v}_k \tag{6.12}$$

where the noise term $\mathbf{v}_k$ represents quantisation and selection of incorrect peaks in the cross-correlation function. Experimentation shows a measurement history length of 6 provides adequate performance whilst processing significantly faster than real time. As a guide to computational loading the dataset shown in figure 6.1 covers a duration of 25 minutes, a MATLAB implementation of the MHT algorithm processes this dataset in less than 45 seconds to produce the results in figure 6.4 on a 2.4 GHz Intel Core 2 Duo processor in a laptop computer.

6.6.2 Results

Figure 6.4 shows MHT results for the click trains shown in figure 6.1. There are three visually identifiable click trains, however eleven have been identified by the MHT. The MHT appears to have broken up the tracks one might visually regard as belonging to a single animal. Specifically, while track 10 appears to correspond to a complete visual track, tracks 4 and 9

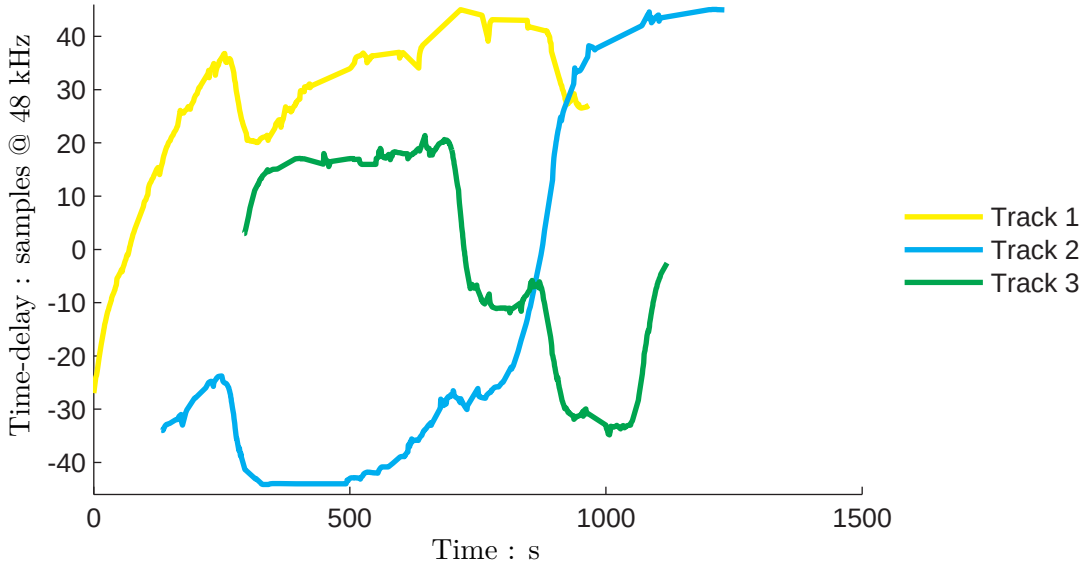

Figure 6.5: Manual corrections to the results in figure 6.4 to establish complete tracks for three vocalising animals

Parameter	Value
System covariance matrix $\mathbf{R_{aa}}$	$\begin{bmatrix} T_k^4/4 & T_k^3/2 \\ T_k^3/2 & T_k^2 \end{bmatrix}$ 0.0177
Measurement variance $\mathbf{R_{bb}}$	22
Measurement history	6
Measurement gate size	5
Probability of detection p_{DT}	0.99999
New track likelihood l_{new}	-500 000
Track ageing term σ	1
Track termination threshold	-100

Table 6.2: MHT parameters for results in figure 6.4

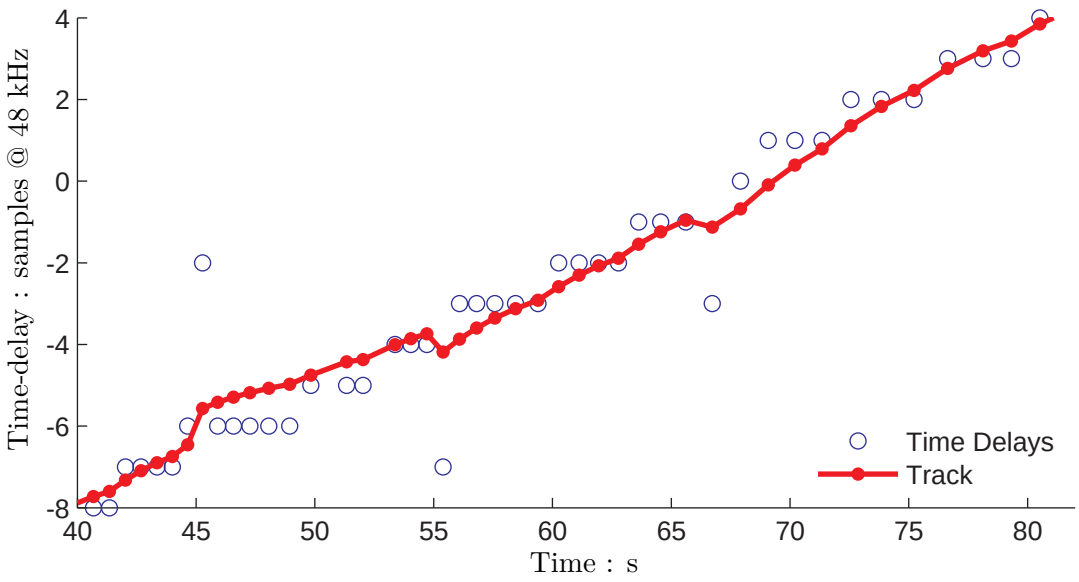

Figure 6.6: The smoothing effect of the MHT on the integer quantised time-delay measurements

appear to be part of the same track and tracks 1, 5 and 6 also appear to be parts of another track. The parameters used for this dataset were found through experimentation and are shown in table 6.2. As animals typically produce click trains continuing for many minutes (including short periods of silence) any track of length one, or shorter than an alternative threshold, can be regarded as clutter and not vocalisations. Track 10 represents the time-delays of the clicks received from the subject animal and upon visual examination appears to be completely tracked, however it only takes minor manual adjustment to obtain complete tracks for the other two vocalising animals, as shown in figure 6.5.

The MHT can be implemented to associate delay measurements to individual animals in two ways:

1. The time indices of delay measurements can be cross-referenced against the time-indices of the MHT tracks thereby allowing the original measurements to be associated to an individual animal and used as the input to the spatial tracking filters;

2. The tracks output by the MHT themselves can be used as the measurements and utilised as input to the spatial tracking filters.

Using the latter method mitigates the effect of outlying mis-associated measurements through smoothing by the Kalman filters within the MHT. Figure 6.6 shows a click received at 45 seconds with a delay of -2 samples, a magnitude of four samples away from the trend, however the tracking result using this measurement is within a sample of the trend. A second useful bi-product of the smoothing effect is that the delay measurements are no longer quantised to integer numbers of samples. The quantisation of the time-delays is clearly observable in figure 6.6 and it can be seen that the track points occur at the same time indices as the measurements but don't suffer from quantisation. This effect may be used as a substitute for the interpolation of acoustic signals or correlation functions when attempting to increase the

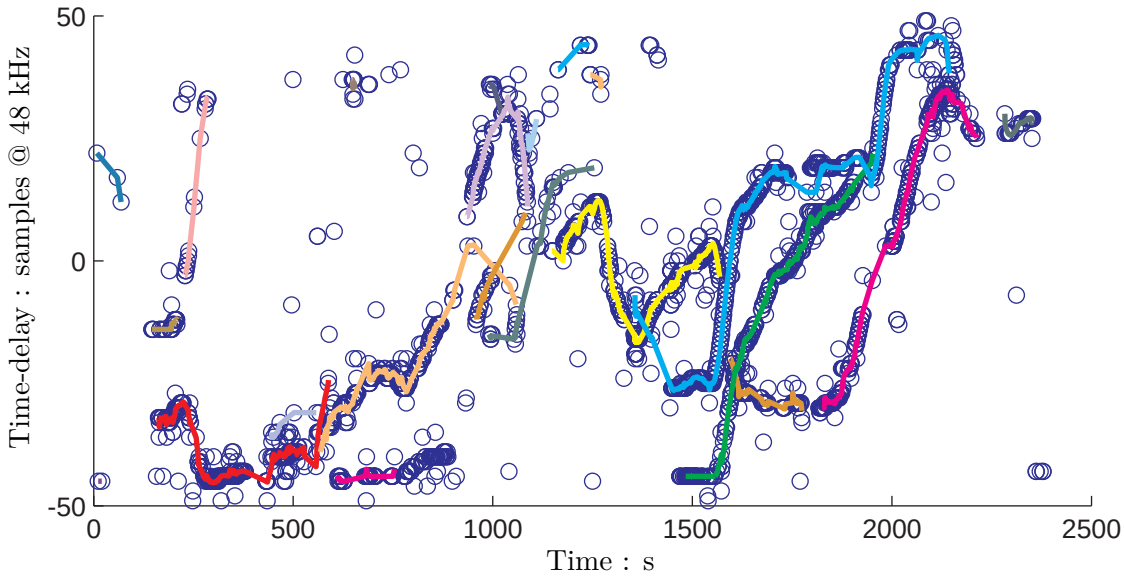

(a) MHT tracks for a set of click trains

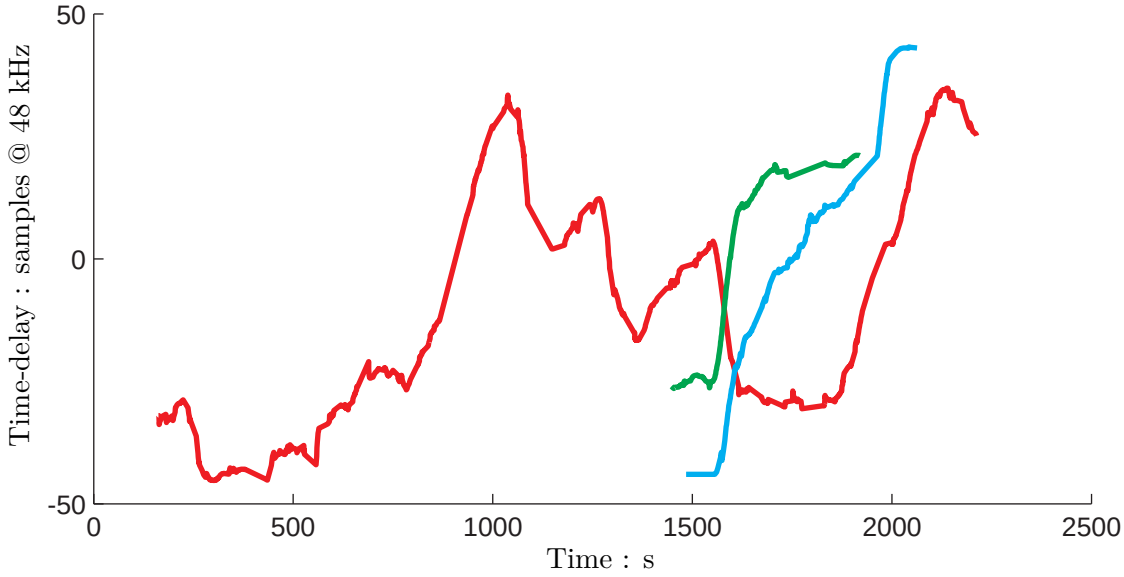

(b) Manually corrected MHT tracks for a set of click trains

Figure 6.7: MHT tracking results and manually adjusted tracks for a set of click trains

resolution of time-delay measurements.

Tracking results for another set of click trains is shown in figure 6.7(a). On inspection the click trains in this set are less clearly observed and MHT tracking appears to be less effective with some tracks making large jumps in state and some tracks being broken across continuing click trains. Manual adjustment of the MHT tracks yields the click train tracks from three animals, shown in figure 6.7(b).

Figure 6.8 shows an example of when a complete click train is successfully tracked for the duration of a complete dive. At first examination the reason for the subject click train being successfully tracked may appear to be because it is the only click train in this dataset, however during this time other impulsive trains do start and stop without affect on the track of the click

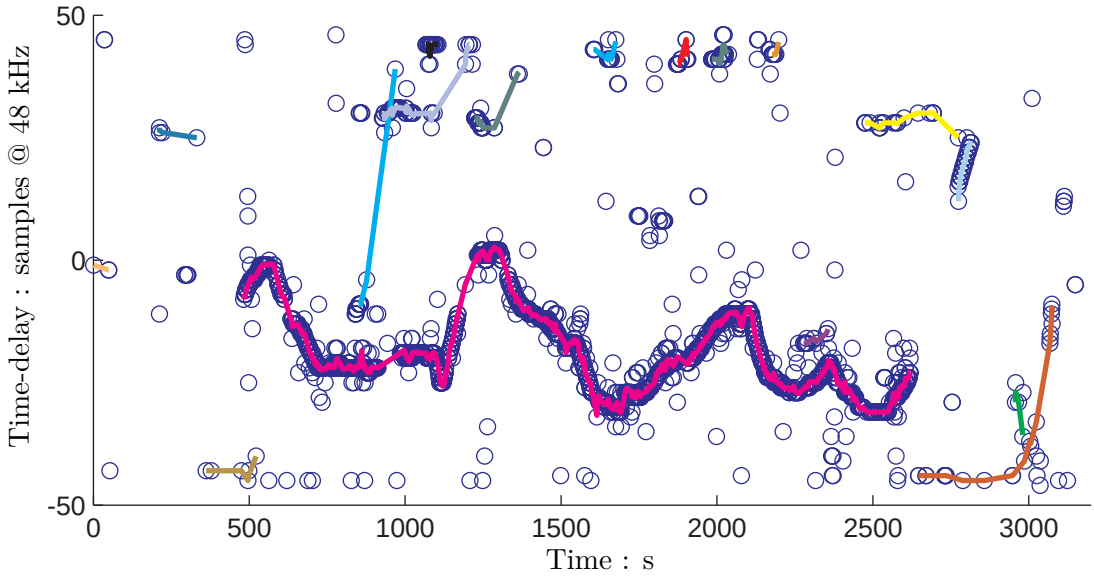

Figure 6.8: MHT tracking results for a click train where the complete click train has been tracked and no manual adjustment is necessary beyond selection of the click trains of interest

train of interest. If another click train were present in this dataset it would not necessarily change the tracking result unless it closely matched or intersected the click train that is present. The results for this dataset demonstrate that the MHT algorithm can track a complete click train, as also shown by the tracking results for track 10 in dataset 1 (figure 6.4), and discriminate against clutter so, even when errors do exist, is still useful for identifying clicks in a click train when only a single animal is vocalising.

6.7 Conclusion and Discussion

Any practical sperm whale tracking solution needs to be able to track multiple animals, the method developed in this chapter enables this by associating received clicks with individual animals so that they can each be spatially tracked within a single target tracking context. The MHT approaches the data association problem as a tracking problem and defers confirmation of association until more measurements have been collected and allows for the detection of previously undetected animals.

The results presented show mixed performance, out of the three datasets two complete click trains have been tracked with others requiring manual adjustment. The performance demonstrated is sufficient for the purposes of testing spatial tracking on the test datasets and under these criteria some manual adjustment of MHT results is acceptable. In practical real-time tracking applications further development of the algorithm may be necessary to improve robustness (discussed below). As well as applications to real-time tracking the methods developed in this chapter can also be used in post-collection data-analysis. During analysis of data collected during line-transect surveys [3] it is often necessary to manually identify sperm whale clicks and associate them with a click train, effectively tracking click trains by hand.

The MHT method developed here automates much of this process and manual correction of MHT results which do include errors would take considerably less time than manually tracking entire click trains. The tracking process utilises Kalman filters which smooth the measurements, where the measurement error is the quantisation effect of the cross-correlation process in the time-delay computation. This results in a similar effect to that achieved when utilising interpolation of the cross-correlation function or acoustic signals to improve time-delay resolution. Smoothing in this manner also aids in the reduction of the impact of mis-associated clicks. An example of this is shown in figure 6.6.

For real-time click train tracking the MHT method may require further development to ensure it is robust enough, primarily in tracking click trains through boat manoeuvres. One approach would be to incorporate a control vector for the array derived from the boat speed and heading into the motion model, or explicit array motion data if it is available. One difficulty with this however relates to the source location ambiguity surface that results from the function between bearing, elevation, range and the time-delay measurement. Depending on the bearing and elevation of the animal from the array, the extent of the effect of the manoeuvre on the measurements would be different for each target; for example the measurements from a target with a zero elevation angle will appear to be affected by the manoeuvre to a much greater extent than that at a steep elevation angle. Such effects would occur because the time-delay is a function of bearing and elevation but a manoeuvre only applies a control vector to the bearing parameter.

An alternative to incorporating the control vector into the motion model would be to use an interacting multiple-model MHT (IMM-MHT) [124, 125]. IMM-MHT combines interacting multiple-model EKFs with MHT so that tracks can be predicted with a constant velocity motion model, a manoeuvring motion model or a random acceleration motion model. Switching of the models is based on an automated manoeuvre detection function of the data received or could be detected from boat or array heading information. This would enable improved tracking of click train time-delays when the array manoeuvres and more precise tracking of time-delays varying at a constant rate through more precise filter settings. A further application of using MHT for click train tracking is in feature extraction for automated classification of odontocete clicks. The capability to track click trains from individual animals allows extraction of information from the complete train rather than simply the isolated clicks, such as the inter-click interval. MHT have also been utilised by Gerard et al. for classifying odontocete buzz clicks by tracking click frequency [32].

The MHT method developed for associating clicks with click trains from individual animals has been shown to perform sufficiently well for the requirements of distinguishing the time-delays of the clicks from the subject animal with those of other animals and clutter in the dataset. As well as being a solution to the multi-target tracking problem there are other possible applications of the methods developed. Manually refined MHT results for several datasets will be utilised as the measurements in chapter 7 in which the spatial tracking methods will be applied to sperm whale data.

Chapter 7

Sperm Whale Tracking

This chapter utilises the tracking algorithms tested in chapter 5 for tracking a sperm whale over several dive cycles. Time-delays are computed from acoustic recordings made from a towed hydrophone array and the MHT method presented in chapter 6 is utilised to identify which clicks originated from the subject animal. Results are compared against pseudotrack reconstructions of the animal's movements from DTAG data. The exact position of the animal when vocalising begins is unknown so the algorithm is initialised using the dive sighting position. Performance consistency is tested over multiple tracking instances of the same dataset with the same test parameters. The tracking error that results from initialising using the sighting position and not the animal's exact position is evaluated by initialising tracking for two datasets from the pseudotrack position when the animal starts vocalising and comparing against the tracking results when initialising using the dive sighting.

7.1 Dataset

The dataset utilised to test the tracking methods developed was collected in the Norwegian sea in northern Norway in 2009 as part of the 3S project [47]. The dataset includes acoustic data from a towed hydrophone array, dive and surface sightings positioning information, DTAG data from which a pseudotrack of the animal's path can be reconstructed and global position system (GPS) positioning logs for the vessel towing the hydrophone array. This section discusses collection of the dataset, processing of the data required to extract the necessary time-delays from the acoustic data and modelling the motion of the array from the GPS data log.

7.1.1 Collection

The dataset was collected in 2009 as part of the Sea Mammals Sonar Safety (3S) project in the Norwegian sea in northern Norway. The project aim was to collect data on the behavioural responses of sperm, pilot and killer whales to low and mid frequency active sonar. Funding

support was provided by the Royal Norwegian Navy and Norwegian Ministry of Defence, the Royal Netherlands Navy and Dutch Ministry of Defence, Office of Naval Research - USA - and the World Wildlife Fund - Norway. Collaborating research organisations were the Norwegian Defence Research Establishment (FFI), the Netherlands Organisation for Applied Scientific Research (TNO), the Sea Mammal Research Unit (SMRU) at St. Andrew's University and Woods Hole Oceanographic Institution (WHOI).

To maximise the information acquired from the trials acoustic, sightings and DTAG information were recorded. Acoustic and sighting data were acquired from two vessels, the 'observation vessel' and the 'source vessel' which also towed the sonar source. Before exposure experiments began the subject animal was tagged with a DTAG to record motion information and acoustic arrivals at the animal. For this work recordings and sightings from only the observation vessel will be utilised. The availability of the sighting and DTAG information provides the data required to initialise the algorithm and references against which acoustic tracking performance can be compared.

7.1.2 Acoustic Data

The hydrophone array comprised of 16 elements within a 1.5 m aperture with 100 m of tow cable. During the exposure experiments the most forward and rearward elements were both fed to a computer and used for tracking and not recorded, the inner most 12 of the remaining elements were fed to a digital multi-track recorder. Of the 12 channels recorded the two outer most channels with 1.4 m separation are used for time-delay computation in these experiments. Recordings were made at 96 kHz and down-sampled to 48 kHz for click detection and time-delay computation. Down-sampling the acoustic data in this manner reduces the resolution of the final computed time-delay measurement, however in this application can be justified for two reasons, firstly the centroid frequency of sperm whale clicks is typically $\sim$ 15 kHz [13], well within the 24 kHz bandwidth of 48 kHz recordings, so little is gained by performing click detection at higher sample rates. Secondly, array snaking (small oscillatory changes in array heading as a consequence of towing motion through the water) becomes more apparent in the time-delay measurements when increasing the resolution of the time-delay computation data. If the array were to maintain a constant course without snaking then ideally the acoustic tracking system would utilise the highest sample rate possible. The error caused by array snaking is known to be large, such that there is little additional contribution to the error due to quantisation, even at 48 kHz. Furthermore, 48 kHz is the typical sample rate used in sperm whale tracking. Resolution of the time-delay measurement can be improved by up-sampling the correlation function via appropriate interpolation methods, that are based on the band-limit of the signal. Finally the computed time-delays are processed by the MHT processing stage developed in chapter 6 to associate measurement with separate source animals and identify which clicks originated from the subject animal. Prior to click detection and time-delay computation both acoustic data channels were high-pass filtered with a roll off at 200 Hz to remove low frequency noise that could interfere with these processes.

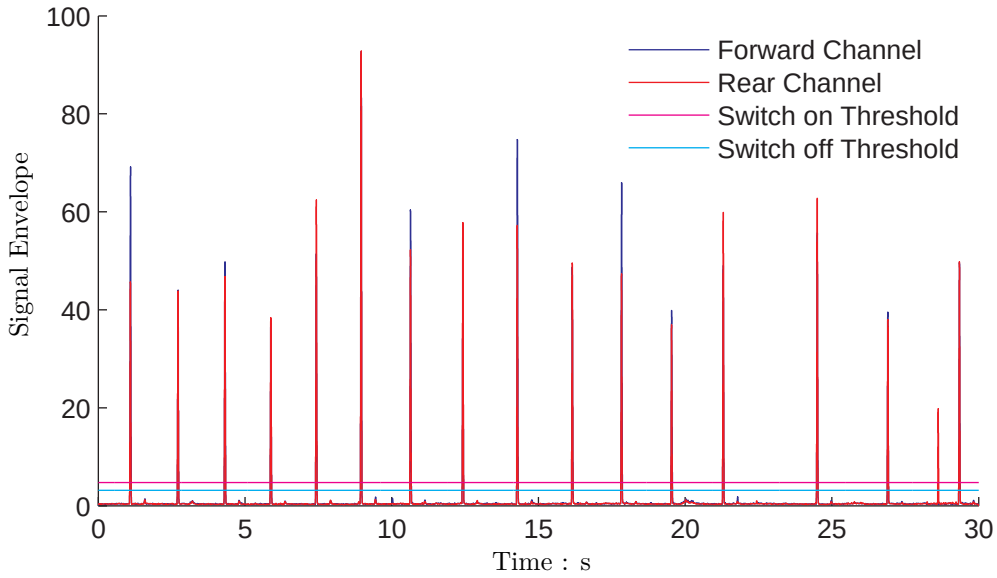

Figure 7.1: The front (blue) and rear (red) hydrophone channel powers for several sperm whale clicks and the switch on (magenta) and switch off (cyan) thresholds.

Click Detection

Click detection is performed using a double threshold method on the signal envelope described in section 2.2.2. One threshold is set higher than the other, when the signal power exceeds the first threshold a click is regarded as having been detected, when the power falls back below the second threshold the click is regarded as having ended. This method of detection is preferable over using a single threshold because it prevents multiple clicks being identified when in fact only a single click is present. Such errors can occur if the signal power exceeds the threshold and drops below it before once again exceeding it within the same click. Example signal envelopes for front (blue) and rear (red) hydrophone channels with switch on (magenta) and switch off (cyan) thresholds are shown in figure 7.1.

Time-Delay Computation

Once a click has been detected the arrival time-delay across the aperture between the hydrophones is computed using cross-correlation of the waveforms on the front and rear channels as described in section 2.2. The two waveforms are windowed at the same start and finish times using a square window of sufficient width so as to include the complete click on both channels within the maximum possible arrival delay. Waveforms for the front and rear channels and the square window are shown in figure 7.2.

7.1.3 DTAG

The DTAG is equipped with three-dimensional accelerometers and magnetometers, a depth sensor and acoustic recorder, however the DTAG lacks positioning instrumentation [112].

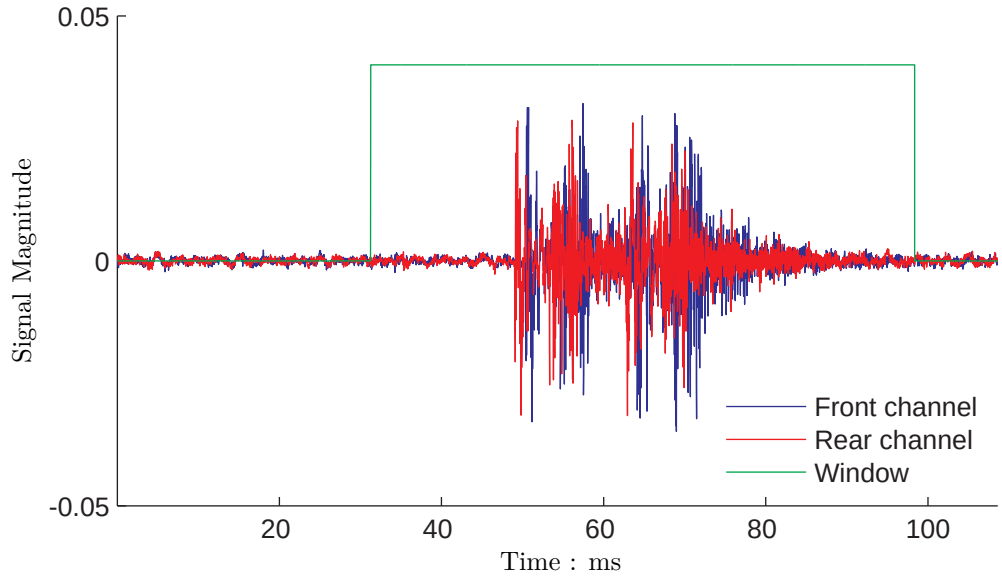

Figure 7.2: The front (blue) and rear (red) hydrophone channel signals and the square windowing (green) applied to both for computing the time-delay.

Reconstruction of positions of the animal is possible using the sightings information and accelerometer, magnetometer and pressure sensor data, the resultant reconstruction is referred to as the 'pseudotrack' because it is a reconstruction from higher order motion data and therefore is subject to error. A full discussion of the pseudotrack reconstruction from DTAG data is beyond the scope of this work, however more information is available in [112]. If the pseudotrack is reconstructed over a complete tag deployment, based on the sighting position of the animal at the first dive and last dive or surfacing at which the tag was still attached, the pseudotrack is unlikely to pass through the locations at which the animal was sighted between dives. It is possible to overcome this problem by transforming the pseudotrack during individual dives so that the reconstruction matches the dive and surface sightings. Justification and validation of such transforming is discussed in section 4.3, however here an alternative validation is possible. Since the position of the boat is known the position of the array can be approximated, as discussed in section 7.2, and the relative bearing and angle of elevation between the array and pseudotrack can be calculated. Using these bearing and elevation angles, (2.9) and rearranging (2.8) the time-delay that would have been measured from the relative pseudotrack positions can be simulated. The level of confidence in the pseudotrack is related to the correlation between the simulated time-delay from the pseudotrack and the true measured time-delay. The greater the correlation the more confidence there is in the pseudotrack.

7.2 Array Motion Modelling

Incorporation of the control vector into the system function to enable use of the deterministic control input of the hydrophone array requires a control vector data-stream. Array motion data is not available for this dataset but GPS data-streams for the towing vessel are available.

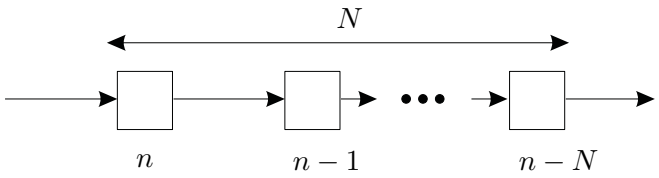

Figure 7.3: The heading data delay line for which the length N is to be found

The array is some distance behind the towing vessel, in this case approximately 100 m, so the GPS data from the boat is not entirely representative of the array's motion.

In the absence of array positioning data it is necessary to model the array motion from the boat GPS by applying an appropriate delay to the heading and positioning data in the boat GPS log. The GPS data-stream delay N, is computed by integrating boat speed with respect to time so that:

$$d_k^{\text{tow}} = \int_{k-N}^{k} v^{\text{boat}}(t)dt \tag{7.1}$$

where d_k^{tow} is the length of the tow cable. In discrete form (7.1) becomes:

$$d_k^{\text{tow}} = \sum_{n=k-N}^{k} v_n^{\text{boat}} T_n \tag{7.2}$$

where T_n is the nth GPS logging time interval. The variable delay line is illustrated in figure 7.3. This model makes several assumptions: the array instantly responds to changes in boat speed; the axis between the array elements is always perfectly horizontal without ever tilting; the array is at a depth of 0 m and the specified array length is the horizontal distance behind the boat. Examination of the boat GPS data shows the boat does not maintain a constant course but varies in heading due to swell and waves. It is unlikely the array responds to these heading variations but may vary in an oscillatory fashion due to turbulent water flow, which can be observed in the measured time-delays as previously discussed. Both of these components can be regarded as noise, the effects of which can be reduced by smoothing both the array heading data and the time-delay measurements which, for the time-delays, is effectively performed by Kalman filters within the MHT at the data association stage.

7.3 Tracking Results

Chapter 5 concluded that tracking performance is more effective when initialised at a specific point rather than when initialising as an ambiguity surface derived from a time-delay measurement. In practice the best known confirmed animal position during a dive is the sighting at dive time, therefore it is logical to initialise the particle filter at this point. After initialisation the particles should be propagated through the state space from the initialisation point proportionally to the time between the sighting and start of the animal's vocalisations. This propagation accounts for the displacement of the animal between the sighting and the start of acoustic tracking.

This section presents tracking results for five datasets. Results are shown in a spherical form, as for the simulations in chapter 5, the bearing angle, elevation angle, slant range and estimated time-delay computed from the estimated bearing and elevation angles. These plots are supplemented with additional plots showing horizontal range and depth estimates computed from the estimated slant range and elevation angle. Horizontal range plots provide a more intuitive range representation for comparing results in spherical coordinates with those reconstructed in latitude and longitude.

System noise is assumed to be normally distributed, where $\mathrm{var}\{\gamma\} = \mathrm{var}\{\beta\} = 1.7453$, $\mathrm{var}\{\dot{v}\} = 10$ and the speed sample rejection function is:

$$\boldsymbol{\chi}(v_{k-1} + \dot{v}_k) = \frac{\tanh(2 - 2((v_{k-1} + \dot{v}_k) - 1)) + 1}{2} \tag{7.3}$$

where the updated speed is accepted on condition (4.39). These values were found through experimentation. Measurement noise is also assumed to be normally distributed with variance $\mathrm{var}\{\mathbf{b}\} = 1$.

Figure 7.4 shows the positions of the animal as estimated by the particle filter from measurements recorded during a dive on 6th June 2009 where the animal was sighted diving at 10:55:10 am and sighted at the surface again at 11:30:15 am. Position estimates are relative to the array with point marks showing the times at which vocalisations occurred. The blue line represents the relative position of the pseudotrack to the boat and the red line shows the animal position estimated from the acoustic measurements. The time-delay plot also shows a green line which are the time-delay measurements that result from the MHT processing stage to associate clicks with the source animals. The particle filter estimated positions closely fit the measurements, however the time-delays computed from the pseudotrack positions are not such a close match to the measured time-delays which limits confidence in the pseudotrack reconstruction, but they do follow the trend of the time-delay measurements. A notable peak in the pseudotrack time-delay is present at 1300 s. This occurs as a manifestation of the corresponding peaks in the pseudotrack bearing and elevation angles, at the same time there are also local slant and horizontal range peaks. At sightings the pseudotrack accurately represents the animal position because it is fitted to those sighting positions so confidence is higher around these points and lower in between these points. Depth measurement is an exception because it is recorded by a calibrated pressure sensor so is considered to be reliable. The plots of the relative pseudotrack positions continue beyond the end of the acoustic tracking until the animal is sighted.

Particle filter estimated bearings and the pseudotrack bearings follow the same trend, with the particle filter tending to estimate the animal bearing as slightly more rearward than the pseudotrack suggests. Elevation angle estimates tend to over-estimate the elevation angle, along with the over-estimated slant range this places the estimated animal depth considerably beyond the depth recorded by the DTAG. Horizontal range estimates, computed from the slant range and elevation angle estimates, match the trend of the horizontal range of the pseudotrack with a relatively large over-estimate beyond 1200 s until the end of acoustic

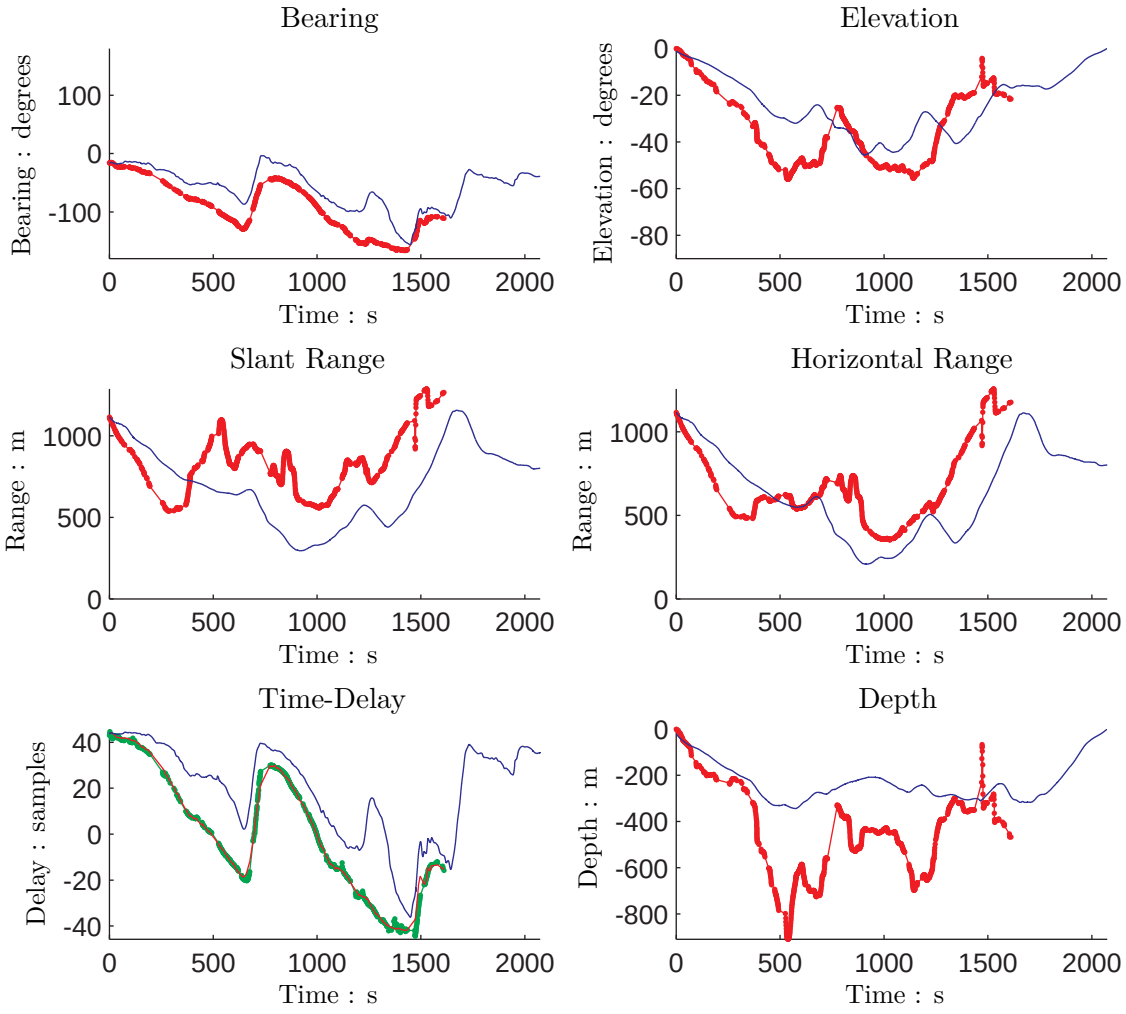

Figure 7.4: Relative particle filter estimated positions for acoustic tracking (red), the pseudo-track (blue) and the measured time-delays as output by the MHT (green) for dataset 1. Red points and green points - in the time-delay plot - show when vocalisations occurred.

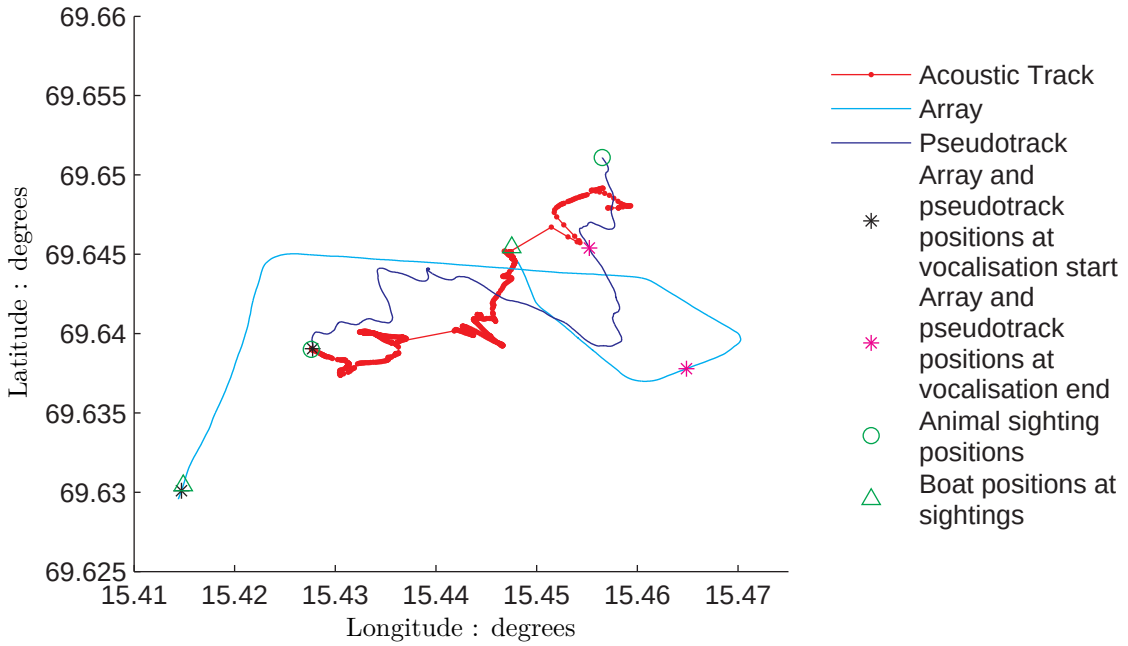

Figure 7.5: Global position reconstructions for the particle filter estimated acoustic track (red), the positions of the array (cyan) and the pseudotrack (blue) for the dataset and results shown in figure 7.4. Also shown are the animal sighting positions (green circles), the boat positions at the sightings (green triangles), the positions of the array and pseudotrack when vocalisations start (black stars) and the positions of the array and pseudotrack when vocalisations end (magenta stars). The points on the acoustic track indicate the occurrence of an animal vocalisation. Date: June 9th 2009. Time: 10:55:10 am - 11:30:15 am

tracking, at which point the extent of the over-estimate reduces.

Figure 7.5 shows a reconstruction of the positions of the array, the pseudotrack and the animal as estimated by the particle filter for the dataset and results shown in figure 7.4. Also shown are dive and surface sighting positions of the animal (green circles), the position of the boat from which the sightings were made (green triangles), the position of the array and pseudotrack when the animal started vocalising and acoustic tracking commenced (black stars) and the position of the array when vocalisation and acoustic tracking ceased (magenta stars). The reconstruction shows periods during which there are no detected vocalisations which do not appear to be matched by the plots in figure 7.4, this occurs because of filter adaptations as a consequence of array manoeuvres which cause the MMSE estimated position to shift rapidly. The difference in horizontal range of the pseudotrack and particle filter estimated track between 1300 and 1600 s is visible. The short-coming of this method of displaying tracking results is that the respective locations of the array, pseudotrack and particle filter estimated positions at a particular time index are not easily discernible. Figures 7.4 and 7.5 show good overall tracking results.

Figure 7.6 shows relative estimated positions for a second dataset where the animal was seen diving at 3:00:54 pm and sighted at the surface again at 3:26:20 pm. The estimated time-delay closely matches the measured time-delay and the pseudotrack time-delay follows the trend and, although does not match exactly, is quite close to the measurements and therefore

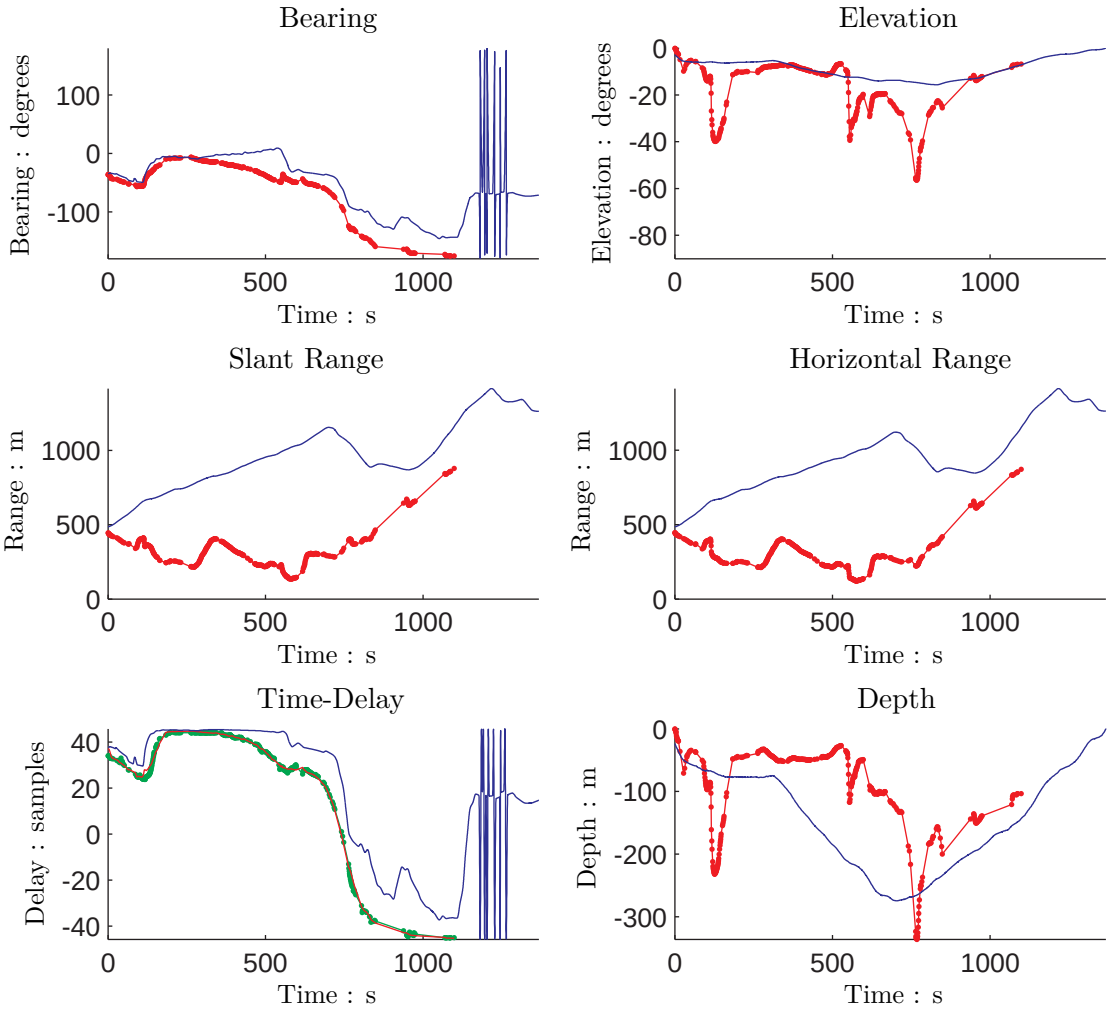

Figure 7.6: Relative particle filter estimated positions for acoustic tracking (red), the pseudo-track (blue) and the measured time-delays as output by the MHT (green) for dataset 2.

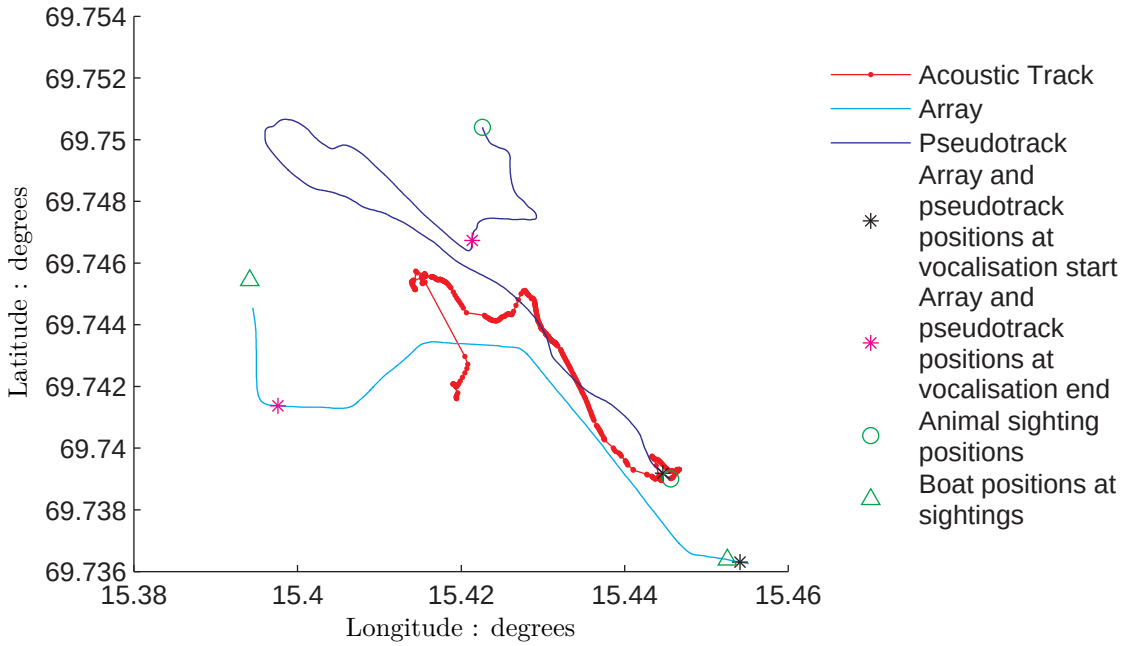

Figure 7.7: Global position reconstructions for the particle filter estimated acoustic track (red), the positions of the array (cyan) and the pseudotrack (blue) for the dataset and results shown in figure 7.6. Date: June 9th 2009. Time: 3:00:54 pm - 3:26:20 pm

there is moderate confidence in the pseudotrack. Bearing and elevation angle estimates follow the trend of the pseudotrack bearing and elevation angles, with obvious occasional errors in the elevation angle estimate. Range is significantly under-estimated and only starts to converge back to the pseudotrack range at 750 s. Depth estimates, computed from the estimated slant range and elevation angle, generally show a depth under-estimate. Elevation angle estimates follow the trend of the pseudotrack elevation angle, so the error in depth estimation is a result of under-estimates of the slant range. Rapid changes in bearing and time-delay of the pseudotrack, between 1200 and 1400 s, in figure 7.6 occur where the heading of the array passes through north and where the relative bearing of the pseudotrack passes between either side of directly ahead of the boat.

Figure 7.7 shows the array and pseudotrack positions and reconstruction from the particle filter estimated positions for the dataset and results in figure 7.6. The final estimated position is directly behind the array, a position suggested by the time-delay measurements. The difference between the pseudotrack time-delay and the measured and estimated time-delays is proportional to the difference in estimated bearing and pseudotrack bearing. This suggests that the pseudotrack reconstruction is in error when vocalisation ceases.

Figure 7.8 shows relative position tracking results for a third dataset where the animal was sighted diving at 12:42:01 pm and sighted at the surface at 1:17:26 pm. A significant difference between the pseudotrack and measured time-delays can be observed, therefore confidence in the pseudotrack is low. Furthermore, between 1100 and 1300 s the estimated time-delays differ slightly to the measured time-delay. Estimates of bearing, elevation and slant and horizontal ranges also differ significantly to the pseudotrack. Depth estimates also do not match the

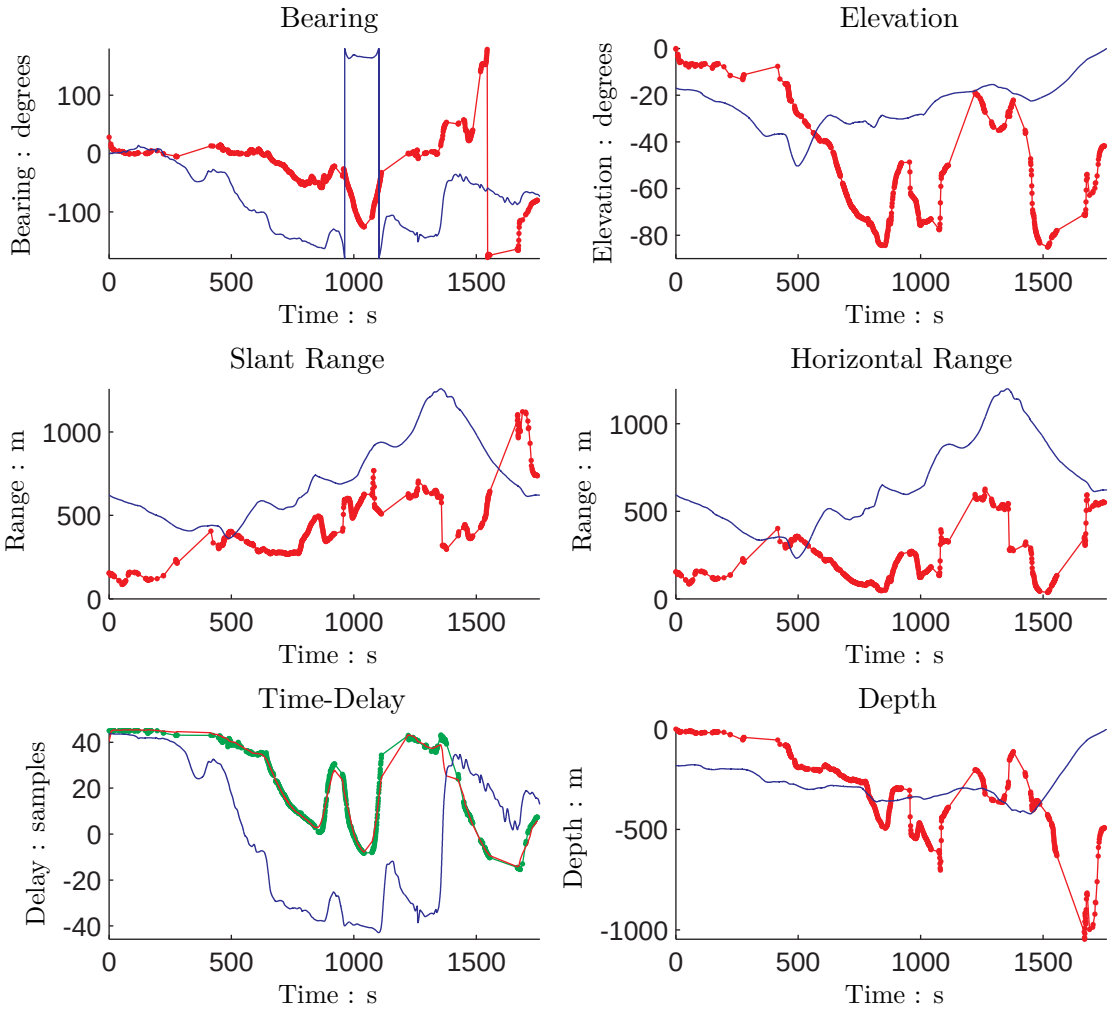

Figure 7.8: Relative particle filter estimated positions for acoustic tracking (red), the pseudo-track (blue) and the measured time-delays as output by the MHT (green) for dataset 3.

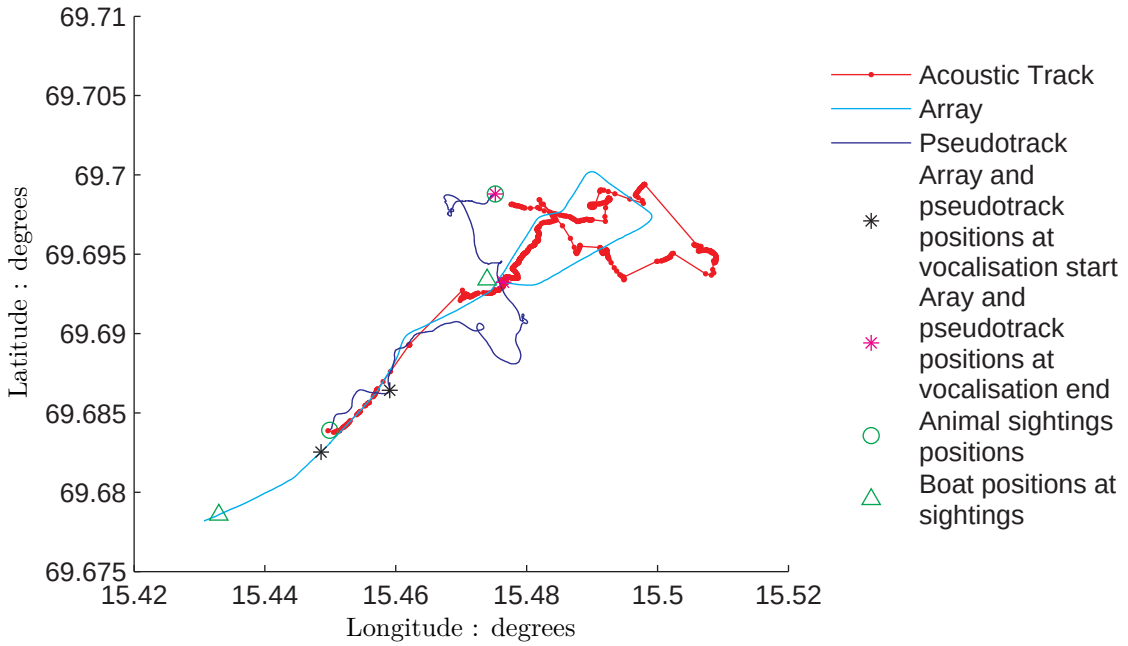

Figure 7.9: Global position reconstructions for the particle filter estimated acoustic track (red), the positions of the array (cyan) and the pseudotrack (blue) for the dataset and results shown in figure 7.8. Date: June 9th 2009. Time: 12:42:01 pm - 1:17:26 pm

depth recorded by the pressure sensor on the DTAG.

Figure 7.9 shows the positions of the array, pseudotrack and particle filter estimated track reconstruction for the dataset and results shown in figure 7.8. Unlike the previous two datasets vocalisation starts a significant time, and therefore distance, from the dive sighting position. The first estimated position however remains at the sighting position even though the time period between sighting and tracking is taken into account by the estimator. This occurs because the sighting position is the mean of the particle positions in the state space. The estimated positions follow the positions of the array during a manoeuvre where the boat and array circle round to form a loop which shows a trend in tracking results to follow the array, however this solution still fits the measurements. When acoustic tracking ceases the range and bearing of the estimated track and the pseudotrack are very similar and the acoustic track finishes close to the surface sighting position.

Figure 7.10 shows tracking position results for a dive cycle where the animal was sighted diving at 1:28:21 pm and sighted at the surface again at 2:05:40 pm. The time-delay measurements and pseudotrack time-delays for dataset 4 in figure 7.10 are not well correlated before 600 s. After 600 s correlation improves and therefore confidence in the pseudotrack improves. Bearing estimates and the pseudotrack are not close matches and there is considerable difference between the pseudotrack and elevation estimate between 900 and 1600 s, however the bearing and elevation estimates fit the time-delay measurements. The over-estimated elevation angle places the animal at a depth significantly greater than the DTAG recorded depth. Slant range estimates follow the trend of the pseudotrack slant range but also include large errors while there are also large differences in the horizontal range estimates and pseudotrack horizontal

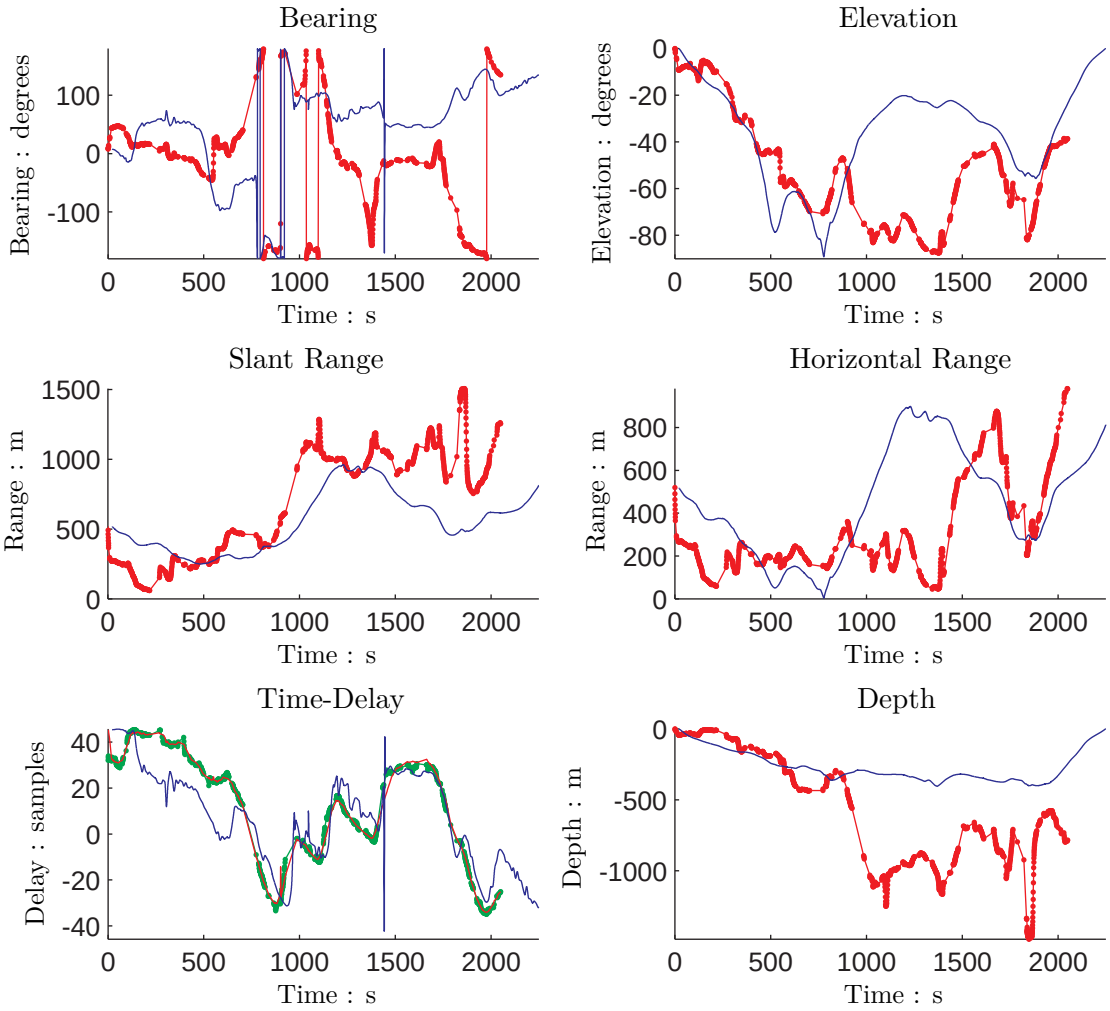

Figure 7.10: Relative particle filter estimated positions for acoustic tracking (red), the pseudotrack (blue) and the measured time-delays as output by the MHT (green) for dataset 4.

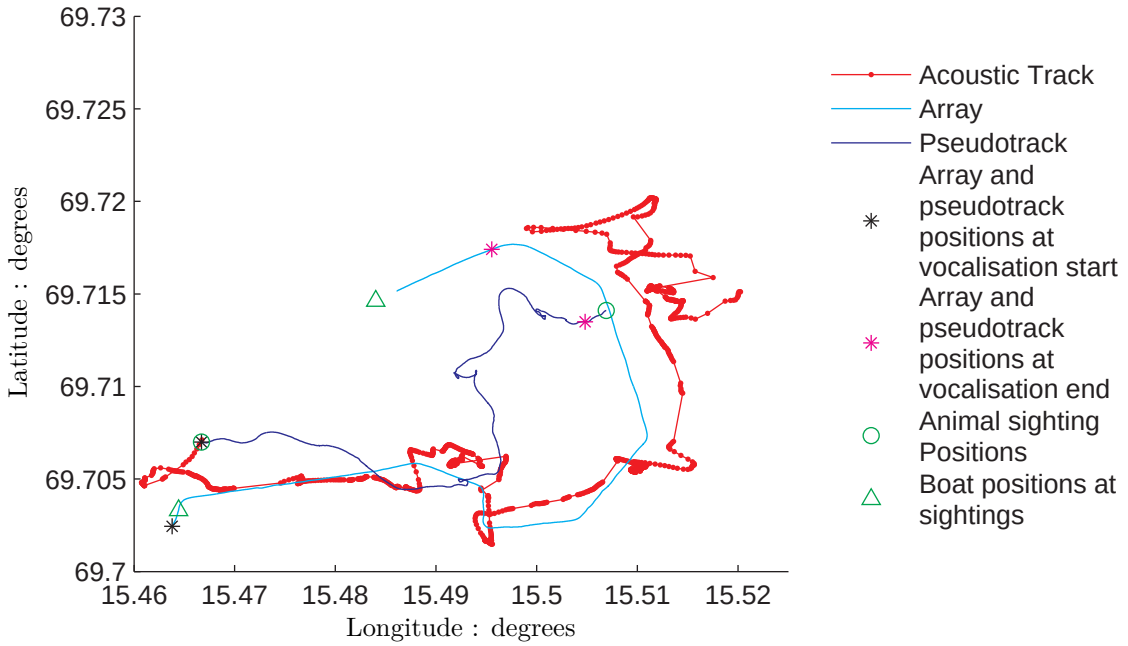

Figure 7.11: Global position reconstructions for the particle filter estimated acoustic track (red), the positions of the array (cyan) and the pseudotrack (blue) for the dataset and results shown in figure 7.10. Date: June 9th 2009. Time: 1:28:21 pm - 2:05:40 pm

range.

Figure 7.11 shows the positions of the array, pseudotrack and particle filter estimated animal positions for the dataset and results shown in figure 7.10. Acoustic tracking results appear to relate to the course taken by the array. This observation is reinforced, at times, by bearing estimates placing the animal ahead of the array and steep elevation angle estimates placing the animal nearly directly below the array. When acoustic tracking ceases the particle filter bearing estimates are close to those of the pseudotrack and the sighting.

Relative position estimates for a fifth dataset, where the dive sighting occurred at 4:31:43 pm and sighted at the surface again at 5:14:07 pm, are shown in figure 7.12. Estimated time-delays correlate with the time-delay measurements and the majority of pseudotrack time-delays also closely match. Bearing, elevation and slant range estimates also follow the general trend of the pseudotrack. Horizontal range estimates don't correlate to the pseudotrack horizontal range as well, however when acoustic tracking ceases estimated horizontal range is fairly close to the pseudotrack horizontal range. The step change in slant range between 500 and 1000 s occurs at the same time as a decrease in elevation angle and manifests as an error in the depth estimate.

Figure 7.13 shows the array positions, pseudotrack positions and reconstructed positions estimated by the particle filter in figure 7.12. The position reconstruction of the particle filter estimated track initially follows the pseudotrack. As tracking continues the bearing estimates tend towards zero which places the animal ahead of the array, however for the earlier stages of tracking the error in the reconstruction is relatively small.

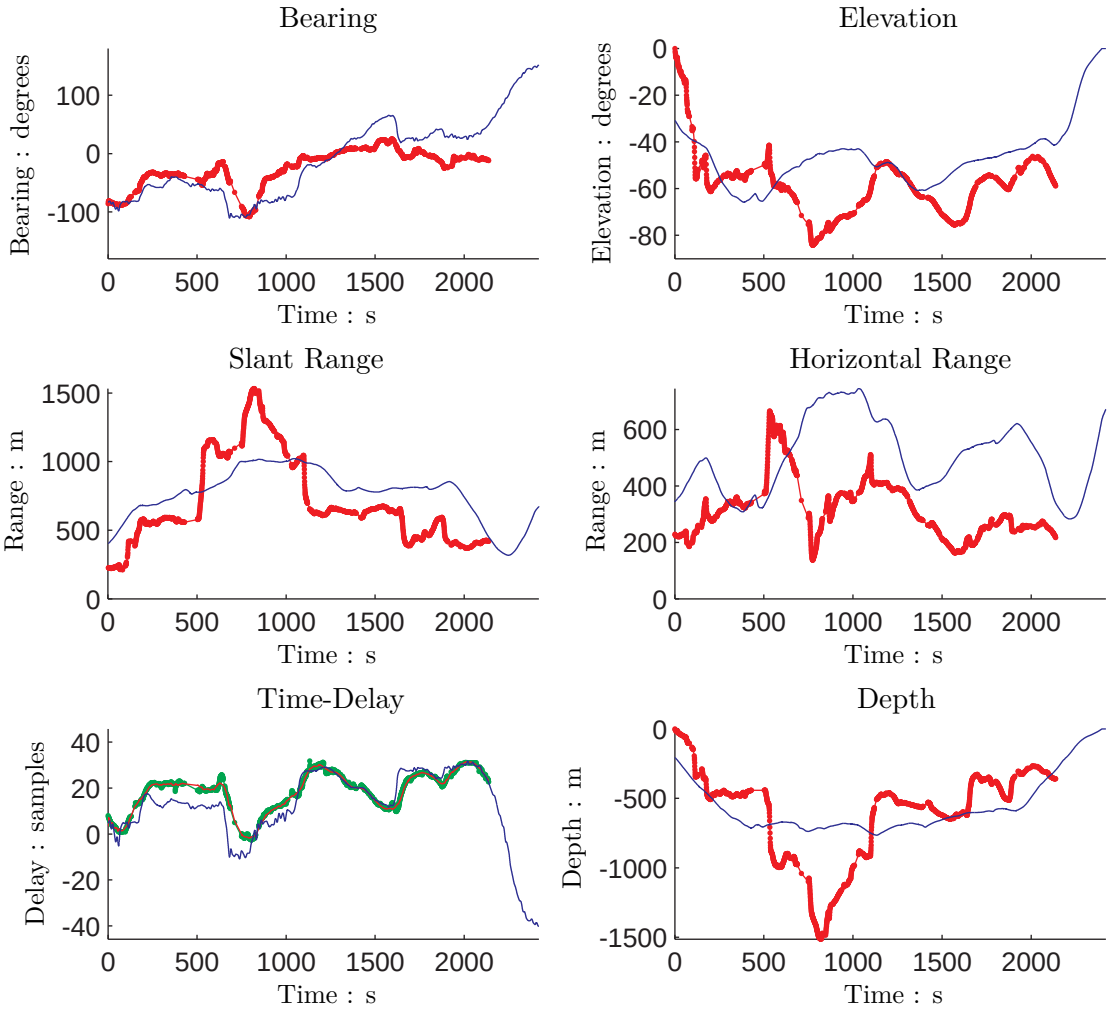

Figure 7.12: Relative particle filter estimated positions for acoustic tracking (red), the pseudotrack (blue) and the measured time-delays as output by the MHT (green) for dataset 5.

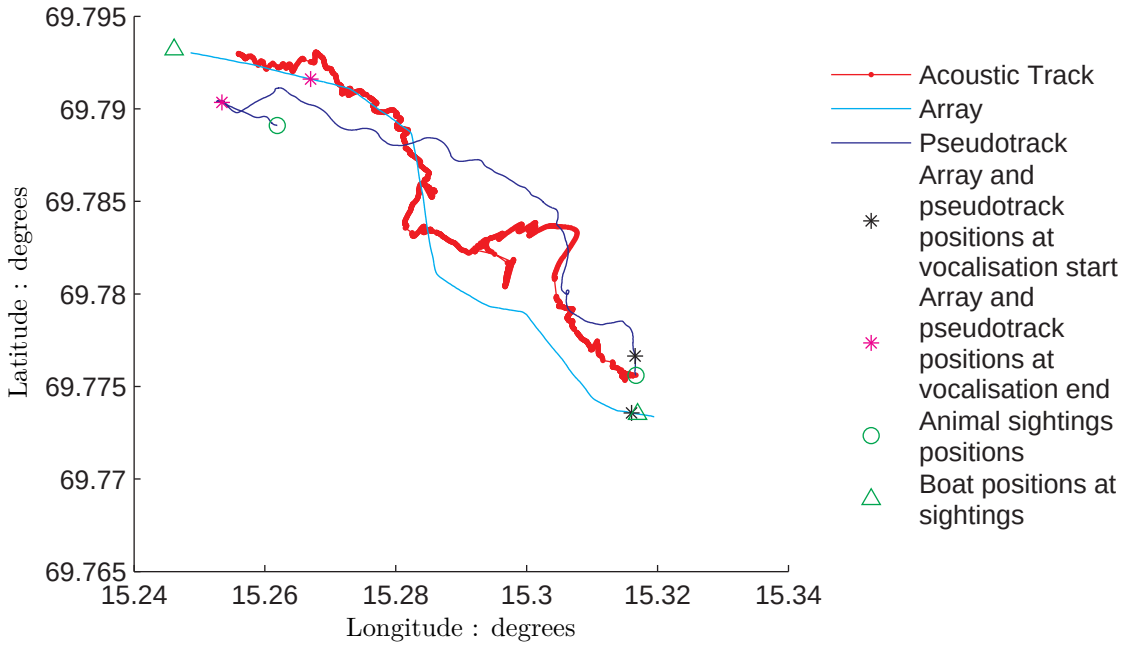

Figure 7.13: Global position reconstructions for the particle filter estimated acoustic track (red), the positions of the array (cyan) and the pseudotrack (blue) for the dataset and results shown in figure 7.12. Date: June 9th 2009. Time: 4:31:43 pm - 5:14:07 pm

7.3.1 Performance Consistency Over Multiple Tracking Instances

Figures 7.14 and 7.15 show multiple particle filter tracking instances for dataset 2, shown in figures 7.4 and 7.5. For all tracking instances time-delay estimates correlate with the measured time-delays. Bearing estimates very closely match across all tracking instances. Elevation, slant range and horizontal range follow the same trends but do not match across tracking instances as consistently as for bearing. Differences in slant range and elevation manifest in the depth estimates which are spread over an interval of 400 m. Across all the tracking instances final position estimates show consistent trends that would cause visual observers to look in the same direction and at similar ranges for the animal surfacing.

7.4 Initialisation From Pseudotrack

Section 7.3 demonstrated that the sighting location provides adequate information for the purposes of initialising the particle filter, however there is often a short delay between the sighting and the start of the animal's vocalisations. Occasionally this delay is significant, such as in dataset 3. Using the pseudotrack reconstruction from the DTAG deployment it is possible to initialise tracking from the animal location provided by the pseudotrack. Although not possible in practice, testing tracking when initialising using more precise location information from the pseudotrack, when vocalisation starts, allows evaluation of tracking error induced by initialisation at the sighting position.

Figures 7.16 and 7.17 show tracking results for dataset 1 where tracking has been initialised

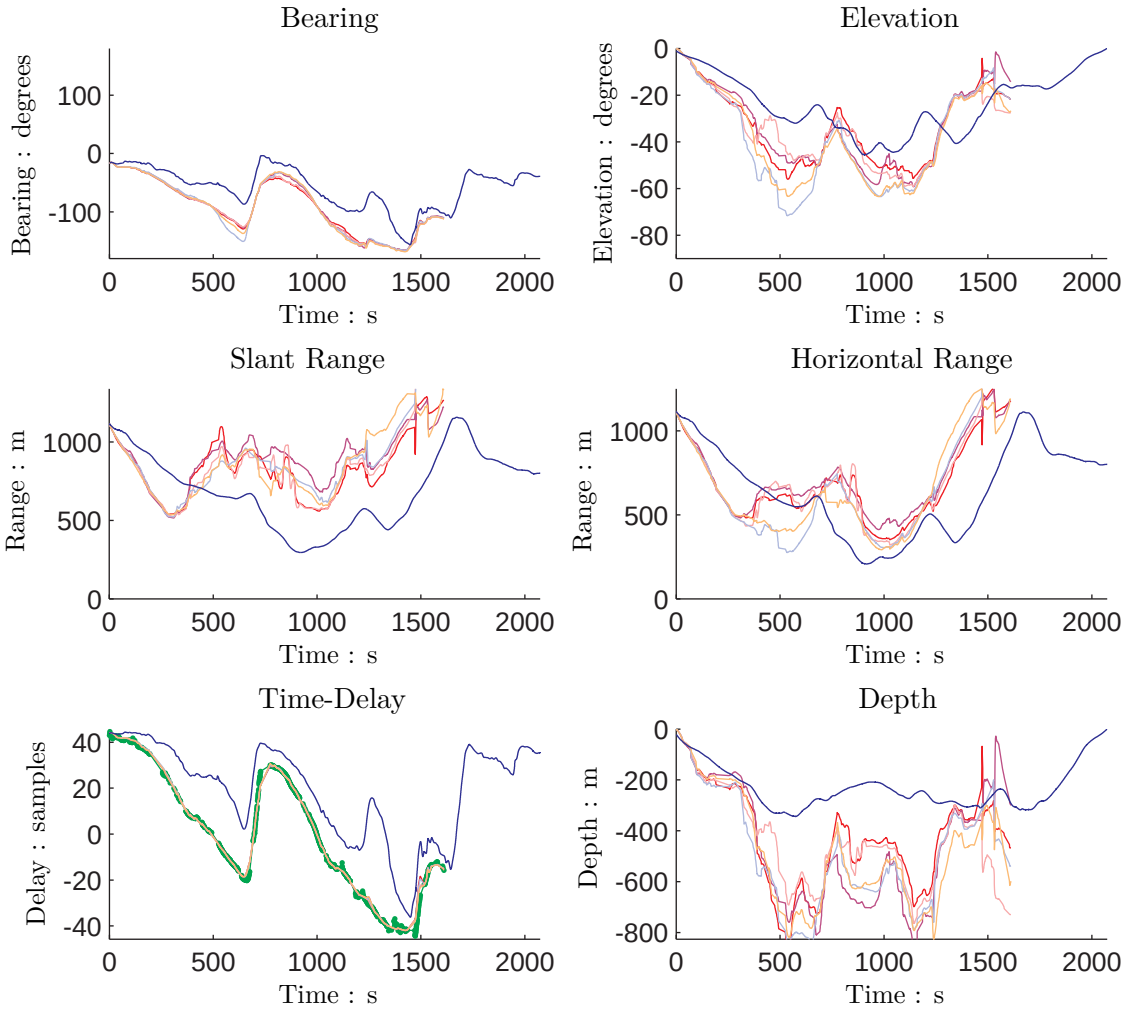

Figure 7.14: Relative positions for multiple particle filter acoustic tracking instances and the DTAG pseudotrack. Points on the estimates indicating the times of vocalisations have been omitted for clarity.

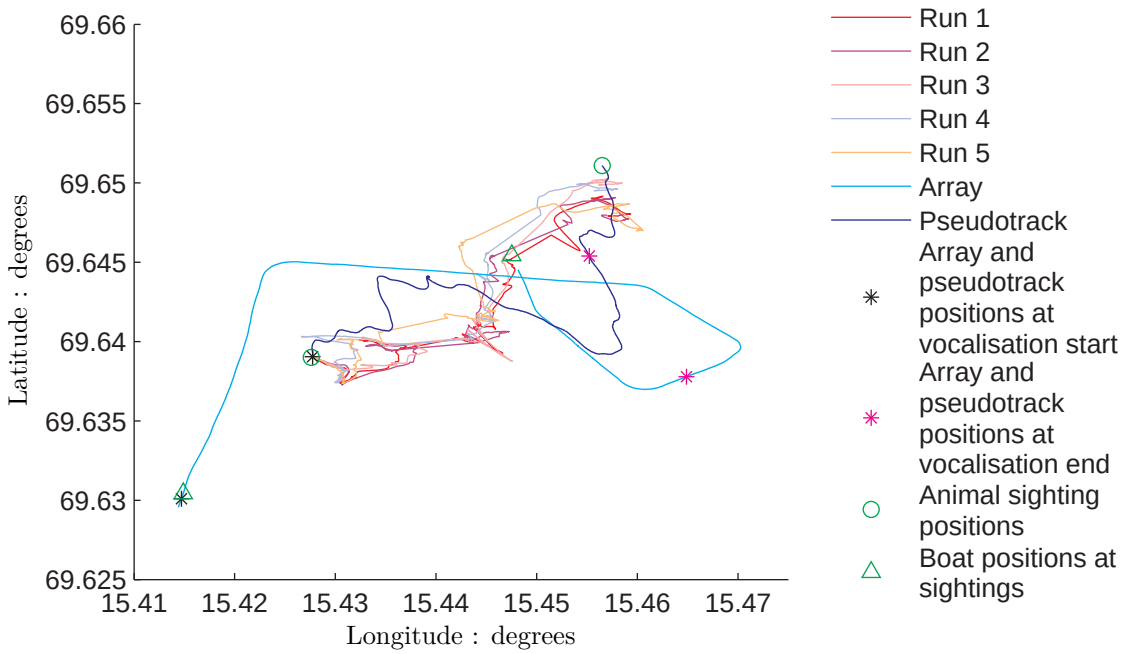

Figure 7.15: Global position reconstructions for multiple particle filter acoustic tracking instances, the DTAG pseudotrack and the array positions for the results shown in figure 7.14. Points indicating the points at which vocalisations occur have been omitted for clarity.

using the pseudotrack. In this dataset vocalisation starts almost immediately after the animal is sighted diving, therefore the animal has not travelled a significant distance and tracking results closely resemble those presented in figures 7.4, 7.5, 7.12 and 7.13.

The time difference between the dive sighting and the start of vocalisations is much longer for dataset 3. Tracking results for initialisation using the sighting position in figures 7.8 and 7.9 demonstrated the algorithm was capable of adapting and over-coming the initial animal location error. Figures 7.18 and 7.19 show tracking results for dataset 3 when initialising from the pseudotrack position for the time at which vocalising, and therefore acoustic tracking, starts. Although overall confidence in the pseudotrack is relatively low, due to the difference between the measured time-delays and the pseudotrack time-delays, confidence is high when vocalisation starts because the measured and pseudotrack time-delays closely match. Differences in results are most easily observed by comparing figures 7.9 and 7.19. The overall shape of the acoustic track reconstructions are very similar with the acoustic track doubling back on itself to form a loop, however the exact shape and position of this loop is different. The final horizontal range estimates differ but final bearing estimates are very similar between figures 7.9 and 7.19.

7.5 Summary and Conclusion

Tracking results have been presented for five datasets. The control vector for the array was derived by assuming a fixed length array tow cable between the array and the boat and

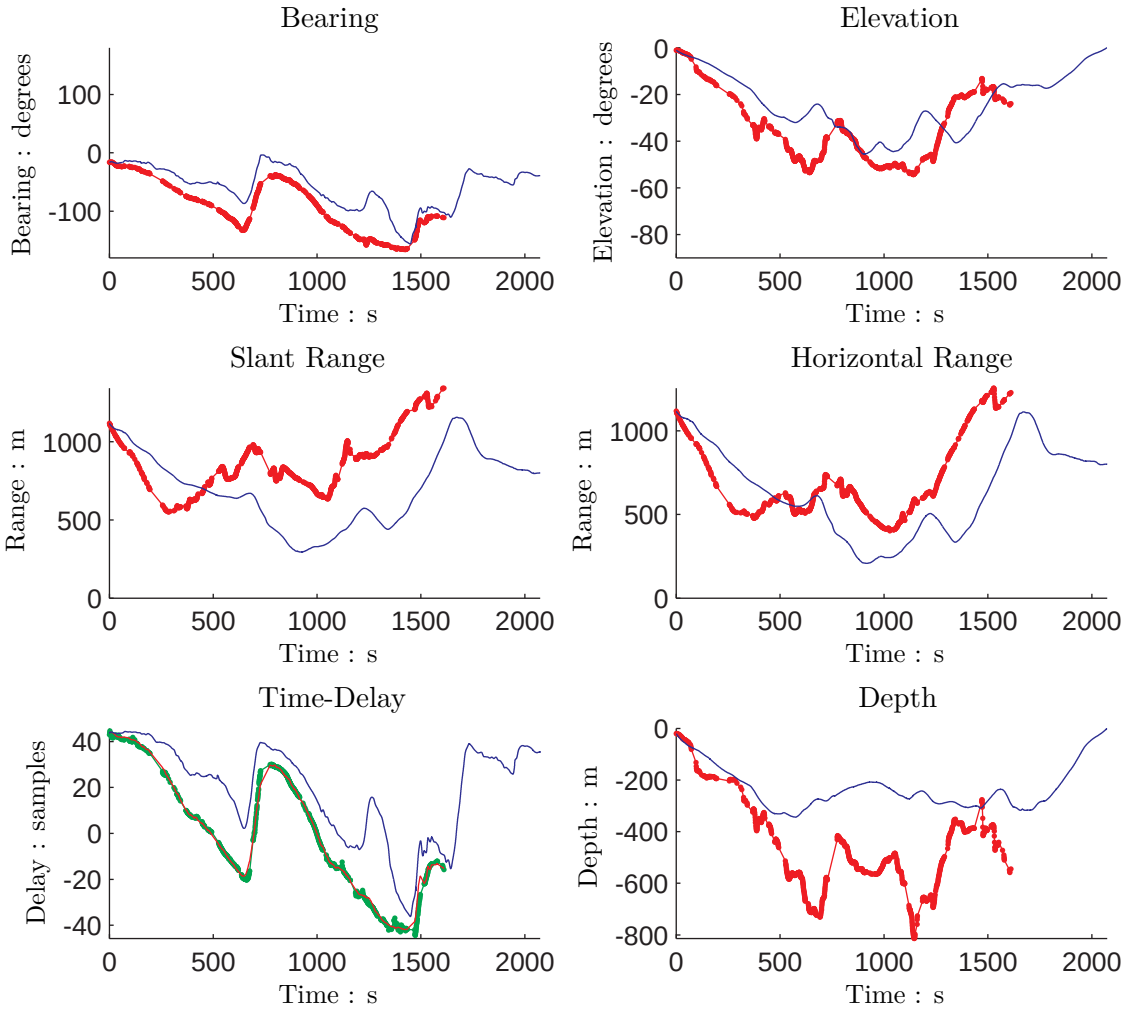

Figure 7.16: Relative positions for multiple acoustic tracking runs and the DTAG pseudotrack

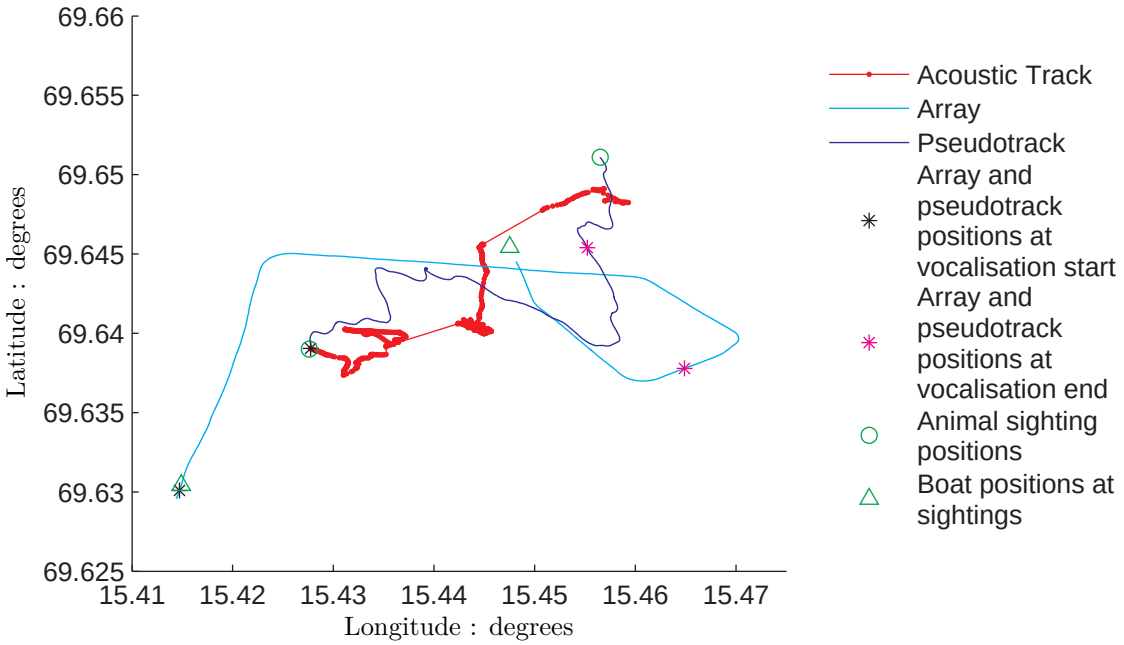

Figure 7.17: Global position reconstructions for multiple acoustic tracking runs and the DTAG pseudotrack

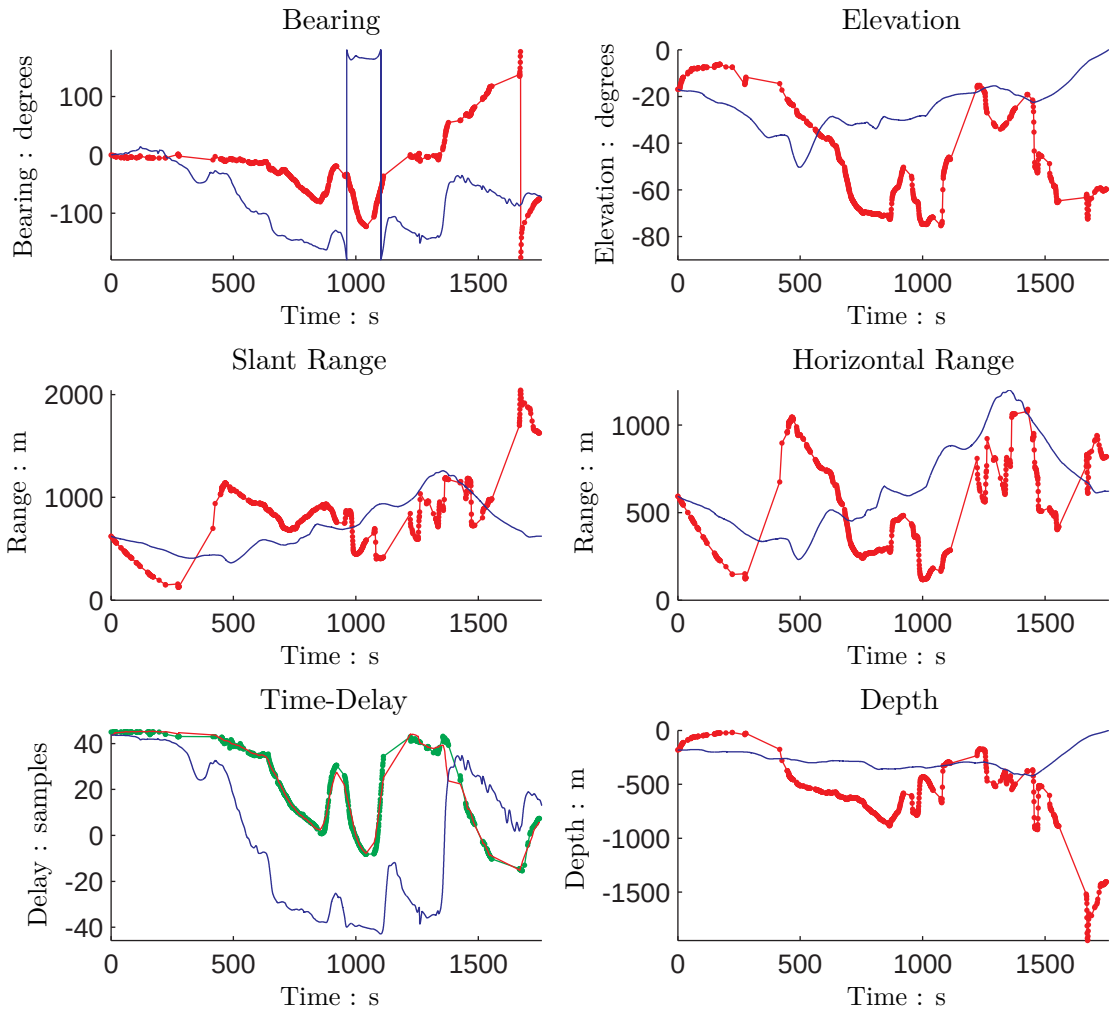

Figure 7.18: Relative positions for multiple acoustic tracking runs and the DTAG pseudotrack

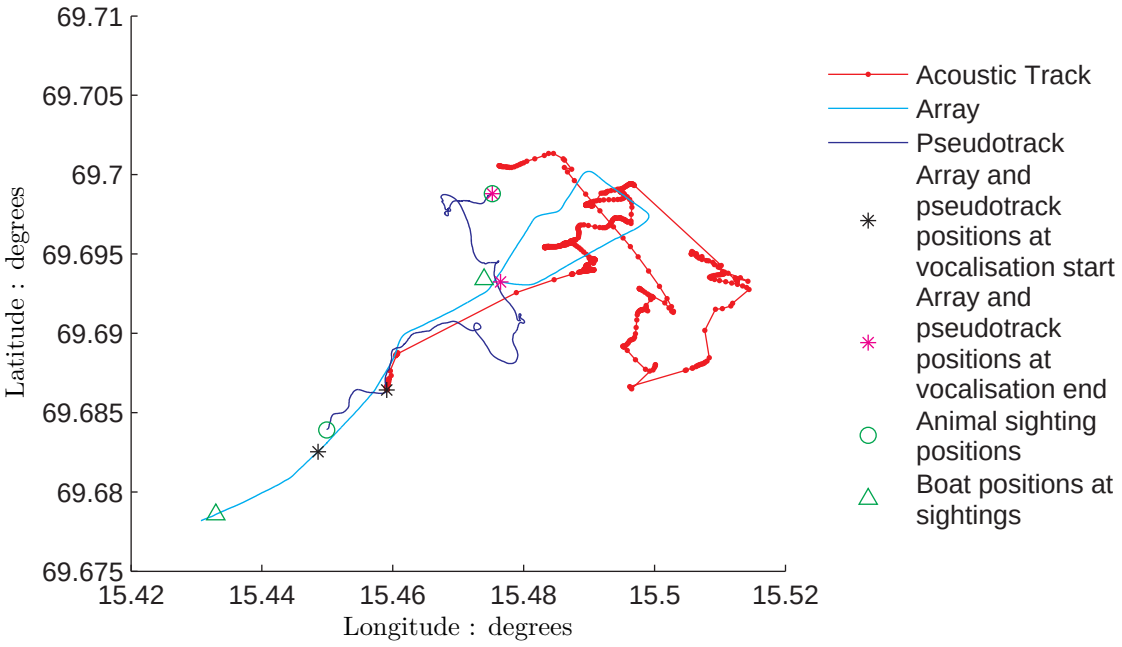

Figure 7.19: Global position reconstructions for multiple acoustic tracking runs and the DTAG pseudotrack

delaying the boat GPS data proportionally to the boat speed. Results for all five datasets were initialised using the position of the sighting when the animal dived. As an indicator of computational time of computing the results shown in figures 7.4 and 7.5, a dataset of 20 minutes duration, takes 2 minutes 40 seconds on a 2.4 GHz Intel Core 2 Duo processor in a laptop computer when implemented in MATLAB and utilising 1000 particles.

Tracking results were compared to the pseudotrack reconstructed from the information acquired by the DTAG and fitted to the sighting positions. Confidence in the pseudotrack was judged by computing the time-delay that would have been received if the animal were in the positions suggested by the pseudotrack and comparing those time-delays to the measured time-delays. The better the correlation between the pseudotrack and measured time-delays the more confidence there was deemed to be in the pseudotrack reconstruction of the whale's positions. Where confidence was low the pseudotrack was deemed to be a poor representation of the ground-truth.

Acoustic tracking results were presented in two forms. Firstly, results were presented in a spherical coordinate system relative to the array with additional horizontal range, depth and time-delay plots for the estimated animal position alongside the equivalent relative positions of the pseudotrack. Secondly, results were shown in a global position reconstruction in latitude and longitude with the positions of the array and pseudotrack. Also shown were the positions of the animal when it was sighted, the position of the boat from which the sightings were recorded and the positions of the array and pseudotrack when the initial and final vocalisations were received. All results placed the final estimated animal position relatively close to the position at which the animal was next sighted at the surface. Repeat tracking realisations of dataset 1 demonstrate that multiple tracking instances do not produce exactly the same results but do demonstrate a consistency in tracking trends.

Between the dive sighting and the animal starting to vocalise it moves, therefore an initial tracking error is incurred by initialising the particle filter using the sighting position. In dataset 1 the interval between the dive sighting and start of vocalisations is relatively short, therefore displacement of the animal over this interval is limited. The difference in tracking results between initialising from the sighting and from the pseudotrack is negligible. In dataset 3 the interval between the dive sighting and start of vocalisations is significant and therefore so is the displacement of the animal. When initialised from the dive sighting the algorithm was able to adapt and estimated a target track that ends close to the surface sighting position. Initialisation from the pseudotrack resulted in a track estimate that was different to the sighting initialised track but followed the same trend.

Several sources of tracking error exist. Firstly, as discussed in chapter 5, the tracking solution is the mean of several tracks that fit the measurements and therefore convergence to the true track is not guaranteed. Secondly, errors in the computation of the time-delays and the MHT data association stages causes measurement noise which reduces tracking performance. Finally, modelling of the array motion and position from the boat GPS data includes several assumptions which can lead to errors manifesting in the control vector input to the system

function. Performance improvements may be gained by equipping the hydrophone array with additional positioning and motion sensing instrumentation.

The conclusions drawn from the results depend on the context of the application within which the tracking algorithm is utilised. In scientific research, where it is simply necessary to follow the dived animal to its next surfacing point, the algorithm has performed satisfactorily. For each tracking realisation of each dataset the algorithm estimates the animal position within a reasonable distance of the position of the pseudotrack when the animal stopped vocalising. In this case a 'reasonable distance' is defined as being in a location that could be seen within a 90° arc of the field of vision of a visual observer. It should be taken into account that this bearing will change if the boat changes heading after vocalisation has ceased. If the algorithm were to be employed in an anthropogenic acoustic impact mitigation application then accurate range estimation is important to ensure a minimum safe distance is maintained between the animal and acoustic source. If the algorithm demonstrated a distinct tendency to over-estimate the range of the animal, though not significantly, then it would be performing suitably well from a conservation viewpoint, which unfortunately is not the case. Overall, results show the proposed algorithm is of practical use for some research purposes. Results may improve given the appropriate array positioning instrumentation and additional hydrophone elements.

Chapter 8

Conclusions

A particle filter solution has been developed and presented for tracking dived and vocalising sperm whales using passive acoustic arrival time-delays between two element towed hydrophone arrays. This concluding chapter summarises the previous chapters and discusses the usefulness of the results produced by the developed algorithms and future work and further development.

8.1 Summary and Results Evaluation

This section summarises the work presented over the previous chapters. Chapter 2 discussed the limitations of localising and tracking sperm whales using a towed hydrophone array. A time-delay measurement acquired using a hydrophone element pair is often assumed to be the animal bearing, either to the left or right of the array. Such assumptions negate animal depth, range is unknown and a left-right ambiguity remains. Range estimates and left-right ambiguity resolution can be established from successive time-delay measurements in conjunction with boat manoeuvres, however these methods fail to account for the animal's motion. It was proposed that the source location ambiguity be modelled as a PDF that can be updated each time a new measurement is received.

Tracking in the manner proposed in chapter 2 can be implemented using the tracking filters discussed in chapter 3. It was concluded that the SIR particle filter is the most suitable tracking filter for the application because the system noise variance is relatively high and the SIR particle filter has previously been successfully applied to bearings and angle only tracking problems.

Critical to the design of a particle filter solution is the design of the importance distribution, which is subject to the system function and system noise distribution. Chapter 4 reviewed several motion models and tracking coordinate systems and developed a suitable system function for modelling sperm whale motion. It was proposed that system noise samples be drawn in a spherical system with motion updates applied in Cartesian coordinates. Samples for changes

in heading, pitch and speed were drawn from a normal distribution. Once drawn, speed noise samples were subjected to a rejection function that limited the maximum speed that could be obtained within the model. Without this rejection stage particles would be able to accelerate to speeds that would not realistically represent sperm whale motion and commonly lead to significant range over-estimates. It was also concluded that MMSE estimates of the animal's position from the particles should be computed in Cartesian space to avoid possible bearing estimation problems where a target passing behind the array could be estimated as being in front.

In chapter 5 the proposed algorithm was tested on several simulated datasets. The complexity of the tracking problem was developed from tracking a simple non-manoeuvring constant velocity target at a known starting position and travelling in a known direction using a time-delay measurement to tracking a manoeuvring varying velocity target at an unknown starting location. As the number of parameters to be estimated increased tracking accuracy and consistency decreased. It was concluded that a manoeuvring and varying velocity target can be tracked using time-delay measurements but information on the starting location is required. In a practical sperm whale tracking situation this location would be a sighting.

Sperm whales are typically encountered in groups, so to maximise its usefulness, a tracking system needs the facility to track multiple animals simultaneously. Association of received clicks to specific click trains is not a trivial task and is a research topic in itself. Multiple animal tracking was separated into a measurement association problem and target tracking problem, whereby once measurement data has been associated each target is individually tracked as a single target tracking problem. Chapter 6 concluded that separating the measurement association and tracking components was the most appropriate solution so that the developed measurement association algorithm could be employed independently of the spatial tracking algorithm.

An MHT measurement association solution was developed and tested, whereby click association was based on the received time-delay. Results demonstrated that the majority of clicks were correctly associated with the correct click train, however breaks in the click trains did occasionally appear. In these cases the algorithm had divided the click train into several click trains. Other click detections were either identified as clutter or incorrectly associated with short trains of impulse detections. For use in chapter 7 some manual adjustment of the MHT data association results was necessary, however the time necessary for this is significantly less than manually associating clicks with animals.

Utilising a MHT based data association solution demonstrated two additional benefits. Firstly identification of click trains is useful for the detection of sperm whales. Isolated sperm whale clicks are unlikely to be received independently of a click train, therefore identifying if a click is part of a click train contributes to identification of sperm whales. This method could be expanded to identifying echo location click vocalisations from other cetacean species, such as beaked whales. Once a click train has been detected classification can then be performed on the complete click train. Secondly, the Kalman filters in the MHT smooth the time-delay

measurements thereby reducing the effect of the integer quantisation that results from the cross-correlation process. This effect achieves the same aim as interpolation of the acoustic signals or cross-correlation function to increase the resolution of the time-delay measurements. Separating the data association algorithm from the spatial tracking algorithm increases the applicability of the developed solution as it can be utilised independently of the particle filter based developments.

Chapter 7 demonstrated the tracking algorithm on five dive cycles of an animal from a real dataset with the sighting position utilised as the initial position. As well as acoustic and sightings data, the dataset also included DTAG data from which the pseudotrack could be reconstructed and against which the acoustic track could be compared. Results were presented relative to the array in spherical form and as a global position reconstruction. Typically the bearing estimate when tracking ended was close to the bearing at which the animal was then sighted when manoeuvres performed after tracking had ceased were taken into account. Range and elevation estimates were less successful, however all tracking results presented a solution that fitted the time-delay measurements. Tracking performance was adequate for applications where it is necessary to follow an animal during a dive, however range measurements are likely to be insufficient for monitoring the relative range of animals for the mitigation of the impact of anthropogenic acoustic sources such as sonar and seismic surveying.

Consistency results for the first dive cycle demonstrated the most consistently estimated parameter is bearing. Estimation of other parameters consistently followed the same trends. Further experiments tested the tracking difference that results from utilising the sighiting as the initial position by initialising from the pseudotrack position when vocalisation begins. When vocalisation commenced shortly after the dive sighting tracking results demonstrated very little difference. When the period between sighting and vocalising was longer the track reconstruction formed a similar shape but in a slightly different position. It was concluded that sighting information was sufficient for initialising the algorithm.

8.2 Future Work

Several points of further development exist for both the MHT data association algorithm and particle filter spatial tracking algorithms. Further developments could improve tracking performance and broaden the application range for the methods developed.

Given a pre-determined sound pressure exposure level regarded as acceptable and assumptions of the environmental parameters affecting acoustic propagation, a minimum safe distance between source and animal can be calculated. The tracking method demonstrated produces tracking results and range estimates that are subject to a degree of error and therefore it is necessary to incorporate this error into the minimum safe distance calculation. Although not entirely accurate, the pseudotracks that yielded effective time-delay estimates close to those actually measured provide the best available data of actual animal position. The error between these pseudotracks and the acoustically derived track could then be computed. The magnitude

of this error, particularly for slant range, could be a potential area of conflict of interest for concerned parties. From a conservation angle this error margin should be wide, and therefore cautious, to minimise the potential of the animal's position incorrectly being estimated as beyond the minimum range when it is in fact within the minimum range boundary. Provision of a larger error margin is unlikely to be favourable with communities such as the oil and gas industry who are unlikely to want to pause a survey when there is doubt surrounding whether an animal's range is less than the minimum safe distance. A decision on the acceptable error margins would have to be based on how the estimation error effects the sound pressure level received by the animal and the corresponding risk.

The data association algorithm tended to fail around the occurrence of array manoeuvres. When using a MHT incorporating Kalman filters there's a trade-off between tracking performance during manoeuvring and non-manoeuvring periods. It could be suggested that performance of the MHT algorithm could be enhanced during both periods by incorporation of manoeuvring information, however applying a control vector to the system function will not alleviate the problem. The received time-delay measurement is a function of both the bearing and elevation angles, therefore the control vector is not representative of the received change in measurement when a manoeuvre is performed. In such cases an interacting multiple model MHT (IMM-MHT) may be more appropriate. An IMM-MHT utilises EKFs instead of Kalman filters and therefore allows system function switching where the utilised system function is dependent on whether the observer is manoeuvring or not [124–126]. If no manoeuvre is in progress a constant velocity motion model is utilised, where a manoeuvre is progress the system function switches to a manoeuvring motion model. Typically manoeuvres are detected from the system dynamics and measurements, however model switching could be controlled by the control vector.

Further improvements in spatial tracking performance could be achieved through both algorithm and hardware development. It has been suggested that improved angle-only tracking is achievable using a locally-linearised particle filter [61], which has not been tested in this work.

Another area that has not been explored is the effect of time-delay measurement error on tracking results both within the MHT time-delay tracking and data-association method and in the particle filter spatial tracking method. There are several potential areas of interest surrounding time-delay error. Firstly the sampling rate the acoustic data streams are captured at directly affects the resolution of the time-delay measurement which, in turn, affects refinement of the gate size in the MHT as well as the measurement covariance matrix. The effects of measurement noise propagate from the MHT output to the particle filter spatial tracking results should also be examined. Further investigation could examine the optimal sample rate that provides the best possible time-delay resolution within the practical constraints of the application so that array snaking does not become apparent in the time-delay measurements. Secondly, the relationship between animal position relative to the hydrophone array and estimation error could be quantified. Acoustic receptions close to end-fire positions suffer from greater quantisation in time-delay computation, as discussed in section 2.2.1, and animals at greater range moving in a comparable manner to animals at closer range will produce less

variation in time-delay measurements. The effects of both of these positioning factors on tracking performance should be investigated.

The towed hydrophone array configuration utilised in this work represents the simplest hydrophone configuration possible and therefore arguably the most difficult tracking problem. Incorporating additional hydrophone element pairs into the hydrophone array, as discussed in section 2.7.1, would provide additional time-delay measurements that could provide ranging information [28,29] and therefore reduce the order of the source ambiguity. This could greatly improve estimation because the measurement set would become a function of bearing, elevation and range. Adaptation of the algorithm to utilise these additional time-delays would require appropriate modification of the measurement function. These modifications would involve computing two time-delays for each particle as would be received by each hydrophone element pair. It would be necessary to treat one element pair as a 'master' pair, which the animal's position is tracked in relation to, and the other as a 'slave' pair who's position is known relative to the master pair. It would be necessary to compute separate control vectors for each element pair because the separation between the sensor pairs results in one responding to manoeuvres before the other. This can be implemented using the method described in section 7.2 with the appropriate distances for each hydrophone pair behind the towing vessel and then calculating the position of the slave pair in relation to the master pair. Such a configuration would also provide initial ranging information so it may be possible to initiate tracking without a dive position sighting.

The hydrophone array could be further enhanced through the addition of positioning and heading sensors on the hydrophone elements. Such instrumentation would reduce errors that arise as a result of the assumptions made when computing the array heading from the boat GPS in section 7.2. Particle filtering could also be utilised in tracking and computing range estimates using measurements received by an acoustic vector sensor [127].

As mentioned in chapter 1, acoustics are utilised in the study of other deep diving and great whale species including the beaked whale family (*Ziphiidae*) [36], north Atlantic right whales, fin whales and blue whales [12]. Given suitable detection and time-delay measurement algorithms, the tracking algorithm could be applied to tracking these other species. Smaller cetacean species can often be tracked visually, are encountered in large groups or do not produce vocalisations at insufficient source sound pressure levels and at frequencies too high to propagate over the distances required for acoustic tracking in the manner as presented here for sperm whales. The tracking algorithm could be combined with frequency contour tracking [128, 129], for tracking cetaceans that produce tonal vocalisations such as humpback whales (*Megaptera novaeangliae*). Scope also exists for development of the tracking algorithms to track non-marine mammal targets such as ships and submarines.

Bibliography

[1] W. C. Cummings and D. V. Holliday, "Passive acoustic location of bowhead whales in a population census off Point Barrow, Alaska," *The Journal of the Acoustical Society of America*, vol. 78, no. 4, pp. 1163–1169, 1985.

[2] M. A. McDonald and C. G. Fox, "Passive acoustic methods applied to fin whale population density estimation," *The Journal of the Acoustical Society of America*, vol. 105, no. 5, pp. 2643–2651, 1999.

[3] T. Lewis, D. Gillespie, C. Lacey, J. Matthews, M. Danbolt, R. Leaper, R. McLanaghan, and A. Moscrop, "Sperm whale abundance estimates from acoustic surveys of the Ionian Sea and Straits of Sicily in 2003," *Journal of the Marine Biological Association of the United Kingdom*, vol. 87, no. 1, pp. 353 – 357, 2007.

[4] O. Boisseau, J. Matthews, D. Gillespie, C. Lacey, A. Moscrop, and N. E. Ouamari, "A visual and acoustic survey for harbour porpoises off North-West Africa: further evidence of a discrete population," *African Journal of Marine Science*, vol. 29, no. 3, pp. 403–410, 2007.

[5] O. Boisseau, C. Lacey, T. Lewis, A. Moscrop, M. Danbolt, and R. McLanaghan, "Encounter rates of cetaceans in the Mediterranean Sea and contiguous Atlantic area," *Journal of the Marine Biological Association of the UK*, vol. First View, pp. 1–11, 2010.

[6] D. H. Cato, M. Savage, R. A. Dunlop, I. Parnum, M. Blewitt, G. Sue, D. Donnelly, J. Cleary, and R. D. McCauley, "Acoustic surveying for beaked whales in the Coral Sea as a mitigation measure for naval exercises," (Sydney, NSW, Australia), 2010.

[7] O. Gerard, C. Carthel, and S. Coraluppi, "Estimating the number of beaked whales using an MHT tracker," in *New Trends for Environmental Monitoring Using Passive Systems, 2008*, pp. 1–6, Oct. 2008.

[8] S. Matthews, J.N.and Brown, D. Gillespie, M. Johnson, R. McLanaghan, A. Moscrop, D. Nowacek, R. Leaper, T. Lewis, and P. Tyack, "Vocalisation rates of the North Atlantic right whale (Eubalaena glacialis)," *Journal of Cetacean Research and Managment*, vol. 3, no. 3, pp. 271–282, 2001.

[9] M. Wahlberg, "The acoustic behaviour of diving sperm whales observed with a hydrophone array," *Journal of Experimental Marine Biology and Ecology*, vol. 281, no. 1-2, pp. 53 – 62, 2002.

[10] P. J. O. Miller, M. P. Johnson, and P. L. Tyack, "Sperm whale behaviour indicates echolocation click buzzes 'creaks' in prey capture," *Proceedings of the Royal Society*, vol. 271, pp. 2239–2247, 2004.

[11] W. M. X. Zimmer, M. P. Johnson, P. T. Madesn, and P. L. Tyack, "Echolocation clicks of free-ranging Cuvier's beaked whales (Ziphius cavirostris)," *The Journal of the Acoustical Society of America*, vol. 117, no. 6, pp. 3919–3927, 2005.

[12] O. Boisseau, D. Gillespie, R. Leaper, and A. Moscrop, "Blue (Balaenoptera musculus) and fin (B. physalus) whale vocalisations measured from northern latitudes of the Atlantic Ocean," *Journal of Cetacean Research and Managment*, vol. 10, no. 1, pp. 23–30, 2008.

[13] H. Whitehead, *Sperm Whales Social Evolution in the Ocean*. The Univeristy of Chicago Press, 2003.

[14] B. Mohl, M. Wahlberg, P. Madsen, L. Miller, and A. Surlykke, "Sperm whale clicks: Directionality and source level revisited," *Journal of the Acoustical Society of America*, vol. 107, no. 1, pp. 638 – 48, 2000.

[15] B. Mohl, M. Wahlberg, P. T. Madsen, A. Heerfordt, and A. Lund, "The monopulsed nature of sperm whale clicks," *The Journal of the Acoustical Society of America*, vol. 114, no. 2, pp. 1143–1154, 2003.

[16] W. Zimmer, P. Tyack, M. Johnson, and P. Madsen, "Three-dimensional beam pattern of regular sperm whale clicks confirms bent-horn hypothesis," *Journal of the Acoustical Society of America*, vol. 117, no. 3, pp. 1473 – 85, 2005.

[17] M. Hansen, M. Wahlberg, and P. Madsen, "Low-frequency components in harbor porpoise (Phocoena phocoena) clicks: Communication signal, by-products or artifacts?," *Journal of the Acoustical Society of America*, vol. 124, no. 6, pp. 4059 – 4068, 2009.

[18] R. Antunes, L. Rendell, and J. Gordon, "Measuring inter-pulse intervals in sperm whale clicks: Consistency of automatic estimation methods," *Journal of the Acoustical Society of America*, vol. 127, no. 5, pp. 3239 – 3247, 2010.

[19] F. I. P. Samarra, V. B. Deecke, K. Vinding, M. H. Rasmussen, R. J. Swift, and P. J. O. Miller, "Killer whales (Orcinus orca) produce ultrasonic whistles," *Journal of the Acoustical Society of America*, vol. 128, no. 5, pp. EL205 – EL210, 2010.

[20] D. H. Cato, "Simple methods of estimating source levels and locations of marine animal sounds," *Journal of the Acoustical Society of America*, vol. 104, no. 3, pp. 1667 – 1678, 1998.

[21] K. M. Stafford, C. G. Fox, and D. S. Clark, "Long-range acoustic detection and localization of blue whale calls in the northeast Pacific Ocean," *The Journal of the Acoustical Society of America*, vol. 104, no. 6, pp. 3616–3625, 1998.

[22] P. White, T. Leighton, D. Finfer, C. Powles, and O. Baumann, "Localisation of sperm whales using bottom-mounted sensors," *Applied Acoustics*, vol. 67, no. 11-12, pp. 1074 – 90, 2006.

[23] E.-M. Nosal and L. N. Frazer, "Track of a sperm whale from delays between direct and surface-reflected clicks," *Applied Acoustics*, vol. 67, pp. 1187–1201, 2006.

[24] R. P. Morrissey, "Passive acoustic detection and localisation of sperm whales (Physeter macrocephalus) in the Tongue of the Ocean," *Applied Acoustics*, vol. 67, pp. 1091–1105, 2006.

[25] F. Desharnais, G. R. Ebbeson, M.-N. R. Matthews, G. J. Heard, D. J. Thomson, and G. H. Brooke, "A generalized beamformer for localization of marine mammals," *Applied Acoustics*, vol. 67, no. 11-12, pp. 1213 – 1225, 2006.

[26] C. Laplanche, "A Bayesian method to estimate the depth and the range of phonating sperm whales using a single hydrophone," *The Journal of the Acoustical Society of America*, vol. 121, no. 3, pp. 1519–1528, 2007.

[27] M. Baumgartner, L. Freitag, J. Partan, K. Ball, and K. Prada, "Tracking large marine predators in three dimensions: The real-time acoustic tracking system," *Oceanic Engineering, IEEE Journal of*, vol. 33, pp. 146–157, April 2008.

[28] A. Thode, "Tracking sperm whale (Physeter macrocephalus) dive profiles using a towed passive acoustic array," *The Journal of the Acoustical Society of America*, vol. 116, no. 1, pp. 245–253, 2004.

[29] A. Thode, "Three-dimensional passive acoustic tracking of sperm whales (Physeter macrocephalus) in ray-refracting environments," *Journal of the Acoustical Society of America*, vol. 118, no. 6, pp. 3575 – 3584, 2005.

[30] E. Skarsoulis and M. Kalogerakis, "Two-hydrophone localization of a click source in the presence of refraction," *Applied Acoustics*, vol. 67, no. 11-12, pp. 1202 – 1212, 2006.

[31] V. Kandia and Y. Stylianou, "Detection of sperm whale clicks based on the Teager-Kaiser energy operator," *Applied Acoustics*, vol. 67, no. 11-12, pp. 1144 – 1163, 2006.

[32] O. Gerard, C. Carthel, and S. Coraluppi, "Classification of odontocete buzz clicks using a multi-hypothesis tracker," in *IEEE Oceans 2009-EUROPE*, pp. 1–7, May 2009.

[33] L. Hamilton and J. Cleary, "Automatic discrimination of beaked whale clicks in noisy acoustic time series," in *IEEE Oceans 2010 - Sydney*, 2010.

[34] B. Mohammad and R. McHugh, "Automatic detection and characterization of dispersive North Atlantic right whale upcalls recorded in a shallow-water environment using a

region-based active contour model," *IEEE Journal of Oceanic Engineering*, vol. PP, no. 99, 2008. Accepted for publication.

[35] M. Wahlberg, B. Mohl, and P. T. Madsen, "Estimating source position accuracy of a large-aperture hydrophone array for bioacoustics," *Journal of the Acoustical Society of America*, vol. 109, no. 1, pp. 397 – 406, 2001.

[36] W. M. X. Zimmer, J. Harwood, P. L. Tyack, M. P. Johnson, and P. T. Madsen, "Passive acoustic detection of deep-diving beaked whales," *The Journal of the Acoustical Society of America*, vol. 124, no. 5, pp. 2823–2832, 2008.

[37] A. von Benda-Beckmann, F. Lam, D. Moretti, K. Fulkerson, M. Ainslie, S. van IJsselmuide, J. Theriault, and S. Beerens, "Detection of Blainville's beaked whales with towed arrays," *Applied Acoustics*, vol. 71, no. 11, pp. 1027 – 1035, 2010.

[38] D. P. Nowacek, L. H. Thorne, D. W. Johnston, and P. L. Tyack, "Responses of cetaceans to anthropogenic noise," *Mammal Review*, vol. 37, no. 2, pp. 1365–2907, 2007.

[39] E. Parsons, S. J. Dolman, M. Jasny, N. A. Rose, M. P. Simmonds, and A. J. Wright, "A critique of the UK's JNCC seismic survey guidelines for minimising acoustic disturbance to marine mammals: Best practise?," *Marine Pollution Bulletin*, vol. 58, no. 5, pp. 643 – 651, 2009.

[40] P. Miller, M. Johnson, P. Madsen, N. Biassoni, M. Quero, and P. Tyack, "Using at-sea experiments to study the effects of airguns on the foraging behavior of sperm whales in the Gulf of Mexico," *Deep-Sea Research Part I: Oceanographic Research Papers*, vol. 56, no. 7, pp. 1168 – 1181, 2009.

[41] L. E. Rendell and J. C. D. Gordon, "Vocal response of long-finned pilot whales (Globicephala melas) to military sonar in the Ligurian Sea," *Marine Mammal Science*, vol. 15, no. 1, pp. 198 – 204, 1999.

[42] T. Cox, T. Ragen, A. Read, E. Vos, R. Baird, J. Balcomb, K. Barlow, J. Cladwell, C. T., L. Crum, A. D'Amico, G. D'Spain, A. Fernandez, J. Finneran, R. Gentry, W. Gerth, F. Gulland, J. Hildebrand, D. Houserp, T. Hullar, P. Jepson, D. Ketten, C. MacLeod, P. Miller, S. Moore, D. Mountain, D. Palka, P. Ponganis, S. Rommel, T. Rowles, B. Taylor, P. Tyack, D. Wartzok, R. Gisiner, J. Meads, and L. Benner, "Understanding the impacts of anthropogenic sound on beaked whales," *Journal of cetacean research and management*, vol. 7, no. 3, pp. 177–187, 2006.

[43] A. Frantzis, "Does acoustic testing strand whales?," *Nature*, vol. 392, p. 29, March 1998.

[44] United States Department of Commerce and United States Navy, "Joint interim report Bahamas marine mammal stranding event of 15-16 March 2000," tech. rep., National Oceanic and Atmospheric Administration, December 2001.

[45] P. D. Jepson, M. Arbelo, R. Deaville, I. A. P. Patterson, P. Castro, J. R. Baker, E. Degollada, H. M. Ross, P. Herraez, A. M. Pocknell, F. Rodriguez, F. E. Howie, A. Espinosa,

R. J. Reid, J. R. Jaber, V. Martin, A. A. Cunningham, and A. Fernandez, "Gas-bubble lesions in stranded cetaceans," *Nature*, vol. 425, pp. 575–576, 10 2003.

[46] S. Rommel, A. Costidis, A. Fernandez, P. Jepson, D. Pabst, W. McLellan, D. Houser, T. Cranford, van Helden A.L., D. Allen, and N. Barros, "Elements of beaked whale anatomy and diving physiology and some hypothetical causes of sonar-related stranding," *Journal of Cetacean Research and Management*, vol. 7, no. 3, pp. 189–209, 2006.

[47] P. Kvadsheim, F.-P. Lam, P. Miller, A. C. Alves, R. Antunes, A. Bocconcelli, S. v. Ijsselmuide, L. Kleivane, M. Olivierse, and F. Visser, "Cetaceans and naval sonar – the 3S-2009 cruise report," tech. rep., Norwegian Defence Research Establishment (FFI), July 2009.

[48] A. Thode, D. K. Mellinger, S. Stienessen, A. Martinez, and K. Mullin, "Depth-dependent acoustic features of diving sperm whales (Physeter macrocephalus) in the Gulf of Mexico," *Journal of the Acoustical Society of America*, vol. 112, no. 1, pp. 308 – 321, 2002.

[49] D. Gillespie, J. Gordon, R. Mchugh, D. Mclaren, D.and Mellinger, P. Redmond, A. Thode, P. Trinder, and X. Deng, "PAMGUARD: Semiautomated, open source software for real-time acoustic detection and localisation of cetaceans," *Proceedings of the Institute of Acoustics*, vol. 30, no. 5, 2008.

[50] R. E. Kalman, "A new approach to linear filtering and prediction problems," *Transactions of the AMSE - Journal of Basic Engineering*, vol. 82, pp. 35 – 45, 1960.

[51] N. Gordon, D. Salmond, and A. Smith, "Novel approach to nonlinear/non-Gaussian Bayesian state estimation," *Radar and Signal Processing, IEE Proceedings*, vol. 140, pp. 107–113, Apr 1993.

[52] N. Gordon, "A hybrid bootstrap filter for target tracking in clutter," *IEEE Transactions on Aerospace and Electronic Systems*, vol. 33, pp. 353 – 8, January 1997.

[53] M. Arulampalam, S. Maskell, N. Gordon, and T. Clapp, "A tutorial on particle filters for online nonlinear/non-Gaussian Bayesian tracking," *IEEE Transactions on Signal Processing*, vol. 50, pp. 174 – 88, February 2002.

[54] Ristic, Arulampalam, and Gordon, *Beyond the Kalman Filter - Particle Filters for Tracking Applications*. Artech House, 2004.

[55] R. Karlsson and F. Gustafsson, "Recursive Bayesian estimation: Bearings-only applications," *Radar, Sonar and Navigation, IEE Proceedings*, vol. 152, pp. 305–313, October 2005.

[56] F. Gustafsson, F. Gunnarsson, N. Bergman, U. Forssell, J. Jansson, R. Karlsson, and P.-J. Nordlund, "Particle filters for positioning, navigation, and tracking," *IEEE Transactions on Signal Processing*, vol. 50, pp. 425 – 37, February 2002.

[57] M. Isard and A. Blake, "Condensation - conditional density propagation for visual tracking," *International Journal of Computer Vision*, vol. 29, no. 1, pp. 5 – 28, 1998.

[58] A. Farina, "Target tracking with bearings-only measurements," *Signal Processing*, vol. 78, pp. 61 – 78, October 1999.

[59] R. Karlsson and F. Gustafsson, "Range estimation using angle-only target tracking with particle filters," *Proceedings of the American Control Conference*, vol. 5, pp. 3743 – 3748, 2001.

[60] C. Hue, J.-P. Le Cadre, and P. Perez, "Sequential Monte Carlo methods for multiple target tracking and data fusion," *IEEE Transactions on Signal Processing*, vol. 50, pp. 309–325, February 2002.

[61] J. Yu, D. Xiao, and X. Yang, "Square root unscented particle filter with application to angle-only tracking," in *Intelligent Control and Automation, 2006. WCICA 2006. The Sixth World Congress on*, vol. 1, pp. 1548–1552, 0-0 2006.

[62] R. J. Urick, *Principles of Underwater Sound*. McGraw-Hill, 3rd ed., 1983.

[63] G. Carter, "Time delay estimation for passive sonar signal processing," *Acoustics, Speech and Signal Processing, IEEE Transactions on*, vol. 29, pp. 463 – 470, jun. 1981.

[64] G. Carter, "Coherence and time delay estimation," *Proceedings of the IEEE*, vol. 75, pp. 236–255, Feb 1987.

[65] W. A. Watkins and W. E. Schevill, "Four hydrophone array for acoustic three-dimensional location," Tech. Rep. 71-60, Woods Hole Oceanographic Institute, Woods Hole, MA, 1971.

[66] J. Spiesberger, "Linking auto- and cross-correlation functions with correlation equations: Application to estimating the relative travel times and amplitudes of multipath," *Journal of the Acoustical Society of America*, vol. 104, pp. 300 – 12, July 1998.

[67] J. Spiesberger, "Finding the right cross-correlation peak for locating sounds in multipath environments with a fourth-moment function," *Journal of the Acoustical Society of America*, vol. 108, pp. 1349 – 52, September 2000.

[68] B. Van Veen and K. Buckley, "Beamforming: a versatile approach to spatial filtering," *ASSP Magazine, IEEE*, vol. 5, pp. 4–24, April 1988.

[69] D. H. Johnson and D. E. Dudgeon, *Array Signal Processing Concepts and Techniques*. Prentice Hall, 1993.

[70] S. D. Richards, D. A. Miles, T. Clarke, and E. J. Harland, "Passive acousitc localization of marine mammals from mobile platforms," in *Proceedings of the Institute of Acoustics Fourth International Conference on Bio-Acoustics*, vol. 29, pp. 133–140, 2007.

[71] O. Adam, J.-F. Motsch, F. Desharnais, N. DiMarzio, D. Gillespie, and R. C. Gisiner, "Overview of the 2005 workshop on detection and localization of marine mammals using passive acoustics," *Applied Acoustics*, vol. 67, no. 11-12, pp. 1061 – 1070, 2006.

[72] D. C. Finfer, P. R. White, T. G. Leighton, M. L. Hadley, and E. Harland, "On clicking sounds in UK waters and a preliminary study of their possible biological origin," *Proceedings of the Institute of Acoustics Fourth International Conference on Bio-Acoustics*, vol. 1, pp. 209–216, 2007.

[73] J. Spiesberger, "Hyperbolic location errors due to insufficient numbers of receivers," *Journal of the Acoustical Society of America*, vol. 109, no. 6, pp. 3076 – 9, 2001.

[74] W. Zimmer, M. Johnson, A. D'Amico, and P. Tyack, "Combining data from a multisensor tag and passive sonar to determine the diving behavior of a sperm whale (Physeter macrocephalus)," *Oceanic Engineering, IEEE Journal of*, vol. 28, pp. 13–28, Jan 2003.

[75] W. H. Press, S. A. Teukolsky, W. T. Vetterling, and B. P. Flannery, *Numerical Recipes in C*. Cambridge University Press, 2nd ed., 1992.

[76] J. Spiesberger and M. Wahlberg, "Probability density functions for hyperbolic and isodiachronic locations," *Journal of the Acoustical Society of America*, vol. 112, pp. 3046 – 52, December 2002.

[77] R. Hartley and A. Zisserman, *Multiple View Geometry in Computer Vision*. Cambridge University Press, 2001.

[78] D. S. Sivia, *Data Analysis A Bayesian Tutorial*. Oxford University Press, 1996.

[79] V. J. Aidala and S. E. Hammel, "Utilization of modified polar coordinates for bearings-only tracking.," *IEEE Transactions on Automatic Control*, vol. AC-28, no. 3, pp. 283 – 294, 1983.

[80] Z. Fei, Z. Xing-peng, C. Xiao-hui, and L. Rui-lan, "Particle filter for underwater bearings-only passive target tracking," in *Computational Intelligence and Industrial Application, 2008. PACIIA '08. Pacific-Asia Workshop on*, vol. 2, pp. 847–851, Dec. 2008.

[81] M. Morelande and S. Challa, "Manoeuvring target tracking in clutter using particle filters," *IEEE Transactions on Aerospace and Electronic Systems*, vol. 41, no. 1, pp. 252 – 70, 2005.

[82] B. Ristic and M. Sanjeev Arulampalam, "Tracking a manoeuvring target using angle-only measurements: algorithms and performance," *Signal Processing*, vol. 83, pp. 1223 – 38, June 2003.

[83] J. V. Candy, *Bayesian Signal Processing Classical, Modern and Particle Filtering Methods*. Wiley, 2009.

[84] S. Bozic, *Digital and Kalman Filtering*. Arnold, 1979.

[85] S. Haykin, *Adaptive Filter Theory.* Prentice Hall, 3rd ed., 1996.

[86] S. M. Kay, *Fundamentals of Statistical Signal Processing - Estimation Theory.* Prentice Hall, 1993.

[87] S. V. Vaseghi, *Advanced Digital Signal Processing and Noise Reduction.* Wiley, 2nd ed., 2000.

[88] S. Julier and J. Uhlmann, "New extension of the Kalman filter to nonlinear systems," *Proceedings of the SPIE - The International Society for Optical Engineering*, vol. 3068, pp. 182 – 93, 1997.

[89] S. Julier, J. Uhlmann, and H. Durrant-Whyte, "A new method for the nonlinear transformation of means and covariances in filters and estimators," *IEEE Transactions on Automatic Control*, vol. 45, no. 3, pp. 477 – 82, 2000.

[90] E. Wan and R. Van Der Merwe, "The unscented Kalman filter for nonlinear estimation," *Proceedings of the IEEE Adaptive Systems for Signal Processing, Communications, and Control Symposium*, pp. 153 – 8, 2000.

[91] R. Allen and S. Blackman, "Angle-only tracking with a MSC filter," in *Digital Avionics Systems Conference, 1991. Proceedings., IEEE/AIAA 10th*, pp. 561–566, Oct 1991.

[92] D. V. Stallard, "Angle-only tracking filter in modified spherical coordinates," *Journal of Guidance Control and Dynamics*, vol. 14(3), pp. 694–696, 1991.

[93] P. N. Robinson and M. R. Yin, "Modified spherical coordinates for radar," *AIAA Guidance, Navigation and Control*, pp. 55–64, August 1994.

[94] R. Van der Merwe and E. Wan, "The square-root unscented Kalman filter for state and parameter-estimation," *2001 IEEE International Conference on Acoustics, Speech, and Signal Processing. Proceedings*, vol. vol.6, pp. 3461 – 3464, 2001.

[95] S. Maskell and N. Gordon, "A tutorial on particle filters for on-line nonlinear/non-Gaussian Bayesian tracking," *IEE International Seminar Target Tracking: Algorithms and Applications*, vol. 2, pp. 1–15, 2001.

[96] C. Hue, J.-P. Le Cadre, and P. Perez, "Tracking multiple objects with particle filtering," *IEEE Transactions on Aerospace and Electronic Systems*, vol. 38, no. 3, pp. 791 – 812, 2002.

[97] M. K. Pitt and N. Shephard, "Filtering via simulation: Auxiliary particle filters," *Journal of the American Statistical Association*, vol. 94, no. 446, pp. 590–599, 1999.

[98] C. Musso, N. Oudjane, and F. LeGland, "Improving regularised particle filters," in *Sequential Monte-Carlo Methods in Practice* (F. G. Doucet, A. de Feritas and N. J. Gordon, eds.), New York: Springer-Verlag, 2001.

[99] S. Maskell, M. Rollason, and D. Gordon, N. Salmond, "Efficient particle filtering for multiple target tracking with application to tracking in structured images," *Image and Vision Computing*, vol. 21, pp. 931–939, 2003.

[100] S. Sarkka, A. Vehtari, and J. Lampinen, "Rao-Blackwellized Monte Carlo data association for multiple target tracking," *Seventh International Conference on Information Fusion*, vol. Vol.1, pp. 583 – 90, 2004.

[101] X. R. Li and V. P. Jilkov, "Survey of maneuvering target tracking. part I: Dynamic models," *IEEE Transactions on Aerospace and Electronic Systems*, vol. 39, no. 4, pp. 1333 – 1364, 2003.

[102] Y. Chan, A. Hu, and J. Plant, "A Kalman filter based tracking scheme with input estimation," *Aerospace and Electronic Systems, IEEE Transactions on*, vol. AES-15, pp. 237–244, March 1979.

[103] P. Bogler, "Tracking a maneuvering target using input estimation," *Aerospace and Electronic Systems, IEEE Transactions on*, vol. AES-23, pp. 298–310, May 1987.

[104] H. Lee and M.-J. Tahk, "Generalized input-estimation technique for tracking maneuvering targets," *Aerospace and Electronic Systems, IEEE Transactions on*, vol. 35, pp. 1388–1402, Oct 1999.

[105] T. Brehard and J.-P. Le Cadre, "A new approach for the bearings-only problem: estimation of the variance-to-range ratio," in *Seventh International Conference on Information Fusion* (P. Svensson and J. Schubert, eds.), vol. 1, pp. 591–8, International Society of Information Fusion, 2004.

[106] R. Singer, "Estimating optimal tracking filter performance for manned maneuvering targets," *Aerospace and Electronic Systems, IEEE Transactions on*, vol. AES-6, pp. 473–483, July 1970.

[107] J. Kendrick, P. Maybeck, and J. Reid, "Estimation of aircraft target motion using orientation measurements," *Aerospace and Electronic Systems, IEEE Transactions on*, vol. AES-17, pp. 254–260, March 1981.

[108] R. F. Berg, "Estimation and prediction for maneuvering target trajectories.," *IEEE Transactions on Automatic Control*, vol. AC-28, no. 3, pp. 294 – 304, 1983.

[109] V. Aidala, "Kalman filter behavior in bearings-only tracking applications," *Aerospace and Electronic Systems, IEEE Transactions on*, vol. AES-15, pp. 29–39, Jan. 1979.

[110] P. J. O. Miller, M. P. Johnson, P. L. Tyack, and E. A. Terray, "Swimming gaits, passive drag and buoyancy of diving sperm whales (Physeter macrocephalus)," *The Journal of Experimental Biology*, vol. 207, pp. 1953–1967, 2004.

[111] S. Watwood, P. Miller, M. Johnson, P. Madsen, and P. Tyack, "Deep-diving foraging behaviour of sperm whales (Physeter macrocephalus)," *Journal of Animal Ecology*, vol. 75, no. 3, pp. 814–825, 2006.

[112] M. Johnson and P. Tyack, "A digital acoustic recording tag for measuring the response of wild marine mammals to sound," *Oceanic Engineering, IEEE Journal of*, vol. 28, pp. 3–12, Jan 2003.

[113] R. Karlsson and F. Gustafsson, "Range estimation using angle-only target tracking with particle filters," *Proceedings of the American Control Conference*, vol. 5, pp. 3743 – 3748, 2001.

[114] S. Blackman, "Multiple hypothesis tracking for multiple target tracking," *Aerospace and Electronic Systems Magazine, IEEE*, vol. 19, pp. 5–18, Jan. 2004.

[115] D. Reid, "An algorithm for tracking multiple targets," *Automatic Control, IEEE Transactions on*, vol. 24, pp. 843–854, Dec 1979.

[116] D. W. Pace, M. Mallick, and W. Eldredge, "Spectral feature-aided multi-target multisensor passive sonar tracking," *Oceans Conference Record (IEEE)*, vol. 4, pp. 2120 – 2126, 2003.

[117] T. Fortman, Y. Bar-Shalom, and M. Sheffe, "Sonar tracking of multiple targets using joint probabilistic data association," *IEEE Journal of Oceanic Engineering*, vol. 8, no. 3, pp. 173–184, 1983.

[118] M. Orton and W. Fitzgerald, "A Bayesian approach to tracking multiple targets using sensor arrays and particle filters," *IEEE Transactions on Signal Processing*, vol. 50, pp. 216 – 23, February 2002.

[119] C. Hue, J.-P. Le Cadre, and P. Perez, "A paricle filter to track multiple objects," in *IEEE Workshop on Multi-Object Tracking*, pp. 61–68, 2001.

[120] G. Casella and E. I. George, "Explaining the Gibbs sampler," *The American Statistician*, vol. 46, pp. 167–174, August 1992.

[121] S. Coraluppi and C. Carthel, "Multi-hypothesis sonar tracking," vol. 1, (Stockholm, Sweden), pp. 33 – 40, 2004.

[122] P. P. A. Storms and F. C. R. Spieksma, "An LP-based algorithm for the data association problem in multitarget tracking," *Computers & Operations Research*, vol. 30, no. 7, pp. 1067 – 1085, 2003.

[123] C. Morefield, "Application of 0-1 integer programming to multitarget tracking problems," *Automatic Control, IEEE Transactions on*, vol. 22, pp. 302–312, Jun 1977.

[124] R. Torelli, A. Graziano, and A. Frarina, "IM3HT algorithm: A joint formulation of IMM and MHT for multitarget tracking," *European Control Conference*, vol. 5, no. 1, pp. 46–53, 1999.

[125] R. Dempster, S. Blackman, and T. Nichols, "Combining IMM filtering and MHT data association for multitarget tracking," pp. 123 –127, mar. 1997.

[126] T. Kronhamn, "Angle-only tracking of manoeuvring targets using adaptive-IMM multiple range models," *IEE Conference Publication*, no. 490, pp. 310 – 314, 2002.

[127] A. Thode, J. Skinner, P. Scott, J. Roswell, J. Straley, and K. Folkert, "Tracking sperm whales with a towed acoustic vector sensor," *Journal of the Acoustical Society of America*, vol. 128, no. 5, pp. 2681 – 2694, 2010.

[128] C. Dubais, M. Davy, and J. Idier, "Tracking of time-frequency components using particle filtering," *ICASSP, IEEE International Conference on Acoustics, Speech and Signal Processing - Proceedings*, vol. I, pp. 9–12 –, 2005.

[129] P. R. White and M. L. Hadley, "Introduction to particle filters for tracking applications in the passive acousitc monitoring of cetaceans," *Canadian Acoustics*, vol. 36, pp. 146 – 152, March 2008.

Appendix A

Particle Filter Algorithms

This appendix presents algorithms for the ASIR particle filter, algorithm A.1, and unscented particle filter, algorithm A.2, discussed in sections 3.6.2 and 3.6.2.

Algorithm A.1 $[\{\mathbf{a}_k, w_k\}^n] = \text{ASIR}\left(\{\mathbf{a}_{k-1}, w_{k-1}\}^{1:N}, \mathbf{b}_k\right)$

for n = 1:N **do**
  Compute $\{\check{\mathbf{a}}_k\}^n$
  Compute weight: $\{\tilde{w}_k\}^n = q\left(n|\mathbf{b}_{1:k}\right) \propto p\left(\mathbf{b}_k|\left\{\check{\mathbf{a}}_k\right\}^n\right)\{w_{k-1}\}^n$
end for
Normalise weights: $\{w_k\}^{1:N} = \frac{\{\tilde{w}_k\}^{1:N}}{\sum_{n=1}^{N}\{\tilde{w}_k\}^n}$
Re-sample set $\{\check{\mathbf{a}}_k\}^{1:N}$:
$[-,-,\{n\}^m] = \text{RESAMPLE}\left(\{\check{\mathbf{a}}_k, w_k\}^{1:N}\right)$
Draw samples from impotance distribution:
for n = 1:N **do**
  Draw sample: $\{\mathbf{a}_k\}^m \sim q\left(\mathbf{a}_k|\{n\}^m, \mathbf{b}_{1:k}\right) = p\left(\mathbf{a}_k|\{\mathbf{a}_{k-1}\}^{\{n\}^m}\right)$
  Assign weight: $\{\tilde{w}_k\}^n = \frac{p(\mathbf{b}_k|\{\mathbf{a}_k\}^m)}{p\left(\mathbf{b}_k|\{\check{\mathbf{a}}_k\}^{\{n\}^m}\right)}$
end for
Normalise weights: $\{w_k\}^{1:N} = \frac{\{\tilde{w}_k\}^{1:N}}{\sum_{n=1}^{N}\{\tilde{w}_k\}^n}$
return $(\{\mathbf{a}_k, w_k\}^n)$

Algorithm A.2 $\left[\{\mathbf{a}_k, \mathbf{P}_k\}^{1:N}\right] = \text{UPF}\left(\{\mathbf{a}_{k-1}, \mathbf{P}_{k-1}\}^{1:N}, \mathbf{b}_k\right)$

for n = 1:N **do**

Update mean and covariance: $\left[\left\{\hat{\mathbf{a}}_k, \hat{\mathbf{P}}_k\right\}^{1:N}\right] = \text{UKF}\left(\{\mathbf{a}_{k-1}, \mathbf{P}_{k-1}\}^{1:N}, \mathbf{b}_k\right)$

Draw importance sample: $\{\mathbf{a}_k\}^n = \mathcal{N}\left(\left\{\mathbf{a}_k; \hat{\mathbf{a}}_k, \hat{\mathbf{P}}_k\right\}^n\right)$

Assign weight: $\{\tilde{w}_k\}^n = \frac{p(\mathbf{b}_k|\{\mathbf{a}_k\}^n)p(\{\mathbf{a}_k\}^n|\{\mathbf{a}_{k-1}\}^n)}{q(\{\mathbf{a}_k\}^n|\{\mathbf{a}_{k-1}\}^n, \mathbf{b}_k)}$

end for

Normalise weights: $\{w_k\}^{1:N} = \frac{\{\tilde{w}_k\}^{1:N}}{\sum_{n=1}^{N}\{\tilde{w}\}^n}$

Resample: $\left[\{\mathbf{a}_k, -, n\}_m^{1:N}\right] = \text{RESAMPLE}\left(\{\mathbf{a}_k, w_k\}^{1:N}\right)$

Assign covariance: $\{\mathbf{P}_k\}_m^{1:N} = \left\{\hat{\mathbf{P}}\right\}_{\{n\}^m}^{1:N}$

return $\left[\{\mathbf{a}_k, \mathbf{P}_k\}^{1:N}\right]$

Appendix B

MHT Intersection Experiment Results

MHT intersection test result plots for results presented in table 6.1 are shown in figures B.1 to B.8. Variable parameters are provided with each figure and invariable parameters are listed in table B.1.

Parameter	**Value**
N_{meas}	6
gate	9
$l^{\text{2nd}}_{\text{threshold}}$	-10000
l_0	-1000
σ	0.2

Table B.1: In variable parameters for MHT intersection tests

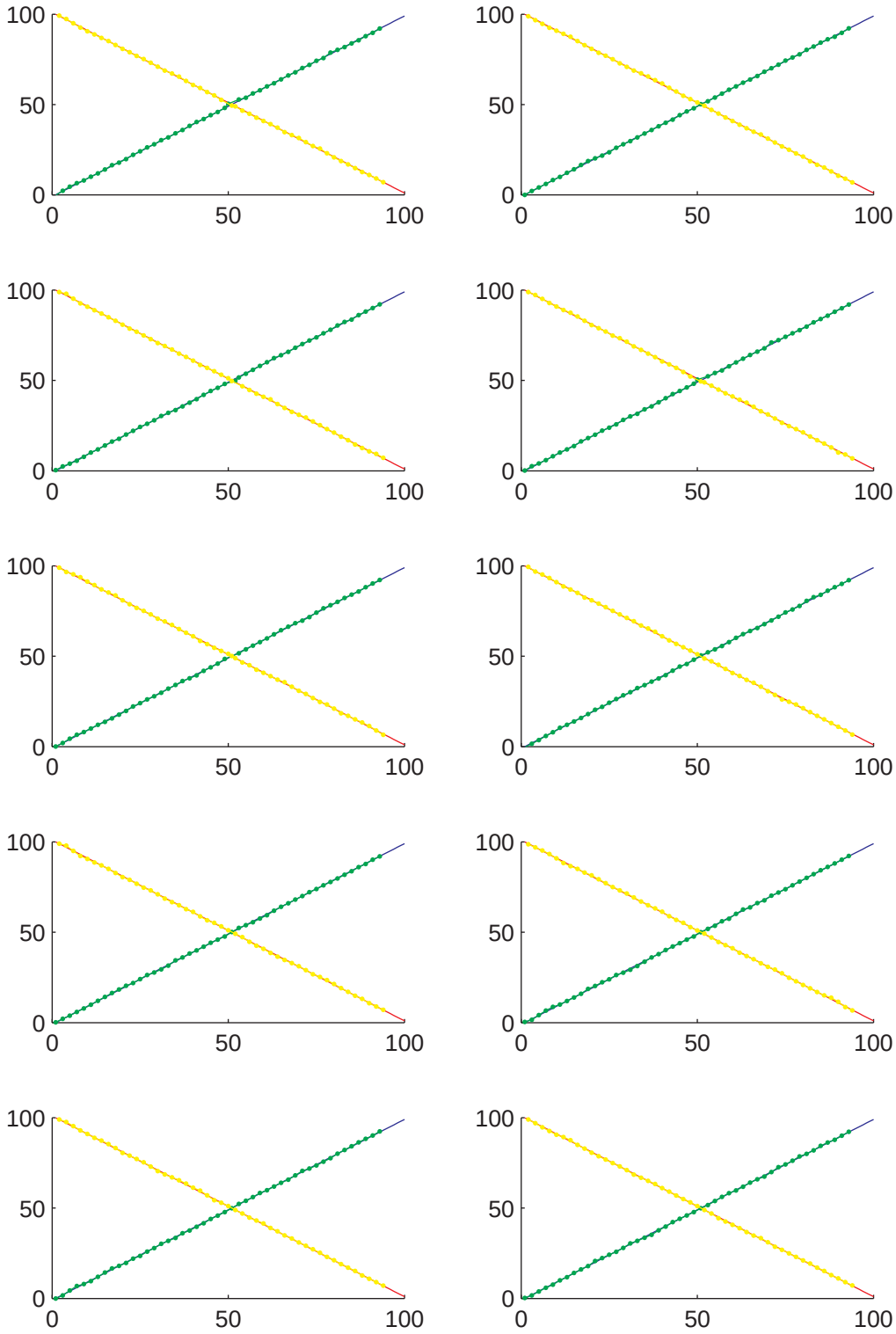

Figure B.1: Intersection angle 90°, system variance $\begin{bmatrix} 0.0025 & 0.005 \\ 0.005 & 0.01 \end{bmatrix}$ and measurement variance 0.1

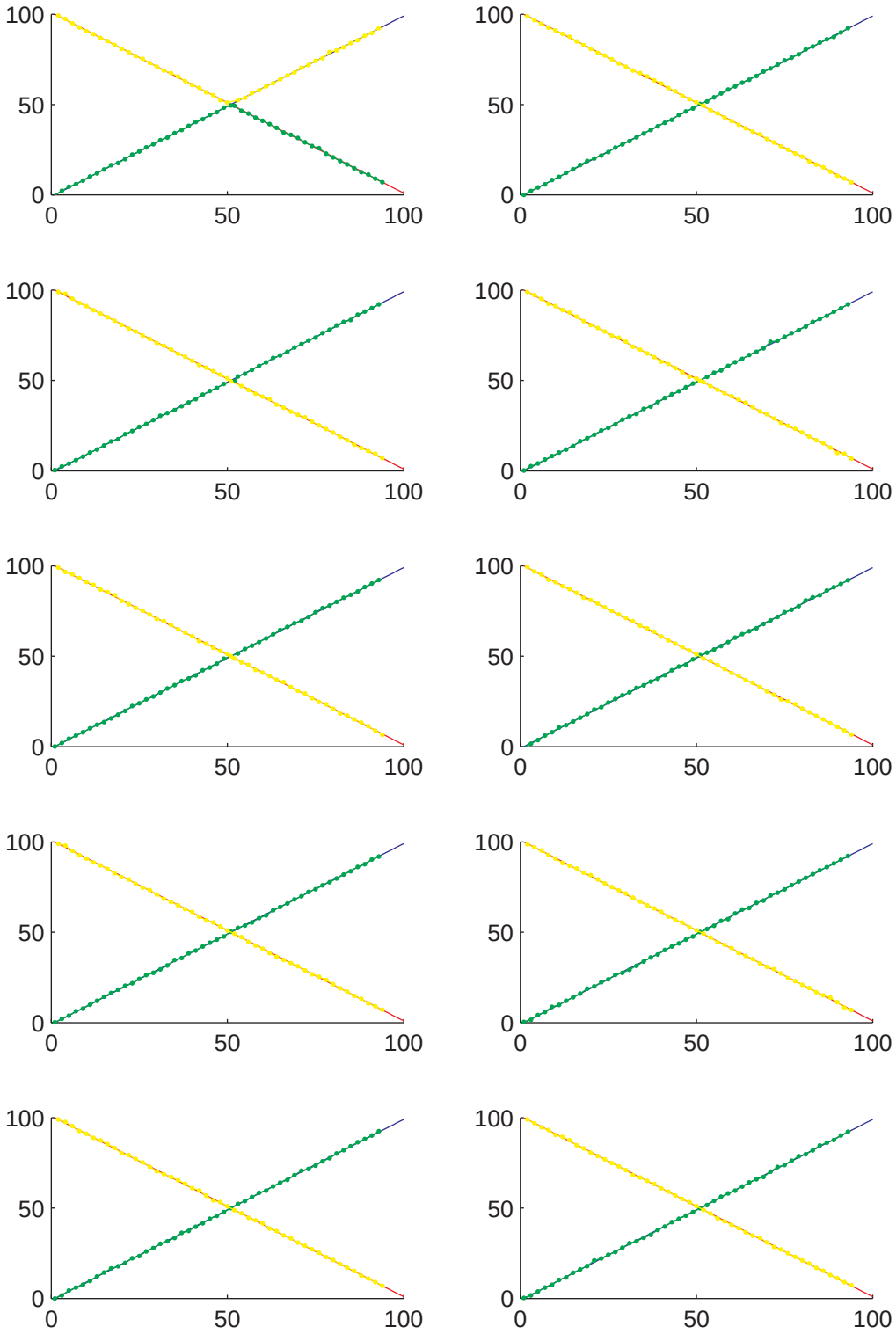

Figure B.2: Intersection angle 90°, system variance $\begin{bmatrix} 0.25 & 0.5 \\ 0.5 & 1 \end{bmatrix}$ and measurement variance 0.1

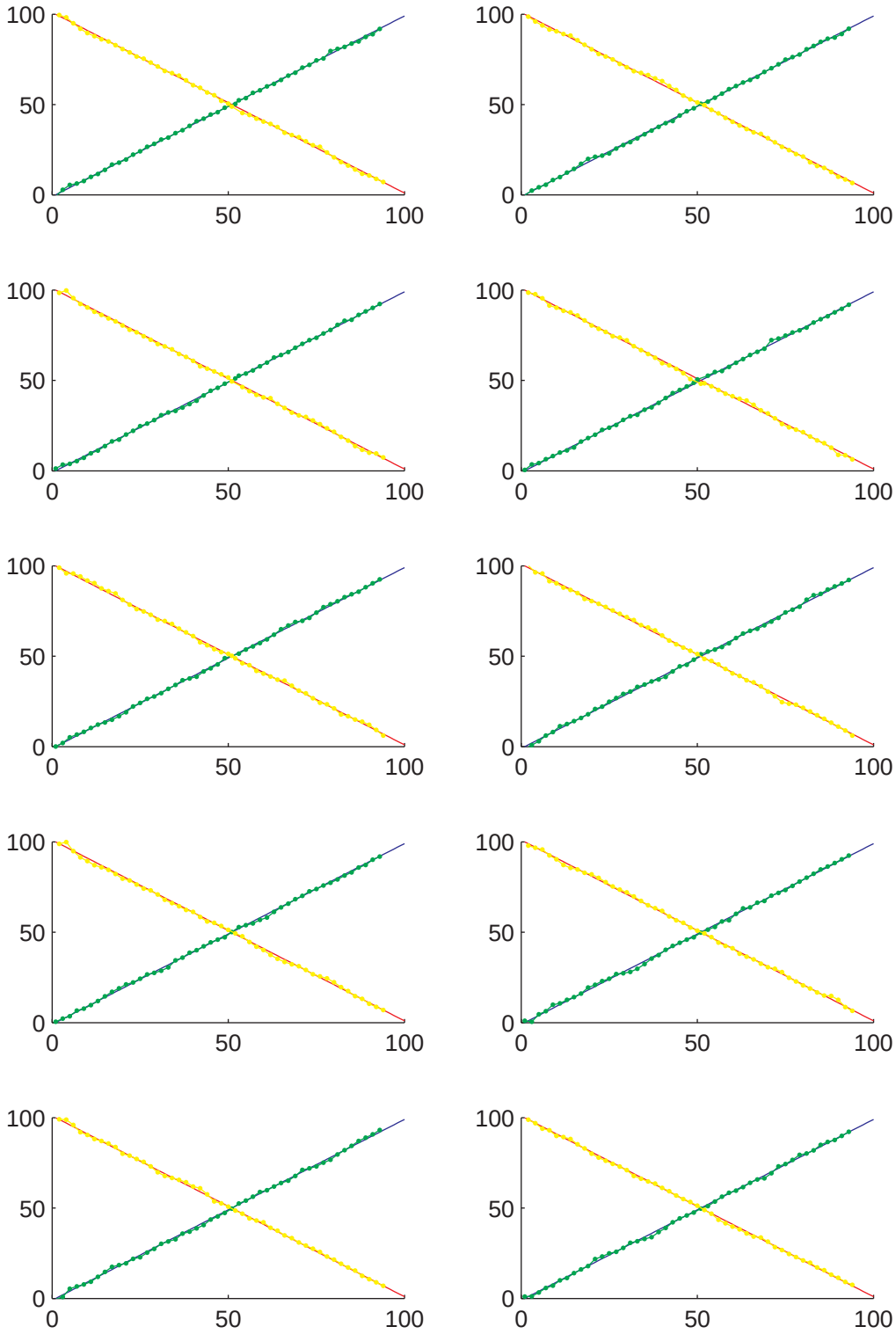

Figure B.3: Intersection angle 90°, system variance $\begin{bmatrix} 0.0025 & 0.005 \\ 0.005 & 0.01 \end{bmatrix}$ and measurement variance 1

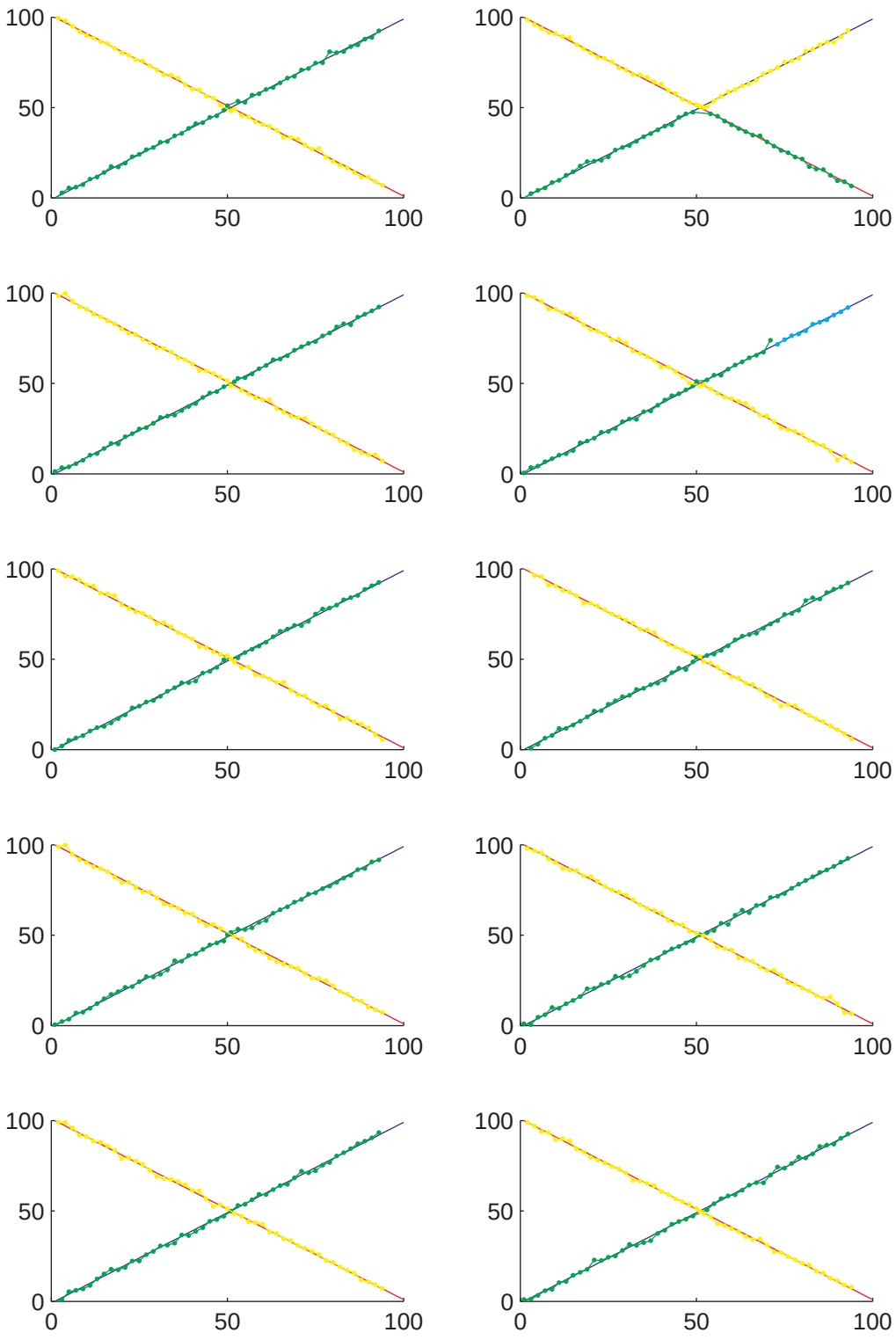

Figure B.4: Intersection angle 90°, system variance $\begin{bmatrix} 0.25 & 0.5 \\ 0.5 & 1 \end{bmatrix}$ and measurement variance 1

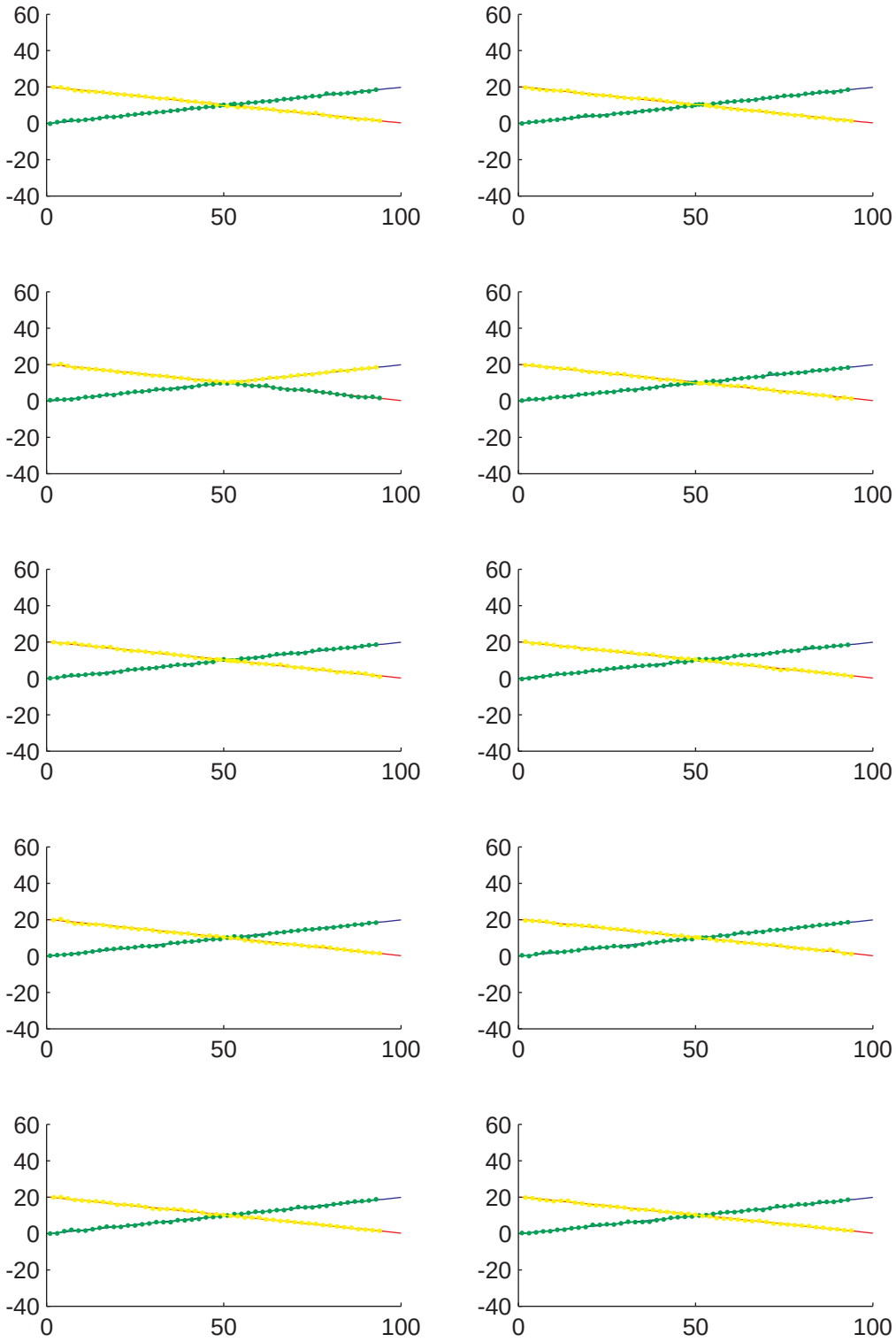

Figure B.5: Intersection angle 18°, system variance $\begin{bmatrix} 0.0025 & 0.005 \\ 0.005 & 0.01 \end{bmatrix}$ and measurement variance 0.1

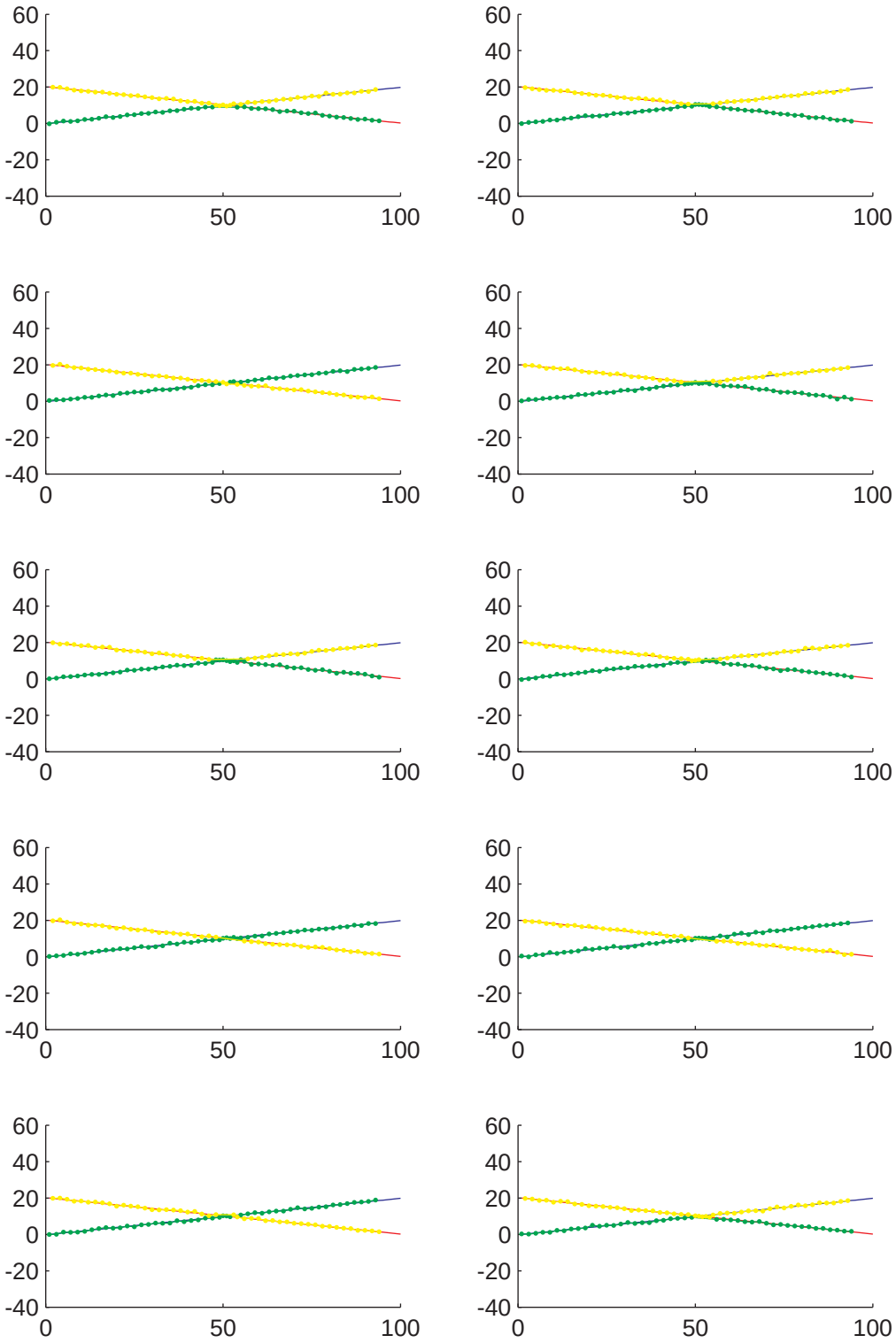

Figure B.6: Intersection angle 18°, system variance $\begin{bmatrix} 0.25 & 0.5 \\ 0.5 & 1 \end{bmatrix}$ and measurement variance 0.1

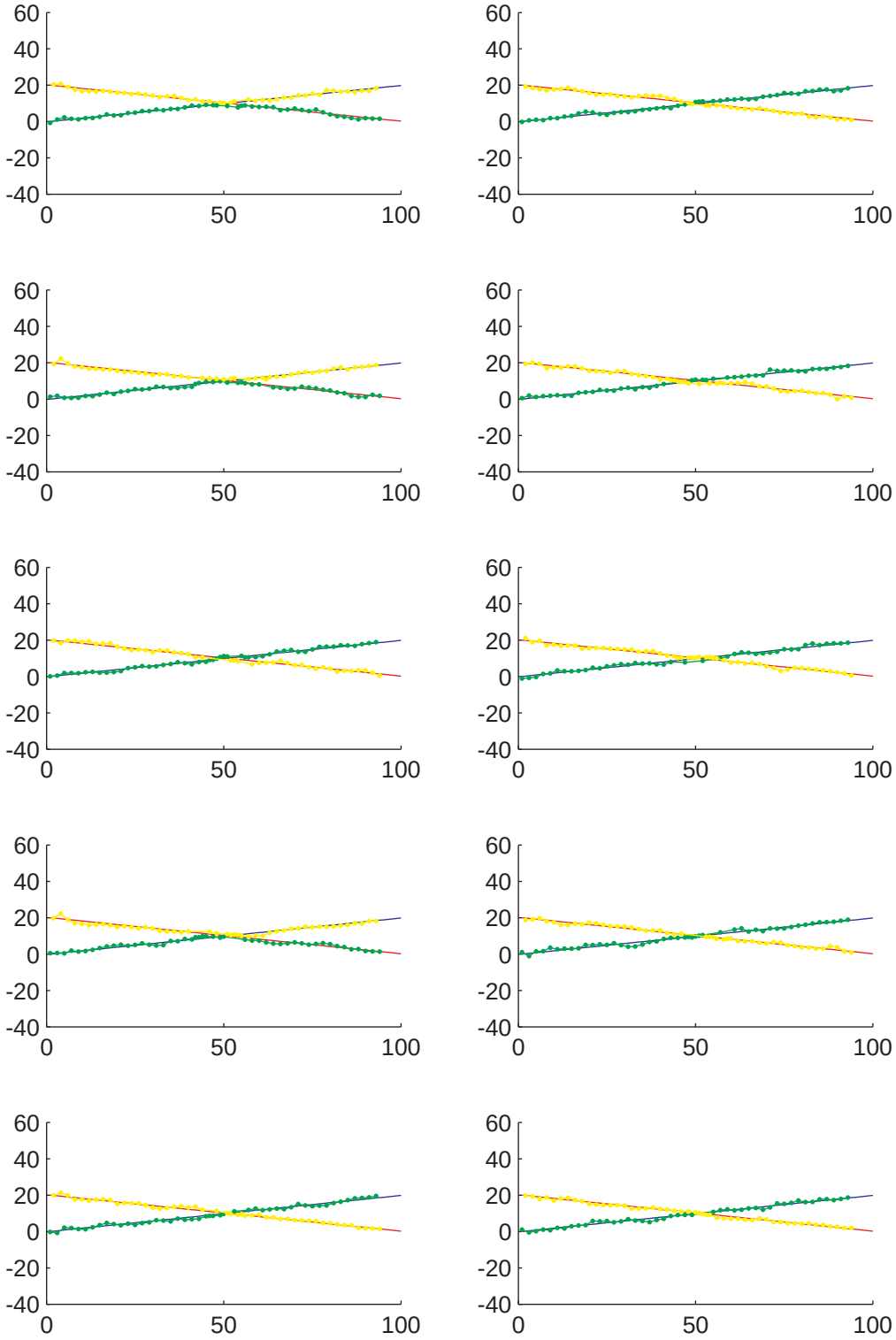

Figure B.7: Intersection angle 18°, system variance $\begin{bmatrix} 0.0025 & 0.005 \\ 0.005 & 0.01 \end{bmatrix}$ and measurement variance 1

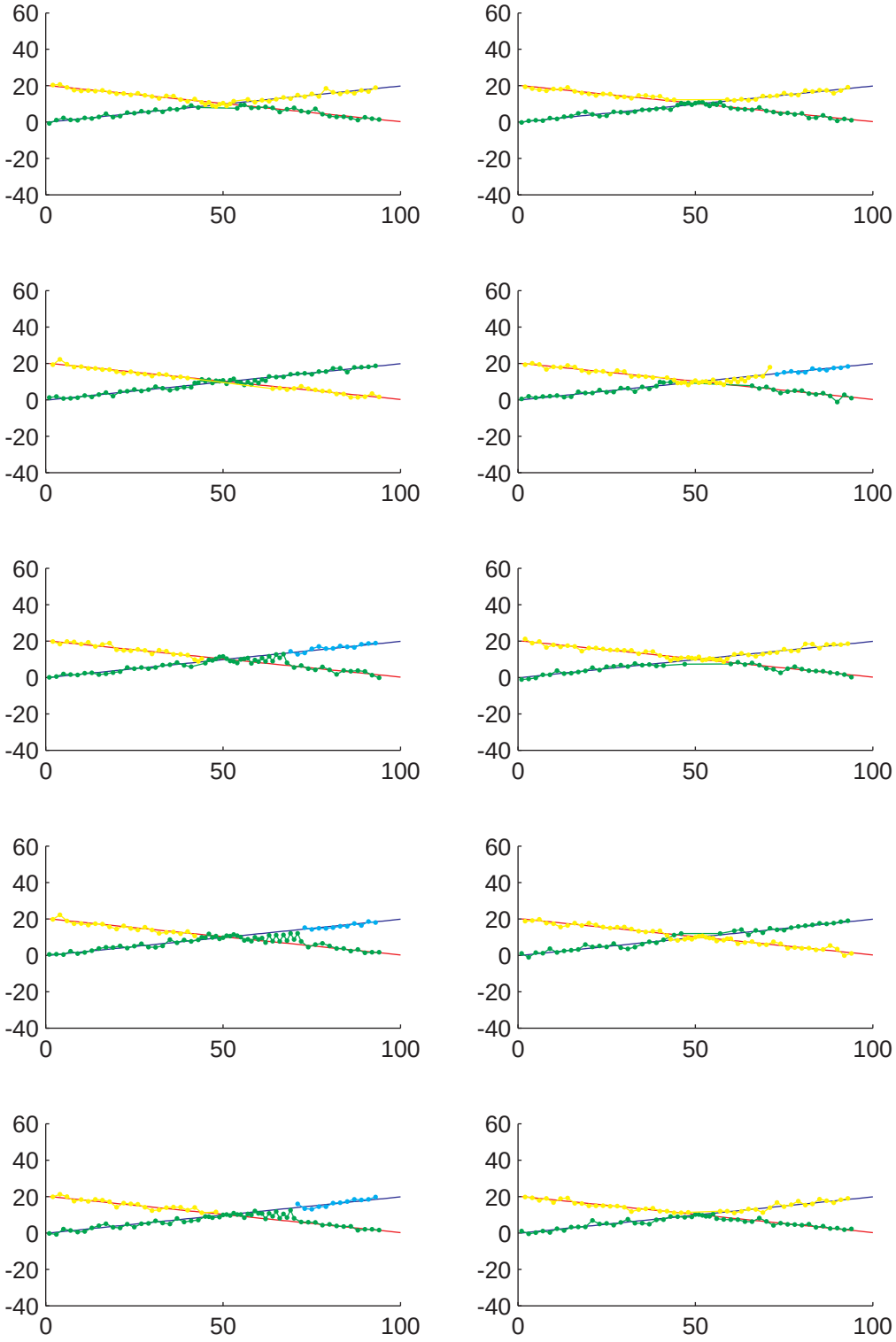

Figure B.8: Intersection angle 18°, system variance $\begin{bmatrix} 0.25 & 0.5 \\ 0.5 & 1 \end{bmatrix}$ and measurement variance 1